UNIVERSITA' DI PADOVA FACOLTA' DI INGEGNERIA

Dipartimento di Ingegneria dell'Informazione

Scuola di Dottorato di Ricerca in Ingegneria dell'Informazione
Indirizzo: Bioingegneria

CICLO XXII

A DETERMINISTIC AND DUCTILE SEGMENTATION ALGORITHM FOR MORPHOLOGIC MRI AND CTA IMAGES AND QUANTITATIVE ANALYSIS OF DYNAMIC SUSCEPTIBILITY-CONTRAST MAGNETIC RESONANCE IMAGING DATA

Direttore della Scuola: Ch.mo Prof. Matteo Bertocco

Supervisore: Ch.mo Prof. Alessandra Bertoldo

Dottorando: Manfredo Atzori

Prefazione

Il lavoro descritto in questa tesi è stato svolto in collaborazione con l'Unità di Ricerca in Brain Imaging e Neuropsicologia (Rubin) del Centro Inter Universitario di Neuroscienze Comportamentali di Udine e Verona (ICBN).
Il gruppo di ricerca studia le alterazioni morfologiche e funzionali del cervello in pazienti affetti da patologie psichiatriche come, ad esempio, la schizofrenia. In letteratura sono presenti numerosi articoli sull'argomento, eseguiti per la maggior parte su immagini ottenute tramite risonanza magnetica strutturale (MRI) o funzionale (fMRI). Le differenze morfologiche e funzionali tra pazienti affetti da schizofrenia e controlli sani descritte dalla letteratura sono di solito molto piccole e caratterizzate da un'elevata variabilità. Questo dipende dalla variabilità del cervello umano, dall'eventuale uso di farmaci da parte dei pazienti (che può influenzare le dimensioni e il comportamento dei tessuti) e dai criteri con cui vengono diagnosticata la schizofrenia (che includono sintomi profondamente diversi).
La realizzazione di procedure in grado di identificare e analizzare con alta accuratezza e sensibilità le piccole differenze morfo-funzionali che esistono tra pazienti affetti da schizofrenia e controlli sani è un problema di elevato interesse allo stato dell'arte.
Il primo obiettivo del lavoro descritto in questa tesi consiste nell'ideazione, la realizzazione e la caratterizzazione di un algoritmo totalmente automatico, robusto, accurato e duttile per la segmentazione del cervello, del fluido cerebro spinale, della materia grigia e della materia bianca in scansioni MRI T1 pesate della testa.
Nel campo delle analisi mediche, la segmentazione può essere definita come l'identificazione dei confini delle diverse strutture anatomiche all'interno delle immagini. Gli algoritmi di segmentazione sono una componente fondamentale nella diagnostica per immagini in quanto svolgono un ruolo fondamentale in numerose applicazioni mediche. Diversi metodi sono stati realizzati per la segmentazione di specifiche strutture anatomiche.
Per analizzare le piccole alterazioni morfologiche del cervello che sono correlate alla malattie psichiatriche, sono necessarie procedure di segmentazione particolarmente sensibili e precise.
Tali procedure devono essere inoltre facilmente modificabili in relazione alle specifiche esigenze di ricerca. L'Unità di Ricerca in Brain Imaging e Neuropsicologia dell'ICBN ha deciso di impegnarsi in questo ambito, anziché utilizzare uno dei software disponibili, perché questi non sono considerati attualmente soddisfacenti per l'ambito di ricerca e perché desiderava avere uno

strumento proprio, ben conosciuto e facilmente adattabile per specifiche esigenze. La duttilità è pertanto, una caratteristica fondamentale per l'algoritmo.
Il secondo obiettivo del lavoro è quello di testare la duttilità dell'algoritmo di segmentazione attraverso la sua applicazione a diverse strutture anatomiche e tecniche di acquisizione di immagini mediche. Le strutture anatomiche studiate comprendono il cranio, il cuore, i reni, la vescica, le vie urinarie, lo scheletro e un tumore del cervello. Le tecniche di acquisizione utilizzate comprendono scansioni MRI T1 e T2 pesate della testa e una scansione di tomografia computerizzata angiografica (CTa) del torace. Tali applicazioni possono essere automatiche o semiautomatiche, a seconda del caso specifico, ma si deve tenere presente che le procedure semi-automatiche sono ideate in modo da essere facilmente automatizzate.
Il terzo obiettivo di questo lavoro consiste nell'ideazione, l'implementazione e la caratterizzazione di una procedura per eseguire voxel per voxel l'analisi Dynamic Susceptibility Contrast MRI (DSC MRI). La DSC-MRI è una tecnica di risonanza magnetica di perfusione che ricorre all'uso di un agente di contrasto esogeno, come il gadolinio, ed è attualmente una delle tecniche più interessanti per lo studio quantitativo dell'emodinamica cerebrale. La DSC MRI permette di ricavare importanti parametri emodinamici che ricoprono un ruolo chiave nello studio di svariate patologie, quali i tumori cerebrali, l'ischemia, l'infarto, ma studi preliminari suggeriscono che questa tecnica possa fornire importanti informazioni cliniche anche sui disturbi neuropsichiatrici (in particolare sulla demenza e la schizofrenia). Allo stato dell'arte non esistono a nostra conoscenza procedure che permettano di confrontare voxel per voxel i parametri ottenuti tramite DSC MRI dei pazienti con quelli dei controlli sani. Questa tecnica potrebbe portare all'individuazione delle regioni anatomiche maggiormente coinvolte in diverse patologie.
Il quarto obiettivo del lavoro consiste nell'analisi delle alterazioni morfologiche e funzionali del cervello, del fluido cerebrospinale, della materia grigia e della materia bianca in pazienti affetti da schizofrenia tramite l'applicazione delle procedure realizzate.
Le alterazioni morfologiche sono quindi studiate attraverso l'analisi delle volumetrie delle strutture anatomiche (segmentate tramite l'algoritmo da me realizzato), mentre le alterazioni funzionali sono studiate utilizzando l'analisi statistica parametrica voxel per voxel dei dati di DSC MRI.

Preface

The work that is described in this thesis has been performed in collaboration with the Research Unit in Brain Imaging and Neuropsychology (RUBIN) of the Inter University Centre for Behavioural Neurosciences of Udine and Verona (ICBN). The research group studies morphological and functional alterations of the Brain in patients affected by psychiatric diseases as schizophrenia.
Several studies have been realized to investigate morphologic and functional alterations in the Brain of patients affected by schizophrenia. Those studies are usually performed on scans of the head acquired using structural Magnetic Resonance Imaging (MRI) or functional MRI.
The morphological and functional differences described in scientific literature between patients affected by schizophrenia and healthy controls are usually very small and characterized by high variability. This fact depends on the high inter-subject variability of the human brain, on the use of drugs by the patients (that can affect the parameters), and on the diagnosis criteria of schizophrenia, that include many different symptoms.
The implementation of procedures able to identify and analyze with high accuracy and sensitivity the small differences that exist between patients affected by schizophrenia and the healthy controls is a challenging problem at the state of the art.
The **first aim** of the work described in this thesis is the ideation, the implementation and the characterization of a fully automatic, robust, accurate and ductile algorithm for the segmentation of the Brain, Cerebro Spinal Fluid, Grey Matter and White Matter in T1 MRI of the head. In medical imaging, segmentation can be defined as the identification of the boundaries of different anatomical structures in the images. Segmentation algorithms are a key component in medical imaging since they play a vital role in numerous biomedical imaging applications. Depending on the state of the art that the processes have reached, various methods have been realized to segment specific anatomical structures.
The procedures to segment the Brain, Cerebro Spinal Fluid, Grey Matter and White Matter in order to analyze the morphological alterations that are related to psychiatric disease need to be very sensitive and accurate. Moreover, the procedures need to be easy modified according to specific needs of the research.
The Research Unit in Brain Imaging and Neuropsychology decided to undertake the way of realizing a segmentation algorithm, rather than using one of the available software, because those are considered unsatisfactory for the research field. Moreover, the RUBIN desired to have an instrument of its own,

well known and easy to be modified according to specific needs. Ductility is therefore a fundamental characteristic for the algorithm.
The realized algorithm is named Orao, it is fully automatic and is based on iterative analyses of global and local intensity distributions, the application of morphologic operators and the analysis of connectivity properties. It shows excellent results in quantitative validation and comparison with the procedures that are most used at the state of the art.
The **second aim** of the work is to test the ductility of the segmentation algorithm through its application to various anatomical structures and medical imaging acquisition techniques. The studied anatomical structures include the Skull, Heart, Kidneys, Urinary Bladder, Urinary Tracts, Bone and a tumour of the Brain. The studied medical imaging acquisition techniques include T1 and T2 weighted MRI of the head and Computed Tomography Angiography of the chest. Those applications are automatic or semiautomatic, depending on the specific case, but it shall be noticed that the semi-automatic applications are ideated in order to be easily automated.
The **third aim** of this work is the ideation, the implementation and the characterization of a procedure to perform voxel by voxel analysis of Dynamic Susceptibility Contrast MRI (DSC MRI). DSC MRI is a technique to perform perfusion magnetic resonance using an exogenous tracer, such as gadolinium, and is one of the most interesting techniques for the quantitative study of the brain hemodynamics. The DSC MRI allows to quantify important hemodynamic parameters that play an important role in the study of several pathologies, such as cerebral tumours, ischemia or infarction, epilepsy, but preliminary works suggest that this technique may provide important clinical information on neuropsychiatric disorders, especially dementia and schizophrenia.
Procedures that can compare voxel by voxel the brains of patients with the ones of the healthy controls are still needed in Dynamic Susceptibility Contrast MRI. A technique to perform DSC MRI analysis voxel by voxel could lead to the identification of the anatomic regions majorly involved in various pathologies as schizophrenia.
The **fourth aim** of the work is the analysis of local and global, morphological and functional, alterations of the Brain, Grey Matter, White Matter and Cerebro Spinal Fluid (CSF) in patients affected by schizophrenia using the procedures realized. First morphological alterations are studied through the analysis of the volumes of the segmented Brain, Grey Matter, White Matter and CSF. Then, functional alterations are studied using statistical parametric DSC MRI mapping.

Introduction

The work that is described in this thesis has been performed in collaboration with the Research Unit in Brain Imaging and Neuropsychology (RUBIN) of the Inter University Centre for Behavioural Neurosciences of Udine and Verona (ICBN). The research group studies morphological and functional alterations of the Brain in patients affected by psychiatric diseases as schizophrenia.

Several studies have been realized to investigate morphologic and functional alterations in the Brain of patients affected by schizophrenia. Those studies are usually performed on scans of the head acquired using structural Magnetic Resonance Imaging (MRI), functional MRI or other techniques.

The morphological and functional differences described in scientific literature between patients affected by schizophrenia and healthy controls are usually very small and characterized by high variability. This fact depends on the high inter-subject variability of the human brain, on the use of drugs by the patients (that can affect the parameters), and on the diagnosis criteria of schizophrenia, that include many different symptoms.

The implementation of procedures able to identify and analyze with high accuracy and sensitivity the small differences that exist between patients affected by schizophrenia and the healthy controls is a challenging problem at the state of the art.

In medical imaging, segmentation can be defined as the identification of the boundaries of different anatomical structures in the images. Segmentation algorithms are a key component in assisting and automating specific radiological tasks, and they play a vital role in numerous biomedical imaging applications such as the quantification of tissue volumes, diagnosis, localization of pathologies, study of anatomical structures, treatment planning, partial volume correction of functional imaging data, and computer integrated surgery. In particular, algorithms for the segmentation of the Brain, Grey and White Matter in Magnetic Resonance Imaging (MRI) structural scans are more and more used in neuroimaging research to analyze volume differences between the patients and healthy controls. Moreover, they can be applied together with the co-registration of different scans and the normalization of the scans to templates in order to localize structural and functional alterations.

Depending on the needs of the research and on the state of the art that the segmentation processes have reached for the specific anatomical structure, three main procedures are used to perform segmentation. Manual segmentation is performed by human tracing of the anatomical structures on the scans. These processes are very time consuming and subjective. Semiautomatic segmentation is performed with algorithms that require the interaction with the human, leading also in this case to time consume and subjectivity. Automatic segmentation of the anatomical structures is performed with automatic

algorithms, which are characterized by accuracy dependent on the specific method. The automatic methods are usually difficult to be modified according to the particular needs of specific researches. The implementation of fully automatic, ductile, robust and reliable segmentation algorithm is therefore a challenging problem in medical imaging analysis, and in particular for the RUBIN and the ICBN.

Procedures that can compare voxel by voxel the brains of patients with the ones of the healthy controls are still needed in some functional MRI techniques (as Dynamic Susceptibility Contrast MRI) to identify the anatomical regions in which exist significant differences.

Quantification of Dynamic Susceptibility Contrast Magnetic Resonance Imaging (DSC MRI) has been applied to study several different pathologies such as cerebral neoplasms and ischemia, but preliminary works suggest that this technique may provide important clinical information on neuropsychiatric disorders, especially dementia and schizophrenia.

The standard evaluation of the DSC MRI quantitative parameters is performed on manually identified regions of interest. Since the procedure is very time consuming, few anatomical regions of the Brain are analyzed in each study, and at the state of the art few studies describe significant hemodynamic alterations related to schizophrenia.

A technique to perform DSC MRI analysis voxel by voxel could lead to the identification of the anatomic regions majorly involved in the pathology

Although the impact of spatial normalization on other functional imaging techniques (as Blood Oxygenation Level Dependent MRI and Positron Emission Tomography) has been addressed, the effects of normalization methods on the sensitivity of DSC MRI analyses are unclear.

Therefore, the implementation and the characterization of a reliable procedure to perform voxel based statistical analysis of the hemodynamic parameters estimated from DSC MRI is an important challenge at the actual state of the art.

The **first aim** of the work described in this thesis is the ideation, the implementation and the characterization of a fully automatic, robust, accurate and ductile algorithm for the segmentation of the Brain, Grey Matter and White Matter in T1 MRI of the head.

The Research Unit in Brain Imaging and Neuropsychology decided to undertake this way, rather than using one of the available software, because those are considered unsatisfactory for the research field. Moreover, the RUBIN desired to have an instrument of its own, well known and easy to be modified according to specific needs. Ductility is therefore a fundamental characteristic for the algorithm.

The **second aim** of the work is to test the ductility of the algorithm through its application to various anatomical structures and medical imaging acquisition techniques. The studied anatomical structures include the Skull, Heart, Kidneys, Urinary Bladder, Urinary Tracts, Bone and a tumour of the Brain. The studied medical imaging acquisition techniques include T1 and T2 weighted MRI of the head and Computed Tomography Angiography of the chest. Those applications are automatic or semiautomatic, depending on the specific case, but it shall be noticed that the semi-automatic applications are ideated in order to be easily automated.

The **third aim** of this work is the ideation, the implementation and the characterization of a procedure to perform voxel by voxel analysis of Dynamic Susceptibility Contrast MRI (DSC MRI). DSC MRI is a technique to perform perfusion magnetic resonance using an exogenous tracer, such as gadolinium, and is one of the most interesting techniques for the quantitative study of the brain hemodynamics. The DSC MRI allows to quantify important hemodynamic parameters that play an important role in the study of several pathologies, such as cerebral tumours, ischemia or infarction, epilepsy, but preliminary works suggest that this technique may provide important clinical information on neuropsychiatric disorders, especially dementia and schizophrenia.

Procedures that can compare voxel by voxel the brains of patients with the ones of the healthy controls are still needed in Dynamic Susceptibility Contrast MRI. A technique to perform DSC MRI analysis voxel by voxel could lead to the identification of the anatomic regions majorly involved in various pathologies as schizophrenia.

The **fourth aim** of the work is the analysis of local and global, morphological and functional, alterations of the Brain, Grey Matter, White Matter and Cerebro Spinal Fluid (CSF) in patients affected by schizophrenia using the procedures realized. First morphological alterations are studied through the analysis of the volumes of the segmented Brain, Grey Matter, White Matter and CSF. Then, functional alterations are studied using statistical parametric DSC MRI mapping.

The first four chapters of this manuscript introduce the research field and the scientific background needed to understand the entire work.

The research field and some basic principles of anatomy and physiology (that are needed to understand the manuscript) are described in Chapter 1.

The medical imaging techniques used to acquire the scans are described in Chapter 2. The greatest part of the data are acquired using structural Magnetic Resonance Imaging. In chapter 2.1 are introduced the physical phenomenon that origins the scans and the principal parameters and factors that determine the differences among different sequences. In chapter 2.2 the DSC-MRI protocol and the model employed to analyze the data are described, with particular attention to the model assumptions. Chapter 2.3 describes Computed Tomography Angiography (CTA).

Chapter 3 is an overview of segmentation in medical imaging. A sufficient knowledge of the problems related to segmentation is fundamental to understand the work, therefore Chapter 3.1 is written with the purpose of introducing them. Chapter 3.2 describes the principal techniques that are used in the sector. Finally, the state of the art is presented in chapter 3.3.

Chapter 4 is an overview of the procedures needed to perform multi-modal imaging analysis. The registration of a source scan to a different scan of the same subject is called co-registration, and it is described in Chapter 4.1. Chapter 4.2 describes the normalization of a scan to a template.

Chapter 5 describes the data set, that includes more than 100 MRI scans of the head acquired with different MRI acquisition sequences and Computed Tomography Angiography data of the chest.

In chapter 6 it is presented and characterized a fully automatic, robust, accurate and ductile algorithm for the segmentation of the Brain, Grey Matter and White

Matter in T1 MRI of the head. The name of the algorithm is Orao. The algorithm is based on deterministic analysis, and is characterized by low assumptions about the brain, high precision, robustness and ductility. Moreover it does not require any pre-processing, nor uses templates, and it works on Nifti, Analyze and Dicom scans. Both detection intensities of the tissues and geometrical aspects influence the intensity distributions, and the problem is quite complex. Therefore Chapter 6.1 describes the problem and the solutions proposed by my method. The segmentation algorithm is subdivided in two parts: the first segments the Brain and the Cerebro Spinal Fluid (CSF), and is described in chapter 6.2. The second segments the Grey and White Matter, and is described in chapter 6.3.

Chapter 7 evaluates the ductility of the algorithm through its application to various anatomical structures and medical imaging acquisition techniques.

Modifications of the algorithm have been done in each case in order to apply it to the particular dataset. Chapter 7.1 describes the application of the algorithm to the segmentation of the skull in T1 MRI scans of the head. Chapter 7.2 describes the application of the algorithm to the segmentation of Tumour and Tumoral Edema in T1 and T2 weighted MRI scans of the head (a secondary aim of this part is to create a mathematical model to simulate the treatment of the tumour with hyperthermia). In chapter 7.3 is described the application of the algorithm to the segmentation of Bone and tissues perfused by contrast medium (Heart, Aorta, Kidneys, Urinary Tracts and Urinary Bladder) in Computed Tomography angiography of the thorax.

Chapter 8 describes the ideation, implementation and the characterization of a procedure to perform voxel by voxel analysis of DSC MRI. Chapter 8.1 describes the state of the art of the field. In Chapters 8.2 and 8.3 the methods for the implementation and the characterization of the algorithm are described, while in Chapter 8.4 the results are presented.

Chapter 9 analyses the alterations of the Brain, the Grey Matter, White Matter and Cerebro Spinal Fluid (CSF) in patients affected by schizophrenia using the procedures realized. Morphological alterations are studied through the analysis of the volumes of the segmented Brain, Grey Matter, White Matter and CSF in Chapter 9.1, while the functional alterations are studied using statistical parametric DSC MRI mapping in Chapter 9.2.

Chapter 1

The Research Field, Anatomy and Physiology Principles

This chapter describes the research field that determined the origin of the work and the basic anatomy principles that are needed to understand it.
Several publications of the medical field enhance correlations between psychiatric illnesses such as schizophrenia and bipolar syndrome and changes in volume, shape and functionality of the brain and its substructures.
The research sector that determined the start of my work is described in chapter 1.1. The principles of anatomy and physiology needed to understand the work are described in chapters 1.2 and 1.3.

1.1 Psychiatric Disease and Morpho-Functional Alterations of the Brain: A Growing Sector

Psychiatric research combines social, biological and psychological perspectives to understand the nature and improve the treatment of mental disorders. Psychiatric clinical researchers look at topics such as neuroimaging, genetics and psychopharmacology in order to enhance diagnostic validity and reliability, to discover new treatment methods, to classify new mental disorders and to understand the origin and the evolution of the pathologies.
Medical imaging analysis is becoming an essential instrument to understand the morphologic and functional alterations of the brain related to psychiatric disease, as can be seen by the number of papers that are written each year on the argument.

1.1.1 Hypotheses on the Origins of Schizophrenia

According to the neurodevelopment hypothesis, the origins of schizophrenia are linked to brain anomalies that arise early during the Central Nervous System development. These structural abnormalities constitute the primary pathological substrate of the disease, and would be responsible of an increased risk of developing it.
The neurodegeneration hypothesis is alternative to the neurodevelopment one. According to this theory, there would be a progressive destruction of neural tissue combined with clinical manifestations of schizophrenia.
Despite of some encouraging data, the hypothesis of neurodegeneration is under discussion *(Weinberger,2001)*. In particular, the Central Nervous System possesses the characteristics of adaptability and plasticity that make it a structure in continuous evolution. The use of different acquisition techniques and different analyses of the images, and the occurrence of physiological changes (due to changes in body weight, hormonal imbalances, assumption of alcohol and drugs) could partly explain the differences obtained by medical imaging analysis results. Physiological changes of the structures and of the distribution of the tissues of the brain (Grey / White Matter) occur as the age advances *(Coffey, 1992)*. However, these physiological changes could be more pronounced and faster in subjects affected by psychiatric disease. Moreover these changes could play a potential role in the pathophysiology of the disorders.
The two theories, of course, could be integrated into a single model instead of cancel each other. Genetic abnormalities arose early during the early brain development (as defects in myelin growth), could be followed in adolescence and throughout lifetime by cerebral neurodegenerative and/or neuroinflammatory aspects.
Another hypothesis, called the disconnection hypothesis, has been made to explain the origin of schizophrenia. Wernicke *(Wernicke, 1906)* had suggested that an alteration of the connectivity between the frontal and the temporal cortex, due to the destruction of the White Matter connecting these areas, could

be the basis of schizophrenia. This idea had been taken up and formulated as precise pathogenetic hypothesis in 1995 by Friston and Frith *(Friston and Frith, 1995)*. One consequence of this theory is that changes should be seen at a supra-regional level, not only in individual structures, but in the connection between these systems. Appears therefore important the study of the White Matter, consisting of axons, that connect the regions of Grey Matter in which abnormalities have been detected *(Sigmundsson, 2001)*.
It was observed that there is a subgroup of schizophrenics who have a reduced physiological asymmetry of some structures of the brain (especially in the frontal and temporal regions) and a decreased lateralization motor cortex, at an early onset of disease *(Maher, 1998)*. It has been suggested that a disturbing factor, (perhaps of genetic origin) could act when the brain becomes asymmetrical, since this moment coincides with the onset of the disease. Therefore the discovery of the factors causing this lateralization could help to identify the genetic factor that predisposes to the development of schizophrenia *(Crow, 1989)*.

1.1.2 Cerebral Volumetric Alterations

Several studies have been realized to investigate the brain globally and the individual brain structures. Usually, these studies have tried to answer the question if the size of the skull and of the brain of the patients affected by schizophrenia were different from those of the healthy controls.
Among the first analyses which found brain differences between schizophrenic and healthy controls, noteworthy is that of Ward *(Ward, 1996)*. It is conducted on works performed between 1972 and 1995 on the size of the brain and on the size of the skull. It was performed on 21 studies with MRI, 2 with Computed Tomography and 4 Post-Mortem.
Another important study is the one realized by Wright *(Wright, 2000)* on works realized with MRI published between 1988 and 1998. This study concerned global and regional brain volumes and the volumes of the ventricles. Studies on subjects with diagnoses related to schizophrenia (which are not specified) were also included. The volume of ventricles results greater of the 15% in people affected by schizophrenia compared to healthy controls. The volume of the entire brain is reduced of the 3%. The Grey Matter is reduced of the 2%, while the White Matter of the 1%. The subjects affected by schizophrenia showed a bilateral reduction of the volume of the frontal lobes, of the temporal lobes, of the amygdale, of the hippocampus, and of the left hemisphere anterior superior temporal gyrus. For most of the structures analyzed the evidence of a sex related effect is only weak. The ventricular enlargement is present in both males and females, and is greater in the males.
A third important analysis *(Sommer, 2001)* is the review of studies published between 1980 and 1999 on anatomical asymmetries in schizophrenia. The conclusions reached by the authors are: the loss of the normal volumetric asymmetry of the brain in subjects affected by schizophrenia due to a decreased lateralization of the brain and the significantly higher incidence of left-handed or ambidextrous in subjects affected by schizophrenia compared to controls.

Currently, the more replicated results in the study of schizophrenia through structural Magnetic Resonance Imaging concern the enlargement of the lateral ventricles and of the cortical sulci, the reduction of the volumes of the structures of the temporal lobe and of the frontal lobe, and the alterations of sub cortical structures *(Shenton, 2001)*.

1.1.3 Blood Perfusion and Functional Alterations

Dynamic Susceptibility Contrast Magnetic Resonance Imaging (DSC MRI) is a method to create high resolution maps of the regional distribution of cerebral blood volume (CBV).
Most DSC MRI studies conducted to date have focused on the evaluation of patients with cerebral neoplasm, ischemia or infarction, and epilepsy. One of the earliest clinical applications of DSC MRI has been to create CBV maps in patients with brain tumours *(Rosen, 1991)*. Using these maps and pathological correlates, it has been shown that differences in local CBV may provide important clinical information in assessing both the type and stage of tumours *(Aronen, 1994;1995)*. Additionally, DSC MRI has proven useful in mapping focal CBV reductions which accompany stroke *(Warach, 1992)*. Increased regional CBV has also been noted during focal status epilepticus using DSC MRI, correlating well with SPECT perfusion and EEG findings *(Warach, 1994)*.
However, preliminary works suggest that DSC MRI may also provide clinically important information for the evaluation of patients with neuropsychiatric disorders, especially dementia and schizophrenia. Additionally, with appropriate modification, DSC MRI may be used to reliably evaluate the effects of pharmacological challenges on cerebral hemodynamic. Since pharmacotherapy is an important component in the treatment of a range of psychiatric disorders, the dynamic assessment of changes in cerebral perfusion associated with drug administration may lead to the development of brain function tests for a wide range of disorders.
However relatively few studies of patients have been published, perhaps owing to the limited availability of the imaging technology.
Functional neuroimaging studies, utilizing PET and SPECT, have consistently reported temporal lobe perfusion abnormalities in the brains of individuals with schizophrenia *(Bajc, 1989; Musalek, 1989; Cleghom, 1990)*.
Blood oxygenation level dependent (BOLD) fMRI *(Ogawa, 1990; Kwong, 1992)* was used to demonstrate a greater occipital cortical response to photic stimulation in schizophrenic patients as compared to age-matched normal control subjects *(Renshaw, 1994)*. This finding has been confirmed by investigators using PET to assess changes in cerebral perfusion *(Taylor, 1997)*.
In order to facilitate the development of more accurate diagnoses and more effective treatments, it is important to undertake studies which are designed to better define the pathophysiological basis of these disorders. In this regard, the development of functional brain imaging techniques such as dynamic susceptibility contrast magnetic resonance imaging (DSC MRI) may hold great promise.

1.1.4 Open Issues

Neuroimaging analysis is one of the most promising sectors in the study of neuropsychiatric disorders, because it offers the possibility to study the neural changes during the evolution of the pathologies. However, many questions are still open, fact that make difficult both to acquire new knowledge and to use the existing one.
The technical complexity of these studies and the probable multifactorial origin of schizophrenia may explain some difficulties. First, it is unclear when the detected alterations of the brain occur, and whether they are progressive *(Lieberman, 2001)*.
According to Sigmundsson *(Sigmundsson, 2001)*, a possible explanation of the inconclusiveness of the literature could be that the alterations of the brain structures are not limited to few and clearly defined areas.
The study of schizophrenia shows a lack of specificity in the morphometric and functional changes observed in the brain. An overlap between the normal range, pathology of schizophrenia and other psychiatric disorders is often displayed *(Sallet, 2003)*. This observation leads to a further problem: even though many brain structures have been investigated, there is general agreement among researchers only on a minority of the found anomalies.
It is therefore clear the importance of the development of more precise and sensitive techniques and analysis procedures to understand the nature and the development of neuropsychiatric pathologies.

1.2 Selected Principles of the Head Anatomy and Physiology

The human head is the uppermost extremity of the body, containing the brain, special sense organs, mouth, nose, ears, and related structures. Most of the tissues are enclosed within the skull.
The head can be anatomically subdivided in the musculoskeletal system (composed by muscles and the skull), the circulatory system, the lymphatic system, the oral cavity, the respiratory system, the nervous system, the endocrine system and the nervous system.
The nervous system is divided broadly into two categories: the peripheral nervous system and the central nervous system. The central nervous system contains the majority of the nervous system and consists of the brain and the spinal cord.

1.2.1 The Brain

The human brain is the centre of the human central nervous system and is a highly complex organ. It has been estimated to contain 50–100 billion neurons.
The adult human brain weights on average about 1.5 kg with a size of around 1130 cm^3 in women and 1260 cm^3 in men *(Cosgrove, 2007)*. It is located in the head, protected by the bones of the skull, suspended in cerebrospinal fluid, and isolated from the bloodstream by the blood-brain barrier.
Situated at the top and covered by the Cerebral Cortex, the cerebrum (subdivided in two cerebral hemispheres) is the largest part of the human brain *(Kandel, 2000)*. Conventionally each hemisphere is divided into four lobes, the frontal lobe, parietal lobe, temporal lobe, and occipital lobe. Underneath the cerebrum lies the brainstem. At the rear of the brain, beneath the cerebrum and behind the brainstem, is the cerebellum, a structure with a horizontally furrowed surface that makes it look different from any other brain area.
The brain can be subdivided in two tissues. The Grey Matter and the White Matter, which are composed by different parts of the same cells: the neurons.
The Grey Matter is composed by the bodies and the dendrites of the neurons. The White Matter is composed by their axons.
While the grey matter mostly covers the surface of the Brain composing the Cerebral Cortex, the White Matter is mostly located inside it connecting different regions of the Grey Matter. Below the fold that separates the right and left hemispheres of the brain, there is a White Matter region with an elongated shape, called the corpus callosum. This region is a necessary path for the axons that connect the right hemisphere to the left. Its posterior part is called the splenius of the corpus callosum, and will be of particular importance during the work. Regarding the White Matter, it is also noteworthy the presence of two lateral ventricles filled with cerebrospinal fluid, a lynfatic liquid.
The cerebral cortex is essentially a sheet of neural tissue, folded in a way that allows a large surface area to fit within the confines of the skull. Anatomists call each cortical fold a sulcus, and the smooth area between folds a gyrus.

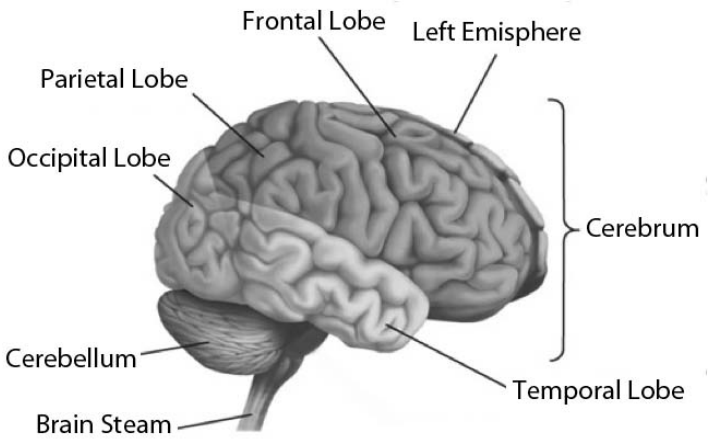

Fig. 1.2.1: Principal anatomical components of the Brain.

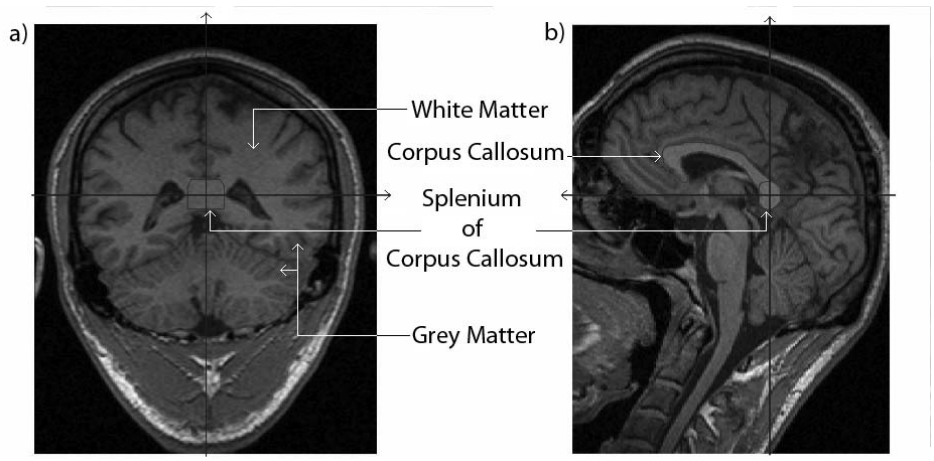

Fig. 1.2.2: Corpus Callosum, Splenium of Corpus Callosum, Grey Matter and White Matter in T1 weighted Magnetic Resonance Imaging of the head. ***a). Coronal view; b) Sagittal view.***

Most human brains show a similar pattern of folding, but there are enough variations in the shape and placement of folds to make every brain unique.
Different parts of the cerebral cortex are involved in different cognitive and behavioural functions. The differences show up in a number of ways: the effects of localized brain damage, regional activity patterns exposed when the brain is examined using functional imaging techniques, connectivity with sub cortical areas, and regional differences in the cellular architecture of the cortex.

1.2.2 The Skull

The human skull is made by 22 bones. All of the bones of the skull (except for the mandible) are joined together by sutures, synarthrodial (immovable) joints formed by bony ossification, with fibres permitting some flexibility.
The neurocranium, a protective vault of bone surrounding the brain and brain steam, is composed by eight bones.
Fourteen bones form the splanchnocranium, which comprises the bones supporting the face. Encased within the temporal bones are the six auditory ossicles of the middle ear.
The bone supporting the larynx, called hyoid bone, is usually not considered as part of the skull, as it is the only bone that does not articulate with other bones of the skull.
The skull also contains the sinus cavities, which are air-filled cavities lined with respiratory epithelium, which also lines the large airways. The exact functions of the sinuses are debatable; they contribute to lessening the weight of the skull with a minimal reduction in strength, they contribute to resonance of the voice, and assist in the warming and moistening of air drawn in through the nasal cavities.

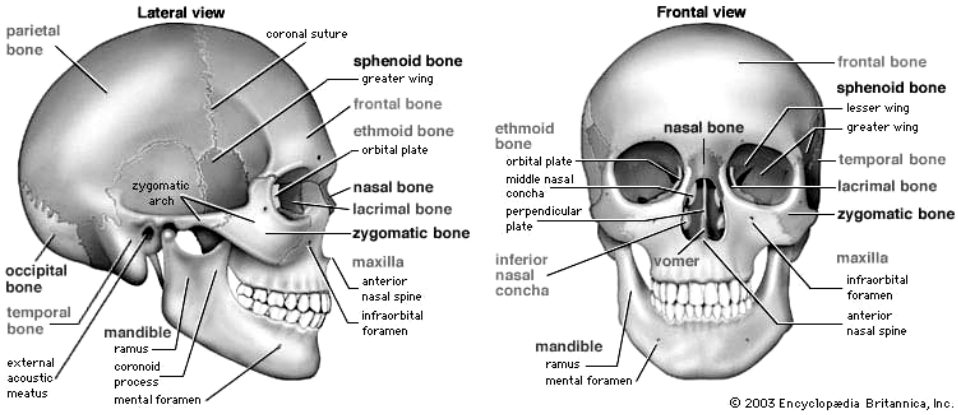

Fig. 1.2.3: Bones forming the Skull.

1.2.3 The Circulatory System

The cerebral circulation refers to the movement of blood through the network of blood vessels supplying the brain. The arteries deliver oxygenated blood, glucose and other nutrients to the brain. The veins carry the deoxygenated blood back to the heart, removing carbon dioxide, lactic acid, and other metabolic products. There are two main pairs of arteries that supply the cerebral arteries and the cerebellum. The internal carotid arteries are the left and right branches of the carotid arteries in the neck which enter the skull (opposed to the external carotid branches which supply the facial tissues). The

internal carotid artery branches into the anterior cerebral artery and continues to form the middle cerebral artery. The vertebral arteries (smaller than the internal carotid arteries) branch from the subclavian arteries, which supply the shoulders, lateral chest and arms. The two vertebral arteries fuse within the cranium into the basilar artery, which supplies the midbrain, the cerebellum, and usually branches into the posterior cerebral artery. The internal carotid arteries are interconnected via the anterior communicating artery within and along the floor of the cerebral vault. The internal carotid arteries are also connected with the basilar artery by the bilateral posterior arteries. The Circle of Willis provides backup circulation to the brain through the interconnection between the internal carotid arteries and the basilar artery along the floor of the cerebral vault.

The venous drainage of the cerebrum can be subdivided in: superficial and deep systems. The superficial system is composed of dural venous sinuses, different from traditional veins because have wall composed of dura mater. The dural sinuses are located on the surface of the cerebrum. The most prominent of these sinuses is the superior sagittal sinus which flows in the sagittal plane under the midline of the cerebral vault. The deep venous drainage is primarily composed of traditional veins inside the deep structures of the brain, which join behind the midbrain to form the vein of Galen. This vein merges with the Inferior sagittal sinus to form the straight sinus which joins the superficial venous system at the confluence of sinuses beneath the occipital protuberance of the skull.

The cerebral blood flow, (CBF), is the blood supply to the brain in a given time. In an adult, CBF is typically 750 ml per minute, or 15% of the cardiac output. This equates to 50 to 54 ml of blood per 100 grams of brain tissue per minute *(Walters, 2007)*. The CBF is tightly regulated to meet the brain's metabolic demands. Too much blood (hyperemia) can raise intracranial pressure, which can compress and damage delicate brain tissue. Too little blood flow (ischemia) results if blood flow to the brain is below 18 to 20 ml per 100 g per minute, and tissue death occurs if flow dips below 8 to 10 ml per 100 g per minute.

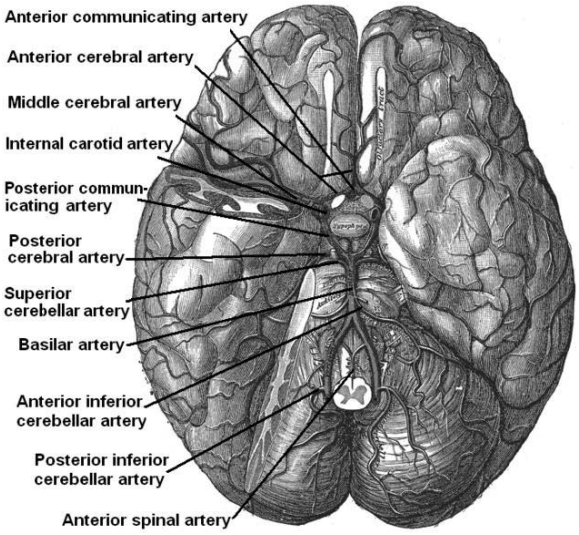

Fig. 1.2.4: Arteries of the Brain.
(Courtesy of Henry Gray, Anatomy of the Human Body, Lea & Febiger, 1918).

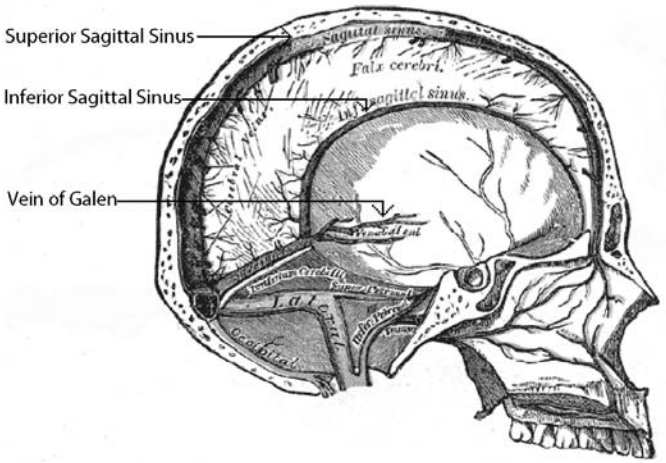

Fig. 1.2.5: Veins of the Brain.
(Courtesy of Henry Gray, Anatomy of the Human Body, Lea & Febiger, 1918).

1.3 Selected Principles of Chest and Abdomen Anatomy and Physiology

In humans, the chest is the region of the body between the neck and the abdomen. It is mostly protected and supported by the ribcage, the spine, and the shoulder girdle.
The chest contains organs (as the heart and lungs), muscles, internal structures (diaphragm, oesophagus and trachea), arteries (as the aorta and the pulmonary artery), veins (as the superior and inferior vena cava) bones (as the spine, the ribcage, the sternum and the scapulae) and the mammary glands.
The thoracic abdomen includes the stomach, the kidneys, the pancreas, the spleen and the lower oesophagus)
The human abdomen is the part of the body between the thorax and the pelvis.
The abdomen contains most of the organs of the digestive tract, as well as several other organs. The spleen, kidneys, adrenal glands also lie within the abdomen, along with many blood vessels including the aorta and inferior vena cava. The urinary bladder, uterus fallopian tubes, ovaries can be considered as either abdominal or pelvic organs.
The abdomen contains an extensive membrane called the peritoneum. Certain organs are completely covered by a fold of peritoneum, whereas some organs (that usually lie closer to the abdominal wall) are covered only at one side.

1.3.1 The Cardiovascular System

The cardiovascular system is an organ system that passes nutrients (such as amino acids and electrolytes), gases, hormones, blood cells, nitrogen waste products, etc. to and from cells in the body.
The main components of the human circulatory system are the heart, the blood, and the blood vessels. The circulatory system includes the pulmonary circulation (a loop through the lungs where blood is oxygenated) and the systemic circulation, (a loop through the rest of the body to provide oxygenated blood to it). An average adult contains 4.7 to 5.7 litres of blood, which consists of plasma, red blood cells, white blood cells, and platelets.
The heart pumps oxygenated blood to the body and deoxygenated blood to the lungs. In the human heart there is one atrium and one ventricle for each circulation.
The deoxygenated blood that arrives to the right atrium is passed into the right ventricle to be pumped through the pulmonary artery to the lungs for re-oxygenation and removal of carbon dioxide.
The oxygenated blood arrives from the lungs to the left atrium and is passed into the left ventricle to be pumped through the aorta to the tissues of the body.
The aorta is an elastic artery. When the left ventricle contracts to force blood into the aorta, the aorta expands. This stretching gives the potential energy that will help maintain blood pressure during diastole, as during this time the aorta contracts passively.

1.3.2 The Kidneys Anatomy

The kidneys are paired organs dedicated to the production of urine as primary function. They are part of the urinary system, but have several secondary functions concerned with homeostatic functions (these include the regulation of electrolytes, acid-base balance, blood pressure and hormones production).
The kidneys are located behind the abdominal cavity, in a space called the retroperitoneum. They are two, one on each side of the spine, approximately at the vertebral level T12 to L3 *(Walter, 2004)*. The right kidney sits just below the diaphragm and posterior to the liver, the left below the diaphragm and posterior to the spleen. Resting on top of each kidney is an adrenal gland (also called the suprarenal gland). The asymmetry within the abdominal cavity caused by the liver typically results in the right kidney being slightly lower than the left, and left kidney being located slightly more medial than the right. The upper (cranial) parts of the kidneys are partially protected by the eleventh and twelfth ribs, and each whole kidney and adrenal gland are surrounded by two layers of fat (the perirenal and pararenal fat) and the renal fascia. Each adult kidney weighs between 125 and 170 g in males and between 115 and 155 g in females *(Walter, 2004)*. The left kidney is typically slightly larger than the right.
The Kidneys are bean-shaped structures, each kidney has concave and convex surfaces. The concave surface is called the renal hilum, and is the point at which the renal artery enters the organ, and the renal vein and ureter leaves.
The substance of the kidney is divided into two major structures: superficial is the renal cortex and deep is the renal medulla.
They receive blood from the paired renal arteries (which branch directly from the abdominal aorta), and drain into the paired renal veins. Each kidney excretes urine into an ureter. The ureteri are a paired structure that empties into the urinary bladder.

1.3.3 The Urinary Tracts and Bladder Anatomy

The urinary bladder is the organ that collects the urine excreted by the kidneys before the disposal by urination.
It is a hollow and distensible muscular organ that sits on the pelvic floor. Urine enters the bladder by the ureteri and exits via the urethra.
In males, the base of the bladder lies between the rectum and the pubic symphysis. It is superior to the prostate, and separated from the rectum by the rectovesical excavation. In females, the bladder sits inferior to the uterus and anterior to the vagina. It is separated from the uterus by the vesicouterine excavation.

1.3.4 The Skeleton Anatomy

The human skeleton is constituted of fused and individual bones, supported and supplemented by ligaments, tendons, muscles and cartilage. It can be described

as a scaffold that supports the organs, anchors the muscles and protects organs such as the brain, lungs and heart. In an adult, the skeleton comprises around 14% of the total body weight *(Marieb, 2006)*.
Fused bones include those of the pelvis and the cranium. The other ones are individual bones
The axial skeleton is constituted by eighty bones. It is formed by the vertebral column (formed by 26 bones), the thoracic cage (constituted by 12 pairs of ribs and the sternum), and the skull.
The axial skeleton transmits the weight from the head, the trunk, and the upper extremities down to the lower extremities through pelvic girdle and the hip joints.
Most of the body weight is located in front of the spinal column. Therefore the spinal column have the erector spine muscles and a large amount of ligaments attached to it, resulting in its characteristic curved shape.
On the axial skeleton there are. 633 skeletal muscles that position the spine, allowing for small movements in the thoracic cage for breathing. Those muscles act also on the head, where they control the minute and complex facial movements *(Tözeren, 2000)*.

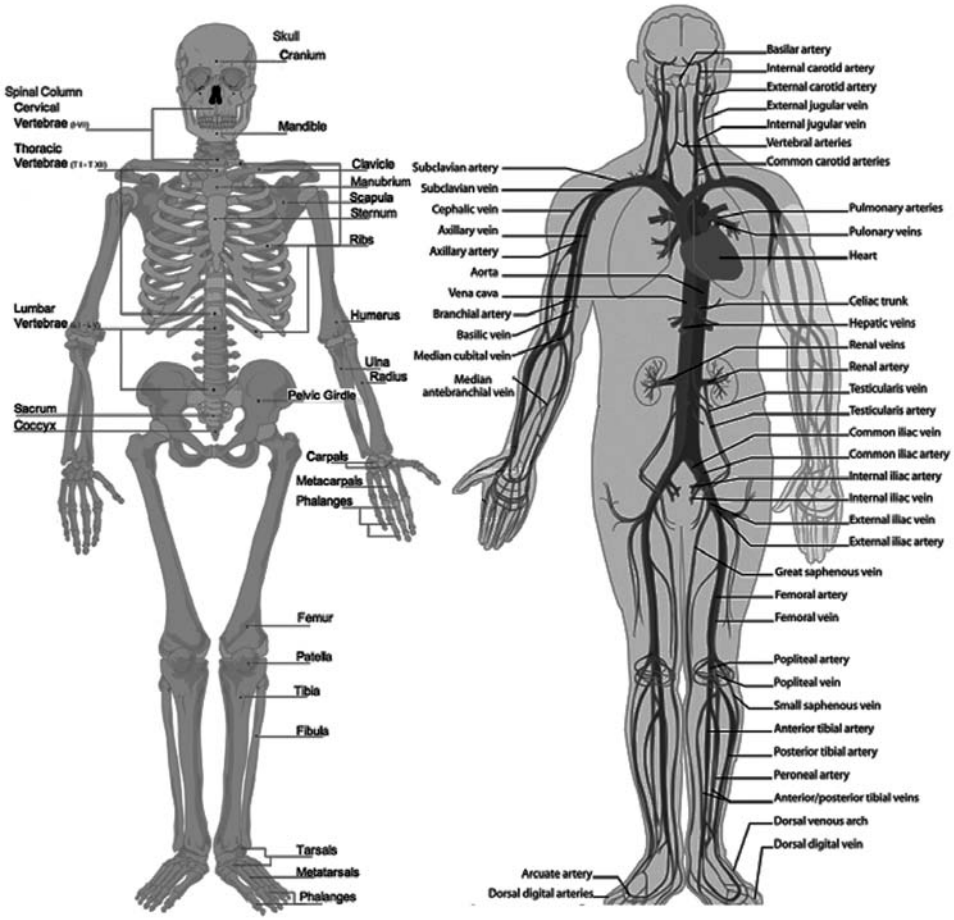

Fig. 1.3.1: Schemes of the human skeleton *(left)* and circulatory system *(right)*.

Chapter 2

Considered Medical Imaging Techniques

This chapter describes the medical imaging techniques used to acquire the data that will be analyzed in the following chapters.
The greatest part of those data is obtained using Magnetic Resonance Imaging *(MRI)*. In Chapter 2.1 it is introduced the physical phenomenon that origins MRI scans and the principal parameters and factors that determine (together with the features of subjects) the differences in the sequences that will be analyzed.
Part of the work will be done on the analysis of Dynamic Susceptibility Contrast (DSC) MRI. Therefore Chapter 2.2 describes the DSC-MRI protocol and the model employed to analyze the data, with particular attention to the model assumptions.
Another part of the work will be done on the segmentation of Computed Tomography Angiography. Chapter 2.3 will introduce this technique.

2.1 Magnetic Resonance Imaging

Magnetic Resonance Imaging (MRI) is a medical imaging technique used in radiology to visualize the internal structure and functionality of the body.
Magnetic Resonance Imaging is a relatively new technology. The first MR image was published in 1973 *(Lauterbur, 1973)* and the first studies performed on humans were published in 1977 *(Damadian, 1977; Hinshaw, 1977).*
MRI provides greater contrast between the different soft tissues of the body than Computed Tomography (CT). This property makes it very useful in neurological, musculoskeletal, cardiovascular and oncological imaging.
MRI uses non-ionizing radiation (high intensity magnetic fields and Radio Frequency (RF) electromagnetic fields), and is therefore a non-invasive technique.
MRI creates 3D scans measuring the local response of the nuclei (with total nuclear spin different from zero, usually Hydrogen) when set into a constant magnetic field and excited with an electromagnetic field of appropriate frequency.

The combination of the spins of all the protons and neutrons inside a generic nucleus and their orbital angular momentum leads to the total nuclear spin vector $\boldsymbol{J}$. The combination of the magnetic moments of all the protons and neutrons inside a generic nucleus leads to a total nuclear magnetic moment vector $\boldsymbol{\mu}$:

Eq. 2.1.1:

$$\vec{\mu} = g_N \mu_N \vec{J} = \gamma \vec{J}$$

Where M_p is the mass of the proton, g_N is the nuclear g factor and μ_N is the nuclear the magneton. The constant γ is called the gyromagnetic ratio and is characteristic of the element in which the nucleus is included (McGervey, 1983).

In the presence of a uniform static magnetic field $\boldsymbol{B_0}$ (directed along the z axis of an arbitrary Cartesian coordinate system), the interaction energy of $\boldsymbol{\mu}$ with $\boldsymbol{B_0}$ is:

Eq. 2.1.2:

$$E = -\vec{\mu} \cdot \vec{B_0} = -\mu_z B_0 = -\gamma \hbar m_I B_0$$

Where $\hbar$ is the Planck Constant and $m_I = \pm ½$..

Nuclei with different value of m_I will have different interaction energy with $\boldsymbol{B_0}$:

Eq. 2.1.3:

$$\Delta E = E_\downarrow - E_\uparrow = \gamma \hbar B_0$$

The difference of population between the nuclei in the two states is determined by their difference in energy, and is governed by the Boltzmann statistics:

Eq. 2.1.4:

$$\frac{N_\uparrow}{N_\downarrow} = e^{\frac{\Delta E}{kT}}$$

Where k is the Boltzmann constant.
Assuming $\boldsymbol{B_0} = 1, 5T$, we have $\Delta E \approx 2, 5 \times 10\text{-}27$ J.
Assuming T = 20 °C, defining N_s as the total number of spins in the system, the difference of population between the nuclei in the two states will be:

Eq. 2.1.5:

$$N_\uparrow - N_\downarrow \cong N_s \frac{\gamma \hbar B_0}{2kT} \cong 2,5 \cdot 10^{-6}$$

The population difference between the two states generates a total magnetization vector **M** (whose components along both the x and y are zero, since $\boldsymbol{\mu}$ has random phase precession around z):

Eq. 2.1.6:

$$\vec{M} = \frac{1}{2}(N_\uparrow - N_\downarrow)\gamma \hbar \vec{k}$$

If the spin system in $\boldsymbol{B_0}$ is upset by his state of thermal equilibrium by a resonant radio frequency pulse $\boldsymbol{B_1}$ (linearly polarized along the x axis), considering the reference system (x',y',z') rotating around the z axis at the Larmor frequency, the total magnetization vector $\boldsymbol{M}$ will precesses around x' with angular velocity *(Liang, 2000):*

Eq. 2.1.7:

$$\vec{\omega}_1 = -\gamma \vec{B}_1$$

The forced precession will lead to a transverse component $\boldsymbol{M_{xy}}$ of $\boldsymbol{M}$.
The inclination angle of $\boldsymbol{M}$ with its equilibrium direction is called Flip Angle:

Eq. 2.1.8:

$$\alpha = \int_0^{\tau_p} \omega_1(t) dit = \int_0^{\tau_p} \gamma B_1^e(t) dt$$

Where τ_p is the duration of the RF pulse.

According the laws of thermodynamics, removed the pulse $\boldsymbol{B_1}$, $\boldsymbol{M}$ will be back to the earlier equilibrium state. This process is not instantaneous, but characterized by the precession of $\boldsymbol{M}$ around $\boldsymbol{B_0}$, called free precession. The free precession depends by the recovery of the *z* component of $\boldsymbol{M}$ (called longitudinal relaxation, characterized by exponential course with time constant T_1) and the suppression of the *xy* components of $\boldsymbol{M}$ (called transverse relaxation, characterized by exponential course with time constant T_2). In general it will be $T2 \leq T1$. The relaxation processes depends on the molecular structure in which the nuclei are included, as from it depends how quickly the nuclei release the energy gained to the surrounding environment.
A number of schemes have been devised for combining field gradients and radio frequency excitation to construct an image; the majority of MR Images today are created by the Two-Dimensional Fourier Transform technique with slice selection or by the Three-Dimensional Fourier Transform technique.
Using the Two dimensional Fourier Transform technique, different sequences can be used to acquire each slice.
One of the most used sequences is called the Spin Echo sequence which is also used to acquire most of the MRI data that will be used in this work. The Spin Echo Sequence can be summarized as follows. First a gradient along the axis *z* is activated. Simultaneously it is produced an RF pulse with a range of frequencies such as to bring into resonance only one slice within the body. (The duration of this pulse is typically about 10 ms and its amplitude is calibrated to

ensure that the magnetization vectors of each volume element of the section precede around $\boldsymbol{B_0}$).
After a fixed time TE/2, the gradient along axis *z* is activated again. At the same time, a wave with same frequency and same application time of the pulse applied before is activated. This pulse will be characterized by an amplitude able to ensure that the total magnetization vector reverses its component along the *z* axis.
In the period between TE/2 and the echo time (TE), the phase encoding gradient G_x is activated in order to mark the signal in the *y* direction.
Finally the frequency encoding gradient G_y is activated in order to mark the signal in the *x* direction. Simultaneously the echo signal emitted from the excited slice is detected.
The time after which this cycle is repeated is called repetition time (TR).
To obtain a *Saturation Recovery* sequence, it is necessary that TR is sufficiently long to allow the excited nuclei to return to the equilibrium state before the beginning of the cycle.
Proton Density, T1-weighted and T2-weighted scans can be obtained by the Spin Echo sequence combining the intensity response of the signal with its temporal components, while the Proton Density scan is obtained analyzing only the signal intensity.

2.2 Dynamic Susceptibility Contrast MRI

Dynamic Susceptibility Contrast *(DSC)* MRI is a first-pass bolus tracking technique, which consists of the injection of a bolus of high-concentrated contrast agent and of the acquisition of a sequence of MR-images to observe the signal changes caused by the bolus passage through the brain.
Figure 2.2.1 shows a typical acquisition protocol: a bolus of contrast agent (i.e. Gadolinium at 0.1-0.3 mmol per kg body weight) is delivered to the patient by a MRI-compatible power injector at a 5-10 ml/sec rate via an antecubital vein. A saline flush of 0.2-0.3 ml/kg follows the bolus injection.
Since bolus transit time is only few seconds, rapid imaging techniques are necessary to obtain sequential images in the wash-in and wash-out periods. Finally, the contrast agent is eliminated by the hepatic biliary system. Typically paramagnetic tracers are employed, such as gadolinium chelate.
The paramagnetic solution causes the presence of inhomogeneities in the applied magnetic field, hence it de-phases the transverse magnetization in the surrounding tissue. Thus it affects transverse relaxation time.
DSC-MRI can be performed by using either Spin Echo (SE) or Gradient Echo (GE) sequences, which are sufficiently fast to track bolus injection *(Simonsen, 2000)*.

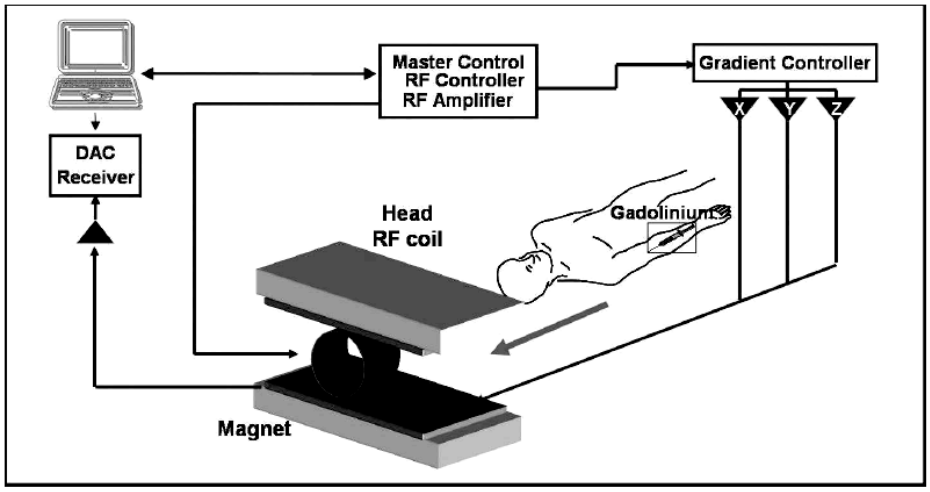

.
Fig. 2.2.1: A typical Dynamic Susceptibility Contrast MRI acquisition setting.

The model used to characterize the dynamic of the tracer which passes through a Volume of Interest *(VOI)* follows the principles of tracer kinetics *(Axel, 1980; Zierler, 1962,1965)* and it is based on the following assumptions:

1. The contrast agent is totally nondiffusible;
2. There is no recirculation of the contrast agent;
3. The Blood Brain Barrier (BBB) is intact, i.e. no tracer leakage can occur from the intravascular to the extra-vascular space;
4. The system is in steady state during the experiment. This means that the blood flow is assumed constant. As a consequence, DSC-MRI technique can be used to estimate either constant flows, or flows varying very slowly within the experiment duration. The latter can be quantified by a series of consecutive experiments;
5. The contrast agent dose must not appreciably perturb the system.

Under these assumptions, the model allows to describe the tissue concentration ($C_{VOI}(t)$) of the contrast agent in a considered VOI at time t using the following functions.
The transport function h(t): consider a unitary amplitude bolus of nondiffusible tracer given in the vessels feeding a VOI at time t=0; h(t) is the density probability function of the transit times of the individual tracer particles passing through the VOI at time t. When a generic input function $C_{AIF}(t)$ is given instead of the bolus, the tracer concentration leaving the VOI at time t ($C_V(t)$) is given by:

Eq. 2.2.1:

$$C_V(t) = C_{AIF}(t) \otimes h(t)$$

h(t) is a system characteristic, it depends on the flow and on the vascular structure of the VOI. It has the dimension 1/time and, when integrated over all time, the area is unitary and dimensionless.

Eq. 2.2.2:

$$\int_0^\infty h(\tau)d\tau = 1$$

The residue function R(t):

Eq.2.2.3:

$$R(t) = 1 - \int_0^t h(\tau)d\tau$$

It represents the tracer fraction present in the VOI at time t after the injection of a non-diffusible tracer bolus with unitary amplitude into the vessels feeding the VOI at time t=0. R(t) is a dimensionless, positive and decreasing function. R(0)=1, that means that at time t=0 the total bolus of contrast agent is ideally present in the VOI. R(t) and, consequently, h(t) completely describe the system; once they are known, the concentration curves of the tracer leaving and remaining in the VOI can be predicted for any given input function.
The Arterial Input Function (AIF): C_{AIF} (t) is the concentration of contrast agent in the vessels feeding the VOI at time t.
Considering the previously defined functions, the model allows to quantify three important parameters characterizing the hemodynamic: the Cerebral Blood Volume (CBV), the Cerebral Blood Flow (CBF), the Mean Transit Time (MTT).
In case of intact BBB, the CBV is defined as the ratio between the blood volume contained in a considered VOI and the VOI volume. CBV can be determined from DSC-MRI images as the ratio between the area under the concentration time curve of the tracer in the VOI(C_{VOI}(t)) and the area under the concentration time curve in the vessels feeding the VOI(C_{AIF}(t):

Eq. 2.2.4:

$$CBV = \frac{k_H}{\rho} \frac{\int_0^\infty C_{VOI}(\tau)d\tau}{\int_0^\infty C_{AIF}(\tau)d\tau}$$

where ρ represents the brain tissue density and k_h accounts for the difference in hematocrit between large and small vessels.

Since only plasma volume is accessible to the tracer, CBV may be split into cerebral plasma volume (CPV) and red cell volume (CRCV) *(Barbier, 2001)*, i.e. CBV=CPV+CRCV. Defining hematocrit as the ratio H=100·CRCV/CBV one can obtain CBV=CPV+H·CBV=CPV/(1−H). Starting from the definition of CBV:

Eq. 2.2.5:

$$CBV = \frac{\text{amount of blood in a VOI}}{\rho \cdot \text{area under the blood input curve}}$$

defining:

Eq. 2.2.6:

$$k_h = (1 - H_{LV})/(1 - H_{SV})$$

and, since the tracer is only in the plasma:

Eq. 2.2.7:

$$CBV = \frac{\text{amount of plasma in a VOI}}{\rho(1 - H_{SV})} \frac{1 - H_{LV}}{\text{area under the plasma input curve}}$$

one can obtain Eq. (2.4):

Eq.2.2.8:

$$CBV = \frac{\int_0^\infty C_{VOI}(\tau)d\tau}{\rho(1 - H_{SV})} \frac{1 - H_{LV}}{\int_0^\infty C_{AIF}(\tau)d\tau} = \frac{k_H}{\rho} \frac{\int_0^\infty C_{VOI}(\tau)d\tau}{\int_0^\infty C_{AIF}(\tau)d\tau}$$

Commonly, CBV units are millilitres per 100 grams of tissue (ml/100g) and microfibers per gram (µml/g).
Another parameter characterizing the VOI is MTT. It is defined as the centre of mass of the distribution h(t) that is the probability density function of the tracer transit time through the VOI. In other words, MTT represents the average time required for any given particle of tracer to pass through the VOI. It can be calculated as:

Eq. 2.2.9:

$$MTT = \frac{\int_0^\infty t \times h(\tau)d\tau}{\int_0^\infty h(\tau)d\tau}$$

keeping in mind Eq. (2.2) and (2.3) one can obtain:

Eq.2.2.10:

$$MTT = \int_0^\infty t \times h(\tau|)d\tau = \int_0^\infty R(\tau)d\tau$$

Applying the Central Volume theorem of indicator dilution theory *(Axel, 1980; Meier, 1954; Stewart, 1894)* MTT can be computed also as the ration between CBV and CBF:

Eq. 2.2.11:

$$MTT = \frac{CBV}{CBF}$$

MTT has dimension of time and it is usually expressed in seconds *(s)*. Considering the above given definition, CBF can be related to the tracer concentration inside a given VOI, the residue function and the AIF:

Eq. 2.2.12:

$$C_{VOI}(t) = \frac{\rho}{k_H} \cdot CBF(C_{AIF}(t) \otimes R(t)) = \frac{\rho}{k_H} \cdot CBF \int_0^t C_{AIF}(t)R(t-\tau)d\tau$$

Eq. (2.2.12) can also be derived from Eq. (2.2.11), (2.2.4) and (2.2.10):

Eq. 2.2.13:

$$CBF = \frac{CBV}{MTT} = \frac{k_H}{\rho}\frac{\int_0^\infty C_{VOI}(\tau)d\tau}{\int_0^\infty C_{AIF}(\tau)d\tau}\frac{1}{\int_0^\infty R(\tau)d\tau}$$

From which:

Eq. 2.2.14:

$$\int_0^\infty C_{VOI}(\tau)d\tau = \frac{\rho}{k_H}CBF \int_0^\infty C_{AIF}(\tau) \cdot \int_0^\infty R(\tau)d\tau$$

thus obtaining Eq. (2.2.12).
The convolution operator can be explained by considering AIF as a sum of consecutive ideal boluses. In the simplest case, i.e. if AIF is an ideal single impulse of amplitude $C_{AIF}(0)$, the tracer concentration within the VOI is the residue function multiplied by the proportionality factor given by the constants $\frac{\rho}{k_H} \cdot CBF \cdot C_{AIF}(0)$. In the generalized case the AIF can be divided into a series of impulses with different amplitudes. The tracer concentration is then given by the integral (i.e. the sum) of the responses to each AIF impulse.
Commonly, CBF units are millilitres per 100 grams of tissue per minute (ml/100g/min) and microlitres per gram per second (μml/g/sec).

2.3 Computed Tomography Angiography

Computed Tomography Angiography (CTA) is a computed tomography technique used to visualize arterial and venous vessels throughout the body.
It is based on Computed Tomography (CT) plus the injection of a bolus of radio-opaque contrast medium. Computed tomography (CT) is a medical imaging method employing digital geometry processing to reconstruct a three-dimensional image of the inside of an object from a large series of two-dimensional X-ray images taken around a single axis of rotation.
X-rays is a form of electromagnetic radiation, characterized by wavelength in the range of 10 to 0.01 nanometres (energies from 120eV to 120KeV).
CT and CTa are invasive techniques, since X-rays are a ionizing radiation.
X-rays are generated by an X-ray tube, a vacuum tube that uses high voltage to accelerate electrons released by a hot cathode. The high velocity electrons collide with a metal target, the anode, creating the X-rays by two different atomic processes: X-ray Fluorescence and Bremsstrahlung.
X-rays are absorbed differently by different tissues. This fact leads to the possibility to construct images of the projections of a body targeted with them, detecting the radiation that passes through it.
In CT, a slice data is generated using an X-ray source that rotates around the object; X-ray sensors are positioned on the opposite side of the body to be imagined. Many data scans are progressively taken. Those data are combined together through mathematical tomographic reconstruction, and a process called Back Projection essentially reverses the acquisition geometry.
The voxels of a scan obtained by CT represent the relative radiodensity.
The attenuation of the tissues is defined in the Hounsfield scale from -1024 (least attenuating) to +3071 (most attenuating). Water has an attenuation of 0 Hounsfield units (HU), air is -1000 HU, trabecular bone is typically +400 HU, cranial bone can reach 2000 HU or more.
CT is used in medicine as a diagnostic tool and as a guide for interventional procedures. Sometimes contrast materials such as intravenous iodinated contrast are used. This is useful to highlight structures such as blood vessels that otherwise would be difficult to delineate from their surroundings. Using contrast material can also help to obtain functional information about the tissues.
CTA is commonly used to examine:

1. The pulmonary arteries in the lungs (to rule out pulmonary embolism).
2. The renal arteries (in patients with high blood pressure suspected of having renal kidneys stenosis).
3. Aneurysms of the aorta or in other major blood vessels. (aneurysms are diseased areas of a weakened blood vessel wall).
4. Dissection of the aorta or its major branches. (peeling away from each other of the layers of the artery wall).
5. Identify aneurysms or arteriovenous malformations inside the brain.
6. Detect artherosclerotic disease.

7. Detect thrombosis in veins (for example large veins in the pelvis and legs)
8. CTA is also used to detect narrowing or obstruction of arteries in the pelvis and in the carotid arteries, which bring blood from the heart to the brain. (When a stent has been placed to restore blood flow in a diseased artery, CTA will show whether it is serving its purpose).

Chapter 3

Segmentation of Anatomical Structures

Magnetic Resonance Imaging (MRI), Computed Tomography (CT), and other medical imaging modalities make possible the mapping of the anatomy of subjects. These technologies have increased the knowledge of normal and diseased anatomy for clinical practice and medical research. Moreover they are a critical component in diagnosis and treatment planning.

Segmentation algorithms are computer algorithms used in medical imaging for the identification of the boundaries between different anatomical structures. They are a key component in assisting and automating specific radiological tasks, and play a vital role in numerous biomedical imaging applications such as the quantification of tissue volumes *(Larie, 1998)*, diagnosis *(Taylor, 1992)*, localization of pathologies *(Zijdenbos, 1994)*, study of anatomical structures *(Worth, 1997)*, treatment planning *(Khoo, 1997)*, partial volume correction of functional imaging data *(Muller-Gartner, 1992)*, and computer integrated surgery *(Grimson, 1997; Ayache 1996)*. In particular, Brain segmentation and Grey and White Matter segmentation algorithms in T1 MRI acquisitions are more and more used in neuroimaging research and clinical practice to combine the anatomical accuracy of T1 structural data to the results obtained by functional MRI, Perfusion MRI, Diffusion MRI, and Diffusion Tensor MRI.

The accuracy of the results of these applications depends by the accuracy of the segmentation algorithms.

Fully automatic, robust and reliable segmentation of human anatomical structures is therefore a challenging problem in medical images analysis.

To well understand the work that is presented in the next chapters, it is useful to know which are the problems that a segmentation algorithm has to face. Such problems will be described in Chapter 3.1. Chapter 3.2 is dedicated to the description of the techniques that are used in the sector. Finally, the state of the art of the field is presented in Chapter 3.3.

3.1 Problem Analysis

3.1.1 Problems Related to the Detection Intensities

The range of intensities with which each tissue is detected depends by the tissue characteristics, by the acquisition technique *(i.e. MRI, CT, CTa)*, by the specific acquisition settings *(i.e. the acquisition sequence in MRI)* and by the characteristics of the specific acquisition apparatus. Therefore, expecting to obtain the same detection intensities for the same tissue in different scans would not be reasonable. It would not be reasonable also to expect the same relationships between the intensities with which different tissues are detected in different scans.
The intensity with which each tissue is detected can also change in different parts of the image, due to inhomogeneities of the scanner (i.e. MRI magnetic field inhomogeneities) or due to other effects (i.e. partial volume effect in CT and CTA).
Nevertheless (once you have acquired the image) the intensity with which each tissue is detected is one of the most important parameters in medical images, since it is the key feature to distinguish one anatomical structure from the others. Therefore, intensity analysis is one of the key factors for the segmentation of anatomical structures.
A contrast medium can be used in order to augment the intensity contrast between a tissue and the surrounding ones, as is done in CTa and DSC MRI. It shall be noticed that, although the contrast medium introduction permits to obtain excellent images of the studied tissues, usually it does not solve segmentation problems.
Since the greatest part of this work is performed on MRI of the head, it is useful to describe with more detail the problem of tissues detection intensities in the scans acquired with this technique.
The average intensities of the principal tissues inside the head, computed on a single slice of a single scan, are shown in Fig.3.1.1.1 as an example. The values obtained for the Grey Matter and Muscle overlap within their standard deviations. The same happens for White Matter and fat tissues. This implies that you cannot use the detection intensity as unique parameter to distinguish the mentioned tissues.
Considering the intensity values obtained for the Grey Matter and White Matter in different scans obtained with the same acquisition sequence and apparatus, (Fig.3.1.1.2) it shall be noticed that the detected ranges change from one scan to another exciding the standard deviations. This fact is determined by differences in the calibration of the acquisition apparatus and in experimental conditions, and makes impossible to define constant intensity ranges for the tissues constant in different scans.

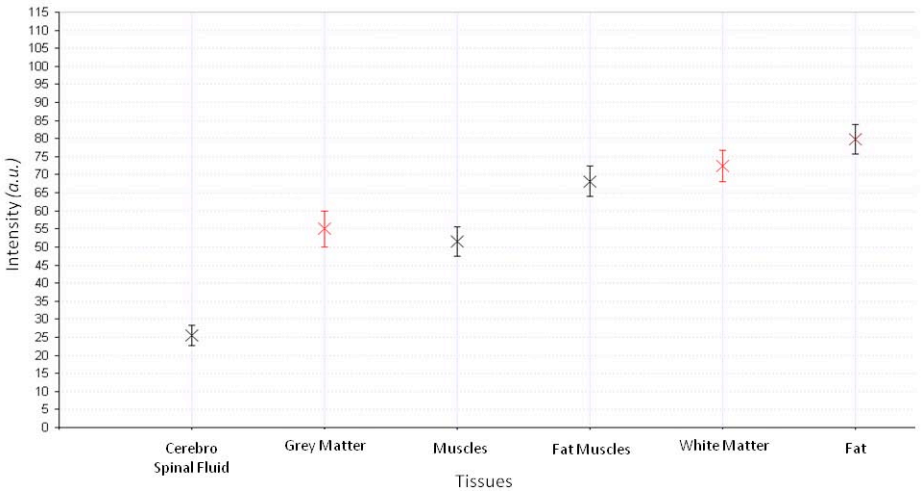

Fig.3.1.1.1: Principal tissues average intensities in a T1-weighted MRI scan of the head.

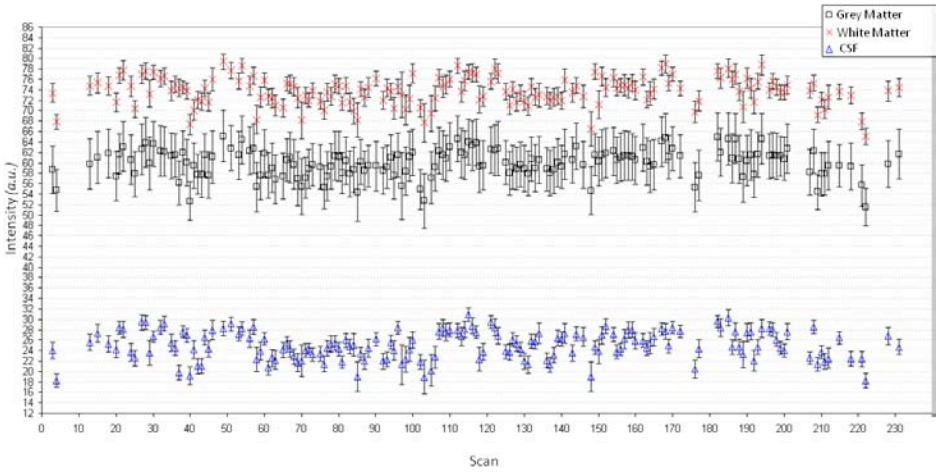

Fig.3.1.1.2: Grey Matter, White Matter, Cerebro Spinal Fluid *(CSF)* intensities in different T1-weighted MRI scans acquired with the same acquisition sequence.

It should be noted however that the relationship between the detection intensities of different tissues in different scans acquired with the same acquisition sequence is approximately constant in each scan *(in particular, in each scan the CSF is detected with lower intensity than the Grey Matter, that is detected in each scan with lower intensity than the White Matter)*. The reason of this has to be searched in the way in which the physical features of the tissues interact with the acquisition sequence. This particular relationship is constant in every T1-weighted scan. This fact make an opportune intensity distribution analysis a useful instrument to analyze one type of acquisition sequences (i.e., the T1-weighted).

3.1.2 Morphologic and Structural Complexity

Different anatomical structures of the human body are characterized by different morphological features.
In example, considering the anatomical structures described in chapter 1.2, the structures in the head are all characterized by an approximate symmetry in the middle sagittal plane. Nevertheless, they are very different on from each other: the skull is characterized by a very thin structure disposed like a shell around the brain, while the brain is a very complex three dimensional approximately convex object.
The structures in the abdomen and in the thorax are in some cases characterized by an approximate symmetry in the middle sagittal plane (the Skeleton and the Bladder), and in some cases they are not (the Heart, the Aorta and each of the Kidneys). Bones with different shapes form the skeleton of the Thorax and Abdomen: the spine is made of short tubular bones with rounded cuspids, the ribs are flat bones, the pelvic girdle is a large flat fused bone and the scapulae are also flat bones. The Bladder is an organ characterized by approximately spherical shape. The Heart does not have any symmetry plane and is characterized by a complex morphology that (in alive subjects) changes continually. The Kidneys are bean-shaped structures; each kidney has concave and convex surfaces.
The morphological differences make the segmentation of the mentioned anatomical structures distinct problems, which are usually approached with different algorithms. In this work those problems will be solved using the same procedure, with little changes from one anatomical structure to another.
The algorithm was initially developed to segment the Brain and its constituent tissues, the Grey Matter and the White Matter, and a large part of this work is dedicated to the segmentation of those structures, that are moreover some of the most morphologically complex in the entire body. Therefore it is necessary to spend some more time on describing the problems related to their morphologic and structural complexity.
The outer surface of the brain is characterized by variable shape depending on the position. It is morphologically simple for substructures as the brainstem the and the White Matter in general. It is very complex for substructures as the cerebral and cerebellar cortex. Those substructures are characterized by the continuous alternation of convex shapes that terminate into concave cuspids. The complexity of those structures is created in order to obtain a large external

surface in comparison with to the underlying volume. The morphologic structure of the inner surface of the Cerebral and Cerebellar Cortex (and therefore the morphology of the outer surface of the White Matter) is strictly related to the complexity of the outer surface of those tissues. The Grey Matter has an approximately thickness of *2-4 mm*. This fact implies that the convex shapes of the external surfaces will be convex shapes also in the inner surface, while the cuspids will become concave surfaces in the inner surface. The presence of holes (like the Ventricles) and of inner anatomical subdivisions make the morphology of the Brain even more complex.
Because of the described structure, the Brain is not usually geometrically connected in different planes (sagittal, coronal or axial). Because of this fact, the use of a three dimensional analysis approach is encouraged.
The mentioned features make the segmentation of the brain a challenging problem in scientific literature.
It shall also be noticed that some morphologic features of the brain make the problem easier in comparison to other anatomical structures. For instance, its coronal symmetry, the approximate emi-roundness of the upper and posterior part of the brain make it possible to approach the segmentation problem with isotropic operations *(as the application of morphologic operators with isotropic structuring elements)*.

3.1.3 Different Tissues Connection

Various anatomical structures are often connected in various parts. The connection is more evident for structures that belong to the same apparatus *(as for structures belonging to the cardiovascular system)* than the others.
If the anatomical structures work together, they need to exchange substances; otherwise they need to be linked one to the other in order to form the body.
Considering the problem of segmenting medical images, the importance of these connections is related to how much they obstruct the segmentation processes.
If the connections are between anatomical structures that are detected by the acquisition apparatus with different detection intensities, they usually do not obstruct the segmentation process. If the connections are between anatomical structures that are detected with similar intensities, they can make the segmentation much more difficult. Because of this fact, the acquisition apparatus and its setting have a fundamental importance for the possibility of segmenting anatomical structures. Magnetic Resonance Imaging is characterized by great possibilities in this perspective, since it differentiates well the tissues.
It shall be noticed that also the use of techniques that well differentiate the various tissues does not eliminate the problems related to tissues connection in segmentation. For example, in MRI of the head, the Brain is connected to other anatomical structures inside the head. Those connections exist in order to connect the Brain to sensory receptors (the Optic Nerves), to connect it to the rest of the Nervous System (the Spinal Cord), to protect it (the meninges), to hold it inside the head and to connect it to the circulatory system. The mentioned tissues are often detected with intensities very similar to the

detection intensities of Grey and White Matter, the principal tissues of the brain.

Considering the CTa of the Thorax and the Abdomen, since the contrast medium moves through the circulatory system, the Heart will be connected to the circulatory system and to the Kidneys by voxels with similar intensity. Moreover the Kidneys will be connected to the Urinary Bladder again by voxels with similar intensity because the contrast medium will be filtered by the kidneys and disposed for urination in the Bladder.
The problems related to geometrical connections of the tissues are probably one of the most challenging problems in the implementation of algorithms for the automatic segmentation of anatomical structures in medical imaging, because it is difficult to identify constant criteria to define the end of one anatomical structure and the beginning of the other in different scans.

3.1.3 Position, Orientation and Dimensions Variability

Another category of issues to be considered for the implementation of segmentation algorithms is related to the variability of the position, orientation and dimensions of the same anatomical structures in different scans.
In different subjects, each anatomical structure is located inside the body approximately in the same position, and it is usually characterized by the same proportions, dimensions and orientation.
But, although the bodies of different subjects are constructed with a similar structure, they are characterized by peculiar features that make each body different from another and each anatomical structure different.
Moreover, the presence of pathologies can affect those variations. This kind of effect can be minimum, as in the case of patients affected by psychiatric diseases as schizophrenia, or higher, as in the case of patients affected by tumours.
The position of the body in different scans is also highly variable. The position and orientation of the body within the data depends by the positioning of the subject into the acquisition apparatus. Usually several precautions are applied during the positioning of the subject in the scanning apparatus. For example, in acquisition of MRI of the head, the subject is lying on a table movable in three directions which is introduced in the apparatus. Its placement inside the acquisition apparatus is adjusted through laser detectors. Supports are set on the table with the aim of positioning the head of the subject correctly. These precautions can locate the head and thus the brain with good accuracy in central position in the scan. However, despite these precautions, differences in the constitution, height, and shape of the head between different subjects lead to changes in different scans.
The techniques used for the positioning of the head into the acquisition apparatus also affect orientation within scan, as one of the most used supports has to be placed below the neck. This support is not usually adjusted in height from one subject to another. In several cases this fact make the subject to keep the head tilted backwards during the course of the analysis.

All of these differences lead to the same problems for the segmentation of medical images.
It is not possible to use constant coordinates for the identification and the segmentation of the same anatomical structure in different scans. It is not moreover possible to use proportion laws alone, since those proportions can change in different directions.
Instead, algorithms keeping account of all the differences, and able to analyze locally the properties of the anatomical structures are needed.

3.2 Techniques

This section describes the most common techniques used in medical images segmentation. For each technique, it is provided an overview of how the method works and discuss its advantages and disadvantages. It shall be noticed that multiple combinations of those techniques are usually applied in segmentation algorithms to solve different problems.

The techniques that are described in this chapter are:

1. Threshold Techniques
2. Mathematical Morphology
3. Watershed Techniques
4. Deformable Models
5. Probabilistic Methods
6. Clustering Techniques

3.2.1 Threshold

Threshold approaches are used to segment scalar images by creating a binary partitioning of the pixels by their intensity values.
A threshold procedure attempts to determine an intensity value, called the threshold value, which separates the image into different classes. The segmentation is then obtained by grouping all pixels with intensity greater (or lower) than the threshold value into one class, and all other pixels into another class.
Determination of more than one threshold value is a process called multithreshold *(Sahoo, 1988)*.
Threshold is a simple and often effective technique to obtain segmentation in images where different structures are characterized by different intensities.
The partition is usually generated interactively, although automated methods do exist *(Sahoo, 1988)*.
Since the threshold operation is implementable in real-time, some interactive methods are based on the visual assessment of the resulting segmentation by the operator.
Threshold approaches are often used as an initial step in a sequence of image processing operations.
The main limitations of this approach are that it does not take into account the geometrical characteristics of the object to be segmented and that it does not take into account possible intensity inhomogeneities of the image. These facts make threshold not useful (if used alone) to segment objects characterized by complex morphology, very sensitive to noise and to artefacts.
For these reasons, variations on classical threshold have been proposed for medical image segmentation that incorporates information based on local intensities *(Li, 1995)* and connectivity *(Lee, 1998)*. A survey on threshold techniques is provided in *(Sahoo, 1988)*.

3.2.2 Mathematical Morphology

Morphological operators are instruments for the analysis and processing of geometrical structures in digital images. They were originally developed for binary images, and were later extended to greyscale functions and images.
The basic idea in binary morphology is to modify an image with a pre-defined shape (structuring element or morphological alteration form) that acts on its surface. The most used morphological alterations forms in three dimensional data analysis are three dimensional spheres and cubes *(Serra, 1982)*.
The basic operations that can be performed using mathematical morphology are erosion and dilation.
Defined E as a n-dimensional Euclidean space, S and A as a closed subsets of E, and the operator:

Eq. 3.2.2.1:

$$B(x) = \{b + x \mid b \in S; x \in E\}$$

the erosion of a A with the morphologic alteration form S can be defined as:

Eq. 3.2.2.2:

$$Erosion_S(A) = \{x \in E \mid B(x) \subseteq A\}$$

Instead, the dilation of a binary matrix A with the morphologic alteration form S can be defined as:

Eq. 3.2.2.3:

$$Dilation_S(A) = \{x \in E \mid B(x) \cap A \neq \varnothing\}$$

3.2.3 Watershed Techniques

Watershed are techniques realized to extract regions of the image that are connected on the basis of some predefined criteria. These criteria can be based on intensity information and/or edges in the image *(Haralick, 1985)*.

In their simplest form, a seed point is manually selected by an operator and the algorithm extracts all the pixels connected to the seed point and characterized by the same intensity value.
Like threshold, watershed techniques are usually used within a set of image processing operations. Their principal disadvantage is that they require the manual or automatic identification of seed points.
Like threshold, watershed is also sensitive to noise and inhomogeneities.

3.2.4 Deformable Models

Deformable models are model-based techniques that delineate region boundaries using closed parametric curves or surfaces that deform under the influence of internal and external forces.
To segment three dimensional scans using this technique, first a closed surface must be placed near the desired boundary. Then it shall be allowed to reach the equilibrium state through an iterative process. The internal forces are computed from within the surface. They are usually defined in order to keep the surface smooth during the deformation.
The external forces are usually derived from the analysis of the data. They are usually defined in order to drive the deformation of the surface towards the desired features of interest.
Mathematically, a deformable model moves according to the equations that define it and seeks the minimum of a given energy functional *(Kass, 1988;)*. An example of a typical bi-dimensional deformable model is described by the following dynamic equation:

Eq. 3.2.4.1:

$$\mu(s) = \frac{\partial^2 x(s,t)}{\partial t^2} + \frac{\partial x(s,t)}{\partial t} = F_{Int} + F_{Ext}$$

where:

$$x(s,t) = x(s,t), y(s,t)$$

is a parametric representation of the position of the model at a given time t, while $\gamma(t)$ and $\mu(t)$ are parameters representing the damping density and the mass density of the model. The internal stretching and bending forces are the most commonly used internal forces represent. The gradient of the data or related functions are the most commonly used external forces.
Deformable models directly generate closed parametric curves or surfaces from images. Moreover they intrinsically incorporate smoothness constraints that provide robustness to noise and spurious edges. These advantages make them a technique useful and stand alone in medical imaging segmentation.

However deformable models are usually very time consuming and they can exhibit poor convergence to boundaries characterized by high concavity or convexity. Moreover they often require human interaction to place the initial model and to choose appropriate parameters.
To solve these problems, much research has been made to reduce the sensitivity to initialization *(Malladi, 1995; Xu, 1998)*. Adaptability of the model to the topology of the anatomical structure has been introduced through implicit representation *(Malladi, 1995)*. This difficulties can be alleviated somewhat through the use of more sophisticated external models of the external forces *(Xu, 1998)*. A complete review on deformable models in medical image analysis can be found in *(McInerney, 1996)*.

3.2.5 Probabilistic Methods

Probabilistic approaches are an important tool for medical image segmentation. They are usually based on standard templates, generated from previously segmented data of the anatomical structure.
The images to be segmented need to be normalized to the atlases, or vice-versa *(Maintz, 1998)*. This process is often called atlas warping. The warping can be performed using linear transformations *(Talairach, 1988; Lancaster, 1997)* or both linear and non-linear transformations *(Collins, 1995; Davatzikos, 1996; Christensen, 1997)*. The second option is more used and more accurate than the first because of inter subject anatomical variability. The atlases are then used as a reference for the segmentation process. Probability approaches have been largely applied in MRI of the Brain.
An advantage of probability approaches is that the labels related to the anatomical structures are transferred during the normalization process.
Moreover, because of the use of the normalization processes, they provide a standard system for studying morphometric properties of the anatomical structures *(Davatzikos, 1996; Thompson, 1997)*.
However, the anatomical variability described in chapters 3.1.1 and 3.1.3 makes difficult to perform accurate segmentations of complex structures even with non-linear registration methods. Therefore they are mostly used together with other methods (i.e. fuzzy clustering) *(Ashburner, 2005)*.

3.2.6 Clustering Techniques

Clustering algorithms are unsupervised methods that analyze the feature space related to the data. They iterate the segmentation of the required number of classes (corresponding to the number of searched tissues) according to the feature vectors and characterize at each step the properties of each class, like training themselves using the available data.
The most commonly used clustering algorithms are the k-means algorithm *(Coleman, 1979)*, the fuzzy c-means algorithm *(Dunn, 1973; Bezdek, 1993)*, and the expectation-maximization algorithm *(Tianhu, 1992; Liang, 1994)*.

The k-means clustering algorithm iteratively computes the mean intensity for each class and segments the image by classifying each pixel in the class with the closest mean *(Jain, 1988)*.
The fuzzy c-means algorithm generalizes the k-means algorithm *(Bezdek, 1993)*, allowing for segmentations based on fuzzy set theory *(Zadeh, 1965)*.
The expectation maximization algorithm applies the same clustering principles assuming that the data can be described by a Gaussian mixture model. At each step it computes the posterior probabilities and the maximum likelihood estimates of the means, covariances and mixing coefficients of the mixture model. The expectation maximization algorithm has demonstrated greater sensitivity to initialization than the k-means or fuzzy c-means algorithms *(Davenport, 1988)*.
Clustering algorithms are sensitive to noise and intensity inhomogenities, since they do not directly incorporate spatial modelling of the anatomical structures. At the same time, since they do not incorporate spatial modelling, they are faster than other methods *(Hebert, 1997)*, as the methods based on deformable models.
Good results have been obtained in decreasing the sensitivity of clustering algorithms to noise and intensity inhomogenities applying them together with other techniques (i.e. Markov random field modelling and Bayesan approaches).

3.3 State of the art

3.3.1 Brain Segmentation in MRI

Numerous algorithms have been implemented for the segmentation of the brain. A large part of them have been projected to work on T1-weighted MRI data, but several algorithms work on different types of acquisition *(Bedell, 1998; Held, 1997)*. Various techniques are used to achieve the segmentation of the Brain with semi-automated or fully automated procedures.
Procedures that use probability techniques use algorithms to normalize the scans to templates, in order to transfer brain labels to each subject *(Christensen, 1996; Collins, 1995)*. These algorithms obtain good results in the segmentation of deep structures of the brain but fail often on the cortical surface due to the large degree of inter-subject variability of sulcal and gyral morphology. Improved atlas techniques that use image registration together with other techniques are having more success in segmentation of complex anatomy structures *(Ashburner, 2005)*.
Sandor et al. *(Sandor, 1997)* developed an automated edge-detection technique using anisotropic diffusion filtering,
A sequence of morphological operators and Marr–Hildreth edge detection has been used by Shattuck et al. *(Shattuck, 2001)* to segment the brain.
Brain identification based on Grey Matter and White Matter intensity estimation, connected component determination, and morphology operations obtained good results *(Lemieux, 1999)*. These techniques have been improved and extended to include the Cerebro Spinal Fluid by *Lemieux et al. (2003)*.
Deformable templates also have been used as guides. The external forces in this cases are usually determined by image intensity analysis aimed to identify the Grey Matter or CSF border. Instead the internal forces usually are based on smoothness constraints that mime general properties of the brain *(MacDonald, 2000; Smith, 2002)*.
Currently, the most used software to perform Brain segmentation in the field of Brain imaging are three: SPM (Statistical Parametric Mapping, written by the Wellcome Department of Imaging Neuroscience at University College London, UK), FSL (FMRIB Software Library, written by the Analysis Group, FMRIB, Oxford, UK) and FreeSurfer (written by a collaboration between the Massachusetts Institute of Technology and the Harvard University).
Statistical Parametric Mapping (SPM) *(Ashburner, 2005)* uses an approach based on probabilistic atlases combined with fuzzy clustering. FMRIB Software Library (FSL) combines an approach based on intensity distributions analysis and deformable models *(Smith, 2002)*. FreeSurfer combines an approach based on watershed algorithms, deformable surfaces and brain atlases *(Sègonne, 2004)*. It shall be noticed that Freesurfer is very time consuming compared to other software (the processing of one scan can consume 12-24 hours in comparison with the 15-30 minutes requested by FSL and SPM).
Various publications evaluate the most used software for the segmentation, while few literature describe the properties of the other software, probably because they are usually difficult to obtain and to be applied.

In particular, two recent publications shall be analyzed to understand the performances of the software at the state of the art. Two senior members of IEEE, Nasser Kehtarnavaz and Issa Panahi *(Tsang, 2008)*, described the values that are shown in Table 3.3.1.1 in the evaluation of the sensitivity and specificity of SPM and FSL on the Internet Brain Segmentation Repository (IBSR). Shattuck et al. obtained the values that are shown in Table 3.3.1.2 during the evaluation of the Jaccard and Dice Indexes, the Sensitivity and the Specificity of the software on which are based FSL and FreeSurfer. This comparison is performed on the on-line segmentation validation engine realized by the Laboratory of Neuro-Imaging (LONI) of the University of California, Los Angeles *(Shattuck, 2009)*.

Algorithm	Sensitivity	Specificity
FSL	0.746	0.986
SPM	0.780	0.988

Table 3.3.1.1: Brain segmentation metrics computed for FSL and SPM on the IBSR Dataset.

Algorithm	Jaccard	Dice	Sensitivity	Specificity
FSL	0.9400 ±0.0089	0.9691 ±0.0048	0.9627 ±0.0117	0.9957 ±0.0014
Freesurfer HWA3	0.8537 ±0.0184	0.9210 ±0.0107	0.9992 ±0.0003	0.9695 ±0.0053

Table 3.3.1.2: Brain segmentation metrics computed for FSL and Freesurfer on the LONI Segmentation validation Engine.

The exact meaning of the reported indexes *(Sensitivity, Specificity, the Jaccard and Dice indexes)* and the methods used to perform the evaluations are accurately described in chapter 6, where they are applied to the evaluation of the segmentation algorithm.
For the purpose of this chapter, it is just useful to note that the reported indexes values can still be improved for SPM, FSL and Freesurfer.
It shall be noticed also that the probabilistic approach adopted by SPM makes it intrinsically low sensitive to small differences between different subjects, and that the high time consume of Freesurfer makes it difficult to use it habitually.
The described state of the art enhances that the implementation of a deterministic brain segmentation algorithm, characterized by high sensitivity, specificity, constancy, ductility (in order to be easily adapted to the requirements of the research laboratory) and ability to detect small inter-subjects differences is a challenging problem for the research in medical imaging analysis.

3.3.2 Grey Matter, White Matter and Cerebro Spinal Fluid Segmentation in MRI

The segmentation of three-dimensional anatomical brain images into tissue classes has applications in both clinical and research sectors. Some methods to segment MRI of the Brain into White Matter, Grey Matter and Cerebro Spinal Fluid have been proposed in the literature.
A part of these algorithms is based on the analysis of the intensity values. Threshold is the most intuitive classification approach *(Ganser, 2004)*. One common difficulty of these methods consists in the realization of algorithms for the automatic selection of the threshold level: some selection approaches have been proposed based on the analyses of the intensity distributions *(Shan, 2002; Jack, 2001)*. Usually these methods are used in combination with morphological operators and region growing techniques *(Stokking, 2000)*.
Methods that are based on Bayesian statistical analysis *(Shattuck, 2002)* are also frequently used. These methods are often used also together with clustering algorithms *(Marroquin, 2002)*.
Other classification methods include neural networks *(Valdes-Cristerna, 2004)* and methods based on Random Model Fields *(Zavaljevski, 2000; Ruan, 2000)*.
Methods based on geometric deformable models are also used. Several external driving forces, derived from brain MRI, have been proposed based on image gradient *(Suri, 2001)*, image intensity *(Chan, 2001)*, and probability density function of tissue classes. Two coupled level set surfaces were proposed by Zeng et al. *(Zeng, 1999)* for cortex segmentation from 3-D MR images, assuming a constant thickness range of the cortical mantle. A similar geometric variational formulation for the propagation of two coupled bounding surfaces was proposed also by Goldenerg et al. *(Goldenberg, 2001)*. The combination of clustering and deformable models has been proposed *(Ballester, 2000)*, while the combination of Bayesian analysis and active surface method have also been proposed *(Shen, 2001)*.
The fully automation of the segmentation process is very important for clinical applications and clinical research. In these sectors the number of subjects to be analyzed is large and the time available is limited.
It shall be noticed that several of the mentioned methods use semi-automated procedures that still require the supervision or the intervention of the operators.
Full automation is achieved using automatic parameter tuning *(Shan, 2002)*, automated initialization *(Stokking, 2000)*, and combination with atlas information *(Marroquin, 2002)*.
The software mentioned in the previous chapter as the most used for Brain segmentation in Brain imaging research (SPM, FSL and Freesurfer) are also the most used also for the segmentation of Grey Matter, White Matter and CSF. Statistical Parametric Mapping (SPM) *(Ashburner, 2005)* uses also for this topic an approach based on probabilistic atlases combined with fuzzy clustering. FSL combines an approach based on maximum likelihood classification with hidden Markov Random Fields *(Zhang, 2001)*. FreeSurfer combines an approach based on template matching, and intensity, geometry and connectivity analysis *(Dale, 1999; Fischl, 1999)*.

Also in this case, various publications evaluate the most used software for the segmentation, while few literature describe the properties of the other software, probably because they are usually difficult to obtain and to be applied.
In particular, Nasser Kehtarnavaz and Issa Panahi describe the Dice coefficients values shown in Table 3.3.2.1 during the evaluation of Grey Matter results from SPM and FSL on the Internet Brain Segmentation Repository (IBSR) *(Tsang, 2008)*.

Algorithm	Dice Coefficient
FSL	75.6%
SPM	79.0%

Table 3.3.2.1: Grey Matter Dice coefficients computed for FSL and SPM on the IBSR Dataset.

For the purpose of this chapter, it is just useful to note that the reported indexes values can be improved for SPM, FSL.
Also in this case it shall be noticed that the probabilistic approach adopted by SPM makes it intrinsically low sensitive to small differences between different subjects, and that the high time consumption of Freesurfer makes it difficult to use it habitually.
Therefore, also for the segmentation of Grey Matter and White Matter, the implementation of a deterministic brain segmentation algorithm, characterized by high sensitivity, specificity and ductility (in order to be easily adapted to the requirements of the research laboratory) is a challenging problem.

3.3.3 Skull Segmentation in MRI

Differently from Computed Tomography, Magnetic Resonance Imaging distinguish soft tissues (including the Brain, Grey Matter, White Matter and blood vessels) with high contrast variations, but it detects the bone with very low intensity signal both in T1 and T2 acquisitions sequences. Therefore, the skull is represented in the scans visualization by very low intensity voxels and it is usually not recognized and analyzed in the clinical practice. Moreover, the bone intensity peak and the air intensity peaks are usually merged together in both T1 and T2 MRI intensity distributions, and it is usually difficult to separate them through analytic methods. The segmentation of the skull in MR images is therefore a challenging problem.
Various MR image segmentation techniques are described in the literature for different anatomical structures, but little research is dedicated to the problem of segmentation of the skull in MR images, since CT is typically used for this purpose.
Held et al. *(Held, 1997)* used a Markov random field approach to classify MR images into Grey Matter, White Matter, CSF, scalp-bone and background. Rifai et al. *(Rifai, 1999)* applied a deformable model to segment the skull in MR images. Chu and Takaya *(Chu, 1993)* detected the skin-skull and skull-brain boundaries using threshold and Laplacian of Gaussian operations on successive

transverse slices. Soltanian-Zadeh and Windham *(Soltanian-Zadeh, 1995)* applied a multi- scale approach where they made use of both CT and MR image information. Studholme et al. *(Studholme, 1996)* also used CT information for the segmentation of the skull in MR images of the same subject. Heinonen et al. *(Heinonen, 1997)* used threshold and region growing to segment bone in MR image volumes.
The mentioned methods offer different pros and cons. The method described by Held et al. *(Held, 1997)* does not guarantee continuous bounding contours and was not intended for segmentation of the skull in MR images. Deformable models can be attracted to incorrect boundaries resulting in the potential inclusion of skin, muscles, eyes and inner ear in the segmented skull. Performing the segmentation on individual slices does not allow the method to exploit the connected 3D structure of the skull. Multi-modal approaches (CT/MR), while attractive in providing accurate detail of both skull and soft tissue, is not generally practical since still needs the CT acquisition. The threshold and region growing methods described in literature do not offer good results in the segmentation of particular bone regions, as ocular globes. This fact is due to a not accurate analysis of the local bone intensity.
These considerations enhance that there is still a need for a robust method to segment the skull boundaries in MR.

3.3.4 Bone and Contrast Medium Perfused Tissues Segmentation in Computed Tomography Angiography of the Chest

Arteries and veins can be visualized in a minimally invasive way with Computed Tomography Angiography (CTA). The resulting data sets are often visualized by means of maximum intensity projection (MIP) images.
Three-dimensional rendering of Computed Tomography (CT) datasets has become an integral component of various applications, particularly vascular and orthopaedic imaging. Current CT technologies yield isotropic datasets that can be rendered in three dimensions with high resolution in any orientation.
However, the volume datasets contain such an abundance of information that segmentation is necessary to remove extraneous structures that could make the evaluation difficult during the three dimensional rendering.
With the improvements in data acquisition and rendering, also volume editing tools and procedures have been developed using a variety of algorithms *(Kang, 2003; Hahn, 2006)*. However these procedures still do not satisfy the requirements needed by the clinical activity, that are high accuracy and low time consume.
Therefore the segmentation of the bone from the tissues perfused by the contrast medium in CTA remains a challenge at the actual state of the art.
When 3D rendering was in its early stages, datasets were manually edited slice by slice removing the bone. However, this is time consuming and prone to error, since it depends on the level of skill and education of the individual performing the procedure.
Alternatively, subtraction of the CT non-enhanced scan has been widely reported and used *(Imakita, 1998)*. A disadvantage of subtraction of two scans

is that the noise of the two scans is added. Moreover, due to inevitable motion of the patient in between the two scans, the CTA data set and the additional data set have to be registered. This fact is a considerable limitation, since a volume may contain multiple bones that can move from the CT scan to the CTA (e.g., in the neck region). Moreover these techniques require the exposure of the patient to a double dose of X-ray.

Such limitations have prompted investigation of computerized editing tools.

Some semi-automatic procedures, based on image processing techniques as threshold and morphological operators, have been developed to identify the bone *(Velthuis, 1997; Fiebich, 1999; Wetzel, 1999)*.

Nevertheless, since the intensities with which the bones are detected by the apparatus are very similar to the intensities with which the contrast-enhanced tissues are detected, those techniques are prone to the choice of parameters and difficult to be automated. Moreover, they sometimes affect the contrast-enhanced structures and lead to mediocre results.

Chapter 4

Procedures for Multi Images Analysis of the Brain

To understand the work that is described in chapters 7.2, 8 and 9.2 it is needed to know what is Multi Image Analysis of the Brain and which are the fundamental procedures used to perform it.
The registration (or co-registration) of a source scan to a reference consists in the application of a transformation to the source in order to make it aligned with the reference. It assumes that the scans are acquired on the same subject. The shape of a human brain changes very little with head movement, so rigid body transformations can be used to model different head positions of the same subject. Registration is important in many aspects of functional image analysis of the Brain.
Normalization is the registration of various scans into the same coordinates system defined by a template scan. In this case, usually non linear transformations shall be applied in order to obtain a good result. Normalization is used in functional imaging to analyze the response of different subjects to the same task.
The fundamental rigid body registration procedures are described in Chapter 4.1. The optimization criteria used for both intra-modality and inter-modality procedures are described in Chapter 4.1.1. The rigid body transformations are described in Chapter 4.1.2. Since resampling is always needed when geometrically transforming a scan, chapter 4.1.3 describes the most used resampling types.
The fundamental normalization procedures are described in Chapter 4.2. Chapter 4.2.1 describes the optimization criteria that can be used to lead the normalization processes. Chapters 4.2.2 and 4.2.3 describe respectively the affine transformations and the non linear transformations needed to warp different scans from different subjects on the same template. In chapter 4.2.4 regularization will be introduced, which is needed by the normalization processes in order to preserve the topology of the scans during the non linear transformations.

4.1 Rigid Body Registration

The registration of scans acquired with different techniques is important in many aspects of functional image analysis of the Brain.
In example, in Blood Oxygen Level Dependent functional MRI (BOLD fMRI), apparent signal differences that can result from subject movement can be greater than the signal differences due to hemodynamic response.
The rigid body registration of the different images that form a functional scan is called realignment. The presence of artefacts due to subject movement that correlate with the experimental paradigm may appear as activations, and therefore decrease the sensitivity. The t-test (that is usually applied to analyze fMRI data) is based on the signal change and the residual variance. The residual variance is computed from the sum of squared differences between the data and the linear model used to fit it. Since movement artefacts add to the residual variance, they reduce the sensitivity of the t-test. Realignment is therefore useful in fMRI because it reduces this effect and increases the sensitivity of the analysis.The registration of functional images with high resolution structural images of the same subject (typically T1 weighted MRI) leads to better knowledge about the anatomy that underlies the functional scan. This fact permits to localize the activated anatomical structures. Finally registration is useful to obtain more accurate spatial normalization of the images, since the normalization algorithms (chapter 4.2) obtain better results being applied on more detailed structural images. If the functional scan is registered to the structural one, the warp computed to normalize the structural image can be applied to the functional scan.
The registration of different scans requires the estimation of a mapping between them. The reference scan is assumed to remain stationary, whereas the source scan is spatially transformed to match it.
The registration of different scans is composed by two different steps.
The first step consists in the estimation of the set of parameters describing the transformation. This phase normally involves iteratively transforming the source image many times, using different parameters, until some optimization criterion is optimized. The optimization criteria must be realized to work in both intra-modality (images acquired using the same acquisition sequence) and inter-modality (images acquired with different sequences or techniques, e.g., T1 to T2 weighted MRI, or MRI to PET) contexts.
The second step consists in the transformation of the source scan according to the estimated parameters. This step is composed by the rigid body transformation and the resampling of the scan.

4.1.1 Intra-Modality and Inter-Modality Optimization Criteria

The optimization criteria must be realized to work in both intra-modality (images acquired using the same acquisition sequence) and inter-modality (images acquired with different sequences or techniques, e.g., T1 to T2

weighted MRI, or MRI to PET) contexts. In order to increase the precision of the result, this procedure can be repeated.
Often, in realignment processes of functional data, instead of matching to one of the scans from the series, the scans are registered to the mean of all the realigned scans.
The intensities with which the different tissues are detected using the same modality are usually very similar, therefore a registration criterion based on the minimization of the sum of squared differences between them obtains good results.
However, for the inter-modality registration there is nothing quite as obvious to minimize, since the intensities with which the different tissues are detected change from one scan to the other. The first methods for the registration of inter modality scans were based on the manual identification of homologous landmarks in the images. The registration of the scans was obtained aligning together the landmarks. Those procedures are very time-consuming, they require a high degree of experience in order to identify correctly the landmarks, and can be rather subjective.
An old and widely used method for the semi-automatic registration of inter-modality scan was the head-hat approach *(Pelizzari, 1988)*. This method was based on the identification of the surfaces of the brain in the two images, and then matching them together. Some other methods for inter-modality registration involve partitioning the images, finding common features between them, and then registering them together.
The first intensity based method for the inter-modality registration of head scans was AIR *(Woods, 1993)*. This method was developed to register PET and MR scans. It involves dividing the MR images into a number of partitions based on their intensities. It assumes predetermined relations between the intensities with which the tissues of the brain are detected by PET and MRI intensity and registers the scans minimizing the variance of the intensities of the corresponding voxels in each partition. This method has the disadvantage of requiring the MR images to be pre-processed removing non-brain tissue.
The most recent registration methods use voxel-similarity measures and are based on information theory. These methods are usually adopted both for intra-modality and inter-modality registration *(Holden, 2000)*. The voxel similarity measures are based on joint probability distributions of the intensities.

4.1.2 Rigid Body Transformations

Rigid body transformations are a subset of the more general affine transformations. They consist of rotations and translations.
Each point $\mathbf{x}=(x_1,x_2,x_3)$ of a scan can be mapped into the co-ordinates $\mathbf{y}=(y_1,y_2,y_3)$ of another space as:

Eq. 4.1.2.1:

$$\begin{bmatrix} y_1 \\ y_2 \\ y_3 \\ 1 \end{bmatrix} = \begin{bmatrix} m_{11} & m_{12} & m_{13} & m_{14} \\ m_{21} & m_{22} & m_{23} & m_{24} \\ m_{31} & m_{32} & m_{33} & m_{34} \\ 0 & 0 & 0 & 1 \end{bmatrix} \begin{bmatrix} x_1 \\ x_2 \\ x_3 \\ 1 \end{bmatrix}$$

The translation of **x** by **q** is defined as:

Eq. 4.1.2.2:

$$\begin{bmatrix} y_1 \\ y_2 \\ y_3 \\ 1 \end{bmatrix} = \begin{bmatrix} 1 & 0 & 0 & q_1 \\ 0 & 1 & 0 & q_2 \\ 0 & 0 & 1 & q_3 \\ 0 & 0 & 0 & 1 \end{bmatrix} \begin{bmatrix} x_1 \\ x_2 \\ x_3 \\ 1 \end{bmatrix}$$

In the three dimensional case, every rotation can be obtained combining in the correct order single rotations around the three orthogonal axes. A rotation of q_1 radians about the horizontal axis (first axis) is normally called pitch, and is performed by:

Eq. 4.1.2.4:

$$\begin{bmatrix} y_1 \\ y_2 \\ y_3 \\ 1 \end{bmatrix} = \begin{bmatrix} 1 & 0 & 0 & 0 \\ 0 & cos(q_1) & sin(q_1) & 0 \\ 0 & -sin(q_1) & cos(q_1) & 0 \\ 0 & 0 & 0 & 1 \end{bmatrix} \begin{bmatrix} x_1 \\ x_2 \\ x_3 \\ 1 \end{bmatrix}$$

The rotation around the antero-posterior axis (second axis) is called roll and is obtained using the following matrix:

Eq.4.1.2.5:

$$\begin{bmatrix} cos(q_2) & 0 & sin(q_2) & 0 \\ 0 & 1 & 0 & 0 \\ -sin(q_2) & 0 & cos(q_2) & 0 \\ 0 & 0 & 0 & 1 \end{bmatrix}$$

The rotation around the vertical axis (third axis) is called yaw and is obtained using the following matrix:

Eq.4.1.2.6:

$$\begin{bmatrix} cos(q_3) & sin(q_3) & 0 & 0 \\ -sin(q_3) & cos(q_3) & 0 & 0 \\ 0 & 0 & 1 & 0 \\ 0 & 0 & 0 & 1 \end{bmatrix}$$

In order to register scans whose voxel sizes are not isotropic (or whose voxels dimensions differ between the scans) zooms are needed.
The zooms represent scaling along the orthogonal axes, and can be represented in the following manner:

Eq. 4.1.2.7:

$$\begin{bmatrix} y_1 \\ y_2 \\ y_3 \\ 1 \end{bmatrix} = \begin{bmatrix} q_1 & 0 & 0 & 0 \\ 0 & q_2 & 0 & 0 \\ 0 & 0 & q_3 & 0 \\ 0 & 0 & 0 & 1 \end{bmatrix} \begin{bmatrix} x_1 \\ x_2 \\ x_3 \\ 1 \end{bmatrix}$$

4.1.3 Resampling

During the application of a rigid transformation, it is required the estimate of the intensity that each voxel of the final scan had in the original image. This operation is usually performed using interpolation.
The simplest approach is called nearest neighbour (or zero-order interpolation) re-sampling. It consists in taking the value of the closest voxel to the desired sample point. This approach has the advantage of preserving the original voxel intensities, but the resulting scan is degraded by a blocky appearance.
Polynomial interpolation uses more neighbours in order to fit a smooth function through the neighbouring voxels, and then read off the value of the function at the desired location (zero-order interpolation is simply a low order polynomial interpolation)
In the real space, the sinc interpolation is the method that gives results with the minimal artefacts. This approach consists in the convolution of the scan with three dimensional sinc functions centred on the point to be re-sampled. Since the sinc function is separable, the implementation of sinc interpolation is performed sequentially in the three dimensions of the volume. To use this approach, every voxel in the scan should be used to sample a single point. Speed and time consuming considerations make this impossible, and usually

approximations using a limited number of nearest neighbours is used. To perform this operation, the sinc function is usually modulated with a Hanning window.

4.2 Normalization

Spatial normalization consists in warping scans from different subjects into the same standard space to allow signal analysis across the various scans.
This technique is used in functional imaging to analyze the response of different subjects to the same task *(Fox, 1995)*.
The deformations required to transform the scans to the same space are not clearly defined. Unlike rigid-body transformations, where the constraints are explicit, those for warping are more arbitrary.
The first main approach to the normalization of scans in constituted by the use of label based techniques. These techniques find the transformations that best match some homologous features (labels) in the source and reference images. The most used homologous features are landmarks, lines or surfaces that are often identified manually. This process is subjective and time consuming. In many instances it is possible to perform it with semi-automatic or automatic algorithms. The spatial transformation is then effected bringing the homologies together. The deformation needed between the homologies is not known, therefore the label based algorithms usually perform those deformations in the smoothest possible way. The fit of the homologies with splines *(Bookstein, 1997)* or other forms of interpolation are often used to achieve the result *(Thompson, 1997)*.
The second main approach to the normalization of scans is based on the matching of the intensity of the scans. The techniques that use this approach identify a spatial transformation that optimizes a measure of the similarity of the voxels between the source and the reference image. Those methods are usually very susceptible to poor starting estimates. Therefore hybrid approaches combining intensity based methods with label based methods have emerged.

4.2.1 Optimization Criteria

Intensity based approaches identify a spatial transformation that optimizes a measure of the similarity of the voxels between the source and the reference image. The most used criteria for the similarity measure are the minimization of the sum of the squared differences between the reference and the source or the maximization of the correlation. Few intensity based methods that optimize a theoretic measure of the information have been described *(Studholme, 2000)*.
In SPM5 the MAP scheme is used to optimize the nonlinear registration. It works by estimating the optimum coefficients for a set of bases, by minimizing the sum of squared differences between the template and source image, while simultaneously minimizing the deviation of the transformation from its expected value.
The estimates of the probability of obtaining the fit given the data is necessary to apply the MAP. Therefore prior knowledge of spatial variability, and also knowledge of the variance associated with each observation is required. The used approach is a type of Empirical Bayesian approach which attempts to

estimate the variance from the residual error. Because the registration is based on smooth images, correlations between neighbouring voxels are considered when estimating the variance. This fact makes the same approach suitable for the spatial normalization of both high quality MR images, and low resolution noisy PET images.

4.2.2 Affine Registration

Usually the spatial normalization algorithm for brain scans determines first the optimal nine or twelve parameter affine transformation that registers the images together. This step is normally performed automatically by minimizing (or maximizing) some mutual function of the images. The images may be scaled quite differently, so an additional intensity scaling parameter can be included.
Prior knowledge of the variability of head sizes is in some cases included within a Bayesian framework in order to increase the robustness and accuracy of the method (i.e. it is included in SPM5).
Using this approach, a parameter will be based more upon the prior information if the error for a particular fitted parameter is known to be large. The prior distribution of the parameters shall be known in order to adopt this approach. The experimental analysis of the parameters obtained from the registration of a large number of brain images to a template can be used to determine the prior distribution.

4.2.3 Nonlinear Registration

The total variability between different scans includes a very high number of local parameters. Therefore the exact nonlinear transformation that warps the source to the reference includes a potentially enormous number of parameters. However, the use of few parameters obtains good results. The small number of parameters will not lead to exact matching of each structure, but it will permit the global head shape to be modelled. Moreover a low dimensional approach will allow rapid modelling of the global brain shape. Some algorithms normalize scans accounting for differences in position, orientation and overall brain dimensions using affine transformation of nine or twelve parameters.
A linear combination of low frequency basis functions can be used to describe low spatial frequency global variability of head shape. Polynomial basis functions are often used with this aim *(Woods, 1998)*. Other forms of basis function used with this aim are Fourier bases, sine and cosine transform basis functions *(Ashburner, 1999)*, B-splines *(Thèvenaz, 2000)*, and piecewise affine or trilinear basis functions *(Glasbey, 1998)*.
A nonlinear spatial normalization example (used by SPM5) is briefly described here. The nonlinear warps are modelled by linear combinations of smooth discrete cosine transform basis functions. This approach assumes that the image has already been approximately registered with the template according to a twelve-parameter affine registration.
The spatial transformation from co-ordinates x_i, to co-ordinates y_i is:

Eq. 4.2.3.1:

$$y_{1i} = x_{1i} + u_{1i} = x_{1i} + \sum_j q_{j1} d_j(\mathbf{x}_i)$$
$$y_{2i} = x_{2i} + u_{2i} = x_{2i} + \sum_j q_{j2} d_j(\mathbf{x}_i)$$
$$y_{3i} = x_{3i} + u_{3i} = x_{3i} + \sum_j q_{j3} d_j(\mathbf{x}_i)$$

where q_{jk} is the j^{th} coefficient for the k dimension, and $d_j(x)$ is the j^{th} basis function at position x.

The choice of basis functions depend upon the distribution of warps likely to be required, and also upon how translations at borders should behave.
Nonlinear spatial transforms are iterated in order to satisfy the optimization criterion that compares the transformed scan with the reference.

4.2.4 Linear Regularization for Nonlinear Registration

Regularization is necessary in order to preserve the topology of the scan when warping it with many parameters. Regularization is included in procedures that have Bayesan approaches, such as the maximum a posteriori (MAP) estimate or the minimum variance estimate (MVE). The most used regularization schemes include the minimization of the membrane energy of the deformation field, the bending energy *(Bookstein, 1997)* or the linear-elastic energy *(Miller, 1993)*, although these procedures do not explicitly preserve the topology of the warped images.
Each of these schemes needs some form of elasticity constants. If the values of these constants are too large, the scheme will provide too much regularization and result in underestimated deformations. If the values are too small, there will not be enough regularization and the resulting deformations will over-fit the data. Other methods involve the iteration of Gaussian smoothing of the estimated deformation fields. In SPM5 three distinct forms of linear regularization are used, based upon membrane energy, bending energy and linear-elastic energy. None of these schemes enforce a strict one to one mapping between the source and the reference, but this makes little difference for the small deformations required.

Chapter 5

Experimental Data Set

This chapter describes the data set used to realize, test and evaluate the procedures that are described in chapters 6,7 and 8.
The algorithm for the segmentation of the Brain, Grey Matter, White Matter and Skull in T1-weighted structural MRI is tested on the dataset of 89 subjects that is described in chapter 5.1. The data set is characterized by very high variability.
Since the Brain segmentation algorithms have been realized with the purpose to analize schizophrenia, 16 scans of Patients affected by schizophrenia are included in this part of the data set. Those data will be used also in Chapter 9 to analyze morphological and functional alterations related to schizophrenia.
The data set described in chapter 5.2 is composed by 7 MRI scans of one patient in critical state due to Brain tumour. The scans are acquired with different acquisition sequences in order to enhance various features of the tissues.
The algorithm that is described in chapter 7.3 consists in the application of the procedures described in chapter 6 to segment the Heart, the Aorta, the Kidneys and the Urinary Bladder in a scan obtained using Computed Tomography Angiography (CTa). Chapter 5.3 describes the CTa data set.
The procedure for multi images statistical analysis that is described in Chapter 8 is based on both a structural T1 weighted MRI data (described in chapter 5.1) and a DSC MRI data. Chapter 5.4 describes the latter. Those data will be used also in Chapter 9 to analyze functional alterations related to schizophrenia.

5.1 T1 Weighted MRI Structural Data of the Brain

The algorithms that are described in chapters 6.1, 6.2 and 7.1 are realized to segment the Brain, the Grey Matter, the White Matter, the Cerebro Spinal Fluid and the Skull in T1 weighted Structural MRI of the head.
I want to test the robustness of these algorithms on a representation of almost all the conditions that can be encountered in the T1-weighted MRI scans of the head. Therefore I realized a dataset characterized by very high variability.
The T1 Weighted MRI Structural dataset is composed by 89 real MRI T1 scans, subdivided in 7 groups acquired with 5 different MRI Scanners and with 7 different acquisition sequences. It includes T1 MRI scans saved in the formats that are most used in MRI of the head: nifti, analyze and dicom. Moreover, the dataset includes scans acquired with different resolutions, from 0.46 mm on the acquisition slice plane to 3.1 mm on the slice encoding direction. The variety of the used MRI scanners and acquisition sequences determines high differences in the intensity distributions.
Finally the subjects included in the dataset are characterized by different genders, ages and health conditions.
This variety makes the database a good test set for Orao.
Twenty scans of the dataset are from the Internet Brain Segmentation Repository (IBSR), provided by the Centre for Morphometric Analysis of the Massachusetts General Hospital (MGH) in association with Harvard Medical School (http://www.cma.mgh.harvard.edu/ibsr).
Forty Scans are from the Segmentation Validation Engine, realized by the Laboratory of Neuro Imaging of the University of California Los Angeles (http://sve.loni.ucla.edu).
Thirty-eight Scans are from the Inter-university Centre of Brain Imaging and Neuropsychology of the Universities of Udine and Verona (ICBN). Seventeen of those are acquired at Policlinico Gian Battista Rossi (Verona, Italy), ten are acquired at the Borgo Trento Hospital (Verona, Italy). One scan is from the University of Padova and one is from the Hospital of Pavia.
The specific characteristics of the scans are reported in Table 5.1.1.
The subjects can be subdivided in healthy controls (55), schizophrenic patients (13), or patients affected by multiple sclerosis (1). The specific characteristics of the subjects related to the scans are reported in Table 5.1.2.
Patients affected by schizophrenia were recruited from the South-Verona Psychiatric Care Register (PCR) *(Tansella, 2003, 2006; Amaddeo, 2009)*, a community-based mental health register.
After reaching clinical consensus diagnoses of schizophrenia by two staff psychiatrists, the clinical diagnosis of schizophrenia for each patient was confirmed using the IGC-SCAN Item Group Checklist of the Schedule for Clinical Assessment in Neuropsychiatry (IGC-SCAN) *(World Health, 1992)*, as previously described *(Andreone, 2007)*.
Since the age of illness is suspected to affect the volumes and functionality of the Brain *(Mathalon, 2001)*, the schizophrenic patients are chosen in order to have an age of illness longer than eight years. The aim of this decision is to have a high effect of the illness. The average age of illness of the

schizophrenic patients is (16.9±5) years. The average age of illness of the male schizophrenic patients group is (14.0±3.6) years, while the average age of illness of the female schizophrenic patients group is (19.7±4.9) years.
This research study was approved by the biomedical Ethics Committee of the Azienda Ospedaliera di Verona. All subjects provided signed informed consent, after having understood all issues involved in study participation.

Data Set	Origin	Scan Format	Bits Allocated	Acquisition Unit	Magnetic Field Intensity	Acquisition Plane	TR range *(ms)*	TE range *(ms)*	Flip Angle	Number of Slices	Slice Thickness *(mm)*	Slice Width (Number of Voxels)	Slice Height (Number of Voxels)	Slice Resolution *(mm^2)*
1	LONI	Nifti	16	GE 1.5T	1.5 T	Coronal	10.0 –12.5	4.22–4.5	20°	124	1.5	256	256	0.86 x 0.86
2	LONI	Nifti	16	GE 1.5T	1.5 T	Coronal	10.0 –12.5	4.22–4.5	20°	124	1.5	256	256	0.78 x 0.78
3	IBSR	Analyze	16	N.D.	N.D.	Coronal or Sagittal	N.D.	N.D.	N.D.	60 – 65	3.1	256	256	1 x 1
4	ICBN *(Inter University Centre for Brain Imaging and Neuropsychology)*	Analyze	8	Siemens Symphony	1.5 T	Coronal	2060	3.93	15°	144	1.25	384	512	0.46 x 0.46
5	ICBN *(Inter University Centre for Brain Imaging and Neuropsychology)*	Dicom	16	Siemens Allegra	3 T	Sagittal	2300	3.93	12°	160	1	256	256	1 x 1
6	ICBN *(Inter University Centre for Brain Imaging and Neuropsychology)*	Dicom	16	Siemens Allegra	3 T	Sagittal	1200	3.93	12°	160	1	256	256	1 x 1
7	University of Padova	Analyze	16	N.D.	N.D.	Axial	N.D.	N.D.	N.D.	120	1.2	256	256	0.98 x 0.98
8	University of Pavia	Analyze	16	N.D.	N.D.	Coronal	N.D.	N.D.	N.D.	180	0.8	256	256	0.98 x 0.98

Table 5.1.1: T1 Weighted MRI of the head dataset acquisition informations. *(N.D. stands for Not Determined)*

Data Set	Origin	Total Subjects		Number of Healthy Controls	Number of Females	Number of Males	Number of Schizophrenic Patients	Number of Multiple Sclerosis Patients
		Number	Age *(Years)*					
1 and 2	LONI	40	29.2 ± 6.3	40	20	20	0	0
3	IBSR	20	N.D.	20	N.D.	N.D.	N.D.	N.D.
4	ICBN *(Inter University Centre for Brain Imaging and Neuropsychology)*	16	38.3 ± 4	8	8	8	8	0
5	ICBN *(Inter University Centre for Brain Imaging and Neuropsychology)*	10	43	5	5	5	5	0
6	ICBN *(Inter University Centre for Brain Imaging and Neuropsychology)*	1	55	1	0	0	0	0
7	University of Padova	1	N.D.	0	0	0	0	1
8	University of Pavia	1	N.D.	1	0	0	0	0

Table 5.1.2: T1 Weighted MRI of the head dataset subjects informations. *(N.D. Stands for Not Determined)*

Data Set	Acquisition Sequence	Scan Format	Bits Allocated	Acquisition Unit	Magnetic Field Intensity	Acquisition Plane	TR *(ms)*	TE *(ms)*	Flip Angle	Number of Slices	Slice Thickness *(mm)*	Slice Width (Number of Voxels)	Slice Height (Number of Voxels)	Slice Resolution *(mm^2)*
1	Proton density	Dicom	16	Siemens Magnetom Vision	1.498	Axial	3800	22	180	21	5 + 0.5	256	256	0.8984 x 0.8984
2	T2-weighted	Dicom	16	Siemens Magnetom Vision	1.498	Axial	3800	90	180	21	5 + 0.5	256	256	0.8984 x 0.8984
3	T1-weighted	Dicom	16	Siemens Magnetom Vision	1.498	Sagittal	650	14	70	19	5 + 0.5	256	256	0.8984 x 0.8984
4	T2-weighted	Dicom	16	Siemens Magnetom Vision	1.498	Coronal	9000	110	180	19	5 + 0.5	256	256	0.8984 x 0.8984
5	T1-weighted	Dicom	16	Siemens Magnetom Vision	1.498	Axial	735	14	70	19	5 + 0.5	256	256	0.8984 x 0.8984
6	T1-weighted	Dicom	16	Siemens Magnetom Vision	1.498	Sagittal	650	14	70	19	5 + 0.5	256	256	0.8984 x 0.8984
7	T1-weighted	Dicom	16	Siemens Magnetom Vision	1.498	Coronal	650	14	70	19	5 + 0.5	256	256	0.8984 x 0.8984

Table 5.2.1: Brain Tumour and Tumoral Edema segmentation in MRI Data Set

5.2 Brain Tumour and Tumoral Edema MRI Data

The algorithm that is described in chapter 7.2 is the application of the algorithm described in chapter 6 to a high altered geometry case. The Brain, the Grey Matter, the White Matter, the Cerebro Spinal Fluid plus Tumour and a Peritumoral Edema will be segmented on MRI of the head.
This data set has been provided by the Department of Electric Engineering of the University of Padova and has been acquired at the Vicenza Hospital. The semi-automatic segmentation algorithm is included in a project for the treatment of tumours with hyperthermia. The segmentation results will be used as a three dimensional numerical model to simulate the response of the various tissues to hyperthermia and to compute the best treatment.
Seven MRI scans of a single patient in critical state are included in this part of the data set. The patient is a Caucasian male 50 years old with a weight of 90 Kg affected by brain tumour. The scans are all acquired with the same MRI scanner: a Siemens Magnetom Vision 1.5 Tesla. Four of the scans are T1-weighted, two are T2-weighted and one is a Proton Density.
All of these scans are saved in the DICOM format. All of them are also acquired with similar resolutions. Instead they are acquired with different acquisition directions. The Proton Density scan, one T1-weighted and one T2-weighted are acquired on the axial acquisition plane. Two T1-weighted scans are acquired on the sagittal acquisition plane. One T1-weighted and one T2 weighted scans are acquired on the coronal acquisition plane.
Moreover, the different types and settings of the acquisition sequences influence the intensities with which the different tissues are detected.
The characteristics of each scan are described in detail in Tab.5.2.1.

5.3 Computed Tomography Angiography Data of the Chest and Abdomen

The algorithm that is described in chapter 7.3 consists in the application of the procedures described in chapter 6 to segment the Heart, the Aorta, the Kidneys and the Urinary Bladder in a scan obtained using Computed Tomography Angiography (CTA).
This part of the data set has been obtained by the DICOM sample image sets of a software for medical images navigation called "Osirix". The dataset is available at the uniform resource locator: *http://pubimage.hcuge.ch:8080* with the name of *Obelix*.
The subject analyzed in the scan is a male healthy control with an age of 43 years.
The scan is a whole body contrast CTA acquired at the University of California, Los Angeles in the 2004.
The CT unit is produced by Siemens, and the type is “Sensation 16”.
The scan has 16 bits allocated. It is constituted by 600 slices acquired on the axial acquisition plane with width and the height of 512 voxels. Each slice ha a thickness of 2 millimetres, while the planar resolution is (0.7422 x 0.7422) mm^2.

5.4 DSC MRI Data of the Brain

The procedure described in Chapter 8 is based on both structural T1 weighted MRI and DSC MRI scans.
The dataset is composed by 16 subjects. Eight of those are patients with DSM-IV schizophrenia (4 males, 4 females; mean age: 38 years; age standard deviation: 3.7 years; all Caucasians, length of illness: 16.8 years; length of illness standard deviation: 5 years), and eight are healthy controls (4 males, 4 females; mean age: 38 years; age standard deviation: 4.5 years; all Caucasians).
Patients were recruited from the South-Verona Psychiatric Care Register (PCR) *(Tansella, 2003, 2006; Amaddeo, 2009)*.
Also in this case the diagnosis of schizophrenia was determined for each patient by clinical consensus of two psychiatrists of the staff, and then confirmed using the IGC-SCAN Item Group Checklist of the Schedule for Clinical Assessment in Neuropsychiatry (IGC-SCAN) *(World Health, 1992)*, as previously described *(Andreone et al., 2007)*.
Patients with comorbid psychiatric disorders, alcohol or substance abuse within the six months preceding the study, history of traumatic head injury with loss of consciousness, epilepsy or other neurological or medical diseases, including hypertension and diabetes, were excluded from the study. None of the patients had history of ECT treatment.
Control individuals were recruited from the same catchment described in chapter and had no DSM-IV axis I disorders, as determined by a brief interview modified from the SCID-IV non-patient version (SCID-NP), no history of psychiatric disorders among first-degree relatives, no history of alcohol or substance abuse, and no current major neurological or medical illness, including hypertension and diabetes. No evidence of central nervous system abnormalities on the serial conventional MR images and on the pre and post-contrast MR acquisitions were detected by the neuroradiologist. None of them was on medication at the time of participation in the study, including drugs for nausea or vertigo.
This research study was approved by the biomedical Ethics Committee of the Azienda Ospedaliera di Verona. All subjects provided signed informed consent, after having understood all issues involved in study participation.
For each subject were acquired a T1 weighted structural MRI as described in Table 5.1.1 at the 4th row and a DSC MRI perfusion weighted scan with a 1,5T Siemens Magneton Symphony Maestro class, (Syngo MR 2002B). A standard head coil was used for RF transmission and reception of the MR signal and restraining foam pads were utilized for minimizing head motion.
Perfusion-weighted acquisitions, consisting of echo-planar imaging of T2-weighted sequence, were acquired in the axial plane parallel to the AC-PC line (20 sequential images for 60 repetitions, TR=2160 ms, TE=47 ms, FOV=230x230 mm2, slice thickness=5mm, matrix size=256x256 interpolated, NEX=1, EPI factor=128) immediately before, during, and after injection of a bolus of gadopentetate dimeglumine -dietilen-tetra-penta-acetic acid (Gd-DTPA), a paramagnetic agent with intravascular space distribution. Contrast material (0.1 mmol/Kg) administration was started after 4s by power injector (Medrad Spectris MR injector) through an 18 or 20-gauge angiocatheter

through the right antecubital vein at a rate of approximately 2,5 ml/s, followed immediately by 25 mL of continuous saline flush. The same neuroradiologist controlled timing and accuracy of gadolinium administration for all patients and controls.

Chapter 6

A Novel Automatic Brain, Grey Matter and White Matter Segmentation Algorithm in T1 MRI

This chapter presents Orao, a novel automatic algorithm for Brain, Grey Matter and White Matter segmentation in T1 MRI scans of the head.
The algorithm is based on deterministic analysis, and is characterized by low assumptions about the brain, high precision, robustness and ductility. Moreover it does not require any pre-processing, nor uses atlases and it works on the most used file formats *(Nifti, Analyze and Dicom)*.
Orao segments the Brain through iterative analyses of global *(Atzori, 2007)* and local *(Atzori, 2009)* intensity distributions, the application of morphologic operators and the analysis of connectivity properties.
The algorithm segments then the Grey Matter and the White Matter in the matrix obtained after Brain Segmentation through iterative local and global analyses of the intensity distributions and of connectivity properties. Due to the needs of the Research Unit in Brain Imaging and Neuropsychology of the ICBN, this part of the algorithm has been realized in order to be restrictive rather than conservative.
Orao obtained excellent results in quantitative and qualitative validation and in comparison with state of the art software on a dataset of 89 scans.
Orao is based on recursive analyses of global and local intensity distributions. The sampling and re-sampling procedures, the detection intensities of the tissues and the geometrical features of the anatomical structures *(Atzori, 2009)* influence the intensity distributions. Therefore, their analysis is quite complex, and it is convenient to analyse the problem separately. Chapter 6.1 describes how the segmentation algorithm approaches it.
The segmentation algorithm is subdivided in two parts: The first is dedicated to the segmentation of the Brain, and is described in chapter 6.2. The second is dedicated to the segmentation of Grey and White Matter, and is described in chapter 6.3.

6.1 Intensity Distributions Analysis

Orao is based on recursive analyses of global and local intensity distributions. The sampling and re-sampling procedures, the detection intensities of the tissues and the geometrical features of the anatomical structures influence the intensity distributions. Therefore, their analysis is a complex problem.
Regarding the effects of the sampling and re-sampling procedures on the intensity distributions, I observed that often the intensity distributions of the head MRI scans are affected by artefacts that modify radically their shape.
The intensity distributions alterations that are most frequently observed are similar to the ones showed in Fig. 6.1.1a, and can be recognized as due to sampling or re-sampling procedures. The intensity distributions that are affected by alterations of this kind include information different from the physical properties of the tissues. Since the analysis procedures that are included in Orao are based on the physical properties of the tissues, artefacts of this type can interfere with the segmentation.
In order to avoid errors in the process, Orao includes an algorithm that modifies the intensities of the scans characterized by intensity distribution artefacts in order to obtain regular intensity distributions. The algorithm scales the intensity values of the scan diminishing the maximal intensity till a continuity based criterion is satisfied.
Finally the algorithm converts the original scan to 8 bit format (if they have been created in a different format), in order to reduce the time needed by the segmentation algorithm to process it. The conversion is made in order to reduce the loss of information useful for the segmentation of the brain tissues.
Long tails over the intensities of interest have been observed in the intensity distributions of the 89 scans data set that has been analyzed. I observed that these tails mostly correspond to Fat tissues, which are not of interest for the purpose. I observed besides that these tissues always occupy more than 1% of the volume of each scan. Therefore, the algorithm scales the scan to 8 bit setting to 255 the intensity values greater than the value I_{Max} described in Equation 6.1.2:

Eq. 6.1.1:

$$\int_0^{I_{Max}} D(I)dI = 0.99 \cdot \int_0^{\infty} D(I)dI$$

Where I stands for Intensity and D(I) is the Intensity distribution.

Finally, in order to remove intensity distributions data that may still include irregularities, a continuity based filter is applied before each global or local intensity distribution analysis.

An example of intensity distribution obtained after the regularization of the data and the conversion to 8 bit is showed in Fig. 6.1.1b.

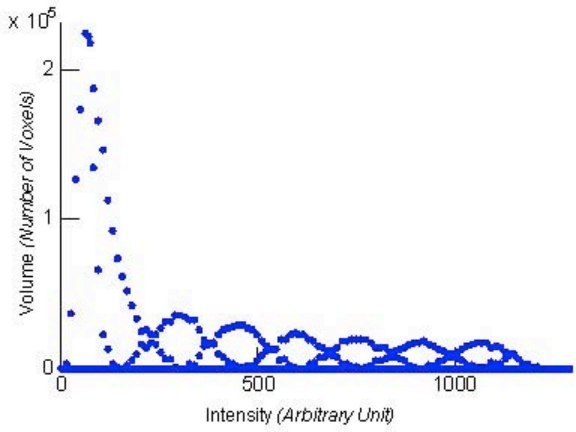

a

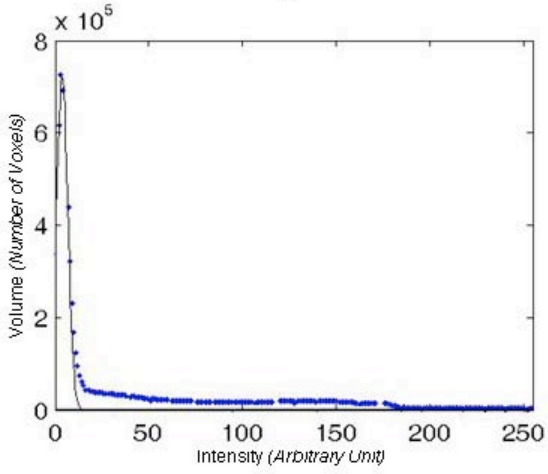

b

Figure 6.1.1: Example of intensity distribution affected by resampling errors, before (a) and after regularization, conversion to 8 bit format and filtering (b).

Some studies in literature describe different approaches to the analysis of Brain intensity distributions. It shall be noticed that most of them do not consider their geometrical features. Models that assume a Gaussian distribution for the scan intensities, are widely used *(Wells, 1996; Schroeter, 1998; Guillemaud, 1997)*. Other algorithms *(Ruan, 2000)* add separate classes to take into account partial volume voxels and model them by independent Gaussian densities. A model of partial volume voxels based on Gaussian mixtures and probabilistic approach is proposed by Santago et al. *(Santago, 1993)*, and it is extensively used by other authors *(Shattuck, 2001; Gonzalez, 2002; Van Leemput, 2003)*. However, the models currently used at the state of the art have the limitation of not considering the spatial information. That is why increasing attention has been paid to methods that model the spatial information by a Markov random field (MRF) *(Shattuck, 2001; Held, 1997; Zhang, 2001; Ruan, 2002);*

The intensity distributions of the Brain, White Matter and Grey Matter a have been analyzed in database of 250 MRI scans of the head, and I propose a deterministic model based on the geometric features of the Brain, the Grey Matter and the White Matter *(Atzori, 2009)*. The model can be applied both in 2 dimensions (on a single slice) or in three dimensions (on the entire volume of the Brain).

The intensity distributions of the tissues are assumed to be Gaussians in absence of geometry dependent effects. For each tissue, the geometry effects are described in a second function included in the model, called *Geometry Dependence Function*, that is obtained in the following manner.

The Brain is modelled as an n-dimensional sphere of radium r_B included in the CSF. The White Matter is modelled as an n-dimensional sphere of radium r_W ($r_W<r_B$). The Grey Matter is obtained as the difference between the Brain and the White Matter. The intensities of the Grey Matter and of the White Matter are assumed to be distributed isotropically in the tissues. The transitions between different tissues are indeed distributed in an interface layer, as in the real scans.

Assuming, for example, that the White Matter, the Grey Matter and the CSF are detected with T1 weighted MRI (i.e.: the White Matter has an intensity range higher than the Grey Matter that has an intensity range higher than the CSF), the intensity distributions of the tissues (that are assumed to be Gaussians in absence of geometry dependent effects) will be affected by the geometry of the system depending on the average radium at which each intensity value is detected. In particular considering the Grey Matter, since the external surface (that interfaces with the CSF, that is detected with lower intensity) has an area greater than the internal surface (that interfaces with the White Matter, that is detected with higher intensity), the number of voxels with intensity lower than the Grey Matter centroid will be greater than the number of voxels with intensity higher than the grey Matter Centroid. Therefore, the intensity distribution of the Grey Matter will be asymmetrical.

In particular, the bi-dimensional intensity distribution model is:

Eq.6.1.2:

$$D_{2D}(I) = \sum_{t=1}^{n_t} A_t e^{-\frac{(I-C_t)^2}{2\sigma_t^2}} \cdot 2\pi\langle r_t(I)\rangle$$

Where: 2D stands for 2-dimensional; I for Intensity; t for tissue (Grey or White Matter), n_t for Number of tissues (2); C_t for Gaussian centroid of the considered tissue; A_t for Gaussian height of the considered tissue; $\sigma_t \approx$ FWHM/2.35 (FWHM=Full Width at Half Maximum); $2\pi<r_t(I)>^2$: Geometry Dependence Function of the considered tissue; $<r_t(I)>$: average intensity radium.

The three-dimensional intensity distribution model is:

Eq.6.1.3:

$$D_{3D}(I) = \sum_{t=1}^{n_t} A_t e^{-\frac{(I-C_t)^2}{2\sigma_t^2}} \cdot 4\pi\langle r_t(I)\rangle^2$$

Where: 3D stands for 3-dimensional; I for Intensity; t for tissue (Gray or White Matter), n_t for Number of tissues (2); C_t for Gaussian centroid of the considered tissue; A_t for Gaussian height of the considered tissue; $\sigma_t \approx$ FWHM/2.35; $2\pi<r_t(I)>^2$: Geometry Dependence Function of the considered tissue; $<r_t(I)>$: average intensity radium.

According to equations 6.1.2 and 6.1.3, the Geometry Dependence Function affects the intensity distributions more in the three-dimensional case than in the bi-dimensional one. Moreover, according to the described model, the effect of the Geometry Dependence Function should diminish as the solid angle of the part of the sphere used to compute the intensity distribution diminishes.
Therefore a Gaussian mixture function should fit better the bi-dimensional intensity distributions than the three dimensional ones, and it should fit with an intermediate result parts of the sphere that correspond to an intermediate solid angle.
To evaluate the model on real data, the intensity distributions of the Brains in the scans described in Chapter 5.1 are analysed. For each of the scan, the Splenium of the Corpus Callosum is automatically identified, and the Brain is automatically segmented. The bidimensional intensity distribution is computed on the coronal slice that includes the splenium of the corpus callosum (Fig.

6.1.2a). The three-dimensional intensity distribution is computed on the whole Brain (Fig. 6.1.2b). The intensity distribution of parts of the Brain that correspond to an intermediate solid angle are computed on each of the octants of a coordinate system centred in the Splenium of Corpus Callosum and with Principal axes that correspond to the rows, columns, and slices directions.
According to the hypotheses, the Gaussians mixture model better adapts to the bi-dimensional intensity distributions (average χ^2 fit test = 0.85) than to the three dimensional ones (average χ^2 fit test = 45.64), while the fit on parts of the entire volume obtain intermediate results (average χ^2 fit test = 23.28) (Fig. 6.1.3).
The experimental evaluation of the model leads to the conclusion that the assumptions made in Eq. 6.1.1 and Eq. 6.1.2 describe correctly the problem, and it enhances a strong dependence of the geometric dependence function from the solid angle considered in the computation of the intensity distributions.

The approach of Orao to the analysis of the intensity distributions is based on the considerations made during the description of the model.
The algorithm reduces the dependence of the intensity distributions from the geometry of the system diminishing during the subsequent phases of the algorithm the solid angle that correspond to the parts of the scan where the intensity distributions are computed. This approach is useful also to keep account into the analysis of possible effects of field inhomogeneities to the detection intensities of the tissues.
The first approximation analyses are performed on the entire volume. The subsequent ones are performed on the octants of a Cartesian coordinates system centred in the Splenium of Corpus Callosum, and characterized by intensity distributions:

Eq.6.1.4:

$$D_{3D}(I) = \sum_{t=1}^{n_t} A_t e^{-\frac{(I-C_t)^2}{2\sigma_t^2}} \cdot \frac{4\pi \langle r_t(I) \rangle^2}{8}$$

Where: 3D stands for 3-dimensional; I for Intensity; t for tissue (Gray or White Matter), n_t for Number of tissues (2); C_t for Gaussian centroid of the considered tissue; A_t for Gaussian height of the considered tissue; $\sigma_t \approx FWHM/2.35$; $2\pi<r_t(I)>^2$: Geometry Dependence Function of the considered tissue; $<r_t(I)>$: average intensity radium.

The final intensity distribution analyses are performed on volumes that correspond to a solid angle of (30°x30°). Therefore the three-dimensional intensity distribution can be approximately described as:

Eq.6.1.5:

$$D_{3D}(I) = \sum_{t=1}^{n_t} A_t e^{-\frac{(I-C_t)^2}{2\sigma_t^2}} \cdot \frac{4\pi\langle r_t(I)\rangle^2}{144}$$

Where: 3D stands for 3-dimensional; I for Intensity; t for tissue (Gray or White Matter), n_t for Number of tissues (2); C_t for Gaussian centroid of the considered tissue; A_t for Gaussian height of the considered tissue; $\sigma_t \approx FWHM/2.35$; $2\pi<r_t(I)>^2$: Geometry Dependence Function of the considered tissue; $<r_t(I)>$: average intensity radium.

In this case the effects of the geometry on the intensity distributions are negligible (χ^2 fit test on the fit with Gaussian mixture approximately equal to 1).

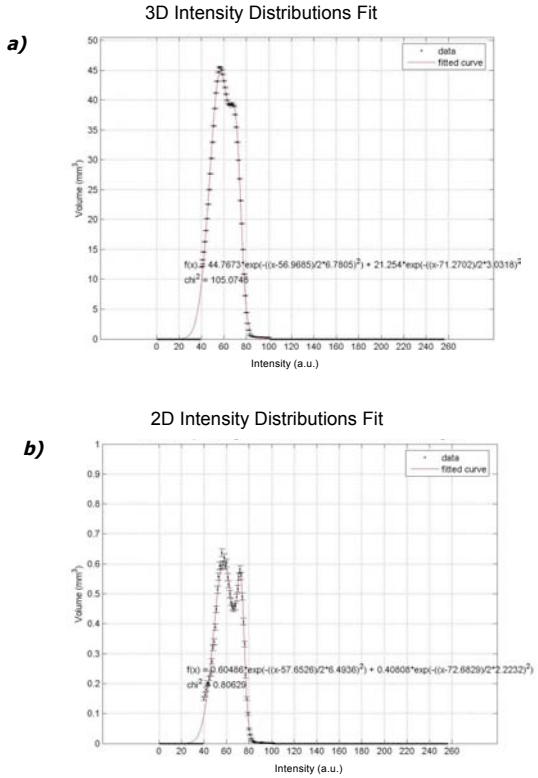

Fig.6.1.2: a) Bi-dimensional intensity distribution of White and Grey Matter in brain MRI fit with a mixture of two Gaussians. b) Three-dimensional intensity distribution of White and Grey matter in brain MRI fit with a mixture of two Gaussians.

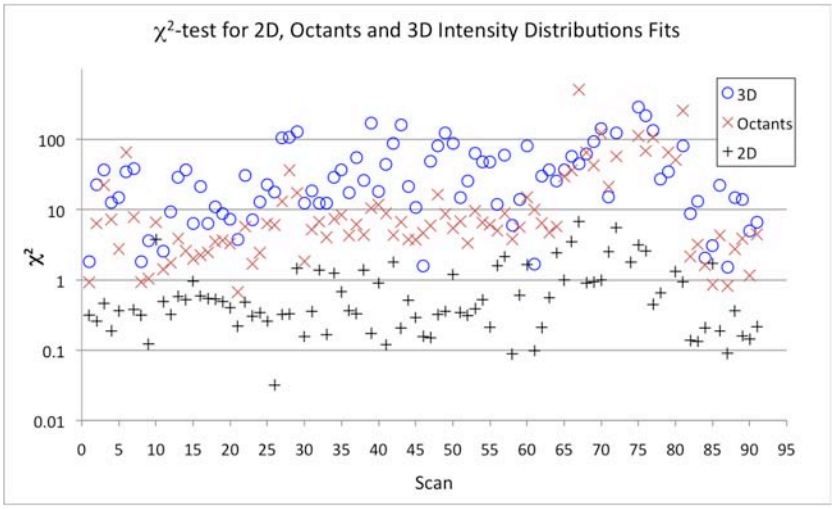

Fig.6.1.3: Results from χ^2-test for double Gaussian fit on bi-dimensional *(red squares)* and three dimensional *(blue triangles)* intensity distribuitons of White Matter and grey matter in 250 different subjects head MRI.

6.2 Brain and CSF Segmentation

6.2.1 Algorithm Implementation

I realized Orao, a novel algorithm for Brain Segmentation in T1 weighted MRI scans of the head.
The algorithm has been implemented with Matlab, is fully automatic and works on Nifti (.nii), Analyze (.hdr, .img) and Dicom (.dcm) scans.
Orao is based on deterministic analysis of the scans. It operates through recursive analyses of global *(Atzori, 2007)* and local *(Atzori, 2009)* intensity distributions (made through Gaussian mixtures fit), on the application of morphological operators (erosion, dilation and conditioned dilation) and connectivity analysis.
First Orao reconstructs the matrix I0 correspondent to the three dimensional scan (both for scans composed by a single file, i.e. Nifti and Analyze, and for scans composed by multiple files, i.e. Dicom files. Then it recognises the orientation of the head through meta-data information.
Orao creates a copy B0 of I0 and analyzes the intensity distribution of B0 in order to identify the head in B0. In the 89 scans analyzed, the highest peak is composed by Air and Bone. The Air and Bone peak is always split from other intensity peaks at its half height. Therefore, the algorithm identifies the air peak as the highest one and fit it with a Gaussian (Fig. 6.2.1):

Eq.6.2.1: $$D_{Air}(I) = H_{Air} \cdot e^{\frac{-(I-C_{Air})^2}{2\sigma_{Air}^2}}$$

Where I stands for intensity, H_{Air} for the height of the Gaussian, C_{Air} for the centroid of the Gaussian, $\sigma_{Air} \approx FWHM/2.35$.

Orao identifies then the entire head in B0. It sets to zero the B0 elements with intensity lower than:

Eq.6.2.2: $$Max_{Air} = C_{Air} + 2 \cdot \sigma_{Air}$$

It identifies the connected object with the highest volume in B0, that corresponds to the head without bone and sinuses, and it sets to zero all the other objects.
Finally it fills the three dimensional holes in B0 and the bidimensional holes in each of the three principal planes (Transverse, Coronal and Sagittal) of B0. The intensity of the holes are set to the correspondent values of I0. This step is

needed in order to permit further and more accurate analysis of the intensity range of the skull and of the surrounding tissues.
The algorithm identifies the Splenium of Corpus Callosum in the head. This anatomical region has been choose as starting point for the algorithm because it is characterized by peculiar properties: it is approximately located in the centre of mass of the Brain, it is easy identifiable and it is usually not strongly modified by pathologies.
To identify the Splenium, the algorithm identifies the region where it is most probably localized in the head through geometrical proportions (Fig. 6.2.2A). It computes the intensity distribution of the region and fits it with the sum of three Gaussians corresponding to Cerebro Spinal Fluid *(CSF),* Grey Matter *(GM)* and White Matter *(WM)* (Fig. 6.2.2B):

Eq. 6.2.3:

$$D_{L,1}(I) = H_{CSF,L,1} \cdot e^{\frac{-(I-C_{CSF,L,1})^2}{2\sigma_{CSF,L,1}^2}} + H_{GM,L,1} \cdot e^{\frac{-(I-C_{GM,L,1})^2}{2\sigma_{GM,L,1}^2}} + H_{WM,L,1} \cdot e^{\frac{-(I-C_{WM,L,1})^2}{2\sigma_{WM,L,1}^2}}$$

Where I is the intensity, H are the heights of the Gaussians, C the centroids of the Gaussians, for each Gaussian $\sigma \approx FWHM/2.35$, *CSF stands for Cerebro Spinal Fluid, GM for Grey Matter and WM for White Matter, L stands for Local.*

Possible candidates to be the Splenium of Corpus Callosum are all the matrix elements included in the probability region that are detected as White Matter, therefore with intensity in the interval $[C_{WM,L,1}-\sigma_{WM,L,1}, C_{WM,L,1}+\sigma_{WM,L,1}]$. The algorithm uses now the geometric and anatomic features of the Splenium to identify it among the other possible candidates.
All of the candidates are considered as the centres of mass of White Matter ellipsoids with variable radium and fixed proportions along the three principal directions (superior-inferior, anteroposterior and mediolateral axes; usually correspondent, not in order, to the directions of rows, columns and slices). The algorithm increases the radium of each of the ellipsoids. When an ellipsoid reaches the internal surface of the Grey Matter, the growth of the ellipsoid is stopped. The Splenium of Corpus Callosum is finally identified as the matrix element that is the centre of mass of the ellipsoid with greatest volume (Fig. 6.2.2A).
The Splenium of the Corpus Callosum is considered as the origin of a Cartesian coordinate system, while the principal axes of the scan are considered as its principal axes.
The identification of the Splenium of Corpus Callosum is particularly important, since the subsequent steps of the algorithm often assume to know its position.

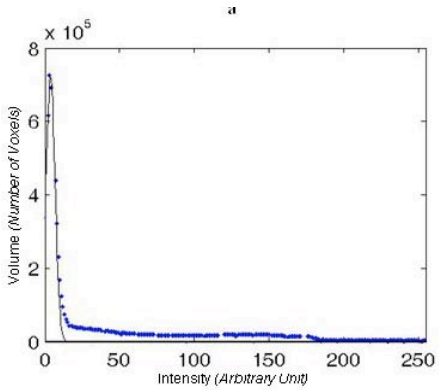

Figure 6.2.1: Gaussian fit of the Air and Skull peak in an example of intensity distribution.

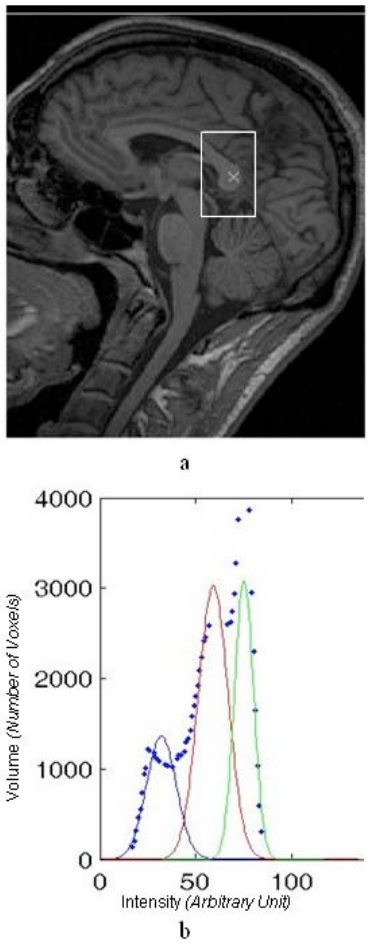

Figure 6.2.2: Example of identification of the Splenium of Corpus Callosum. a) Probability region and final result; b) Local Intensity Distribution Fit with three Gaussians.

The analysis of the head global intensity distribution is performed, in order to identify the Skull intensity peak and first approximation parameters for Cerebro Spinal Fluid, Grey Matter and White Matter Peaks. The analysis is performed making a fit with the sum of four Gaussians:

Eq.6.2.4:

$$D_{G,1}(I) = H_{Sk,G,1} \cdot e^{\frac{-(I-C_{Sk,G,1})^2}{2\sigma_{WM,G,1}^2}} + H_{CSF,G,1} \cdot e^{\frac{-(I-C_{CSF,G,1})^2}{2\sigma_{CSF,G,1}^2}} + H_{GM,G,1} \cdot e^{\frac{-(I-C_{GM,G,1})^2}{2\sigma_{GM,G,1}^2}} + H_{WM,G,1} \cdot e^{\frac{-(I-C_{WM,G,1})^2}{2\sigma_{WM,G,1}^2}}$$

Where I is the intensity, H are the heights of the Gaussians, C the centroids of the Gaussians, for each Gaussian $\sigma \approx FWHM/2.35$*, Sk stands for Skull, CSF for Cerebro Spinal Fluid, GM for Grey Matter and WM for White Matter, G stands for Global.*

The skull and air cavities connected to the skull are roughly segmented as the biggest object inside the head with intensity in the interval $[C_{Sk,G,1}-\sigma_{Sk,G,1}, C_{Sk,G,1}+\sigma_{Sk,G,1}]$ connected in three dimensions. Both those constituents are set to zero in the matrix B0.
Local intensity distributions analyses are then performed on the octants of the Cartesian coordinates system, in order to identify the local intensity peaks of the Cerebro Spinal Fluid, Grey Matter and White Matter. The analyses are performed making a fit with the sum of three Gaussians (Fig. 6.2.3):

Eq.6.2.5:

$$D_{L,2,i}(I) = H_{CSF,L2,i} \cdot e^{\frac{-(I-C_{CSF,L,2,i})^2}{2\sigma_{CSF,L,2,i}^2}} + H_{GM,L,2,i} \cdot e^{\frac{-(I-C_{GM,L,2,i})^2}{2\sigma_{GM,L,2,i}^2}} + H_{WM,L,2,i} \cdot e^{\frac{-(I-C_{WM,L,2,i})^2}{2\sigma_{WM,L,2,i}^2}}$$

$(i \in \mathrm{N}, 1 \le i \le 8)$

Where I is the intensity, H are the heights of the Gaussians, C the centroids of the Gaussians, for each Gaussian $\sigma \approx FWHM/2.35$*, CSF stands for Cerebro Spinal Fluid, GM for Grey Matter and WM for White Matter, L stands for Local.*

Two intensity limits are computed for each octant from the results of the fits *Eq. 6.2.5*. The values $GM_{L,2,i,Min}$ are computed for each octant as the intersection between the local *CSF* and Grey Matter Gaussians. The values $WM_{L,2,i,Max}$ are computed as $C_{WM,L,2,i} + 3\ \sigma_{WM,L,2,i}$.
For each octant, the elements of B0 characterized by intensities inferior to the correspondent $GM_{L,2,i,Min}$ value are set to zero in B0. The same is performed for the elements of B0 characterized by intensities greater than $WM_{L,2,i,Max}$ (Fig. 6.2.4a,b).

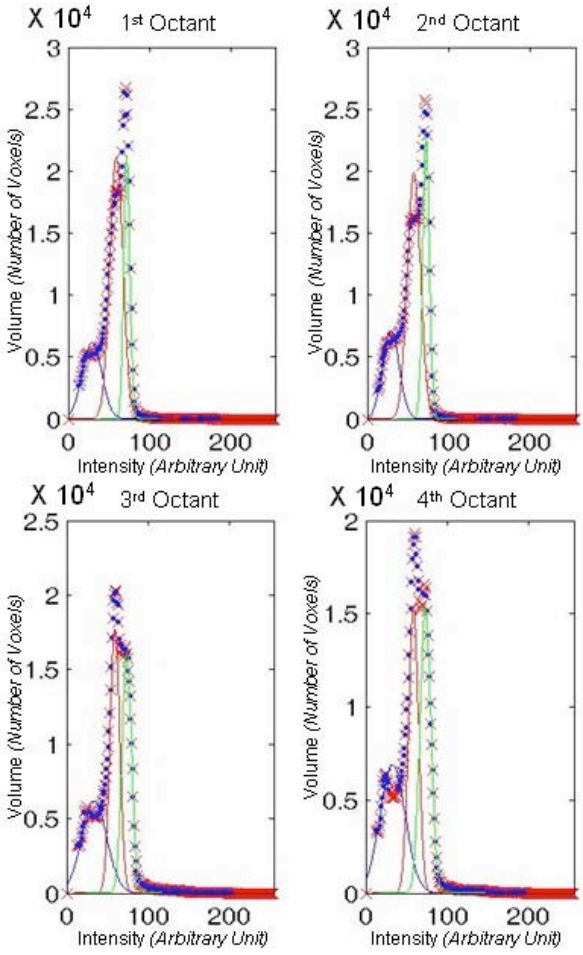

Figure 6.2.3: Examples of Local Intensity Analyses on the octants of the scan.

Now the algorithm analyses the connectivity of the tissues of B0. As described in chapters 1.2.1 and 3.1.3 the Brain is connected in three dimensions, therefore the tissues that are not connected in 3D with the Splenium of Corpus Callosum are set to zero in B0.
Since the tissues of the Brain are usually connected in two dimensions at least in one of the principal planes, the algorithm evaluates the bidimensional connectivity of B0 separately in the coronal, sagittal and transverse plane. A copy L0 of B0 is created in logical form, with the values greater than zero in B0 converted to 1 in L0. Two zero matrices C0 and C1 are created of the same size of B0. The coronal, sagittal and transverse planes of C0 intersecting in the Splenium of Corpus Callosum are imposed to be equal to their correspondents

in L0. The objects of C0 that are not connected in three dimensions with the Splenium of Corpus Callosum are set to zero. Every coronal, sagittal and transverse slice of L0 is then analyzed. The elements of the slice that are connected in two dimensions with the voxels different from zero of the correspondent slice of C0 are identified. The value of one is added to the elements of correspondent coordinates in C1. Orao identifies then the C1 elements with values inferior to three (which correspond to the elements of L0 that are not connected to the Splenium of the Corpus Callosum in the three principal planes), and sets the B0 elements of correspondent coordinates to zero.

In order to cut the remaining links between Grey Matter, White Matter and the other tissues of the head with similar intensities, the morphologic operators of Erosion, Dilation and Conditioned Dilation are now applied to B0.

A copy L1 of B0 is created in logical form. The erosion morphological operator is applied on L1 till the ratio between volume of the voxels connected to the Splenium of the Corpus Callosum and the volume of the entire head is inferior to a fixed value (determined empirically) (Fig. 6.2.4c,d). The used morphological alteration form is a sphere of 3.5 mm of diameter.

In order not to lose the connection of the Splenium of Corpus Callosum with peripheral data, plan regions around it (in the coronal, sagittal and transverse plan, with sizes empirically determined through proportion laws) are substituted in each erosion step with the correspondent regions of L1, keeping in them only the elements connected with the splenium of corpus callosum. Let's call the matrix obtained after the erosion step E.

A copy D0 of the matrix E is created. The dilation morphologic operator is then applied to D0 a number of times 5% greater than the number of iterations applied with the erosion morphologic operator (Fig. 6.2.4e). The used morphological alteration form is again a sphere of 3.5 mm of diameter.

A copy B1 of the matrix I0 is created. The voxels equal to zero in D0 are set to zero in B1.

Local intensity distributions analyses are then performed on B1 on the octants of the Cartesian coordinates system centred in the Splenium, in order to identify the local intensity peaks of the Cerebro Spinal Fluid, Grey Matter and White Matter. The analyses are performed making a fit with the sum of three Gaussians:

Eq. 6.2.6:

$$D_{L,3,i}(I) = H_{CSF,L,3,i} \cdot e^{\frac{-(I-C_{CSF,L,3,i})^2}{2\sigma_{CSF,L,3,i}^2}} + H_{GM,L,3,i} \cdot e^{\frac{-(I-C_{GM,L,3,i})^2}{2\sigma_{GM,L,3,i}^2}} + H_{WM,L,3,i} \cdot e^{\frac{-(I-C_{WM,L,3,i})^2}{2\sigma_{WM,L,3,i}^2}}$$
$$(i \in \mathrm{N}, 1 \le i \le 8)$$

Where I is the intensity, H are the heights of the Gaussians, C the centroids of the Gaussians, for each Gaussian $\sigma \approx$ FWHM/2.35, CSF stands for Cerebro Spinal Fluid, GM for Grey Matter and WM for White Matter, L stands for Local.

The values $GM_{L,3,i,Min}$ are computed for each octant as the intersection between the local *CSF* and Grey Matter Gaussians.
For each octant, the elements of B1 characterized by intensities inferior to the correspondent $GM_{L,3,i,Min}$ value are set to zero in B0.
In B1, the tissues that are not connected in three dimensions with the Splenium of Corpus Callosum are set to zero. The bidimensional connectivity of B1 is then evaluated in the coronal, sagittal and transverse plane: as was done previously for B0, the tissues that are not connected in each of the three dimensions with one of the principal planes slices that include the Splenium of Corpus Callosum are set to zero in B1.
Dilation is now iterated to the matrix obtained after the erosion step E (Fig. 6.2.4d), conditioned to B1 (Fig. 6.2.4f). The used morphological alteration form is again a sphere of 3.5 mm of diameter.
The end of the conditioned dilation iteration is determined through an empirical criterion based on the ideas that the Brain is an approximately convex and isotropic shape. At each conditioned dilation step, two matrices (both of the same size of E) P_{i-1} and P_i are created: P_{i-1} is the matrix correspondent to the outlier surface of E before the conditioned dilation step; P_i is the matrix correspondent to the outlier surface of E after the conditioned dilation step. Let's call N_{i-1} as the number of elements of P_{i-1}; N_i as the number of elements of $P_{i-1} \cap P_i$. Let's define R_i as the ratio between N_i and N_{i-1}, and R_{i-1} as the ratio between N_i and N_{i-1} at the previous conditioned dilation step. The iteration of the conditioned dilation step is concluded if:

$R_i < 0.03$

or if:

$R_i > R_{i-1}$

The definition of the limit is based on three assumptions empirically verified:

1. Since the matrix E is about equidistant from the surface of the brain in each of its parts, its dilation will reach the surface of the brain in the same number of dilation steps in each part of it.
2. The surface of connection points of the brain with other tissues of the head (as the meninges and the eyes) is inferior to the 3% of the total brain surface.
3. Since the brain is almost a convex shape, we will have $R_i < R_{i-1}$ unless the brain segmentation is growing up in connection points of the brain with other tissues of the head (as the meninges and the eyes).

A copy B2 of I0 is created. The voxel equal to zero in E are set to zero in B2.

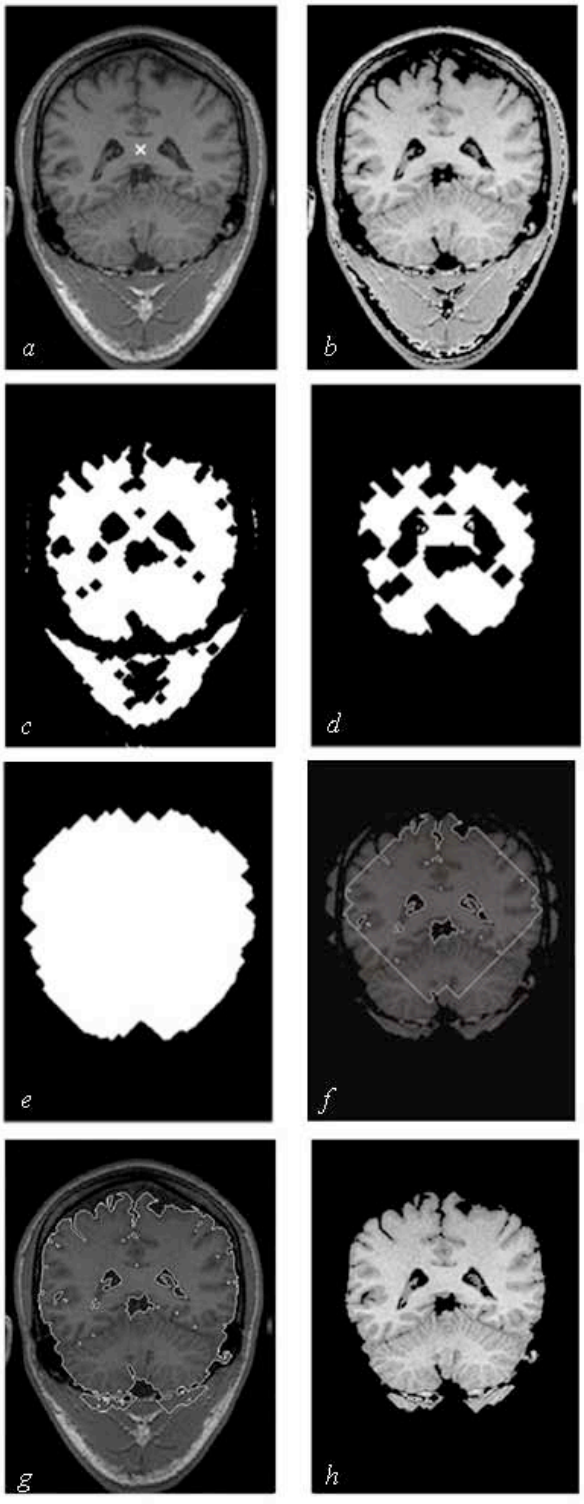

Figure 6.2.4: Brain Segmentation process. a) Splenium Identification; b) Intensity threshold; c) Erosion d) End of the erosion phase; e) Dilation; f) Conditioned Dilation; g,h) Final Result.

A filter to remove the spinal column and a filter to refine the Brain segmentation near the eyes are then applied.
The filter to remove the spinal column identifies the height at which the spinal column ends as the height at which the grey matter starts from the bottom of the head. Then it sets to zero all the B2 elements under the evaluated height.
The complete removal of the eyes is a tricky problem in Brain segmentation of T1 MRI scans, since the intensity range with which the eyes are detected by the apparatus is very similar to the range with which White Matter is detected.
The idea on which is based my algorithm is that some voxels corresponding to the eyes will be included in B2. Therefore, if the algorithm identifies a part of those voxels, it will be able to identify also the others by neighbourhood.
The filter identifies on each octant of B2 the elements with intensity in the interval $[C_{WM,L,3,i}-\sigma_{WM,L,3,i}, C_{WM,L,3,i}+\sigma_{WM,L,3,i}]$ *(i Є N, 1≤i≤8)*. It selects the part of those elements that is not connected with the Splenium of Corpus Callosum. It creates a zero matrix F1 of the same size of B2. It set the obtained elements to one. It dilates F1 using a sphere of 3.5 mm of diameter as morphological alteration form and removes the obtained elements by B2. It creates a copy F2 of B2 in logical form. It dilates F2 using a sphere of 3.5 mm of diameter as morphological alteration form. It computes the intersection of F1 with F2. Finally the filter sets to zero the elements of each octant of B2 that correspond to elements with value 1 in F1 ∩ F2 and that in B2 have value out of the interval $[C_{GM,L,3,i}-\sigma_{GM,L,3,i}, C_{GM,L,3,i}+\sigma_{GM,L,3,i}]$ *(i Є N, 1≤i≤8)*.
Orao segments then the Cerebro Spinal Fluid using its intensity and geometrical properties. The CSF is localized inside the Brain (in the Ventricles) and outside the Brain (surrounding it). Moreover the CSF is characterized by the local intensities described in *Eq. 6.2.6.*
A copy CSF of B2 is created in logical form.
In order to include the internal Cerebro Spinal Fluid, the three-dimensional and bi-dimensional holes of CSF are filled, respectively in 3D and in the Axial, Coronal and Sagittal planes.
In order to include the external CSF, the matrix D0 (Fig. 6.2.4e), obtained previously, is again considered. The non zero elements of D0 are set to the correspondent values of the matrix I0.
The values $CSF_{L,3,i,Min}$ are computed for each octant as $[CSF_{L,3,i,Min}-2\bullet\sigma_{GM,L,3,i}]$.
For each octant, the elements of D0 characterized by intensities inferior to the correspondent $CSF_{L,3,i,Min}$ value are set to zero in the matrix D0.
In D0, the tissues that are not connected in three dimensions with the Splenium of Corpus Callosum are set to zero. The bidimensional connectivity of D0 is then evaluated in the coronal, sagittal and transverse plane (as was previously done for B0): the tissues that are not connected in each of the four cases with the Splenium of Corpus Callosum (or with one of the principal planes slices that include it) are set to zero in D0.
Dilation is now iterated 6 times to the matrix CSF, conditioned to D0. The used morphological alteration form is again a sphere of 3.5 mm of diameter. The number of iterations has been determined empirically on the basis of the maximal distance between the CSF and the Brain surface observed in the subjects of the dataset.

The Cerebro Spinal Fluid is finally segmented setting the non zero voxels of the matrix CSF to the correspondent values of the matrix I0.

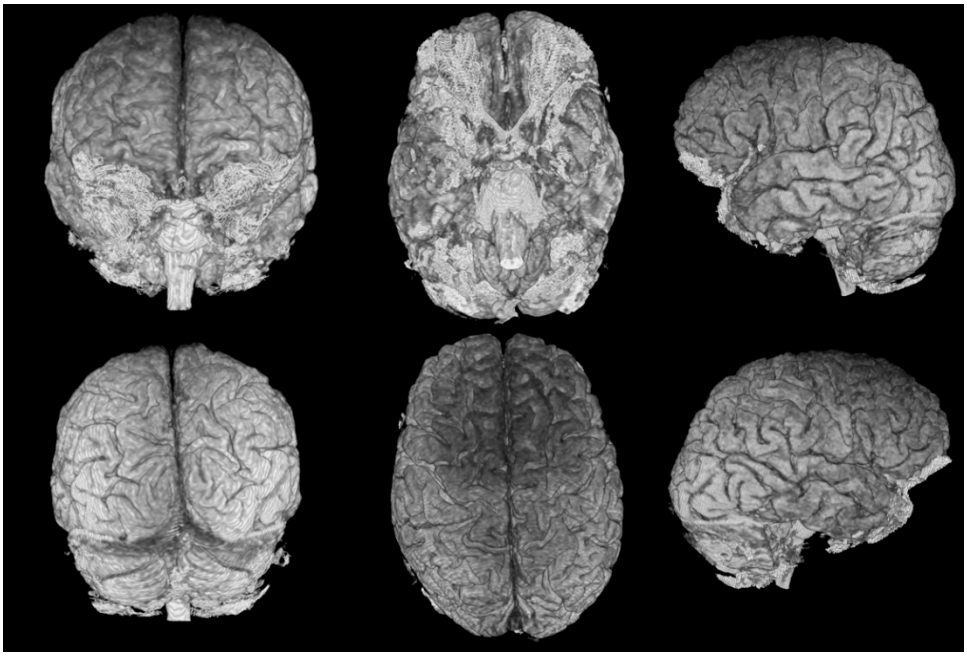

Figure 6.2.5: 3D reconstruction of the results from the application of the Brain segmentation phase of the algorithm.

6.2.2 Algorithm Characterization

The database on which the algorithm has been tested is described in Chapter 5.1. It is composed by 89 real MRI T1 scans, subdivided in 7 data sets acquired with 5 different MRI Scanners and with 7 different acquisition sequences.
The database is very various. It includes T1 MRI scans characterized by different formats (nifti, analyze and dicom), resolutions, acquisition sequences, intensity distributions and subjects (characterized by different sex, ages and health conditions). This variety makes the database a good test set for Orao.
The test of the Brain segmentation part of Orao is performed on the described database in the following manner.
The evaluation of the identification of the Splenium of corpus Callosum is performed through visual inspection made by experts of the field.
The quantitative evaluation of the results of Orao is made through comparison with ground truth data. This is performed on the scans from the LONI Segmentation Validation Engine (40 Scans from the Laboratory Of Neuro Imaging of the University of California Los Angeles Segmentation Validation Engine, http://sve.loni.ucla.edu) and from the IBSR dataset (20 scans from the Internet Brain Segmentation Repository, provided by the Centre for Morphometric Analysis of the Massachusetts General Hospital in association with Harvard Medical School, http://www.cma.mgh.harvard.edu/ibsr).
The Brain segmentation ground truth of the LONI Segmentation Validation Engine is obtained in the following manner *(Shattuck, 2009)*. A cerebrum mask is obtained after realignment of the scan. Each MRI volume is first aligned with a rigid-body rotation to the MNI-305 average brain (181×217×181) voxels; Ten standard anatomical landmarks are identified manually in each MRI volume by a trained operator *(Narr, 2002; Sowell, 1999)*. The landmarks for the subject are matched with a set of corresponding point locations defined on the MNI-305 average brain using a least-squares fit *(MacDonald, 1994)*. Each scan is resampled into a common coordinate system with the same dimensions and resolution as the atlas using trilinear interpolation. Magnetic field inhomogeneities are corrected using a nonparametric non-uniformity normalization method *(Sled, 1998)*. Extra-meningeal tissues are removed in the resampled data using the FSL Brain Extraction Tool (FSL BET) *(Smith, 2002)*. Manual correction is applied to the automated segmentation of the brain. The cerebellum and brainstem are removed manually to produce a cerebrum mask. A set of 56 structures is labelled in each of the 40 brain MRIs. For each scan an initial brain mask is created taking the union of the voxels that are contained in the cerebrum mask and structure label volumes. BrainSuite is used to fill brain areas that have not been included and also to exclude any additional voxels that were determined not to be brain, and finally any internal cavities in the brain masks are filled. The labels and brain masks are then resampled to the space of the subject's original MRI using nearest-neighbour interpolation. Any internal cavities or disjoint brain voxels in the resampled brain masks are removed using a connected-components labelling program.
The Brain segmentation ground truth of the Internet Brain Segmentation Repository is obtained by manual segmentations performed by experts at the Massachusetts General Hospital.

To perform the quantitative validation of the Brain segmentation results, the Sensitivity, Specificity and Dice coefficient *(Dice, 1945)* are computed for the Brain segmentation results both on the LONI and the IBSR datasets. The Jaccard coefficient *(Jaccard, 1912)*, also known as the Tanimoto coefficient, is computed only for the results the on the LONI dataset.
The description of the mentioned evaluation metrics is here summarized. Let X be the set of all voxels in the image, $T \in X$ the ground truth, $S \in X$ the set of voxels that were labelled as Brain by the segmentation method being tested. The true positive set is defined as $TP = T \cap S$. The true negative set is defined as $TN = T \setminus S$ (the set of voxels that were labelled as non-brain in both sets). The false positive set is $FP = T \setminus S$ and the false negative set is $FN = T \setminus S$.
The used evaluation metrics are:

Eq.6.2.7: $$Sensitivity = \frac{|TP|}{|TP| + |FN|} = \frac{|TP|}{|T|}$$

Eq.6.2.8: $$Specificity = \frac{|TN|}{|TN| + |FP|} = \frac{|TN|}{|\overline{T}|}$$

Eq.6.2.9: $$Jaccard(T,S) = \frac{|T \cap S|}{|T \cup S|} = \frac{|TP|}{|TP| + |FP| + |FN|}$$

Eq.6.2.10: $$Dice(T,S) = \frac{|T \cap S|}{\frac{1}{2}(|T| + |S|)} = \frac{|TP|}{\frac{1}{2}(|TP| + |FN| + |TP| + |FP|)}$$

The quantitative validation of the results of Orao makes possible its comparison with the software most used in Brain Imaging (FSL, Freesurfer and SPM, described in chapter 3.3.3).
The comparison on the LONI Segmentation Validation Engine is made with the results described by Shattuck et al. *(Shattuck, 2009)* for FSL's Brain Extraction Tool *(Smith, 2002)*, FreeSurfer's Hybrid Watershed Algorithm (HWA) *(Sègonne, 2004)* and Brain Surface Extractor (BSE) *(Shattuck, 2001)*. FSL Brain Extraction Tool (BET) version 2.1 is included as part of the FSL 4.1 package. The script for FSL BET offers the following options that may improve the results: -R: robust brain centre estimation (iterates FSL BET several times); -S: eye and optic nerve cleanup; -B: bias field and neck cleanup. FSL BET was tried with its default settings, as well as each of the options listed above. The used version of Freesurfer Hybrid Watershed Algorithm (Freesurfer HWA) is distributed as part of FreeSurfer 3.0.5. The software is tested with different combinations of the options: atlas (use the atlas information to correct the segmentation); less (shrink the surface); more (expand the surface).
The used version of Brain Surface Extractor **(**BSE) is BSE08a, which is LONI internal development version. This version includes the features described in Shattuck et al., 2008 *(Shattuck, 2008)*. The parameters available include: n (the

number of diffusion iterations applied), d (the diffusion constant used), s (the edge detection constant used), p (post-processing dilation of the brain mask). The default values for BSE correspond to the settings: n=3, d=25, s=0.64. Other settings based on an empirical evaluation of one test subject were also tried (n=3, d=15,s=0.7, p; n=3, d=18, s=0.7, p; n=5, d=18, s=0.7, p).
For each of the software, only the best results obtained are considered.
The comparison on the Internet Brain Segmentation Repository is made with the results described by Tsang et al. *(Tsang, 2008)* for FSL's Brain Extraction Tool *(Smith, 2002)* and SPM5 Brain Segmentation algorithm *(Ashburner, 2005)*. In FSL, the brainmask utility from the Neuroimage Processing Toolkit (NPTK), developed in the Signal and Image Processing Lab at the University of Texas at Dallas, is used after the skull stripping. (In a previous work, the brainmask utility was found to augment the output of the brain extraction tool for a more complete image of the brain *(Tsang, 2007)*.
A qualitative evaluation of the Brain segmentation results is performed through visual inspection on the entire dataset.
A further characterization is made comparing the ability of Orao and SPM5 (actually the most used Brain segmentation software in Brain imaging) to distinguish differences between the healthy controls and patients affected by schizophrenia. Since both age and gender affect the brain volumes *(Caserta, 2009; Cosgrove, 2007),* the group of the healthy controls and the group of the patients affected by schizophrenia are matched in order to have comparable ages and gender distributions. Since the age of illness is suspected to affect the volumes and functionality of the Brain *(Mathalon, 2001)*., the schizophrenic patients group is chosen in order to have an age of illness longer than eight years The aim of this decision is to have a high effect of the illness.
The scans are acquired with the ICBN T1-weighted structural MRI acquisition sequence described in Chapter 5.1 (Tab. 5.1.1, Dataset 5).
To perform the t-test characterization, a 2 tails t-test is applied to the Brain and Cerebro Spinal volumes of the healthy controls and of the patients affected by schizophrenia. The p-values of the t-tests are computed for Orao and for SPM5 (Fig. 6.2.6). Since SPM5 returns probabilistic segmentation maps, a probability threshold of 0.5 is applied in order to obtain the Brain volumes.
The Splenium of the Corpus Callosum is correctly identified in 80 scans, therefore in the 90% of the database. In the other 10% cases the voxel identified as splenium is usually a neighbour one made of White Matter, and does not created problems to the successive steps of the algorithm.
The quantitative validation of the Brain segmentation phase results made on the data from the LONI Segmentation Validation Engine through comparison with ground truth data shows good results for average Specificity, Sensitivity, Dice and Jaccard coefficients (Table 6.2.1).
The quantitative validation of the results made on the data from the Internet Brain Segmentation Repository through comparison with ground truth data shows very good results for average Specificity, Sensitivity and Dice coefficient (Table 6.2.2).
The comparison with the state of the art of the Brain segmentation results on the LONI Segmentation Validation Engine shows that Orao average performance is comparable to the performances of FSL BET, BSE and FreeSurfer Brain segmentation algorithms (Table 6.2.1).

The comparison with the state of the art of the Brain segmentation results on the Internet Brain Segmentation Repository shows that Orao has an average performance similar for specificity but more than 20% higher for sensitivity than FSL BET and SPM5 (Table 6.2.2).
The qualitative evaluation of the Brain (performed through visual inspection on the entire dataset) shows agreement with the anatomy of the subjects results on the 96% of the entire database. This evaluation is useful because it proves the robustness of the algorithm and its ability to work on very different datasets .
The comparison of the ability of Orao and SPM5 to distinguish differences between the healthy controls and patients affected by schizophrenia obtains excellent results. Orao shows greater ability than SPM to identify differences between the two categories. The average t-test p-value obtained with Orao is (0.18 ± 0.21), while the average p-value obtained with SPM5 is (0.54 ± 0.32).
The analysis of the volume differences obtained with Orao and SPM5 has been performed too, and it enhances that the differences are equally distributed among the healthy controls and the patients. This fact supports the use of Orao for the segmentation of both the healthy controls and patients groups.
Orao is fast using a 3-GHz Pentium 4, 1 GB RAM. The average time needed for Brain segmentation process is 6.2 minutes on the data from the LONI Segmentation Validation Engine, 3.6 minutes on the data from the Internet Brain Segmentation Repository.

Method	Jaccard	Dice	Sensitivity	Specificity
FSL BETv2.1	0.9400 ±0.0089	0.9691 ±0.0048	0.9627 ±0.0117	0.9957 ±0.0014
BSE v08a	0.9394 ±0.0330	0.9684 ±0.0188	0.9725 ±0.0382	0.9937 ±0.0028
Freesurfer HWA3	0.8537 ±0.0184	0.9210 ±0.0107	0.9992 ±0.0003	0.9695 ±0.0053
Orao	0.9308 ±0.0165	0.9641 ±0.0090	0.9627 ±0.0159	0.9937 ±0.0048

Table 6.2.1: Metrics computed for the 4 Brain Segmentation approaches on the LONI Segmentation validation Engine.

Algorithm	Sensitivity	Specificity
FSL FAST	74.6%	98.6%
SPM	78.0%	98.8%
Orao	99.0%	98.6%

Table 6.2.2: Metrics computed for the 3 Brain Segmentation approaches on the IBSR Dataset.

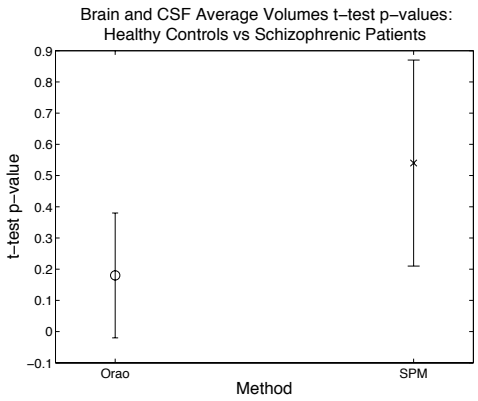

Fig. 6.2.6: Healthy controls vs. patients affected by schizophrenia: average 2 tails t-test p-values for Brain and CSF average Volumes. Comparison between Orao and SPM.

6.2.3 Discussion

Our goal was to develop a fully automatic algorithm for the segmentation of the brain. The algorithm had to be characterized by low assumptions about the brain, high precision, robustness and ductility. My segmentation process seems to have reached the desired characteristics.
Orao is based on deterministic analysis of the data, made through recursive analyses of global *(Atzori, 2007)* and local *(Atzori, 2009)* intensity distributions of the scan, mathematical morphology and the analysis of connectivity properties.
The use of Gaussians mixtures to model the intensity distributions is justified by the considerations described in Chapter 6.1 *(Atzori, 2009)*.
The algorithm does not use any prior knowledge about the brain, except for the assumption of the existence of the Splenium of Corpus Callosum and of the Brain. Moreover it does not require any pre-processing as spatial or intensity normalization procedure, nor uses atlases or templates.
The algorithm has been implemented with Matlab. It is fully automatic and works on Nifti (.nii), Analyze (.hdr, .img) and Dicom (.dcm) scans.
The algorithm has been quantitatively validated and compared with state of the art procedures.
The quantitative validation of the Brain segmentation has been performed comparing the results with ground truth segmentations on the LONI Segmentation Validation Engine dataset and on the IBSR dataset. Orao obtained excellent results for Sensitivity, Specificity, Dice coefficient and Jaccard Coefficient on both the datasets.
The comparison of the results of Orao on the LONI Segmentation Validation Engine with the results of brain segmentation tools of FSL, Freesurfer and BSE shows that the accuracy of Orao is comparable with the state of the art. The comparison on the IBSR dataset with the results of brain segmentation tools of FSL, SPM shows that the Specificity of Orao is more than 20% greater than the state of the art.
The results of the qualitative evaluation enhance the high robustness of Orao. Actually the database was created in order to include very different T1 MRI scans, characterized by different formats (nifti, analyze and dicom), resolutions, acquisition sequences, intensity distributions and subjects (characterized by different sex, ages and health conditions).
The comparison of the ability of Orao and SPM5 to distinguish differences between the healthy controls and patients affected by schizophrenia enhances that Orao has greater ability than SPM to identify differences between the two categories (average t-test p-values respectively of 0.18±0.21 and 0.54±0.32).
The equal distribution of the volume differences of Orao and SPM5 between the healthy controls and the patients supports the use of Orao for the segmentation of both the subject classes.
Orao is fast (one process takes 3-6 minutes on a 3-GHz Pentium 4 running Windows XP, 1 GB RAM).

6.3 Grey Matter and White Matter Segmentation

6.3.1 Algorithm Implementation

The segmentation of Grey Matter and White Matter is performed on segmented data of the Brain (for example, the Grey-Matter segmentation algorithm can be applied on the matrix B2 obtained in the end of Chapter 6.2.1).
The segmentation algorithm need to know the position of the Splenium of Corpus Callosum. If the position of the Splenium have not been yet computed, the algorithm described in the beginning of Chapter 6.1 can be applied.
First the algorithm identifies the matrix elements that correspond with the highest confidence to Grey Matter. This is performed on the basis of the geometrical and intensity properties of the tissue. The Grey Matter is mostly localized on the surface of the brain, and it has an average thickness of approximately 2 mm: therefore the algorithm searches for the voxels on the surface of the Brain characterized by intensity values that correspond with high probability to the Grey Matter.
Orao makes a copy B3 and a logical copy B4 of the matrix that includes the segmented data of the Brain *(B2)*. The erosion morphological operator is applied on B4 using as morphological alteration form a sphere of 3.5 mm of diameter. The algorithm creates a copy G of B3. It finds the elements equal to zero in B4 and greater than zero in G. It sets to zero the elements of correspondent coordinates in G. Then it sets to zero the elements of G that, according to geometrical proportions (computed from the position of the Splenium of Corpus Callosum), could be localized in the Brainstem, since those voxels do not include Grey Matter.
Local intensity distributions analyses are then performed on B3 on the octants of a Cartesian coordinates system centred in the Splenium of Corpus Callosum, with principal axes correspondent to the principal axes of the scan (superior-inferior, anteroposterior and mediolateral axes; usually correspondent, not in order, to the directions of rows, columns and slices). The analyses are performed making a fit with the sum of two Gaussians:

Eq. 6.3.1:

$$D_{L,3,i}(I) = H_{GM,L,3,i} \cdot e^{\frac{-(I-C_{GM,L,3,i})^2}{2\sigma_{GM,L,3,i}^2}} + H_{WM,L,3,i} \cdot e^{\frac{-(I-C_{WM,L,3,i})^2}{2\sigma_{WM,L,3,i}^2}}$$
$$(i \in \mathrm{N}, 1 \le i \le 8)$$

Where I is the intensity, H are the heights of the Gaussians, C the centroids of the Gaussians, for each Gaussian $\sigma \approx$ *FWHM/2.35, GM stands for Grey Matter and WM for White Matter, L stands for Local.*

For each octant of G, the algorithm sets to zero the elements that do not belong to the local interval $[C_{GM,L,3,i}-\sigma_{GM,L,3,i}, C_{GM,L,3,i}+\sigma_{GM,L,3,i}]$ (i Є N, $1 \le i \le 8$) (Fig. 6.3.1a).
Orao makes then a further analysis of the matrix G, in order to perform a stronger selection of the voxels that correspond with high confidence to the Grey Matter . At the mean time, the algorithm uses the local analysis made on G and the results from the fit described in Eq.6.3.1 to identify the voxels that correspond to the White Matter. In order to perform this operation, it creates a copy W0 of B3 and a zero matrix W of the size of B3.
Considering the Splenium of Corpus Callosum as the centre of a spherical coordinates system, the algorithm analyses the matrix G with solid angle step of $\pi/12$. For each angular step Orao searches (from the extremes of G in the direction of the Splenium) for elements of G greater than zero. (Fig. 6.3.1b).
If it finds them, it selects the voxels of G included in a cube centred in the identified point, with edges (parallel to the principal axes of G) of length $l=Radium \cdot sin(\pi/12)$.
It analyzes the intensity distribution of the considered matrix elements fitting it with a single Gaussian:

Eq.6.3.2: $$G_{GM,L,4,i}(I) = H_{GM,L,4,i} \cdot e^{\frac{-(I-C_{GM,L,4,i})^2}{2\sigma_{GM,L,4,i}^2}}$$
$$(i \in \mathrm{N}, 1 \le i \le 144)$$

Where I is the intensity, H is the height of the Gaussian, C the centroid of the Gaussian, $\sigma_{GM} \approx FWHM/2.35$, GM stands for Grey Matter, L stands for Local.

The algorithm identifies then the voxels of G included in the cube and characterized by intensity values that are not included in the interval $[C_{GM,L,4,i}-\sigma_{GM,L,4,i}, C_{GM,L,4,i}+\sigma_{GM,L,4,i}]$, and it sets them to 0.
Orao considers then the correspondent cube in the matrix W0. It sets to zero the voxels of W0 included in the cube that are not included in the interval:

$[max(C_{WM,L,3,i}-\sigma_{WM,L,3,i}, C_{GM,L,4,i}+\sigma_{GM,L,4,i}), C_{WM,L,3,i}+\sigma_{WM,L,3,i}]$

It analyzes the intensity distribution of the considered matrix elements of W0, fitting it with a single Gaussian:

Eq.6.3.3: $G_{WM,L,4,i}(I) = H_{WM,L,4,i} \cdot e^{\frac{-(I - C_{WM,L,4,i})^2}{2\sigma_{WM,L,4,i}^2}}$

$(i \in \mathrm{N}, 1 \le i \le 144)$

Where I is the intensity, H is the height of the Gaussian, C the centroid of the Gaussian, $\sigma_{WM} \approx FWHM/2.35$*, WM stands for White Matter, L stands for Local.*

The algorithm identifies then the voxels of W0 included in the cube and characterized by intensity values that are included in the interval $[C_{WM,L,4,i} - \sigma_{WM,L,4,i}, C_{WM,L,4,\mathrm{i}} + \sigma_{WM,L,4,i}]$, and it sets the correspondent voxels of W to the same values.
At this point, two matrices G and W have been obtained with local intensity values for the Grey Matter and the White Matter.
Orao now diffuses the intensity information in G and W and obtains two matrices filled with the local Grey Matter and White Matter values
To perform this operation, it subdivides G and W in cubes with edges length of 5 mm, and it sets the zero voxels of each cube to the mean of the non zero values. This operation is iterated increasing the length of the edge of the cubes multiplying it at each step for the number of repetitions that have been performed. The iteration is stopped when all the voxels with values greater than zero in B3 have values greater than zero in the correspondent voxels of W and G.
The matrices G and W are then smoothed, and it is created the matrix GW1, in which each voxel corresponds to the separation intensity between the Grey Matter and the White Matter (Fig. 6.3.1d):

Eq.6.3.4:

$$GW = G + \frac{W - G}{2}$$

Finally, the Grey Matter and the white Matter are segmented according to their intensity and connectivity properties.
To segment the Grey Matter, a copy GF of B3 is created. The elements of GF with values greater than the correspondent GW voxels are set to zero. Grey Matter is identified setting to zero the GF elements not connected with the object characterized by the greatest volume in GF (Fig. 6.3.1e).
White Matter is segmented as (Fig. 6.3.1f):

Eq.6.3.5: $WF = (B > GW) \setminus GF$

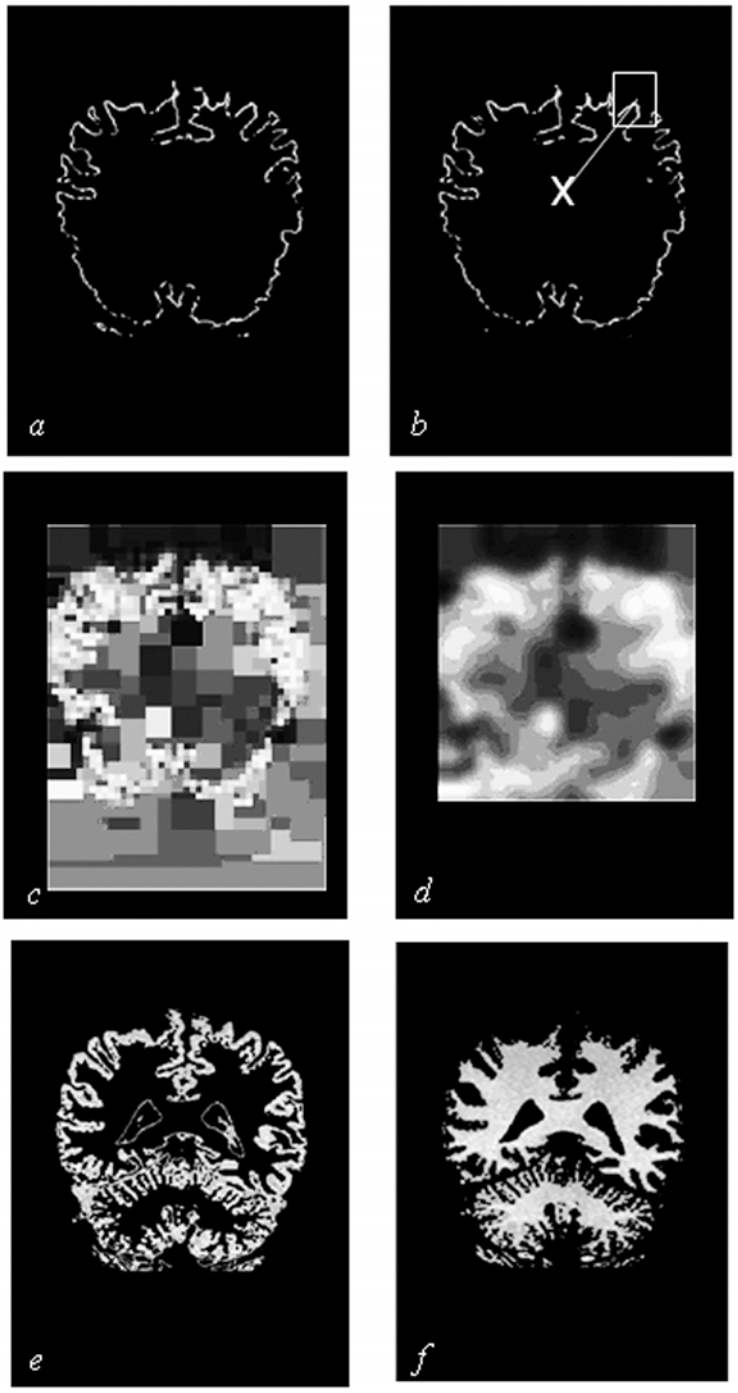

Figure 6.3.1: Grey Matter and White Matter Segmentation process. a) Identification of Grey Matter high confidence voxels; b) Local Intensity Analysis and Filtering; c) Creation of the Grey Matter Intensity Values Matrix; d) Creation of the Grey Matter – White Matter Local Threshold Matrix; e) Grey Matter Segmentation results; f) White Matter Segmentation results.

6.3.2 Algorithm Characterization

The grey matter and White Matter segmentation algorithm is tested on the same database described for the Brain segmentation algorithm, composed by 89 real MRI T1 scans.
Quantitative evaluation of the results of the Grey Matter and White Matter segmentation part of the algorithm is performed on the scans from the IBSR dataset. The Grey Matter and White Matter segmentation ground truth of the Internet Brain Segmentation Repository is obtained by manual segmentations performed by experts at Massachusetts General Hospital. To perform the quantitative validation of the Grey Matter and White Matter segmentation results, the Sensitivity, Specificity and Dice coefficient (described in chapter 6.1.3) are computed.
A qualitative evaluation of the Grey Matter and White Matter segmentation results is performed through visual inspection on the entire dataset.
A comparison of the segmentation results with the state of the art is performed comparing Orao quantitative validation results on the IBSR dataset with the results described by Tsang et al. *(Tsang, 2008)* for FSL's Automated Segmentation Tool (FAST) *(Smith, 2002)* and SPM5 Brain Segmentation algorithm *(Ashburner, 2005)*.
A further characterization is made comparing the ability of Orao and SPM5 (currently the most used Grey and White Matter segmentation software in Brain imaging) to distinguish differences between the healthy controls and patients affected by schizophrenia. Since both age and gender affect the brain volumetries *(Caserta, 2009; Cosgrove, 2007),* the group of the healthy controls and the group of the patients affected by schizophrenia are matched in order to have comparable ages and gender distributions. Since the age of illness is suspected to affect the volumes and functionality of the Brain *(Mathalon, 2001)*, the schizophrenic patients group is chosen in order to have an age of illness longer than eight years. The aim of this decision is to have a high effect of the illness. The scans are acquired with the ICBN T1-weighted structural MRI acquisition sequence described in Chapter 5.1 (Tab. 5.1.1, Dataset 5).
To perform the characterization, a 2 tails t-test is applied to the Grey Matter and White Matter volumes of the healthy controls and of the patients affected by schizophrenia. The p-values of the t-tests are computed for Orao and for SPM5 (Fig. 6.3.3). Since SPM5 returns probabilistic segmentation maps, a probability threshold of 0.5 is applied in order to obtain the Brain volumes.
The quantitative validation results of the Grey Matter segmentation shows that Orao has an excellent average Specificity, but a low average Sensitivity (Table 6.3.1). This is expected since Orao have been realized in order to be restrictive rather than conservative due to the needs of the Research Unit in Brain Imaging and Neuropsychology,.
The quantitative validation of the White Matter segmentation shows good results for both average Sensitivity and Specificity (Table 6.3.1).
The fact that Orao is realized in order to be restrictive rather than conservative, also affects the comparison with the state of the art of the Grey Matter segmentation results. The average Dice coefficient result is inferior to the ones obtained by FSL BET and SPM5 (Table 6.3.2).

The qualitative evaluation for the Grey Matter and White Matter segmentation results, is performed on the entire dataset through visual inspection made by experts of the field. It shows agreement with the anatomy of the subjects on the 96% of the entire database. As noticed before in the Brain segmentation results, this evaluation is useful because it proves the robustness of the algorithm and its ability to work on very different datasets (89 real MRI T1 scans, subdivided in 7 data sets acquired with 5 different MRI Scanners and with 7 different acquisition sequences, nifti, analyze and dicom formats, different resolutions, acquisition sequences and subjects, characterized by different sex, ages and health conditions).
The comparison of the ability of Orao and SPM5 to distinguish differences between the healthy controls and patients affected by schizophrenia obtains excellent results. Orao shows greater ability than SPM to identify differences between the two categories.
The average t-test p-value obtained with Orao is (0.36 ± 0.34), while the average p-value obtained with SPM5 is (0.56±0.33).
The analysis of the volume differences obtained with Orao and SPM5 has been performed too, and it enhances that the differences are equally distributed among the healthy controls and the patients. This fact supports the use of Orao for the segmentation of both the healthy controls and the patients groups.
Orao is fast (one process takes 1-4 minutes on a 3-GHz Pentium 4 running Windows XP, 1 GB RAM).

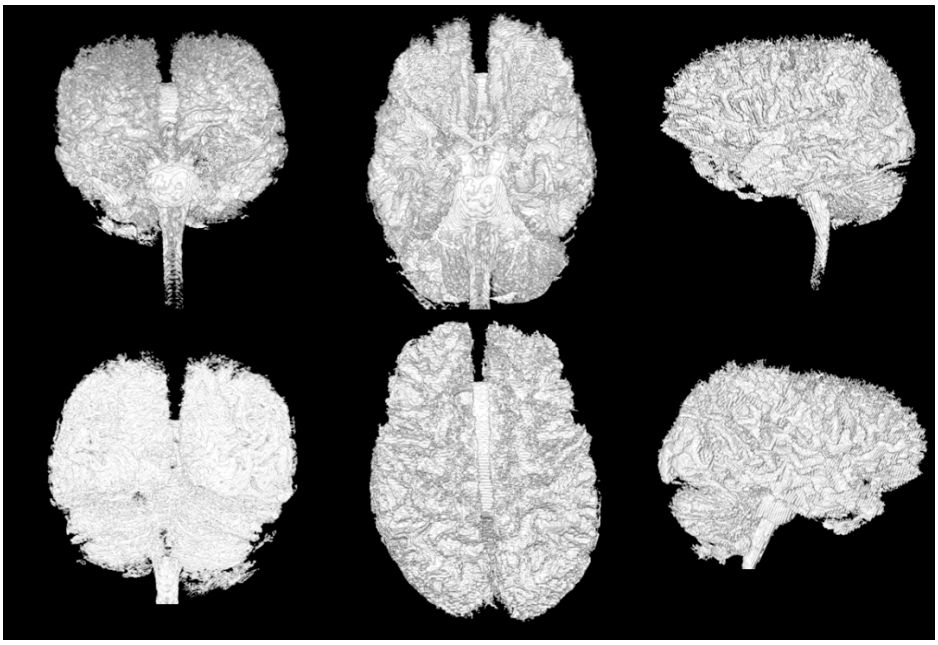

Figure 6.3.2: 3D reconstruction of the results from the application of the White Matter segmentation phase of the algorithm.

Algorithm	Anatomical Structure	Sensitivity	Specificity
Orao	Grey Matter	50.0%	99.6%
Orao	White Matter	72.6%	95.5%

Table 6.3.1: Orao metrics computed for the Grey and White Matter segmentation on the IBSR Dataset.

Algorithm	Dice Coefficient
FSL FAST	75.6%
SPM	79.0%
Orao	63.7%

Table 6.3.2: Dice coefficient computed for the 3 Grey Matter Segmentation approaches on the IBSR Dataset.

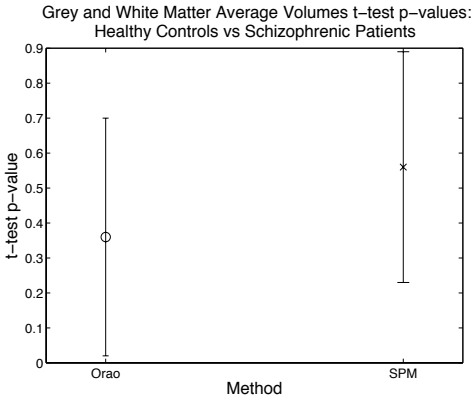

Fig. 6.3.3: Healthy controls vs. patients affected by schizophrenia: average 2 tails t-test p-values for Grey and White Matter average volumes. Comparison between Orao and SPM.

6.3.3 Discussion

I developed Orao, a fully automatic algorithm for the segmentation of grey matter and White Matter. The algorithm is characterized by low assumptions about the brain, high precision, robustness and ductility. Orao is based on deterministic analysis of the data, made through recursive analyses of global *(Atzori, 2007)* and local *(Atzori, 2009)* intensity distributions of the scan, morphological operators and connectivity properties.
The use of Gaussians mixtures to model the intensity distributions is justified by the considerations described in Chapter 6.1 *(Atzori, 2009)*.
The algorithm is implemented with Matlab. It is fully automatic and works on Nifti (.nii), Analyze (.hdr, .img) and Dicom (.dcm) scans.
Before the application of the White Matter and Grey Matter segmentation phase of Orao, it is needed the application of a Brain segmentation algorithm.
The algorithm does not use any prior knowledge about the brain, except for assumption of the existence of the Brain, of the Grey and White Matter of the Splenium of Corpus Callosum. Moreover it does not require any pre-processing as spatial or intensity normalization procedure, nor uses atlases or templates.
The quantitative validation of the White Matter and Grey Matter segmentation algorithm has been performed comparing the results with ground truth segmentations on the IBSR dataset. Orao obtained good results for Sensitivity, Specificity and Dice coefficient for White Matter. Lower results were obtained for the Grey Matter.
The comparison with the results of Grey Matter segmentation tools of FSL and SPM shows that Orao has higher Specificity, but lower Sensitivity. This result is justified by the fact that Orao has been realized in order to be restrictive rather than conservative, due to the needs of the Research Unit in Brain Imaging and Neuropsychology of the ICBN.
The results of the qualitative evaluation enhance the high robustness of Orao. Actually the database was created in order to include very different T1 MRI scans, characterized by different formats (nifti, analyze and dicom), resolutions, acquisition sequences, intensity distributions and subjects (characterized by different sex, ages and health conditions).
The comparison of the ability of Orao and SPM5 to distinguish differences between the healthy controls and patients affected by schizophrenia enhances that Orao has greater ability than SPM to identify differences between the two categories (average t-test p-values respectively of 0.36±0.33 and 0.56±0.33).
The equal distribution of the volume differences of Orao and SPM5 between the healthy controls and the patients supports the use of Orao for the segmentation of both the subject classes.
Orao is fast (one process on the LONI and IBSR datasets takes 1-4 minutes on a 3-GHz Pentium 4 running Windows XP, 1 GB RAM).

Chapter 7

Other Applications of the Segmentation Algorithm

As described in chapter 3, fully automatic, robust and reliable segmentation algorithms are a challenging problem in the analysis of the data from MRI, CT, CTA and other imaging modalities.
Chapter 6 describes the functioning of a novel automatic algorithm for the segmentation of the Brain, CSF, White Matter and Grey Matter in MRI of the head.
In order to test the ductility of the algorithm, I decided to test the procedure on different anatomical structures and image acquisition modalities.
This chapter describes the methods and the results of these applications. Since the mentioned applications are realized to evaluate the ductility of the algorithm (and not in order to be applied straightaway to medical analysis), the qualitative evaluation of the results is considered sufficient.
Modifications of the algorithm are done in each case in order to adapt it to the specific anatomic structure.
Chapter 7.1 describes the application of the algorithm to the segmentation of the skull in T1 MRI scans of the head.
Chapter 7.2 describes the application of the algorithm to the segmentation of the Brain, Grey Matter, White Matter, Cerebro Spinal Fluid, Tumour end Tumoral Edema in T2 MRI scan of the head.
Chapter 7.3 describes the application of the algorithm to the segmentation of Bone and tissues perfused by contrast medium (Heart, Aorta, Kidneys, Urinary Tracts and Urinary Bladder) in Computed Tomography angiography of the Thorax and Abdomen.

7.1 Skull Segmentation in T1 MRI

The state of the art described in Chapter 3.3.3 enhances that there is still a need for a robust method to segment the skull boundaries in MRI.
Therefore I decided to test a modified version of the algorithm described in chapter 6 on this problem.
The features of the analysed scans are described in chapter 5.1.

7.1.1 Algorithm Implementation

The algorithm has been implemented with Matlab, is fully automatic and works on Nifti (.nii), Analyze (.hdr, .img) and Dicom (.dcm) scans.
As the Brain Segmentation algorithm, the algorithm is based on deterministic analysis of the scans. It operates through recursive local and global analyses of the intensity distributions (made through Gaussian mixtures fit), on the application of morphological operators (dilation) and connectivity analysis.
As described in Chapter 6 for the Brain, Grey and White Matter segmentation algorithm, the intensity distributions data are filtered through the analysis of their continuity properties before each intensity analysis, because the intensity distributions can be often affected by resampling alterations.
The skull segmentation algorithm uses for the first part of the analysis the same processes of the Brain segmentation algorithm.
First it is reconstructs the matrix I0 correspondent to the three dimensional scan (both for scans composed of a single file (Nifti, Analyze) or of multiple files (dicom files). Then it recognises the orientation of the head through meta-data information.
The algorithm converts I0 in 8 bit format, (if it is of a different format), in order to reduce the time needed to process it. The conversion is made in order to minimize the useful information loss, as described in Chapter 6.
The algorithm creates a copy Sk0 of I0 and analyzes the intensity distribution of Sk0. In the 89 scans analyzed, the highest peak is composed by the union of the air peak and the bone peak. Moreover the air-bone peak is always split from other intensity peaks at its half height.
Therefore, the algorithm identifies the air and skull peak in the intensity distribution as the highest one and fits it with a Gaussian (Fig. 7.1.1a):

Eq.7.1.1:

$$D_{Air\&Skull}(I) = H_{Air\&Skull} \cdot e^{\frac{-(I - C_{Air\&Skull})^2}{2\sigma_{Air\&Skull}^2}}$$

Where D(I) is the intensity Distribution, I is the intensity, $H_{Air\&Skull}$ is the height of the Gaussian, $C_{Air\&Skull}$ the centroid of the Gaussian, $\sigma_{Air\&Skull} \approx FWHM/2.35$.

Orao identifies then the entire head in B0. It sets to zero the B0 elements with intensity lower than:

Eq.7.1.2: $Max_{Air\&Skull} = C_{Air\&Skull} + 2 \cdot \sigma_{Air\&Skull}$

It identifies the connected object with the highest volume in Sk0, that corresponds to the head without bone and sinuses, and it sets to zero all the other objects.
Finally it fills the three dimensional holes in Sk0 and the bidimensional holes in each of the three principal planes (Transverse, Coronal and Sagittal) of Sk0 (Fig. 7.1.1b). This step is needed in order to permit further and more accurate analysis of the intensity range of the skull and of the surrounding tissues. The voxels greater than zero in Sk0 are set to the correspondent values of I0.
The algorithm identifies the Splenium of Corpus Callosum as described in Chapter 6.2. The algorithm identifies the region where the Splenium is most probably localized in the head through geometrical proportions. It computes the intensity distribution of the region and fits it with the sum of three Gaussians corresponding to Cerebro Spinal Fluid, Grey Matter and White Matter:

Eq. 7.1.3:

$$D_{L,1}(I) = H_{CSF,L,1} \cdot e^{\frac{-(I - C_{CSF,L,1})^2}{2\sigma_{CSF,L,1}^2}} + H_{GM,L,1} \cdot e^{\frac{-(I - C_{GM,L,1})^2}{2\sigma_{GM,L,1}^2}} + H_{WM,L,1} \cdot e^{\frac{-(I - C_{WM,L,1})^2}{2\sigma_{WM,L,1}^2}}$$

Where I is the intensity, H are the heights of the Gaussians, C the centroids of the Gaussians, for each Gaussian $\sigma \approx FWHM/2.35$, CSF stands for Cerebro Spinal Fluid, GM for Grey Matter and WM for White Matter, L stands for Local.

Possible candidates to be the Splenium of Corpus Callosum are all the matrix elements included in the probability region that are detected as White Matter, therefore with intensity in the interval $[C_{WM,L,1}-\sigma_{WM,L,1}, C_{WM,L,1}+\sigma_{WM,L,1}]$. All of the candidates are considered as the centres of mass of White Matter ellipsoids with variable radium and fixed proportions along the three principal directions

(superior-inferior, anteroposterior and mediolateral axes; usually correspondent, not in order, to the directions of rows, columns and slices). The algorithm increases the radium of each of the ellipsoids. When an ellipsoid reaches the internal surface of the Grey Matter, the growth of the ellipsoid is stopped. The Splenium of Corpus Callosum is finally identified as the matrix element that is the centre of mass of the ellipsoid with greatest volume.
The algorithm computes then the intensity distribution of the voxels that are included in the head.
In T1 weighted MRI, most of the tissues of the head are detected with intensity ranges that are similar to those of the Cerebro Spinal Fluid, of the Grey Matter and of the White Matter, while the Skull is detected with a peculiar and lower intensity range. Fat tissues are indeed detected with higher intensities.
The algorithm analyzes the intensity distribution of the head fitting it with the sum of four Gaussians:

Eq.7.1.4:

$$D_{L,2}(I) = H_{Sk,L,2} \cdot e^{\frac{-(I-C_{Sk,L,2})^2}{2\sigma_{WM,L,2}^2}} + H_{CSF,L,2} \cdot e^{\frac{-(I-C_{CSF,L,2})^2}{2\sigma_{CSF,L,2}^2}} + H_{GM,L,2} \cdot e^{\frac{-(I-C_{GM,L,2})^2}{2\sigma_{GM,L,2}^2}} + H_{WM,L,2} \cdot e^{\frac{-(I-C_{WM,L,2})^2}{2\sigma_{WM,L,2}^2}}$$

Where D(I) is the intensity Distribution, I is the intensity, H are the heights of the Gaussians, C the centroids of the Gaussians, for each Gaussian $\sigma \approx FWHM/2.35$, Sk stands for Skull, CSF for Cerebro Spinal Fluid, GM for Grey Matter and WM for White Matter, L stands for Local.

The fitting procedure does not include the fat tissues peak because their percentage in the head volume changes a lot in different subjects. Moreover, the fitting procedure is set in order to analyze only the intensities that are similar to those of the CSF, Grey Matter and White Matter on the basis of parameters computed from the intensity distribution analysis described in Eq. 7.1.3 (Fig.7.1.1c).
The intensity value $Sk_{Max,0}$ is then computed as the solution of the equation:

Eq.7.1.5:

$$H_{Sk,L,2} \cdot e^{\frac{-(I-C_{Sk,L,2})^2}{2\sigma_{Sk,L,2}^2}} = H_{CSF,L,2} \cdot e^{\frac{-(I-C_{CSF,L,2})^2}{2\sigma_{CSF,L,2}^2}}$$

($C_{Sk,L,2} < I < C_{CSF,L,2}$)

The matrix Sk1 is obtained through the segmentation of the Skull obtained applying threshold to the voxels of the matrix Sk (Fig. 7.1.1d):

$$Sk1 = \begin{cases} Sk > 0 \\ Sk < Sk_{Max,0} \end{cases}$$

The Skull is identified in Sk1 through its geometric relationship with the Splenium of Corpus Callosum *(Atzori, 2007)*.
The matrix Sk1 is converted in logical form in order to reduce computational time, and the dilation morphologic operator is applied to it. The used morphological alteration form is a sphere with radium 1.5 cm. The non-zero elements of Sk1 are set to the correspondent values of I0 (Fig. 7.1.1e).
The algorithm computes the intensity distribution of Sk1 and fits it with the sum of three Gaussians (Fig. 7.1.1f):

Eq.7.1.6:

$$D_{L,3}(I) = H_{Sk,L,3} \cdot e^{\frac{-(I-C_{Sk,L,3})^2}{2\sigma_{WM,L,3}^2}} + H_{CSF,L,3} \cdot e^{\frac{-(I-C_{CSF,L,3})^2}{2\sigma_{CSF,L,3}^2}} + H_{GM,L,3} \cdot e^{\frac{-(I-C_{GM,L,3})^2}{2\sigma_{GM,L,3}^2}}$$

Where D(I) is the intensity Distribution, I is the intensity, H are the heights of the Gaussians, C the centroids of the Gaussians, for each Gaussian $\sigma \approx FWHM/2.35$, Sk stands for Skull, CSF for Cerebro Spinal Fluid and GM for Grey Matter, L stands for Local.

The White Matter is not considered in this intensity distribution analysis because the percentage of White Matter included in the matrix Sk1 is usually very low.
The intensity value $Sk_{Max,1}$ is then computed as the solution of the equation:

Eq.7.1.7:

$$H_{Sk,L,3} \cdot e^{\frac{-(I-C_{Sk,L,2})^2}{2\sigma_{Sk,L,2}^2}} = H_{CSF,L,3} \cdot e^{\frac{-(I-C_{CSF,L,2})^2}{2\sigma_{CSF,L,2}^2}}$$

($C_{Sk,L,3} < I < C_{CSF,L,3}$)

The matrix Sk2 is obtained by the segmentation of the Skull obtained applying threshold to the voxels of the matrix Sk1 (Fig. 7.1.2):

$$Sk2 = \begin{cases} Sk1 > 0 \\ Sk1 < Sk_{Max,1} \end{cases}$$

Again the Skull is identified in Sk1 through its geometric relationship with the Splenium of Corpus Callosum.

7.1.2 Algorithm Characterization

I implemented an automatic algorithm for the segmentation of the skull in T1 weighted MRI of the head.
The algorithm has been implemented with Matlab, is fully automatic and works on Nifti (.nii), Analyze (.hdr, .img) and Dicom (.dcm) scans.
The algorithm is based on deterministic analysis of the scans. It operates through recursive local and global analyses of the intensity distributions (made through Gaussian mixtures fit), on the application of mathematical morphology operators (dilation) and connectivity analysis.
The robustness of the algorithm have been tested applying it on the T1 MRI database described in chapter 5.1. The algorithm is quick. It takes about 2 minutes to segment the skull.
The results have been qualitatively evaluated on the analysed scans through visual inspection. The algorithm showed good agreement with the morphological features of the Skull in 85% of the scans *(Fig. 7.1.2)*.

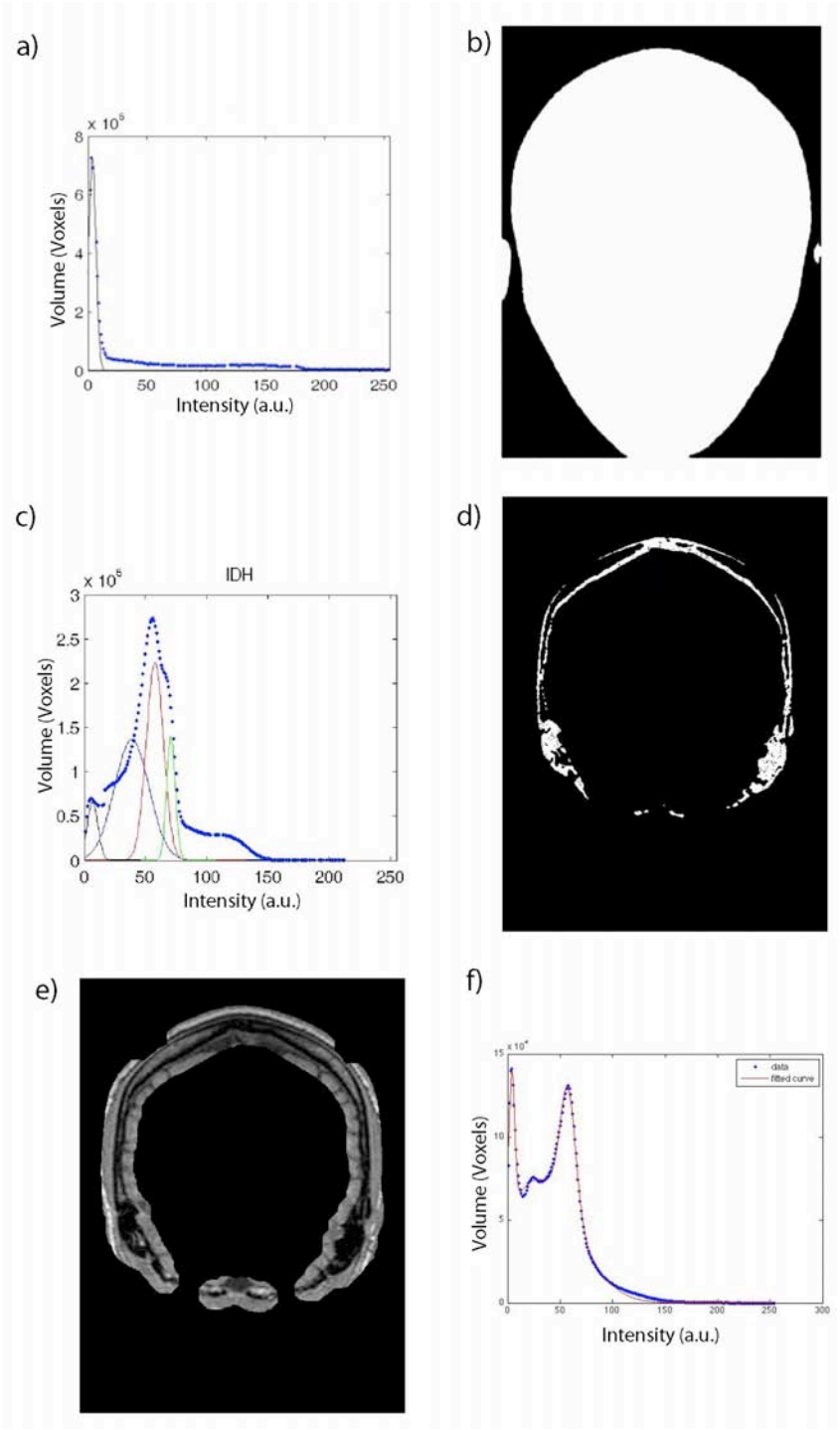

Fig. 7.1.1: Skull segmentation procedure: a) Identification of the air and skull peak in the global intensity distribution; b) Identification of the head; c) Analysis of the head intensity distribution; d) Threshold segmentation of the skull; d) Dilation of the skull; e) Intensity distribution analysis of the matrix obtained in step d.

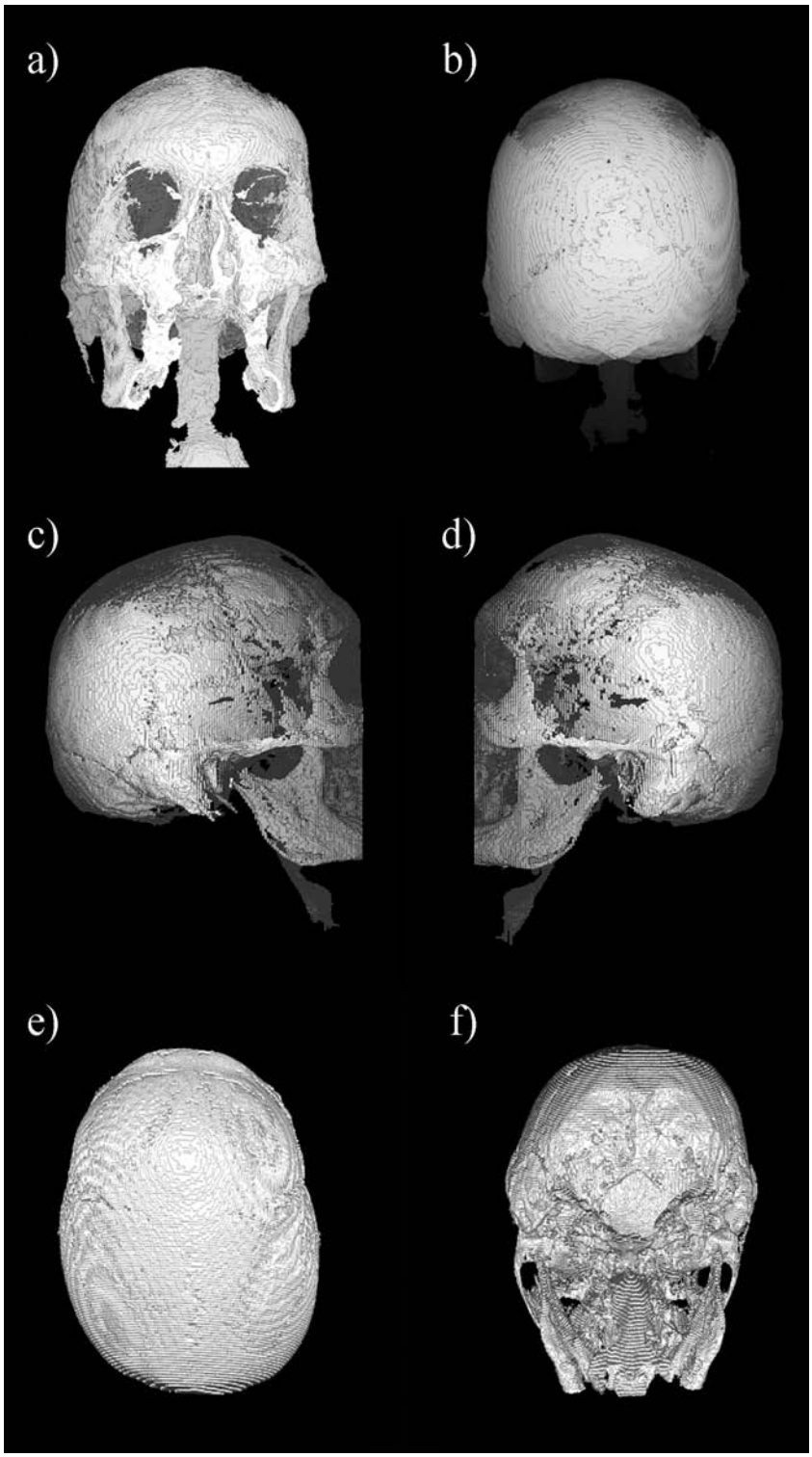

Fig. 7.1.2: Example of the results from Skull segmentation procedure in T1 MRI of the head.

7.2 Brain Tumour and Tumoral Edema Segmentation in MRI

The segmentation procedure is applied in this chapter to segment a Tumour and a Peritumoral Edema in T1 and T2 MRI scans of the head.
The purpose of this work is to create a 3D mathematical model of the head of the patient, in order to model the treatment of the tumour with Hyperthermia.

7.2.1 Data Selection and Merging

As described in Chapter 5.2, seven MRI scans are available for this work: four T1-Weighted, two T2-Weighted and one Proton Density. The first part of the work consists in the analysis of the scans, in order to select the most useful ones for the purpose.
The scans have similar resolutions (Tab. 5.2.1), but they show high differences in the intensity ranges with which the tissues are detected (Tab.7.2.1, Fig.7.2.1). The average intensities and standard deviations described in Tab.7.2.1 are obtained manually selecting a square with sides of 5 pixels in an approximately central slice of the scan.

	Scan	Cerebro Spinal Fluid	Grey Matter	White Matter	Tumour	Peritumoral Edema
1	Proton Density	1152,6 ± 7,3	1030,9 ± 5,2	838,2 ± 9,9	1150,3 ± 8,4	1181,1 ± 7,8
2	t2 tse tra	1151,1 ± 9,9	616,3 ± 7,3	435,4 ± 5,4	1158,4 ± 6,8	1185,6 ± 7,2
3	t1 se sag	367,4 ± 5,8	450,6 ± 9,9	516,2 ± 8,9	389,0 ± 6,4	360,5 ± 9,0
4	t2 tirm cor ark	722,8 ± 7,4	413,3± 6,2	230,0 ± 9,1	686,8 ± 7,2	746,5 ± 8,9
5	t1 se tra	387,0 ± 9,6	517,8 ± 6,8	608,1 ± 8,0	961,7 ± 6,1	422,3 ± 8,3
6	t1 se sag	276,8 ± 9,6	426,0 ± 9,0	506,7 ± 6,0	821,4 ± 6,5	287,8 ± 7,0
7	t1 se cor	350,3 ± 5,5	559,7 ± 8,7	623,5 ± 7,6	1080,7 ± 9,9	410,6 ± 7,0

Tab. 7.2.1: Principal tissues average intensities and standard deviations in the available scans.

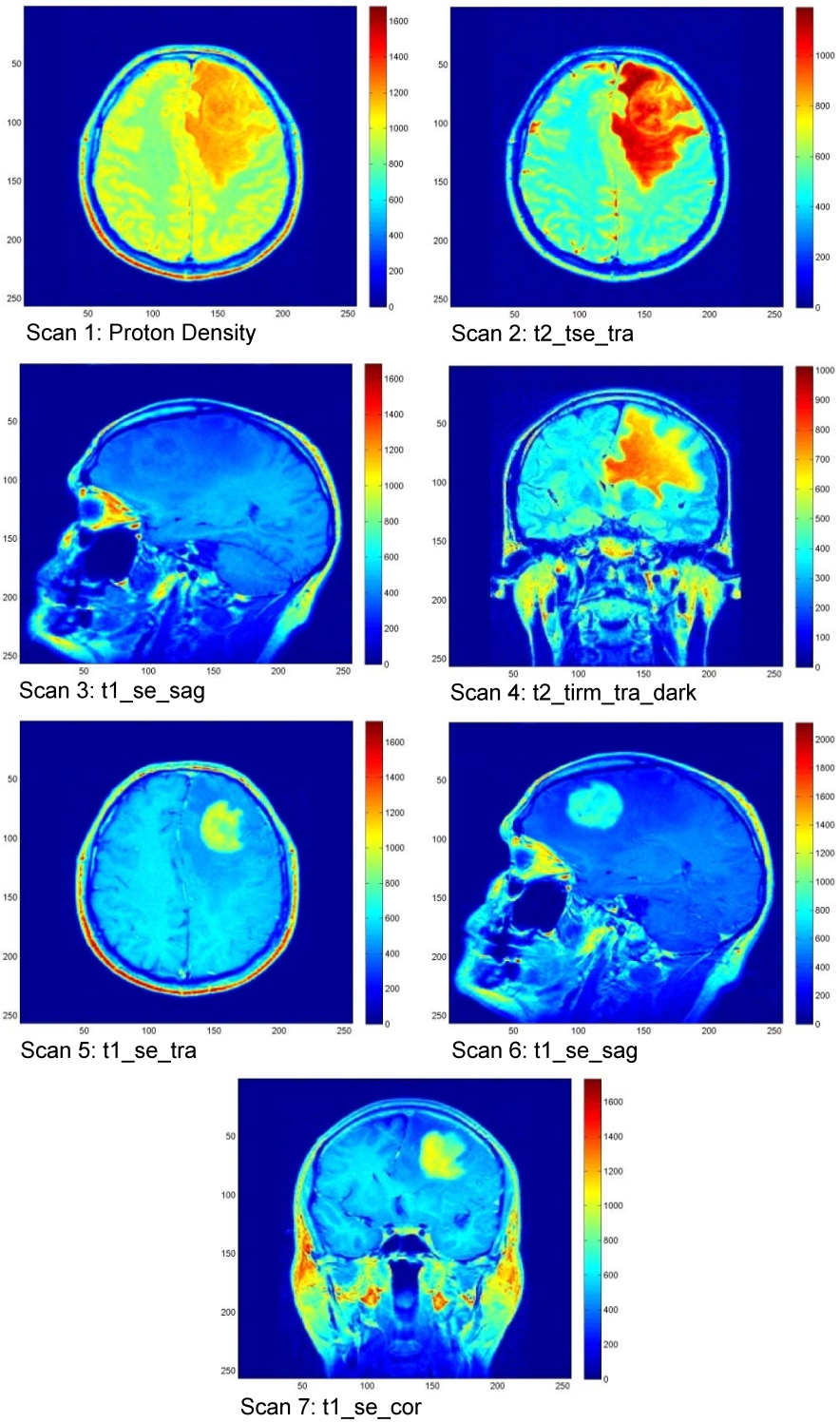

Fig.7.2.1: Middle slices of the scans available for the segmentation process.

In order to select the best scans for the purpose, I analyse the contrast between the principal tissues in the scans.
The contrast between two tissues A and B is defined as:

Eq.7.2.1: $C(A,B) = \left|\bar{I}(A) - \bar{I}(B)\right|$

Where $\bar{I}(X)$ *is the average intensity of the tissue X.*

Since the aim of the work described in this chapter is the segmentation of the Tumour and of the Peritumoral Edema, I analyse the contrast between these structures and the other tissues. The Tumour is fully enclosed in the Peritumoral Edema, therefore it is compared only with the Edema. The Edema includes the Tumour and it is surrounded by Grey Matter, White Matter and CSF, therefore it is compared with all of these tissues.

	Scan	CSF-Edema	GM-Edema	WM-Edema	Tumour-Edema
1	pd_tra	28,5	150,1	342,8	30,7
2	t2_tse_tra	34,5	569,2	750,2	27,2
3	t1_se_sag	6,8	90,1	155,6	28,4
4	t2_tirm_cor_dark	23,8	333,2	516,5	59,7
5	t1_se_tra	35,3	95,5	185,8	539,4
6	t1_se_sag	11,0	138,2	218,9	533,6
7	t1_se_cor	60,2	149,1	212,9	670,1

Tab. 7.2.2: Principal tissues contrast in the available scans. ***(CSF stands for Cerebro Spinal Fluid, GM stands for Grey Matter; WM stands for White matter)***

The results in Table 7.2.2 show that the greatest contrast between Tumour and Edema is obtained in the 7th scan.
To further analyses, this scan appears to be affected by intensity heterogeneity, therefore I consider the 5th scan instead of the 7th as the one characterized by the highest Tumour-Edema contrast.
The greatest contrast between Grey Matter, White Matter and Edema is instead obtained in the 2nd scan.
The results in Table 7.2.2 show that the contrast between Tumour and Edema is low in the scans characterized by high contrast between Grey or White Matter and the Peritumoural Edema, and vice-versa. Therefore, in order to obtain the best results for the segmentation of the structures, I merge the information from the 2nd and 5th scan using the co-registration processes described in Chapter 4

and segment the Peritumoural Edema in the 2nd scan and the Tumour in the 5th scan. The co-registration is performed with SPM5 *(Ashburner et al., 2005)* using the standard parameters to co-register the 2nd scan (T2-wighted) to the 5th (T1 weighted).

7.2.2 Algorithm Implementation

This application of the segmentation algorithm proceeds in the following manner. First the Tumour and the Peritumoural Edema are segmented in the scans chosen in chapter 7.2.1. To perform these operations it is used semi automatically a simplified version of the Brain segmentation algorithm described in chapter 6.2.
Then the Brain, Grey Matter and White Matter are also segmented. The segmentation final results are obtained setting to different intensity values the results obtained from each segmentation step.
As described in chapter 7.2.1, the scan chosen for the segmentation of the Tumour is the 5th one of the seven available *(i.e. the t1_tse_tra scan)*. The scan has been acquired with axial acquisition direction, it is T1 weighted, with dimensions *(256 x 19 x 256) voxels* and resolution *(0.899 x 5.5 x 0.899) mm^3* respectively along the left-right, dorso-ventral and rostro-caudal directions. First the three-dimensional matrix T0, corresponding to the entire scan, is reconstructed. A seed point P_0 approximately in the centre of the Tumour is manually identified (Fig.7.2.2a). Then a three-dimensional cubic region enclosing the tumour is manually identified (Fig.7.2.2b). The intensity distribution of the voxels in the selected region is computed. The intensity distribution is fitted with the sum of two Gaussians (Fig.7.2.2c):

Eq.7.2.2:

$$D_{Tumour}(I) = H_{Edema,0} \cdot e^{-\frac{(I - C_{Edema,0})^2}{2\sigma_{Edema,0}^2}} + H_{Tumour,0} \cdot e^{-\frac{(I - C_{Tumour,0})^2}{2\sigma_{Tumour,0}^2}}$$

Where D(I) is the Intensity Distribution, I is the intensity, H is the height of the Gaussian, C the centroid of the Gaussian, for each Gaussian $\sigma \approx FWHM/2.35$.

According to the fit results, threshold is applied and the voxels of T0 with intensity values that are not included in the interval $[C_{Tumour}-2\cdot\sigma_{Tumour}, C_{Tumour}+2\cdot\sigma_{Tumour}]$ are set to zero (Fig.7.2.2d). Finally the voxels not connected with P_0 in T0 are set to zero (Fig.7.2.2e).

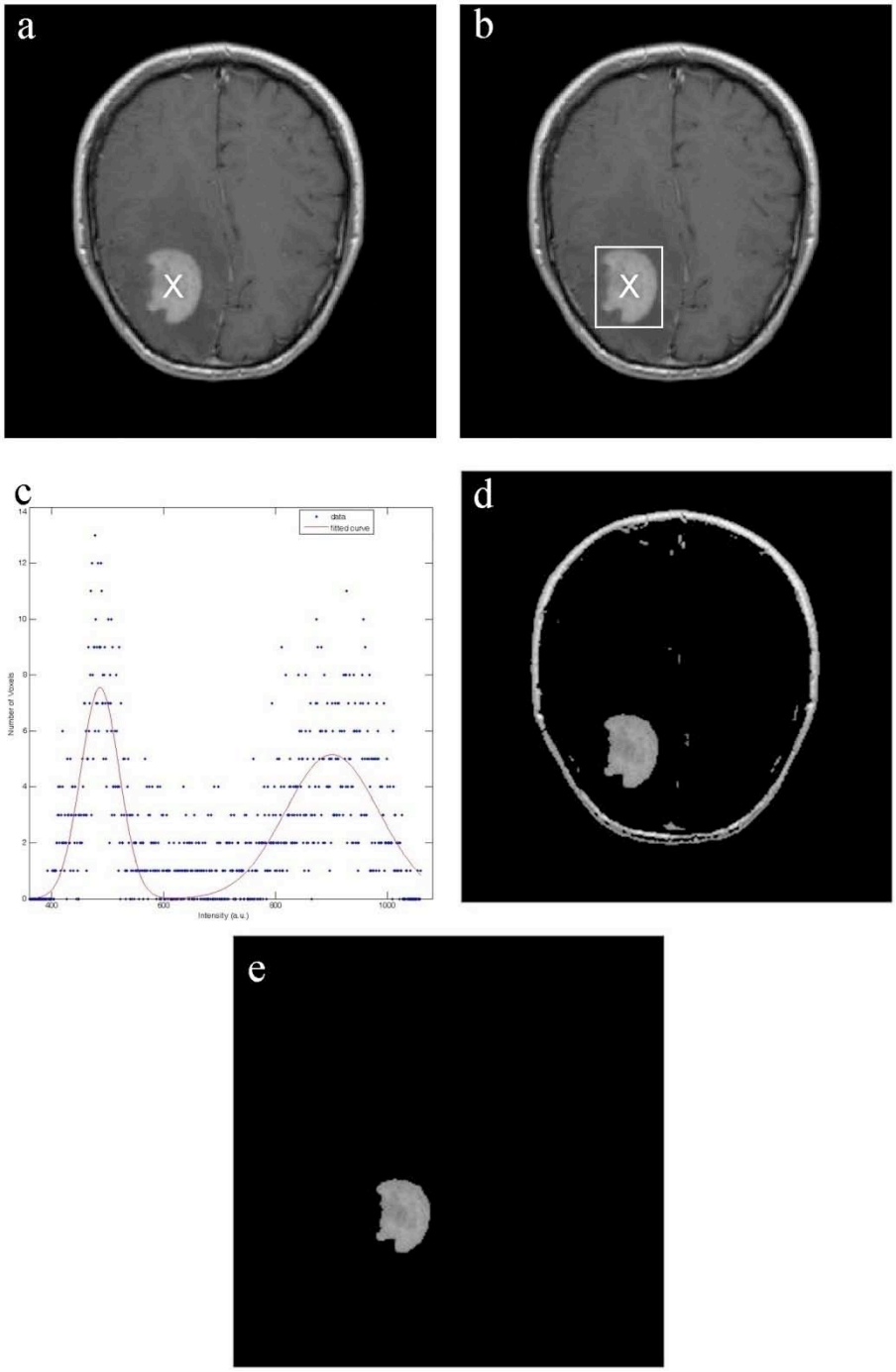

Fig.7.2.2: a) Seed point identification; b) ROI Identification; c) ROI Intensity Distributions Analysis; d) Threshold; e) Connectivity Analysis

The scan chosen for the segmentation of the Peritumoural Edema is the 2nd one of the seven available *(i.e. the t2_tse_tra scan)*. The scan, is T2 weighted, has dimensions *(256 x 21 x 256) voxels* and resolution *(0.899 x 5.5 x 0.899)* mm^3 respectively along the left-right, dorso-ventral and rostro-caudal directions and it has been acquired with axial acquisition direction.
The procedure used in this case is very similar to the one used in the Tumour segmentation, adding one step before the intensity analysis (in order to remove the tumour from the data) and one step after the threshold selection (based on the application of morphologic operators).
The three-dimensional matrix E0 corresponding to the entire scan is reconstructed (Fig.7.2.3a).
The voxels with values greater than zero in T0 are identified and the voxels of correspondent coordinates set to zero in E0.
A seed point P_1 approximately in the centre of the Edema is manually identified. A three-dimensional cubic region enclosing the Edema is identified (Fig.7.2.3b).
Then the intensity distribution of the selected region is computed and it is fitted with the sum of two Gaussian functions, one correspondent to the Edema intensities and one to the Grey and White Matter intensities (Fig.7.2.3c):

Eq.7.2.3:

$$D_{Edema,1}(I) = H_{GWM,1} \cdot e^{-\frac{(I-C_{GWM,1})^2}{2\sigma_{GWM,1}^2}} + H_{Edema,1} \cdot e^{-\frac{(I-C_{Edema,1})^2}{2\sigma_{Edema,1}^2}}$$

Where D(I) is the Intensity Distribution, I is the intensity, H is the height of the Gaussian, C the centroid of the Gaussian, for each Gaussian $\sigma \approx FWHM/2.35$. *GWM stands for Grey and White Matter.*

$I_{Edema,Min}$ is computed as the solution of the equation:

Eq.7.2.4:

$$H_{GWM,1} \cdot e^{-\frac{(I-C_{GWM,1})^2}{2\sigma_{GWM,1}^2}} = H_{Edema,1} \cdot e^{-\frac{(I-C_{Edema,1})^2}{2\sigma_{Edema,1}^2}}$$

$(C_{GWM,L,2} < I < C_{Edema,1})$

Then threshold is applied, setting to zero the voxels of E0 with intensity lower than $I_{Edema,min}$(Fig.7.2.3d).
Then the algorithm analyses the connectivity properties of the Edema, and it sets to zero the voxels that are not connected with P_1 in E0 (Fig.7.2.3e). The detection intensity of the Edema is very closed to the detection intensity of the Cerebro Spinal Fluid *(Tab. 7.2.1)* and the Peritumoural Edema is connected

with the Cerebro Spinal Fluid. Therefore the voxels connected to P_1 include a large volume of Cerebro Spinal Fluid. In order to delete the connection voxels, the application of mathematical morphology operators is needed.
The algorithm creates then a copy E1 of E0 in logical form, and applies the morphologic erosion operator to E1 till the object connected to P_1 is fully included in the Peritumoural Edema. This parameter is checked at each erosion cycle through visual inspection. The used morphological alteration form is a sphere of 3.5 mm of diameter. At the end of the erosion step, the voxels that are not connected with P_1 in E1 are set to zero (Fig.7.2.3f).
The dilation morphologic operator is applied to the object connected to P_1 in E1 a number of cycles 5% greater than the number of iterations that were needed for the erosion process. The voxels equal to zero in E1 are set to zero in E0.
In order to obtain an estimate of the intensity range of the Peritumoural Edema not affected by the Cerebro Spinal Fluid intensities, the intensity distribution of the voxels in the ROI previously identified is computed and fitted with a single Gaussian:

Eq.7.2.5: $$D_{Edema,2}(I) = H_{Edema,2} \cdot e^{-\frac{(I - C_{Edema,2})^2}{2\sigma_{Edema,2}^2}}$$

Where D(I) is the Intensity Distribution, I is the intensity, H is the height of the Gaussian, C the centroid of the Gaussian, $\sigma_{Edema,2} \approx FWHM/2.35$.

Threshold is applied, setting to zero the voxels of E0 with intensity that is not included in the interval $[C_{Edema,2} - 3 \cdot \sigma_{Edema,2}, C_{Edema,2} + 2 + 3 \cdot \sigma_{Edema,2}]$, and again the analysis of the connectivity properties of the Edema is performed. The voxels that are not connected to P_1 are set to zero in E0, and the Edema is obtained (Fig.7.2.3g).

7.2.3 Algorithm Characterization

I implemented a semiautomatic algorithm for the segmentation of Tumour and Peritumoural Edema on a MRI scan.
In order to obtain results with the highest precision possible, two different scans were selected for the segmentation of the Tumour and of the Peritumoural Edema. The scan chosen to segment the Tumour is T1-weighted, the one chosen to segment the Peritumoural Edema is T2-weighted.
The choice to use different scans for different structures required the co-registration of the used scans, in order to make possible the merging of the results. This step was performed with SPM5 *(Ashburner et al., 2005)*.
The implemented method was quick and easy to be applied.
The semi-automatic application of the segmentation process to the segmentation of the Tumour and Peritumoural Edema obtained excellent results to visual inspection made by experts of the field *(Fig. 7.2.4-7.2.10)*.

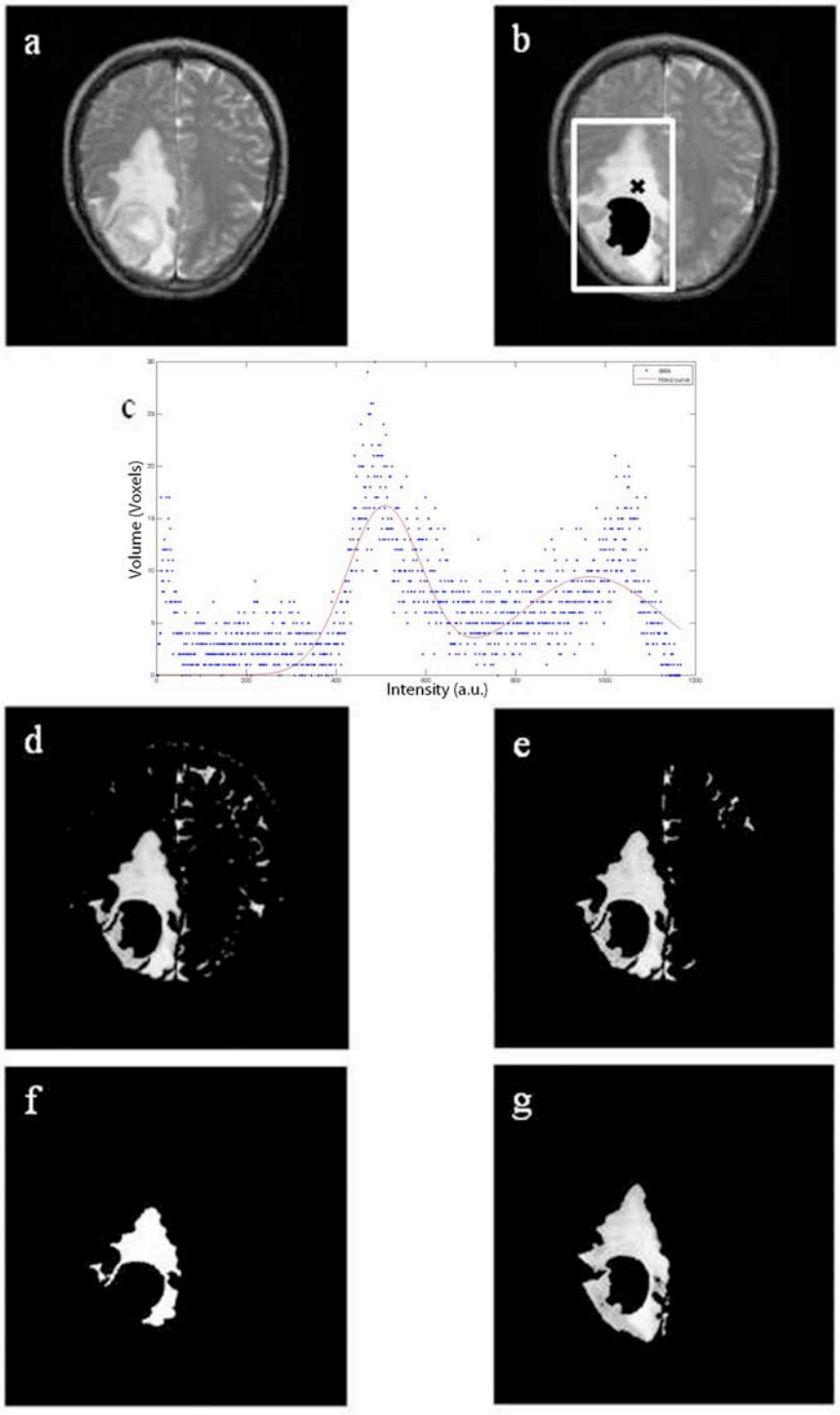

Fig.7.2.3: a) Original data; b) Seed Point and Region of Interest identification; c) Intensity distribution analysis; d) threshold; e) Analysis of the connectivity properties; f) Erosion; e) Final Result.

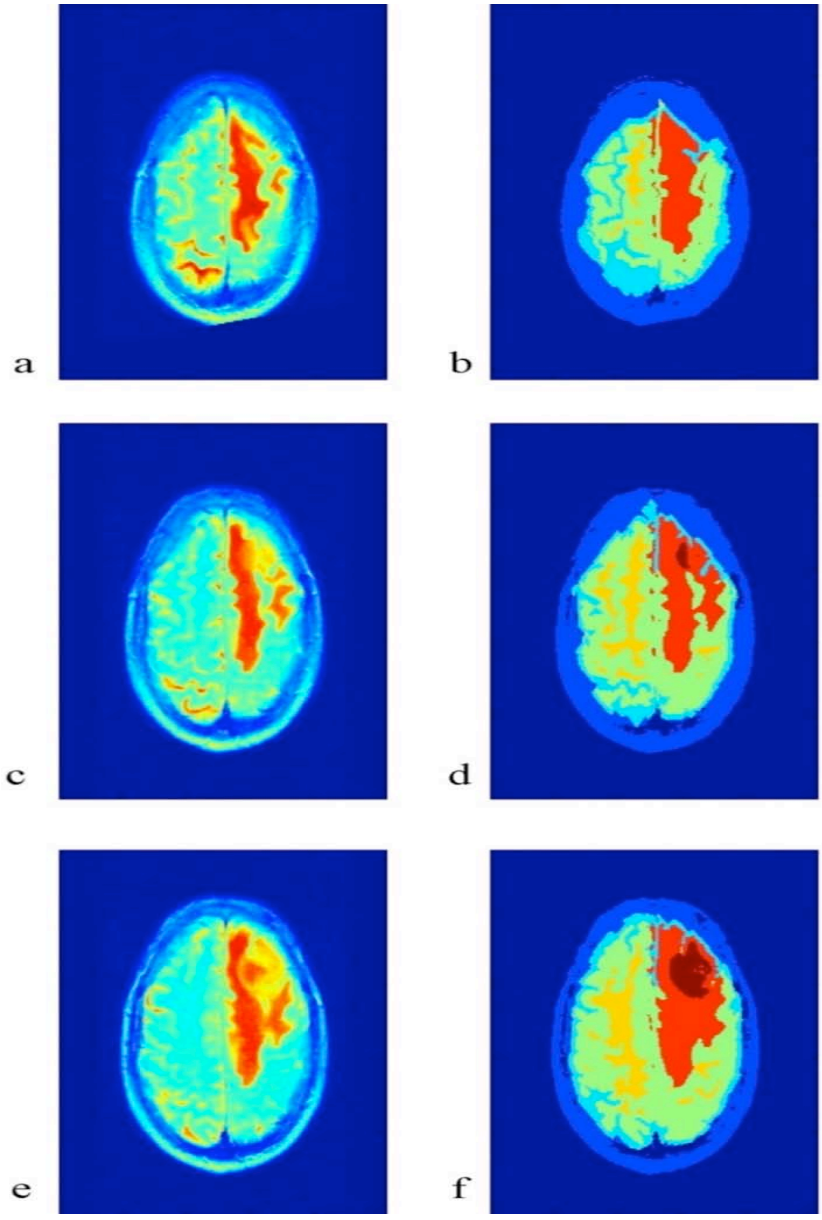

Fig. 7.2.4: Slices 1,2,3. Left: Original T2 Data; Right: Segmented Data ***(Dark Red: Tumour; Light Red: Peritumoural Edema; Green: Grey Matter; Yellow: White Matter; Light Blue: Cerebro Spinal Fluid; Dark Blue: Other Tissues).***

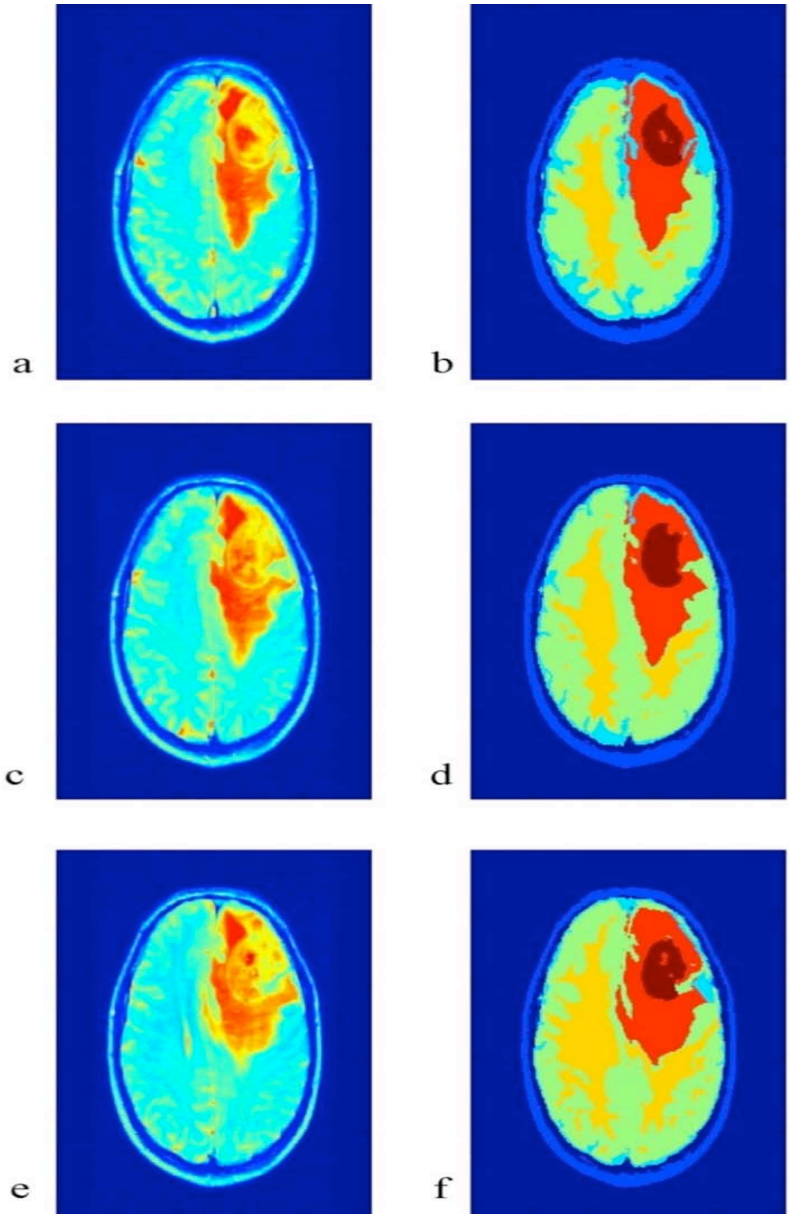

Fig. 7.2.5: Slices 4,5,6. Left: Original T2 Data; Right: Segmented Data ***(Dark Red: Tumour; Light Red: Peritumoural Edema; Green: Grey Matter; Yellow: White Matter; Light Blue: Cerebro Spinal Fluid; Dark Blue: Other Tissues).***

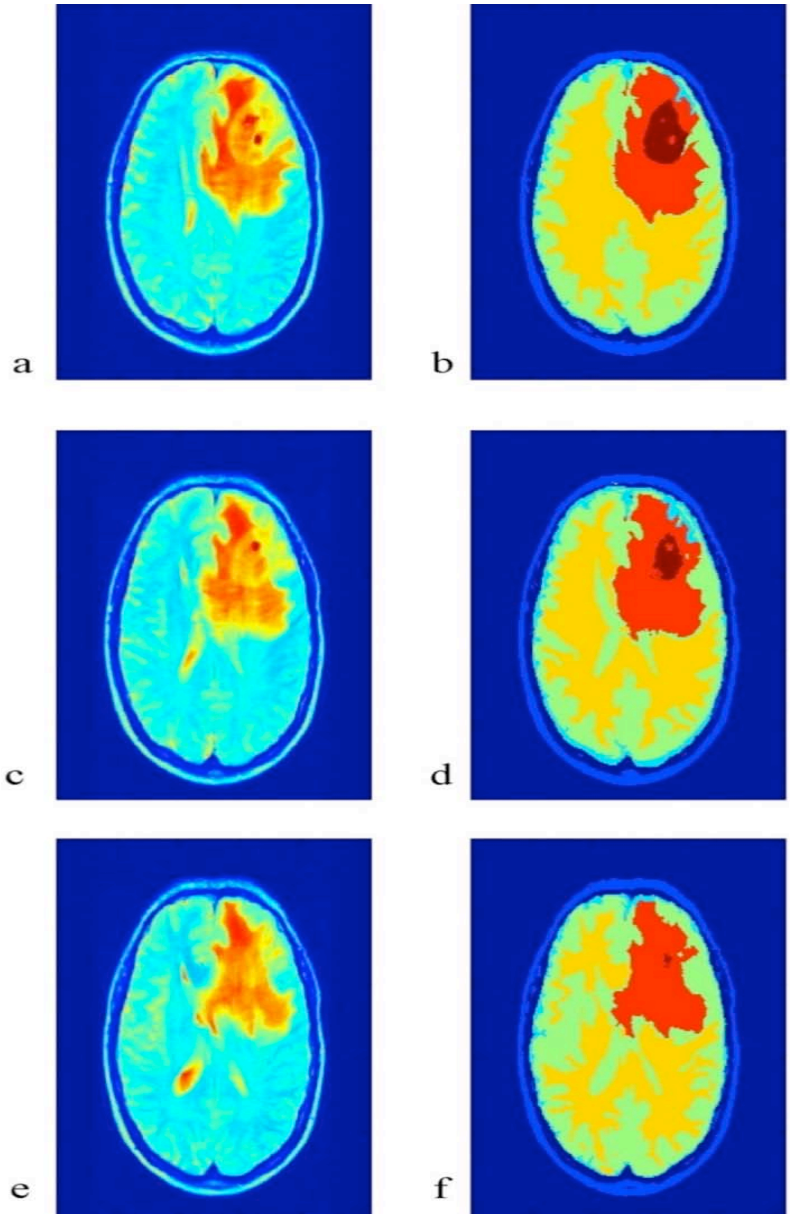

Fig. 7.2.6: Slices 7,8,9. Left: Original T2 Data; Right: Segmented Data ***(Dark Red: Tumour; Light Red: Peritumoural Edema; Green: Grey Matter; Yellow: White Matter; Light Blue: Cerebro Spinal Fluid; Dark Blue: Other Tissues).***

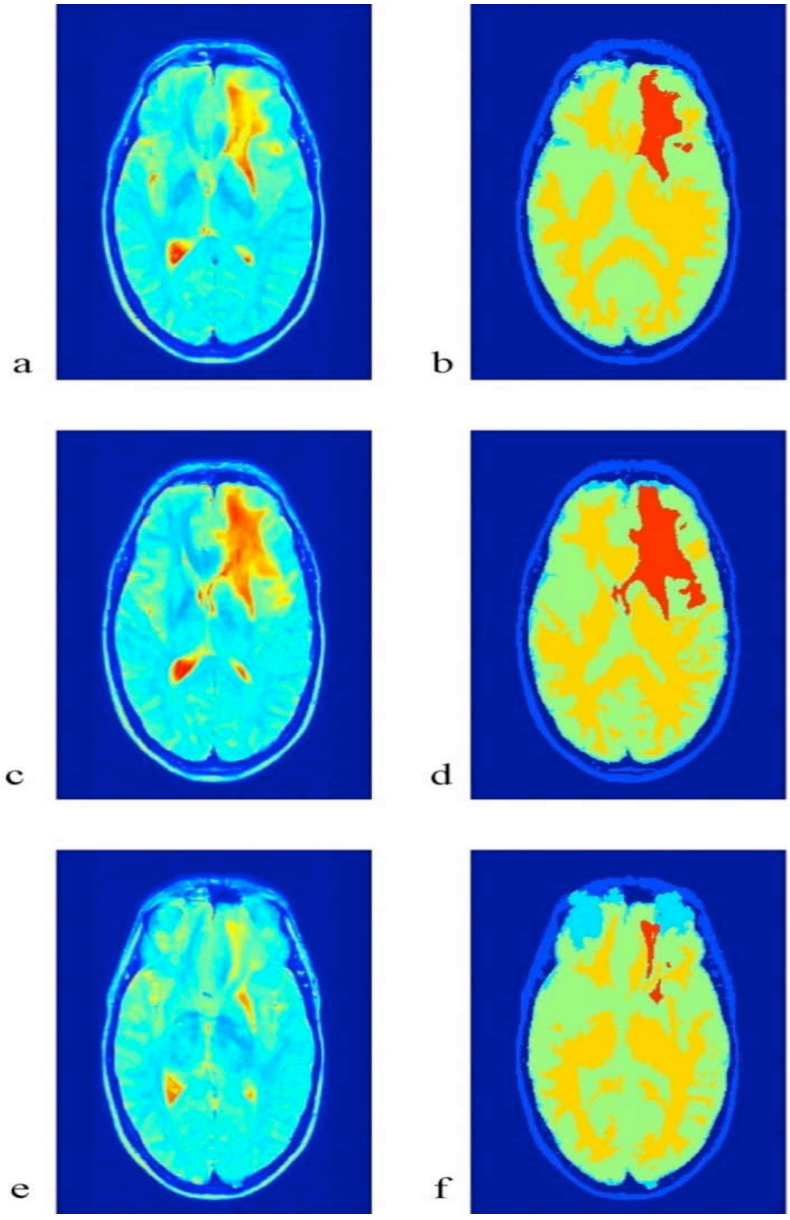

Fig. 7.2.7: Slices 10,11,12. Left: Original T2 Data; Right: Segmented Data ***(Dark Red: Tumour; Light Red: Peritumoural Edema; Green: Grey Matter; Yellow: White Matter; Light Blue: Cerebro Spinal Fluid; Dark Blue: Other Tissues).***

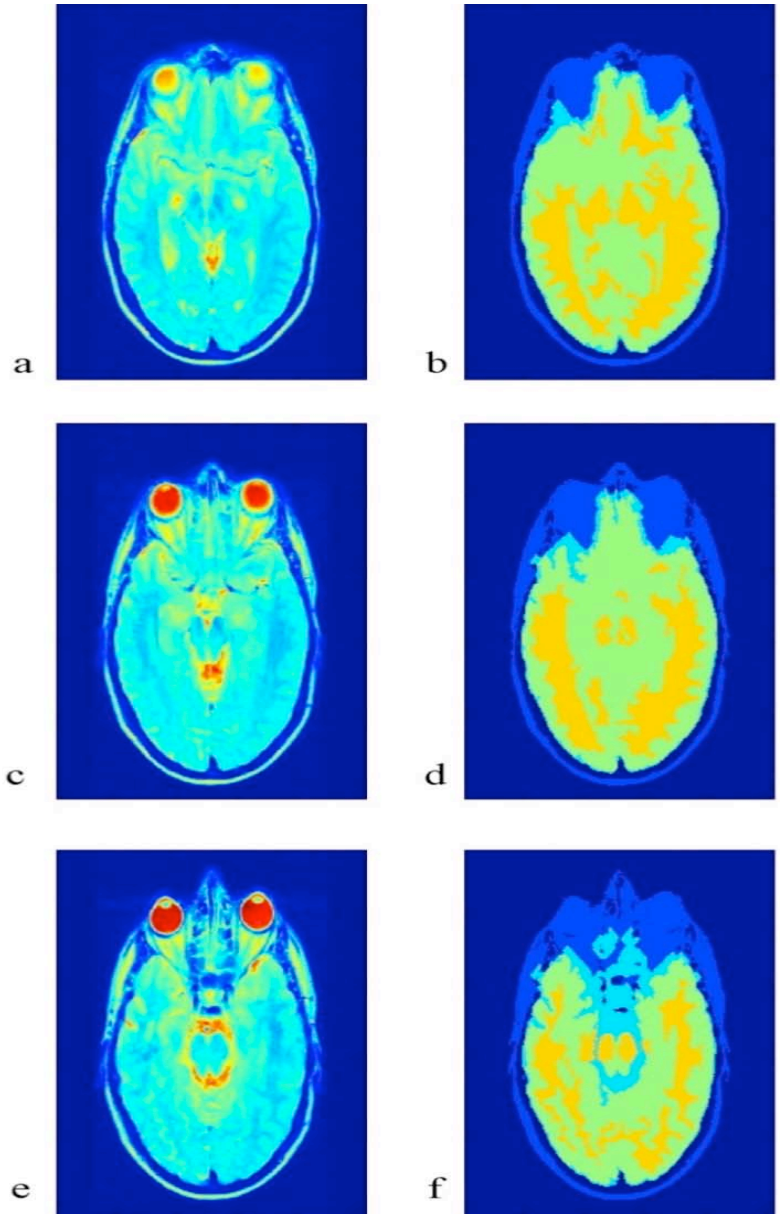

Fig. 7.2.8: Slices 13,14,15. Left: Original T2 Data; Right: Segmented Data ***(Dark Red: Tumour; Light Red: Peritumoural Edema; Green: Grey Matter; Yellow: White Matter; Light Blue: Cerebro Spinal Fluid; Dark Blue: Other Tissues).***

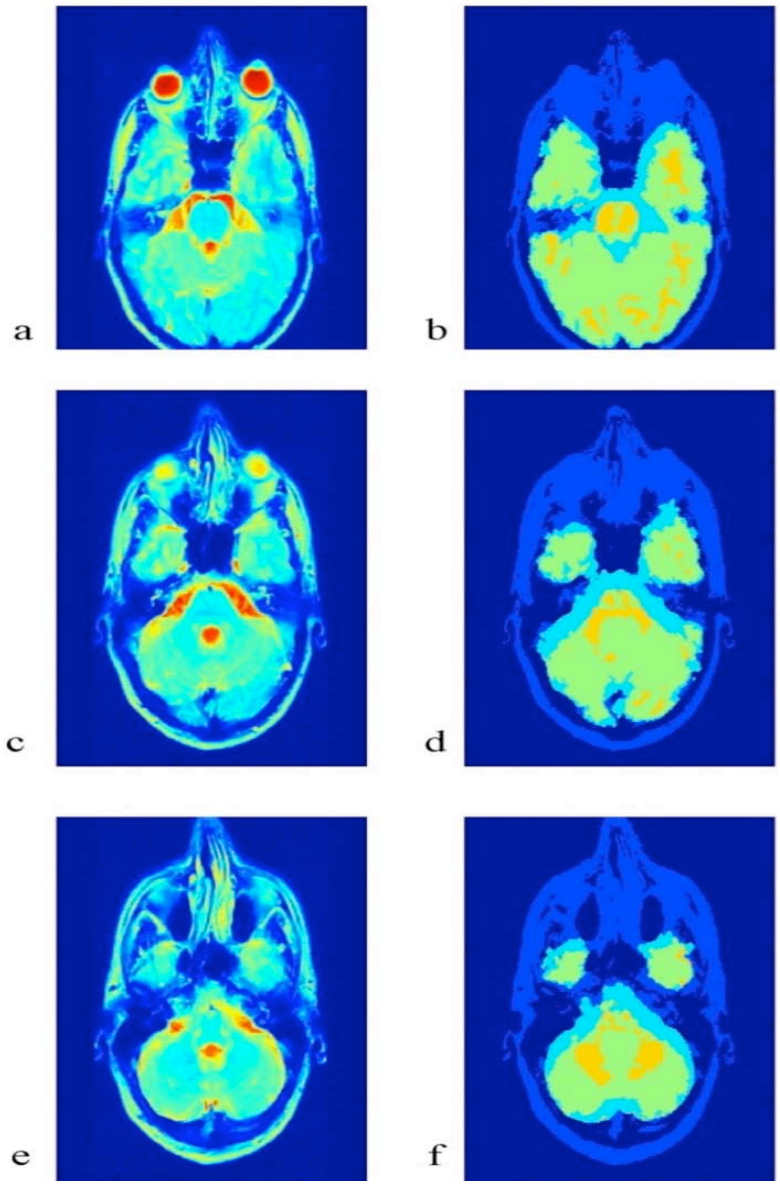

Fig. 7.2.9: Slices 16,17,18. Left: Original T2 Data; Right: Segmented Data ***(Dark Red: Tumour; Light Red: Peritumoural Edema; Green: Grey Matter; Yellow: White Matter; Light Blue: Cerebro Spinal Fluid; Dark Blue: Other Tissues).***

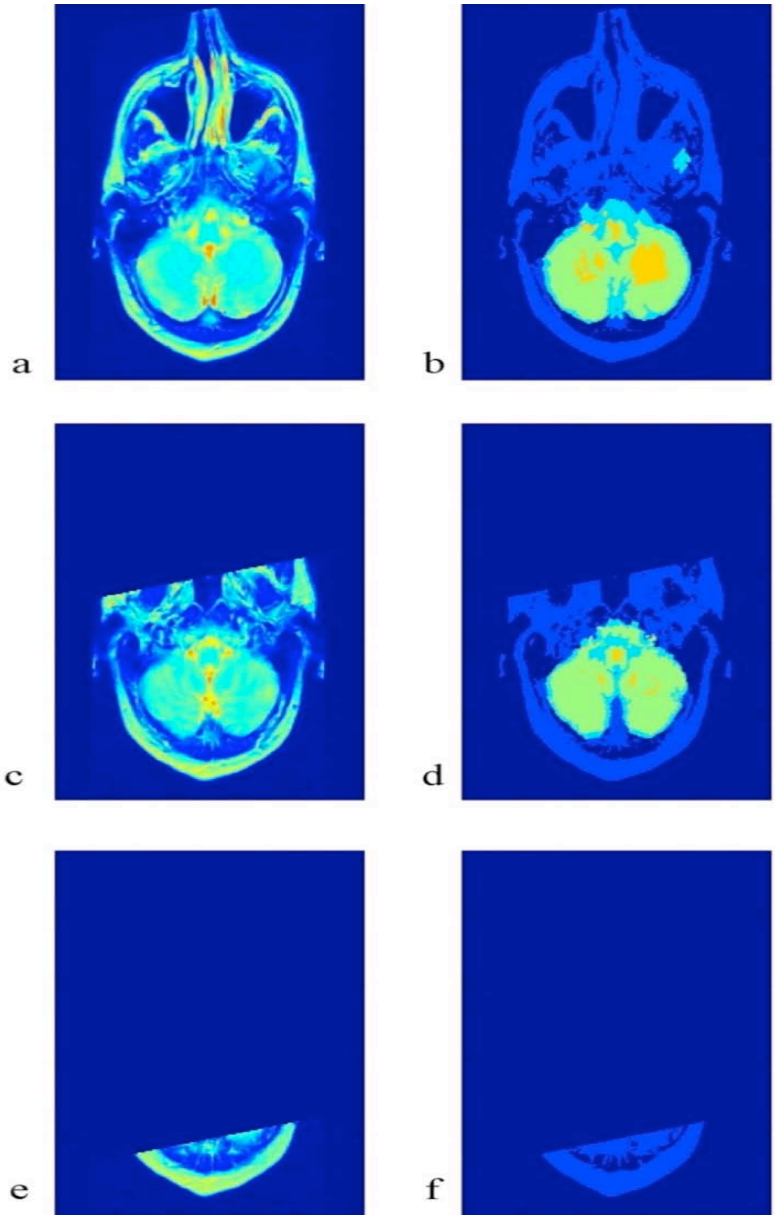

Fig. 7.2.10: Slices 19,20,21. Left: Original T2 Data; Right: Segmented Data ***(Dark Red: Tumour; Light Red: Peritumoural Edema; Green: Grey Matter; Yellow: White Matter; Light Blue: Cerebro Spinal Fluid; Dark Blue: Other Tissues).***

7.3 Segmentation of the Tissues Perfused by Contrast Medium in Computed Tomography Angiography of the Thorax and Abdomen

The segmentation procedure is applied in this chapter to segment the Bone, the Heart, the Aorta, the Kidneys, the Urinary Tracts and the Urinary Bladder on Computed Tomography data of the Thorax and Abdomen.
As described in Chapter 3.3.4, the automatic segmentation of the tissues perfused by contrast medium in CTA is a challenging problem at the current state of the art.
The procedure is a modified version of the algorithm described in Chapter 6. It is semi-automatic as in the case of almost all the software described at the state of the art, but it is ideated in order to be very easily automated *(Atzori, 2008)*.
The features of the analysed scan are described in Chapter 5.3.

7.3.1 Algorithm Implementation

The algorithm is based on manual landmarks localization, iterative global and local intensity analysis, threshold, analysis of the connectivity properties and mathematical morphology.
First the algorithm reconstructs the three dimensional matrix I0 that corresponds to the entire CTA scan.
Then, it removes the air from I0. To perform this operation, it computes the intensity distribution of the matrix I0. The peak correspondent to the air is identified as the first peak in the intensity distribution. The air peak is fitted with a single Gaussian function (Fig.7.3.1):

Eq.7.3.1:

$$D_{Air}(I) = H_{Air} \cdot e^{\frac{-(I-C_{Air})^2}{2\sigma_{Air}^2}}$$

Where D(I) is the intensity Distribution, I is the intensity, H is the height of the Gaussian, $\sigma_{Air} \approx FWHM/2.35$.

The algorithm sets to zero the voxels of I0 with intensity greater than the value:

Eq.7.3.2: $\mathrm{Air}_{\mathrm{Max}} = C_{Air} + 2 \cdot \sigma_{Air}$

The algorithm creates a copy I1 of the matrix I0, and converts it to logical form. It fills the three dimensional holes of I1, and then fills the bidimensional holes in the sagittal, coronal and axial planes. The voxels greater than zero in the matrix I1 are set to values of the correspondent voxels of the matrix I0.
Then, the intensity distribution $ID_1(I)$ of the matrix I1 is computed. In order to identify the intensity ranges that correspond respectively to the muscular and fat tissues, the intensity distribution is fitted with the sum of two Gaussian functions (Fig.7.3.1):

Eq.7.3.3:

$$D_{G,1}(I) = H_{T1,G,1} \cdot e^{\frac{-(I - C_{T1,G,1})^2}{2\sigma_{T1,G,1}^2}} + H_{T2,G,1} \cdot e^{\frac{-(I - C_{T2,G,1})^2}{2\sigma_{T2,G,1}^2}}$$

Where D(I) is the intensity Distribution, I is the intensity, H are the heights of the Gaussians, C the centroids of the Gaussians, for each Gaussian $\sigma \approx FWHM/2.35$*, G stands for Global.*

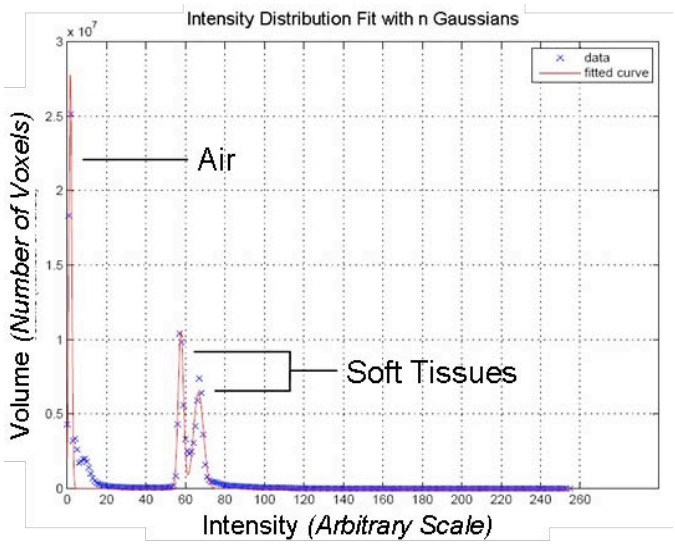

Fig. 7.3.1: Global intensity distribution analyses. Air peak and soft tissues.

The algorithm computes then the intensity distribution $ID_{G,2}(I)$:

$ID_{G,2}(I) = ID_{G,1}(I)-D_{G,1}(I)$

The intensity distribution $ID_2(I)$ is fitted with a single Gaussian function in order to obtain preliminary intensity values for the bone intensity interval:

Eq.7.3.4:

$$D_{Bone,1}(I) = H_{Bone,1} \cdot e^{\frac{-(I-C_{Bone,1})^2}{2\sigma_{Bone,1}^2}}$$

Where D(I) is the intensity Distribution, I is the intensity, H is the height of the Gaussian, C the centroid of the Gaussian, $\sigma_{Bone} \approx FWHM/2.35$.

The landmark P_0 is semi-automatically identified on the spine according to the conditions that its intensity is included in the interval $[C_{Bone,1}-\sigma_{Bone,1}\ ,\ C_{Bone,1}+\sigma_{Bone,1}]$ and that it is closed to the sagittal symmetry plane of the matrix I1 (Fig.7.3.2).

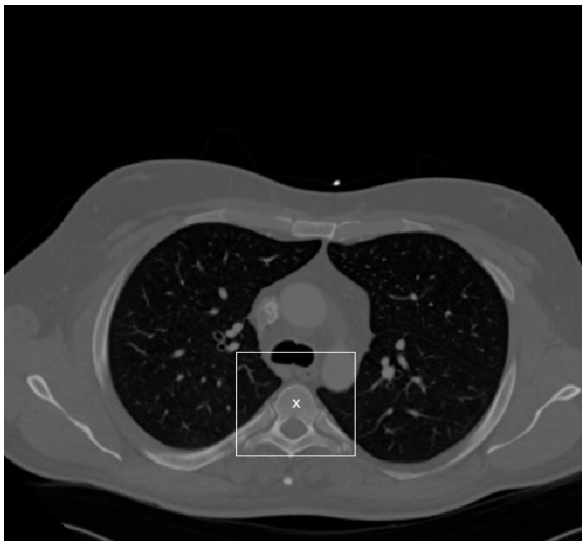

Fig.7.3.2: Axial intermediate section of the CTA scan. Vertebral column semi-automatic seed point localization and region of interest localization.

A cube Q_1, centred in P_0, with faces of 10 cm^2 is identified in I1 (Fig.7.3.2). The algorithm computes the local intensity distribution $ID_{L,1}(I)$ on Q_1. The intensity distribution is then fitted with two Gaussians (Fig.7.3.3):

Eq.7.3.5:

$$D_{L,1}(I) = H_{T1,,L,1} \cdot e^{\frac{-(I-C_{T1,L,1})^2}{2\sigma_{T1,L,1}^2}} + H_{T2,L,1} \cdot e^{\frac{-(I-C_{T2,L,1})^2}{2\sigma_{T2,L,1}^2}}$$

Where $D_{Loc,1}(I)$ is the intensity Distribution, I is the intensity, H are the heights of the Gaussians, C the centroids of the Gaussians, for each Gaussian $\sigma \approx FWHM/2.35$, L stands for Local; $C_{T1,L,1} < C_{T2,L,1}$.

The algorithm computes then the intensity distribution $ID_{L,2}(I)$:

Eq.7.3.6: $ID_{Loc,2}(I) = ID_1(I) - D_1(I)$

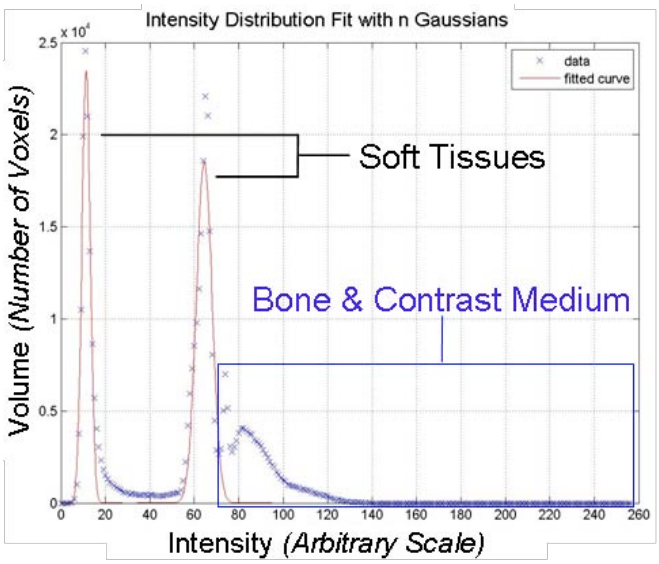

Fig. 7.3.3: Local Intensity distributions analysis in the region near the vertebral column.

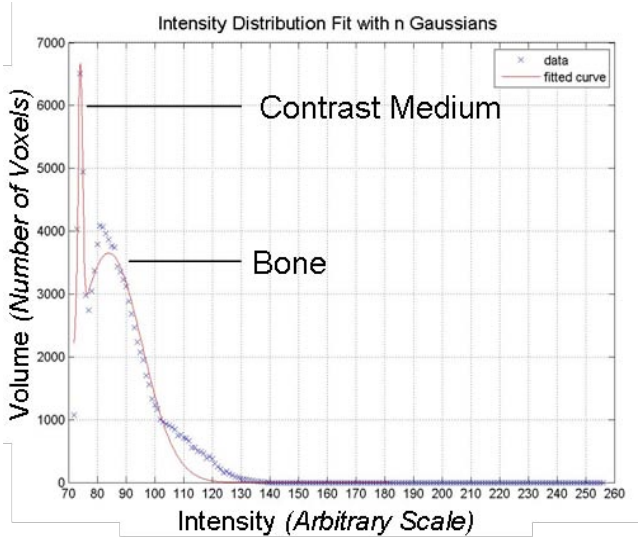

Fig. 7.3.4: Peaks of interest intensity analysis.

Then, the intensity distribution $ID_{Loc,2}(I)$ of the matrix is fitted (Fig.7.3.4) with the sum of two Gaussian functions in order to obtain the intensity ranges for the Bone and the tissues perfused by the contrast medium:

Eq.7.3.7:

$$D_{Loc,2}(I) = H_{CM,1} \cdot e^{\frac{-(I-C_{CM,1})^2}{2\sigma_{CM,1}^2}} + H_{Bone,2} \cdot e^{\frac{-(I-C_{Bone,2})^2}{2\sigma_{Bone,2}^2}}$$

Where D(I) is the intensity Distribution, I is the intensity, H are the heights of the Gaussians, C the centroids of the Gaussians, for each Gaussian $\sigma \approx FWHM/2.35$*, CM stands for Contrast Medium.*

The minimum intensity value for the tissues perfused by the contrast medium CM_{Min} is computed as the solution of the equation:

Eq.7.3.8:

$$H_{CM,1} \cdot e^{\frac{-(I-C_{CM,1})^2}{2\sigma_{CM,1}^2}} = H_{T2,L,1} \cdot e^{\frac{-(I-C_{T2,L,1})^2}{2\sigma_{T2,L,1}^2}}$$

$(C_{CM,1} < I < C_{T2,L,1})$

Threshold is then applied to the matrix I1: the voxels with intensity values lower than CM_{Min} are set to zero. (Fig.7.3.5b, Fig.7.3.6B).

The value CM_{Max} is then calculated as the solution of the equation:

Eq.7.3.9:

$$H_{CM,1} \cdot e^{\frac{-(I-C_{CM,1})^2}{2\sigma_{CM,1}^2}} = H_{Bone,2} \cdot e^{\frac{-(I-C_{Bone,2})^2}{2\sigma_{Bone,2}^2}}$$

($C_{CM,1} < I < C_{Bone,2}$)

Now the algorithm segments the bone in the matrix in a copy B1 of the matrix I1. The algorithm applies threshold to the matrix B1, and the voxels with intensity values lower than CM_{Max} are set to zero (Fig. 7.3.5c).
The connectivity properties of the matrix B1 are then evaluated. B1 is converted in logical form and the voxels that are not connected to P_0 in the matrix B1 are set to zero.
The algorithm fills then the three dimensional holes of B1. Then it fills the bidimensional holes in the sagittal, coronal and axial planes. The Erosion morphologic operator is then applied to the matrix B1 using as morphologic alteration form sphere with diameter of 2 mm.
The dilation morphologic operator is then applied on the matrix B1 using as morphologic alteration form a sphere with diameter of 1cm.
The voxels with values greater than zero in B1 are set to the values of the correspondent voxels in the matrix I0.
The voxels with intensities that are not included in the interval $[C_{Bone,2} - 2 \cdot \sigma_{Bone,2}, C_{Bone,2} + 2 \cdot \sigma_{Bone,2}]$ are set to zero in the matrix B1.
Again the algorithm analyses the connectivity properties of the matrix B1. It converts B1 in logical form, and sets to zero the voxels that are not connected to the landmark P_0. The bone together with the urinary bladder are segmented (Fig. 7.3.5d).
The matrix CM1, that corresponds approximately to the segmented tissues perfused by the contrast medium, is created as the difference between the matrices I1 and B1 (Fig. 7.3.5e):

Eq.7.3.10: $CM1 = I1 - B1$

The connectivity properties of the matrix CM1 are then evaluated. To perform this operation faster, the algorithm converts CM1 in logical form and computes the volumes of all the unconnected objects included in CM1. The algorithm identifies the object characterized by the greatest volume and sets to zero the voxel that are not connected to it. The voxels that are equal to zero in the

matrix CM1 are then set to the values of the correspondent voxels in the matrix I0.
The algorithm computes the global intensity distribution of the matrix CM1 and fits it with a single Gaussian function:

Eq.7.3.11:

$$D_{CM,2}(I) = H_{CM,2} \cdot e^{\frac{-(I-C_{CM,2})^2}{2\sigma_{CM,2}^2}}$$

Where $D_{CM,2}(I)$ is the intensity Distribution, I is the intensity, H are the heights of the Gaussians, C the centroids of the Gaussians, for each Gaussian $\sigma \approx FWHM/2.35$.

The algorithm converts again the matrix CM1 in logical form, and it fills the three dimensional holes of I1. Then it fills the bidimensional holes in the sagittal, coronal and axial planes.
The dilation morphologic operator is then applied on the matrix CM1 using as morphologic alteration form a sphere with diameter of 1cm.
The voxels with values greater than zero in CM1 are set to the values of the correspondent voxels in the matrix I0.
The voxels with intensities that are not included in the interval $[C_{CM,2}-2\cdot\sigma_{CM,2}, C_{CM,2}+2\cdot\sigma_{CM,2}]$ are set to zero in the matrix CM1.
Again the algorithm analyses the connectivity properties of the matrix CM1. It converts CM1 in logical form and computes the volumes of all the unconnected objects included in CM1. The algorithm identifies the object characterized by the greatest volume and sets to zero the voxels that are not connected to it. The voxels that are equal to zero in the matrix CM1 are then set to the values of the correspondent voxels in the matrix I0, and the segmentation of the tissues perfused by the contrast medium is obtained (Fig. 7.3.5f, Fig.7.3.6C).
In the end, the Urinary Bladder is semi automatically removed from the matrix B1. To perform this operation, a copy U1 of B1 is created. A landmark P_1 is manually set in the centre of the bladder in the matrix U1. U1 is converted in logical form. The erosion morphologic operator is iterated on U1 a number of time n_E, correspondent to the cycles needed until the bladder is disconnected from the bone (this parameter is checked through visual inspection at each iteration of the erosion process). The used morphologic action form is a sphere with diameter of 1cm. The connectivity properties of the matrix U1 are analyzed, and the voxels that are not connected to P_1 in the matrix U1 are set to zero.
The dilation morphologic operator is applied to U1 a number of times n_E. The used morphologic action form is again a sphere with diameter of 1cm.
The algorithm analyses then the connectivity properties of U1 and sets to zero the voxels that are not connected with P_1. The voxels greater than zero in U1

are set to the values of the correspondent elements in the matrix I0, and the segmented Urinary Bladder is obtained (Fig.7.3.6C).
The non zero elements of the matrix B1 are set to the intensity values of the correspondent voxels in I0.
The matrix B2 is created as:

Eq.7.3.12: B2 = B1-U1

and the segmented bone is obtained (Fig.7.3.6D).

7.3.2 Algorithm Characterization

The algorithm was applied on CTA of the body to solve the problem of segmenting bone from tissues supplied by contrast medium, and therefore characterized by intensities very similar to the skeletal system *(Atzori, 2008)*.
Its application obtained easily results in the segmentation of the Heart, Aorta, Urinary Tracts, Bladder and Kidneys.
The results have been qualitatively evaluated through visual inspection by a medical radiologist, with very positive judgement.
The implemented method is quick and easy to be applied.
The algorithm is currently semi-automatic because it requires three manual operations: the identification of two landmarks and the assisted segmentation of the Urinary Bladder. The first landmark has to be located on the Spine, and it is required for the segmentation of the bone and the tissues perfused by the contrast medium. The second landmark is located on the Urinary Bladder, and it is required both for the segmentation of the Bone and of the Urinary Bladder.
I developed both the landmark localization procedures in order to be easily automated.
The automatic segmentation of the urinary bladder could be easily automated on the basis of proportions, applying a criterion to stop the erosion step very similar to the one described in chapter 6.1 for the erosion of the Brain.
The automatic implementation of those steps would lead to a fully automatic segmentation software.
Automatic localization of other landmarks located into the kidneys and into the heart would lead easily to automatic segmentation of each of the single anatomical structures.
The obtained results enhance the efficiency and adaptability of the procedure described in chapter 6 to imaging acquisition techniques different from MRI. Moreover they enhance the applicability of the procedure to anatomical structures that are not included in the head and that are characterized by different geometrical features from the Brain, Grey Matter and White Matter.

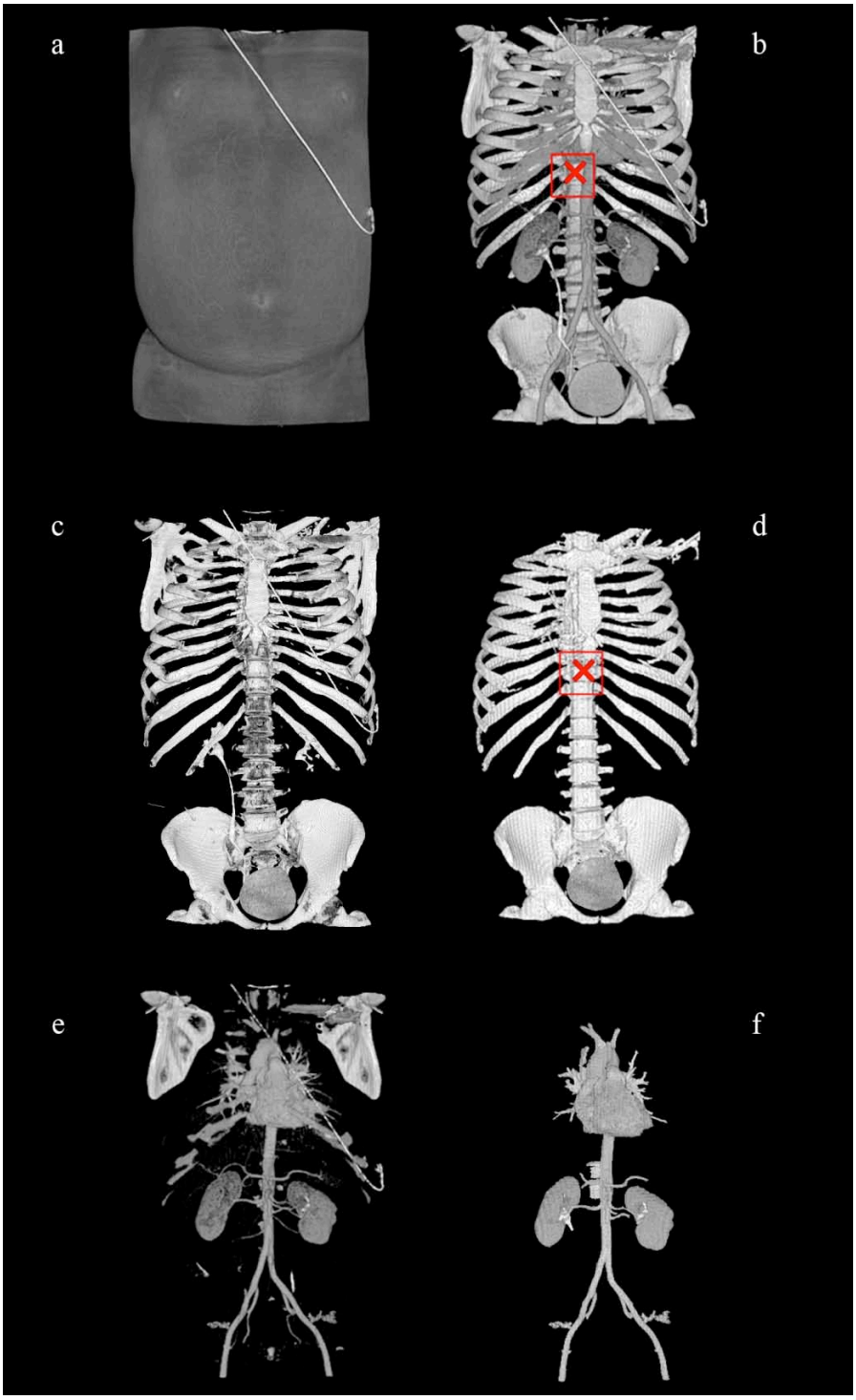

Fig.7.3.5 : Representation of segmentation process: a) Raw data; b) Threshold and vertebral landmark localization; c) Bone threshold; d) Bone Connectivity Analysis and morphological operators application; e) Remaining tissues; f) Contrast medium perfused tissues.

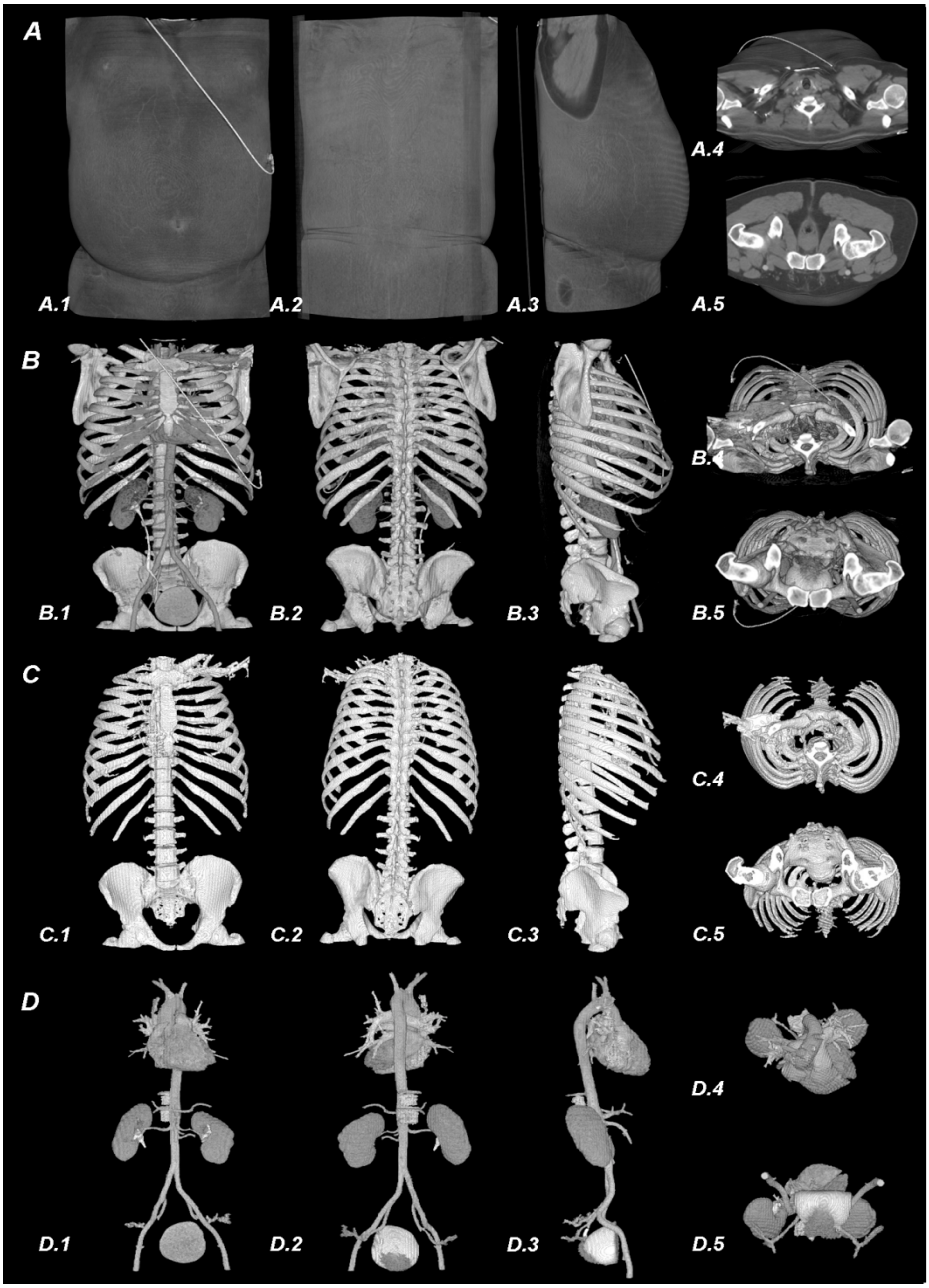

Fig. 7.3.6: 3D Visualization of the semi-automatic segmentation results on body CTA: A) Raw data, B)Threshold, C) Bone Segmentation, D) Heart, Aorta, Kidneys, Urinary Tracts and Bladder Segmentation. ***[.1 Front, .2 Rear, .3 Side, .4 Top, .5 Bottom]***

Chapter 8

Voxel-Based Statistical Analysis of the Quantitative Dynamic Susceptibility Contrast MRI Perfusion Estimates

This chapter describes a semi-automatic method to perform voxel-based statistical analysis of the hemodynamic parameters estimated in DSC-MRI.
DSC MRI is a technique to perform perfusion magnetic resonance using an exogenous tracer, such as gadolinium, and is one of the most interesting techniques for the quantitative study of the brain hemodynamics. The DSC MRI allows to quantify important hemodynamic parameters that play an important role in the study of several pathologies, such as cerebral tumours, ischemia, infarction and epilepsy.
Procedures that can compare voxel by voxel the brains of patients with the ones of the healthy controls are still needed in Dynamic Susceptibility Contrast MRI. A technique to perform DSC MRI analysis voxel by voxel could lead to the identification of the anatomic regions majorly involved in various pathologies as schizophrenia.
Two different strategies could be applied to perform the required spatial co-registration and normalization steps: performing them on the original DSC-MRI data (method A) or on the perfusion maps (method B). Both the strategies are applied and the results are compared with the quantification performed using the standard approach.

8.1 State of the Art

Quantification of Dynamic Susceptibility Contrast Magnetic Resonance Imaging (DSC-MRI) has been applied to study several different pathologies such as cerebral neoplasms *(Aronen, 1994)* and ischemia *(Warach, 1992)*. DSC-MRI with a Gadolinium-based contrast agent has been increasingly applied in cerebral perfusion studies *(Calamante, 1999)*. DSC-MRI combined with diffusion MR is frequently used in acute stroke patients to assess the extent and severity of ischemia *(Baird and Warach, 1998)*.
When an arterial input function (AIF) is determined, CBF, CBV, and MTT can be calculated by deconvolution analysis *(Rempp, 1994; Østergaard, 1996a,b)*. Preliminary works suggest that DSC MRI may also provide important clinical information on neuropsychiatric disorders, especially dementia and schizophrenia *(Cleghom, 1990)*.
As described in Chapter 4, to perform multi images voxel by voxel analyses, co-registration and normalization processes are needed. The spatial normalization procedures have an important impact on statistical sensitivity of functional images.
Although the impact of spatial normalization on positron-emission tomography (PET) *(Crivello, 2002; Senda, 1998; Kjems, 1999)* and blood oxygenation level-dependent (BOLD) functional magnetic resonance imaging (fMRI) functional images has been addressed *(Ardekani, 2004)*, the effects of normalization methods on the sensitivity of pMRI analyses are still unclear. Normalization of perfusion data obtained with Positron Emission Tomography and Single Photon Emission Tomography to structural MRI data (or vice versa) is widely used. Ibaraki et al. *(Ibaraki, 2007)* used this technique to evaluate the differences between the perfusion parameters obtained with PET and DSC MRI on manually identified Regions of Interest (ROIs). Dai et al. *(Dai, 2008)* evaluated the normalization of perfusion ASL data, and used normalization to analyze brain aging in regions of interest. Karnath et al. *(Karnath, 2005)* used the normalization of Time To Peak maps to evaluate alterations in patients with Basal Ganglia neglect.
This chapter describes a semi-automatic method to perform voxel-based statistical analysis of the hemodynamic parameters estimated in DSC-MRI. Such procedure could be very useful to identify automatically regions affected by hemodynamic alterations in patients affected by various pathologies.

8.2 Methods

The hemodynamic parameters are computed on the basis of the principles of tracer kinetics for nondiffusible tracers *(Zierler, 1962; Zierler, 1965)*.
The concentration curve is obtained from the MR signal S(t) following the relation:

Eq. 8.2.1:

$$C(t) = -\frac{1}{TE}\ln\left(\frac{S(t)}{S_0}\right)$$

where S_0 is computed by averaging the signal samples before the tracer injection *(Østergaard, 1996a)*.
Subsequently, a fit with a gamma-variate function is computed to eliminate the recirculation as reported in *(Benner, 1997, Østergaard, 1996a,b; Porkka, 1991)*.
The Arterial Input Function (AIF) is extracted from the DSC data on the middle cerebral artery using a semi-automatic procedure based on a hierarchical clustering applied dichotomously (i.e. at each step one of the two clusters is chosen to be reclusterized on the basis of the peak height or, if the difference is not significant, of the time to peak) *(Peruzzo, 2006)*.
The Cerebral Blood Flow (CBF) and the Cerebral Blood Volume (CBV) are computed using the Singular Value Decomposition (SVD) method *(Østergaard, 1996a,b)*.

Eq. 8.2.2:

$$CBV = \frac{\int C_{Voxel}(t)dt}{\int C_{AIF}(t)dt}$$

The MTT values are computed as the ratio between CBV and CBF *(Østergaard, 1996a,b)*.
Two different modalities (modality A and modality B) are tested during this study in order to apply the co-registration of the DSC MRI perfusion scans to the T1 weighted structural scans and the spatial normalization to a common template.
In the modality A (Fig. 8.1A), the DSC-MRI scans are linearly registered to the structural T1 weighted anatomical scans applying to the first DSC-MRI

scan the co-registration algorithm of SPM5 *(Ashburner, 1997)* described in Chapter 4.1.
Then, the structural T1 weighted scans are normalized to the standard template of SPM5 (defined by the ICBM, NIH P-20 project) with SPM5. The software uses non-linear warps modelled by linear combinations of smooth discrete cosine transform basis functions to perform the normalization to of the data to the template *(Ashburner, 1998, 1999)*, as described in Chapter 4.2.The obtained spatial transformation is applied to the co-registered DSC-MRI scans to normalize them.
Subsequently, it is performed the quantitative analysis of the DSC-MRI co-registered and normalized.
In the modality B (Fig. 8.1B), the CBF, CBV and MTT maps are quantified from the original DSC-MRI data, using the Singular Value Decomposition (SVD) method *(Østergaard, 1996a,b)*.
The DSC MRI scans are at the meantime co-registered to the structural T1-weighted scans using the co-registration algorithm of SPM5, and the structural T1 scans are then normalized to the standard template of SPM5 (defined by the ICBM, NIH P-20 project) with SPM5.
The CBF, CBV and MTT maps are co-registered applying the spatial transformations obtained by the co-registration of the perfusion scans to the T1 weighted MRI scan with SPM5. Finally the CBF, CBV and MTT maps are normalized applying to the co-registered scans the spatial transformations obtained after the normalization of the T1 weighted MRI scans to the atlas. Also this procedure is performed using SPM5.

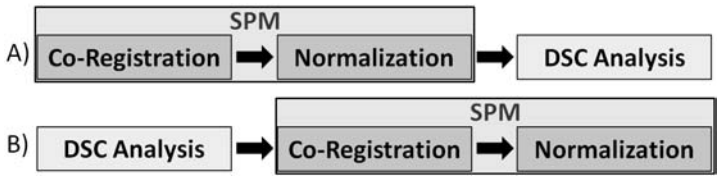

Fig. 8.1: Quantitative Analysis, Registration and Normalization Combination. A) Modality 1; B) Modality 2.

8.3 Characterization

In order to verify the correct functioning of the SPM5 rigid body co-registration algorithms on the DSC perfusion data, a visual inspection test is performed on the co-registered DSC MRI scans and on the structural T1 weighted. The test is performed on 4 subjects. In each of them, 9 anatomical locations (Posterior Right Ventricle, Posterior Left Ventricle, Anterior Right Ventricle, Anterior Left Ventricle Position, Right Eye, Left Eye, Extreme Upper Central Position of The Cerebellum, Extreme Posterior Position of the Cerebellum, Splenium of Corpus Callosum) are identified by experts and compared (Fig. 8.2).
Modality A and modality B are evaluated comparing the CBF, CBV and MTT maps provided by the two modalities with those obtained by the DSC-MRI quantitative analysis of the original data ("reference method"). Since the hemodynamic parameters change in the Grey Matter and in the White Matter, the comparison is performed distinctly on the two tissues.
For each subject, the T1 weighted scans are segmented into Grey Matter and White Matter using SPM5 (Ashburner, 2005) and applying a threshold of 0.5 in both the Grey Matter and White Matter probability maps.
The Grey Matter and White Matter maps are Normalized to the standard template of SPM5 applying the same procedure described for the normalization of the co-registered hemodynamic maps in method B. The mean values of the CBF, CBV and MTT maps are computed for Method A, method B and the reference method in both the Grey Matter and the White Matter. The computation is performed for method A and method B on the normalized maps, while for the reference method it is performed on the original data.
The comparison between the CBF, CBV and MTT mean values obtained with the two methods is performed computing the Pearson's correlation coefficient between the values obtained with modalities A and B with those obtained with the reference method on the Grey Matter and on the White Matter.
Note that Orao was still being developed while the voxel-based statistical analysis of DSC MRI perfusion estimates procedures was characterized. Because of this fact it was used SPM5. Currently I am working on the application of Orao to the characterization, in order to evaluate more specific differences between the two procedures in the Grey Matter and White Matter.

8.4 Results

The visual inspection test on the results of the co-registration of the DSC MRI data to the structural T1 weighted obtains excellent results. The test is performed on 4 subjects on 9 anatomical locations. The matrix coordinates of the Posterior Right Ventricle, Posterior Left Ventricle, Anterior Right Ventricle, Anterior Left Ventricle Position, Right Eye, Left Eye, Extreme Upper Central Position of The Cerebellum, Extreme Posterior Position of the Cerebellum and of the Splenium of Corpus Callosum correspond in the structural T1-weghted MRI scan and in the co-registered DSC perfusion scan (Fig. 8.2). Therefore the SPM5 rigid body co-registration algorithms are assumed to work properly on the DSC perfusion data.
The results on the comparison of modality A and modality B with the reference method enhance the higher accuracy of method B.
The scatter plot in Figure 8.3 shows the Gray and White Matter CBF mean values that are obtained with the two modalities for each subject. On the Grey Matter, the two modalities show a CBF correlation coefficient of 0.10 for Method A Vs Reference and 0.99 for Method B Vs Reference. On the White Matter, the CBF correlation coefficients are 0.02 (Method A) and 0.99 (Method B), respectively.
The scatter plot in Figure 8.4 shows the Gray and White Matter CBV mean values that have been obtained for each subject with the two modalities. On the Grey Matter, the two modalities show a CBV correlation coefficient of 0.08 for Method A Vs Reference and 0.95 for Method B Vs Reference. On the White Matter, the CBV correlation coefficients are 0.01 (Method A) and 0.94 (Method B), respectively.
The scatter plot in Figure 8.5 shows the Gray and White Matter MTT mean values that have been obtained for each subject with the two modalities. On the Grey Matter, the two modalities show a MTT correlation coefficient of 0.60 for Method A Vs Reference and 0.99 for Method B Vs Reference. On the White Matter, the MTT correlation coefficients are 0.55 (Method A) and 0.99 (Method B), respectively.
In conclusion, method B is less affected by distortion than method A in comparison with the results obtained with the reference method.

a)

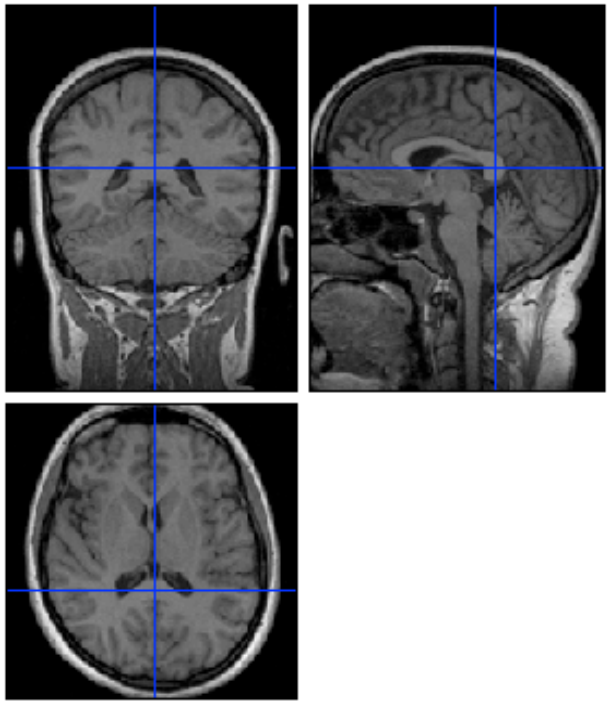

b)

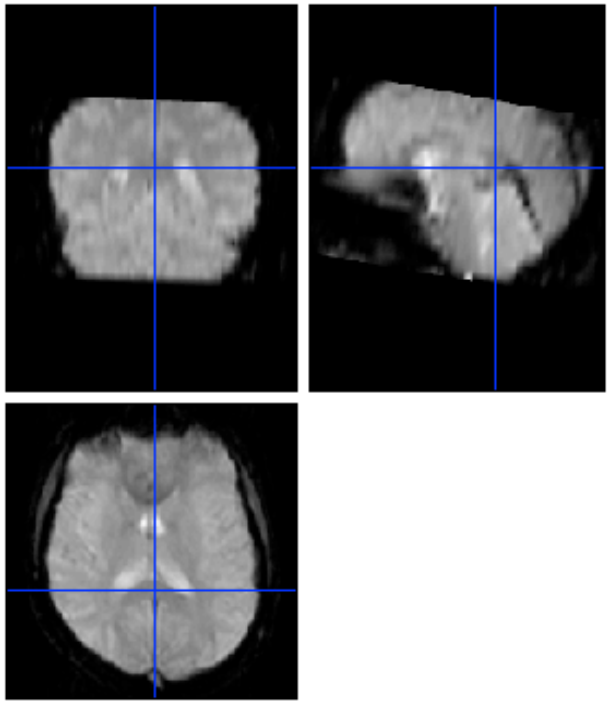

Fig. 8.2: Example of the visual inspection test on the results from the co-registration of the DSC MRI to the structural T1 data: a) Splenium of Corpus Callosum in the structural T1-weghted MRI scan; b) Splenium of the Corpus Callosum in the co-registered DSC perfusion scan.

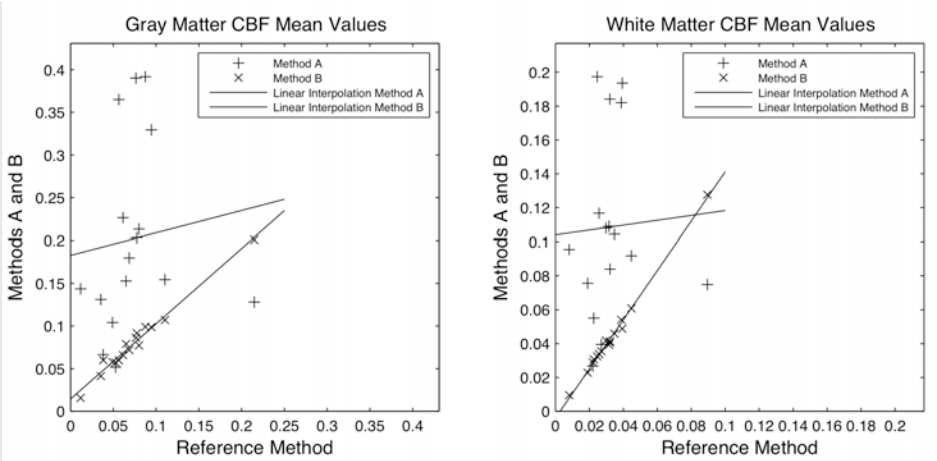

Fig. 8.3: Comparison Between Gray and White Matter CBF mean values obtained with Method A, Method B and Reference Method for each subject.

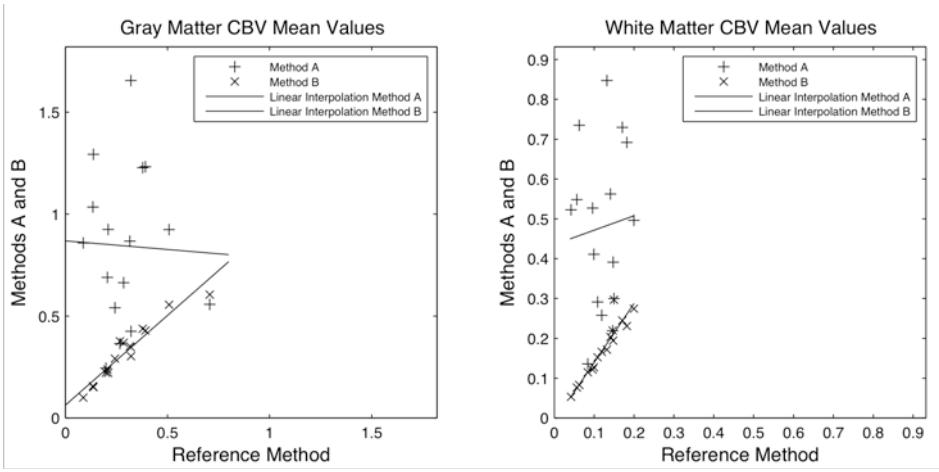

Fig. 8.4: Comparison Between Gray and White Matter CBV mean values obtained with Method A, Method B and Reference Method for each subject.

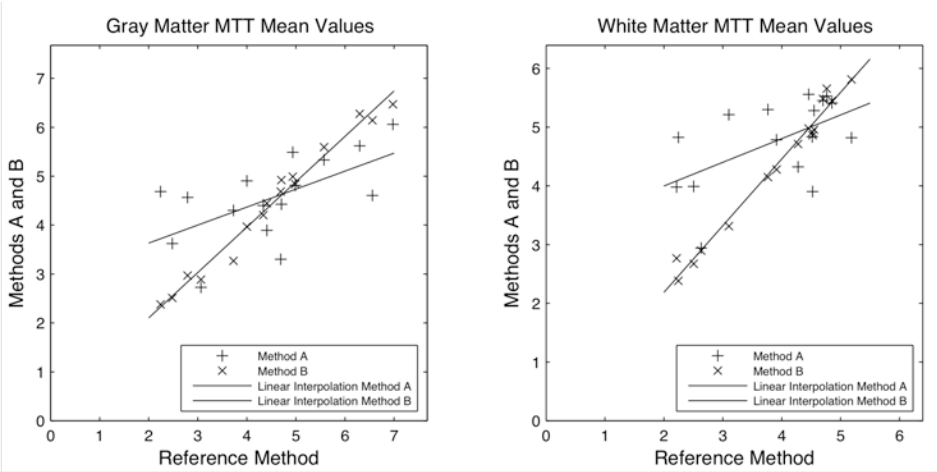

Fig. 8.5: Comparison Between Gray and White Matter MTT mean values obtained with Method A, Method B and Reference Method for each subject.

Chapter 9

Applications to the Study of Schizophrenia

Morphological and functional alterations related to schizophrenia are studied in this chapter through the application of the segmentation algorithm described in Chapter 6 and of the voxel-based statistical DSC-MRI analysis procedure described in Chapter 8.
The chosen data set is composed by a group of eight healthy controls and eight patients affected by schizophrenia.
Chapter 9.1 describes the analysis of volumetric alterations. The analyses will be performed on the entire brain or locally. Chapter 9.1.1 describes the analysis of the absolute volumes of the Brain, Grey Matter, White Matter and Cerebro Spinal Fluid. Chapter 9.1.2 describes the analysis of the ratio between the volumes of the Brain and of the CSF and the Intra Cranial Volume. Chapter 9.1.3 describes the analysis of the ratio between the volumes of the Grey or White Matter and the Total Brain Volume.
Chapter 9.2 describes the analysis of perfusion differences between healthy controls and schizophrenic patients.

9.1 Volumetric Analyses of the Brain

The volume differences of the Brain, the Grey Matter, the White Matter and the Cerebro Spinal Fluid (CSF) between schizophrenic patients and healthy controls are analyzed in this chapter.
Since both age and gender affect the brain volumetries *(Caserta, 2009; Cosgrove, 2007),* the group of the healthy controls and the group of the patients affected by schizophrenia are matched in order to have comparable ages and gender distributions. The eight healthy controls have an average age of (38.0 ±4.5) years, while the eight schizophrenic patients of (38.6±3.7) years. The healthy controls group is subdivided in a group of four males with average age of (36.0±6.0) years and four females with average age of (39.7±3.8) years. The schizophrenic patients group is subdivided in a group of four males with average age of (38.7±3.6) years and four females with average age of (38.5±4.4) years.
Since the age of illness is suspected to affect the volumes and functionality of the Brain *(Mathalon, 2001)*, the schizophrenic patients group is chosen in order to have an age of illness longer than eight years. The aim of this decision is to have a high effect of the illness. The average age of illness of the schizophrenic patients is (16.9±5) years. The average age of illness of the male schizophrenic patients group is (14.0±3.6) years, while the average age of illness of the female schizophrenic patients group is (19.7±4.9) years.
It shall be noticed that also the use of drugs can affect on the volumetry of the structures of the Brain *(Moncrieff, 2010)*. This factor increases the variability of the schizophrenic patients results.
The scans are acquired with the ICBN T1-weighted structural MRI acquisition sequence described in Chapter 5.1 (Tab. 5.1.1, Dataset 5).
The chapter 9.1 describes the analysis of the volumetric alterations between schizophrenic patients and healthy controls. The analyses is performed on the entire brain or locally on the octants of a Cartesian coordinates system centred in the Splenium of the Corpus Callosum with principal axes correspondent to the principal axes of the scans (superior-inferior, anteroposterior and mediolateral axes; usually correspondent, not in order, to the directions of rows, columns and slices). The octants 1 and 2 will correspond roughly respectively to the right and left frontal lobes. The octants 3 and 4 will correspond roughly to the right and left temporal lobes. The octants 5 and 6 will correspond approximately to the right and left parietal and occipital lobes, while the octants 7 and 8 to the right and left cerebellum.
Chapter 9.1.1 describes the analysis of absolute volume differences of the Brain, Grey Matter, White Matter and Cerebro Spinal Fluid. Chapter 9.1.2 describes the analysis of the ratio between the volumes of the Brain and of the CSF and the Intra Cranial Volume. The Intra Cranial Volume (ICV) is defined as the sum of the volume of the Brain and of the CSF. Chapter 9.1.3 describes the analysis of the ratio between the volumes of the Grey or White Matter and the Total Brain Volume. The Total Brain Volume (TBV) is defined as the sum of the volume of Grey Matter and White Matter.

The significance of the results is tested for each analysis considering the p-values of a two tailed t-test performed between the values obtained for the healthy controls and the values obtained for the patients affected by schizophrenia.

9.1.1 Volume Analyses

This chapter compares the average volumes and standard deviations of the Intra Cranial Volume, the Brain, the Grey Matter, the White Matter and the Cerebro Spinal Fluid in the healthy controls and patients affected by schizophrenia.
As can be seen in Fig.9.1.1.1, the mean Intra Cranial Volume is lower in the schizophrenic patients group than in the healthy controls. This difference is about 7% for the males, 8% for the females group. The significance of the difference between the two groups is low for the males (t-test p-value = 0.33), while it is higher considering the females (t-test p-value = 0.07).

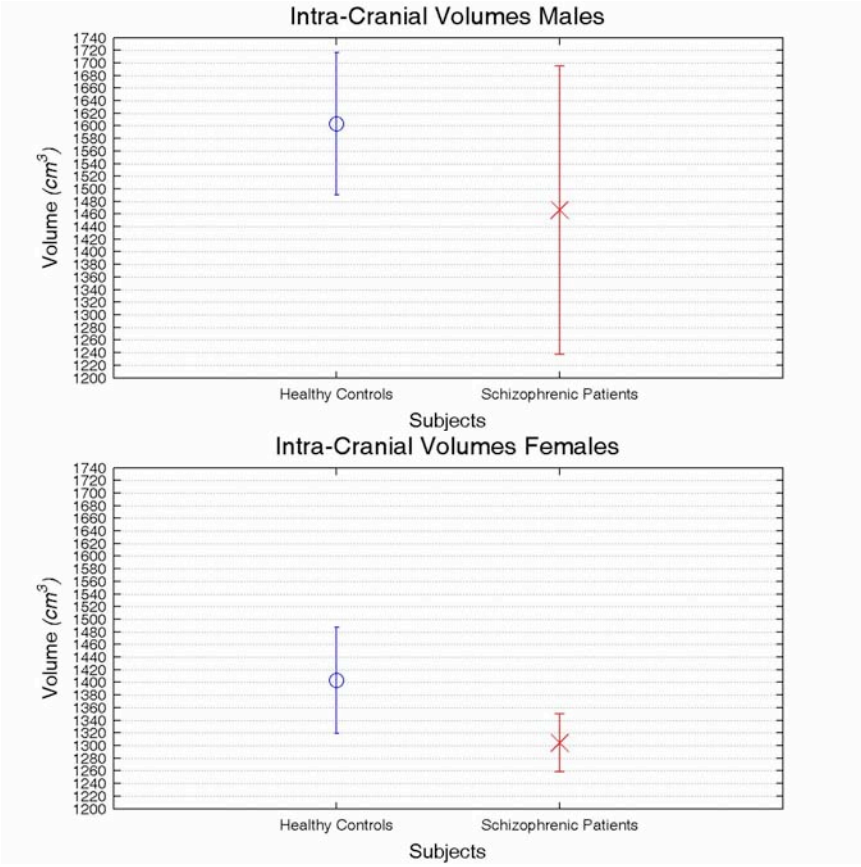

Fig. 9.1.1.1: Males and females intra cranial mean volumes and standard deviations.

Also the average Total Brain Volume is lower in the schizophrenic patients group than in the healthy controls. The difference is about 11% for the entire groups, 13% considering only the males, 9% considering only the females group. Due to the great standard deviation obtained for the schizophrenic patients, the significance of the difference between the two groups is very low for the males (t-test p-value = 0.18) (Fig. 9.1.1.2). The significance is instead higher for the difference between the entire two groups (t-test p-value = 0.06) and the females group (t-test p-value = 0.05) (Fig. 9.1.1.2). A significant difference can be seen in the local volumes of the males too. In the octants 5 and 6 (correspondent respectively to the right and left occipital and parietal lobes), the Brain volume is decreased of the 17 %. The t-test p-values are respectively 0.03 and 0.04 (Fig. 9.1.1.3).
Also the mean Grey Matter Volume is lower in the schizophrenic patients group than in the healthy controls (Fig. 9.1.1.4). This difference is about 8% for the entire groups, 10% considering only the males, 6% considering only the females group. Because of the high standard deviations the results are not significant. A significant result is obtained also in this case in the local analysis on the octants 5 and 6 (correspondent respectively to the right and left occipital and parietal lobes). The Grey Matter Volume is there decreased respectively of the 18% and 16%, with t-test p-values of 0.01 (Fig. 9.1.1.4).
The White Matter mean volume is decreased of the 15 % in the males and of the 11% in the females, but with low significance (Fig. 9.1.1.5).
The Cerebro Spinal Fluid mean volume is increased in the schizophrenic patients globally of the 6% and in the males of the 11%, while it does not increase in the females. Also the significance of these results is poor (Fig. 9.1.1.6).
It shall be moreover noticed that the patients affected by schizophrenia have lower average Total Brain Volumes, Intra Cranial Volumes, Grey Matter and White Matter Volume than the healthy controls, while they have higher Cerebro Spinal Fluid Volumes. This result has low statistical significance but is a trend followed by both the males and the females groups.

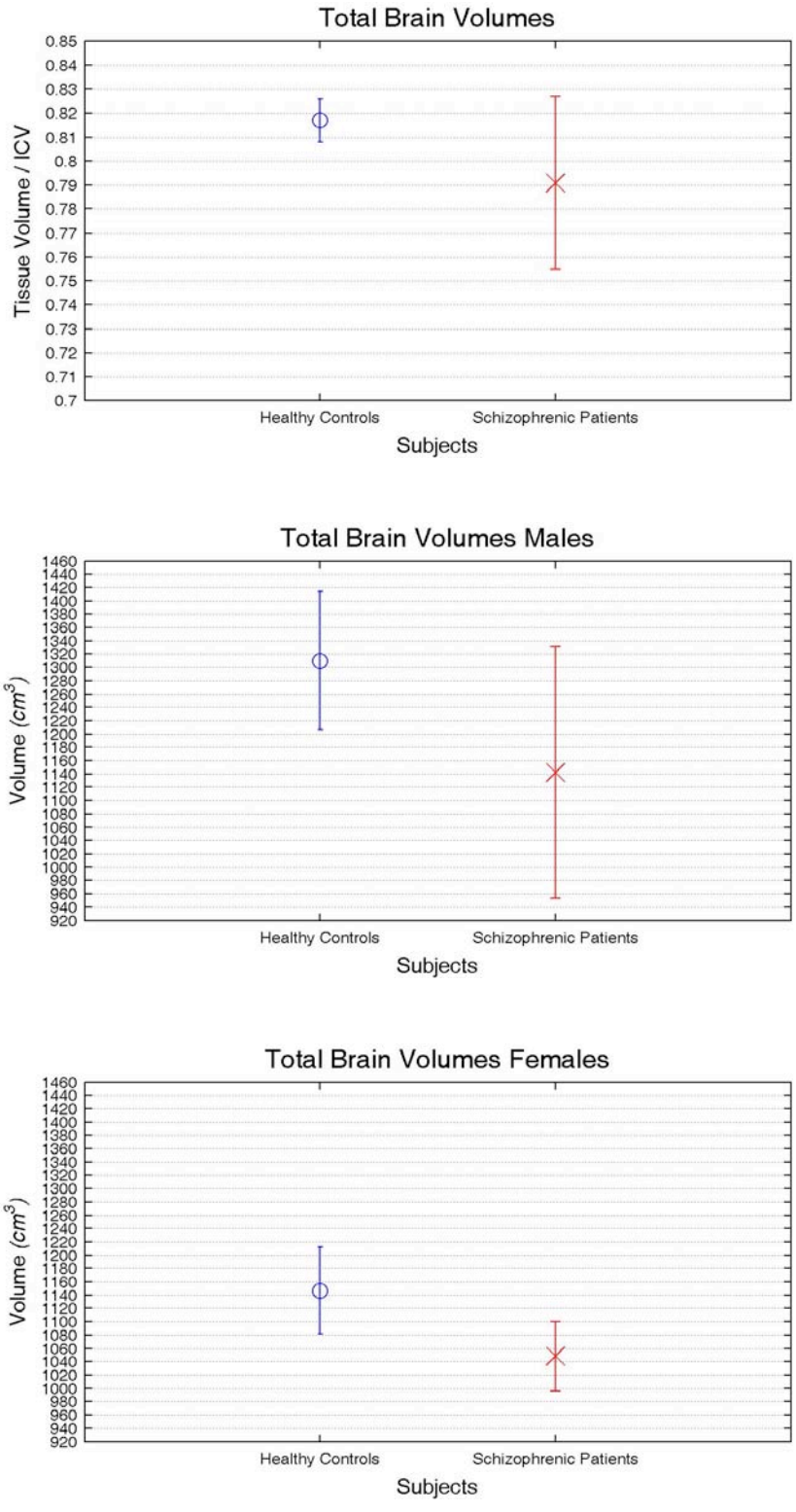

Fig. 9.1.1.2: Global and gender groups mean total Brain volumes and standard deviations.

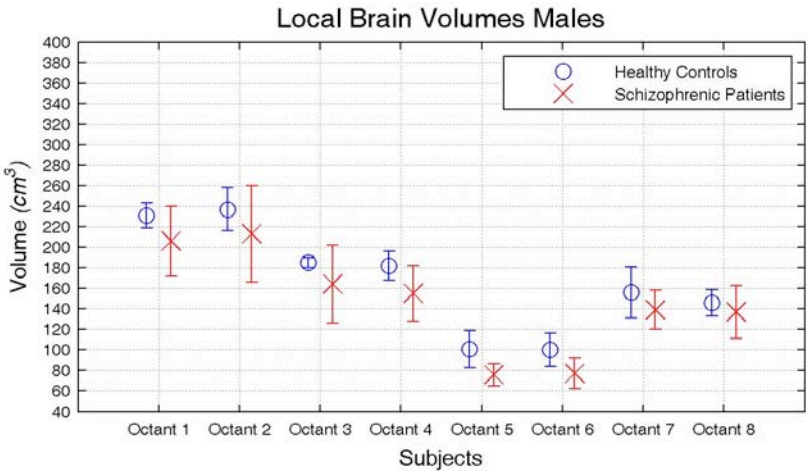

Fig. 9.1.1.3: Males local Brain mean volumes and standard deviations.

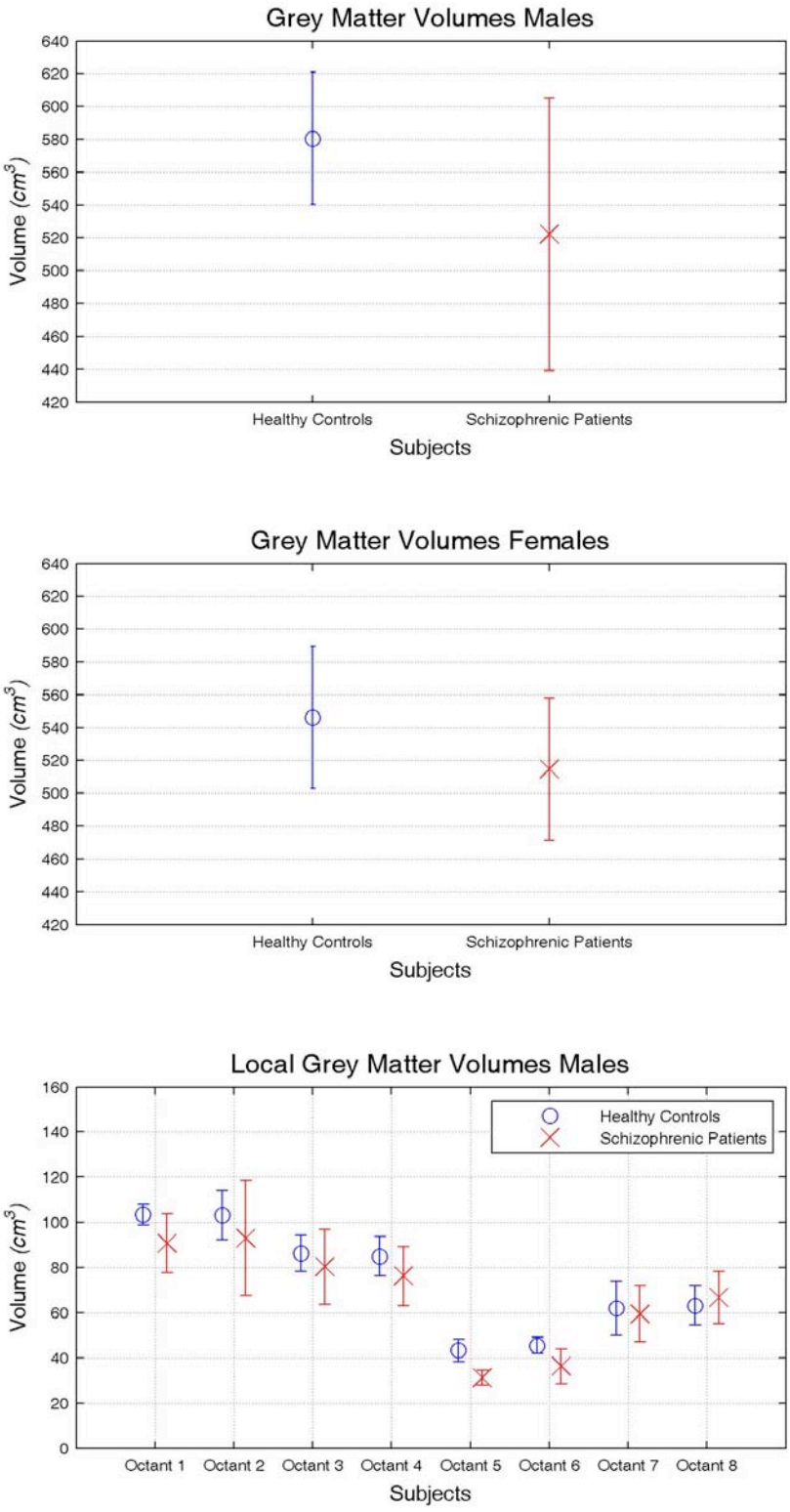

Fig. 9.1.1.4: Grey Matter mean volumes and standard deviations.

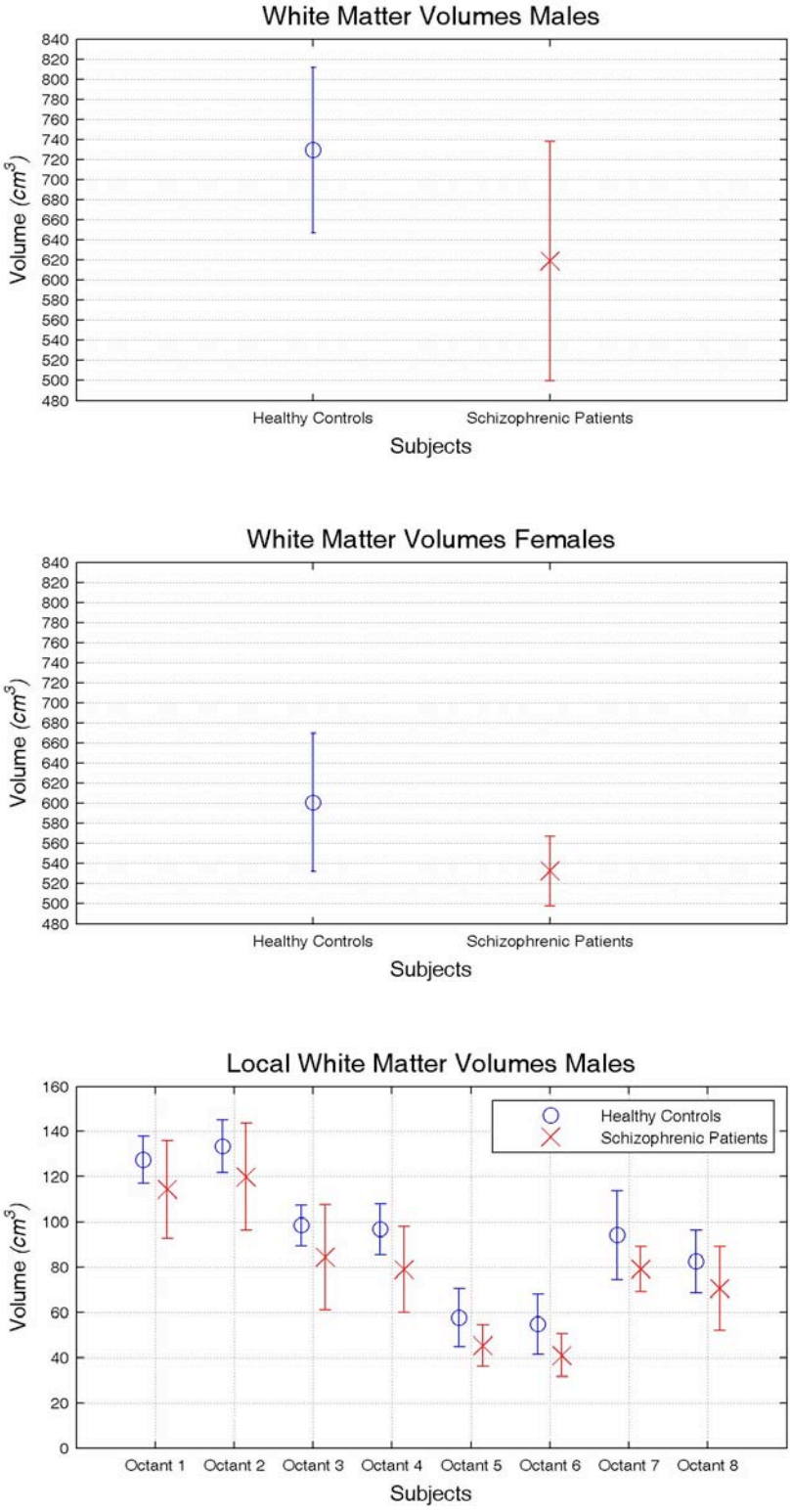

Fig. 9.1.1.5: White Matter mean volumes and standard deviations..

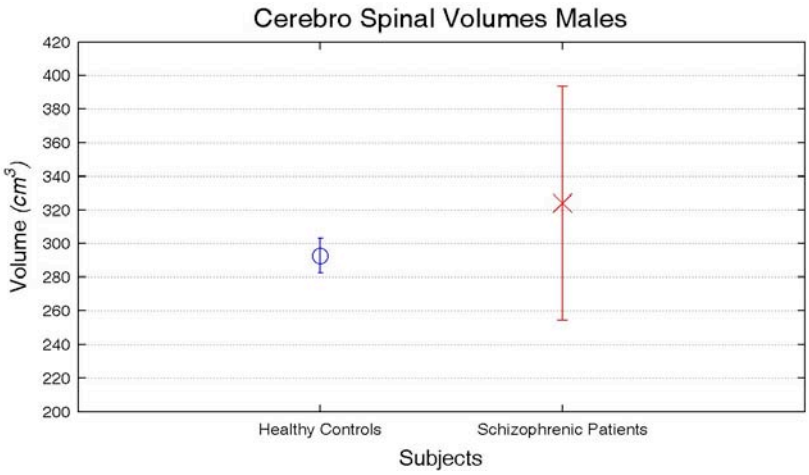

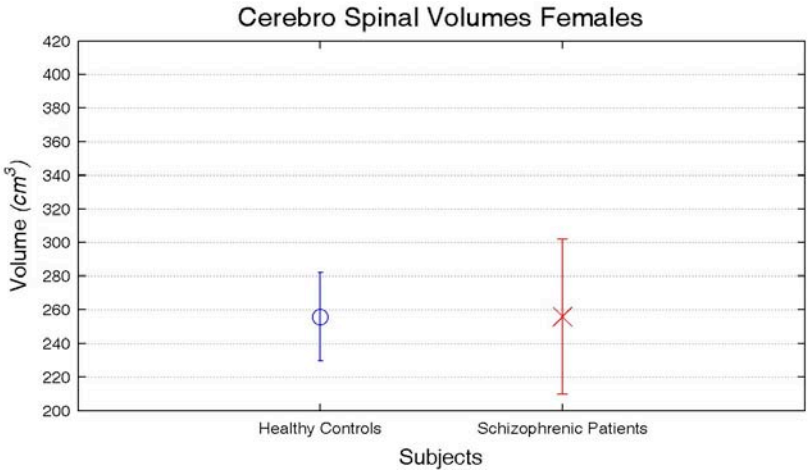

Fig. 9.1.1.6: Cerebro Spinal Fluid mean volumes and standard deviations.

9.1.2 Intra-Cranial Volume Relative Analyses

This chapter compares healthy controls and patients affected by schizophrenia analysing the averages and the standard deviations of the ratios between the Brain, the Cerebro Spinal Fluid and the Intra Cranial Volume.
The Intra Cranial Volume (ICV) is made of both the Total Brain Volume (which is made of the White Matter and the Grey Matter) and the Cerebro Spinal Fluid.
The mean of the ratio of the total Brain volume and the Intra Cranial Volume is lower in the schizophrenic patients group than in the healthy controls. This difference is 3% for the entire groups, 4% considering only the males, 2% considering only the females group (Fig. 9.1.2.1). The significance of the difference between the two groups is low in all the three analyses.
Two significant differences between the schizophrenic patients and the healthy controls can be seen locally in the mean ratio between the total Brain volume and the Intra Cranial Volume in the Octants 1 and 6. These regions correspond respectively to the frontal right lobe and the occipital and parietal left lobe. The ratios are inferior in patients affected by schizophrenia of the 3% considering the frontal right lobe and of the 6% considering the occipital and parietal left lobe. The obtained t-test p-value are respectively 0.05 and 0.01 (Fig. 9.1.2.2).
The mean ratio between the Cerebro Spinal Fluid Volume and the Intra Cranial Volume is increased in the schizophrenic patients globally of the 15%. Considering only the males it increased of the 21%, while considering only the females it increased of the 8%. The significance of the difference between the two groups is low in all the three analyses (Fig. 9.1.2.3).
Two significant differences between the schizophrenic patients and healthy controls can be seen locally in the mean ratio of the Cerebro Spinal Fluid and the Intra Cranial Volume in the Octants 1 and 6. The Cerebro Spinal Fluid is increased in schizophrenic patients of the 15% in the frontal right lobe and of the 3% in the occipital and parietal left lobe. The obtained t-test p-value are respectively 0.05 and 0.01 (Fig. 9.1.2.2).
It shall be noticed that both the males and the females schizophrenic patients have standard deviations usually greater than the healthy controls, that is a possible effect of the use of drugs.
It shall be moreover noticed that the schizophrenic patients have usually lower mean percentage of Total Brain Volume than the healthy controls, while they have usually higher percentage of Cerebro Spinal Fluid. This result has low statistical significance but is a trend followed by both the males and the females groups.

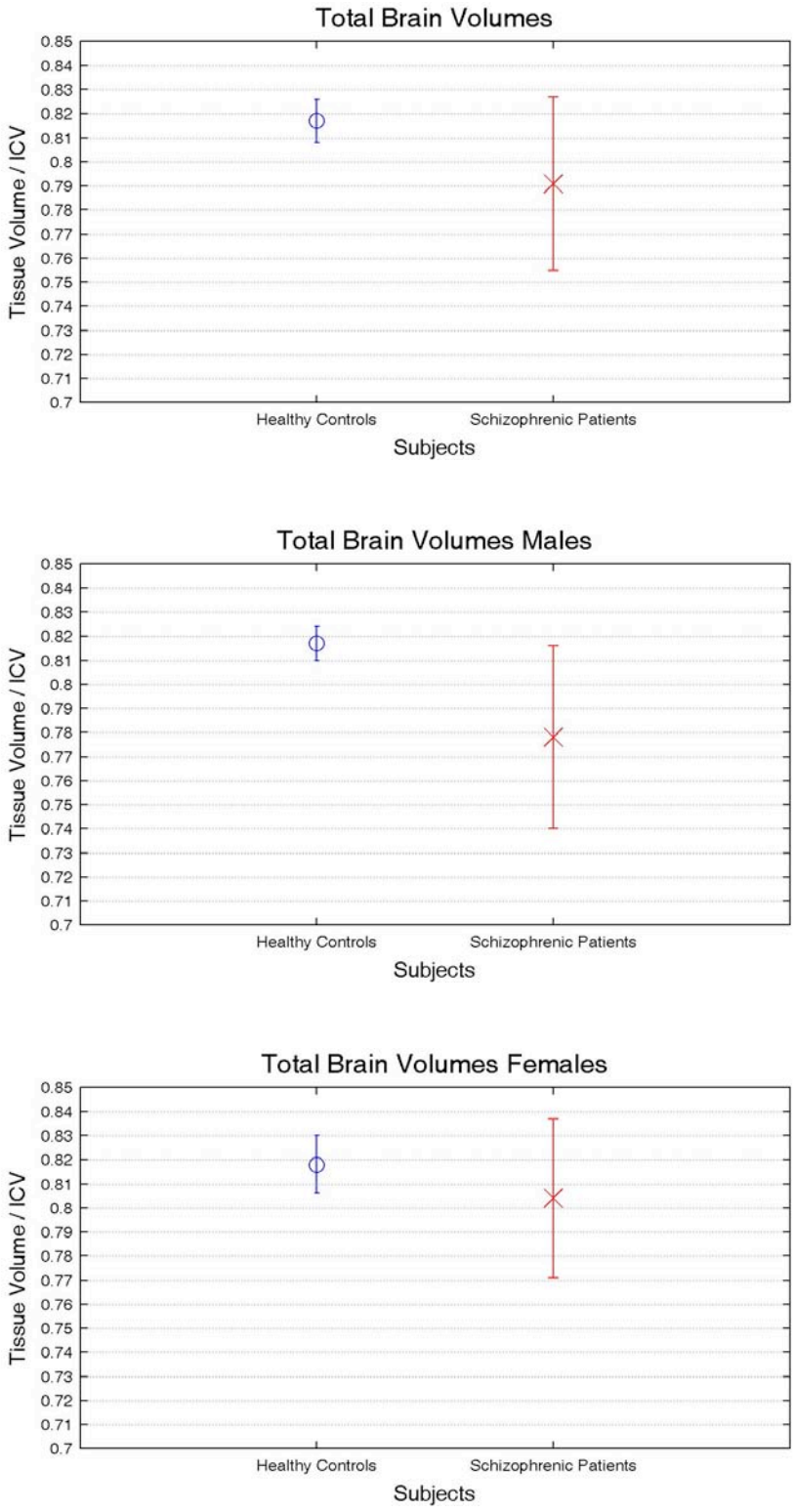

Fig.9.1.2.1: Total and local mean ratio between Brain volumes and Intra Cranial Volume and their standard deviations.

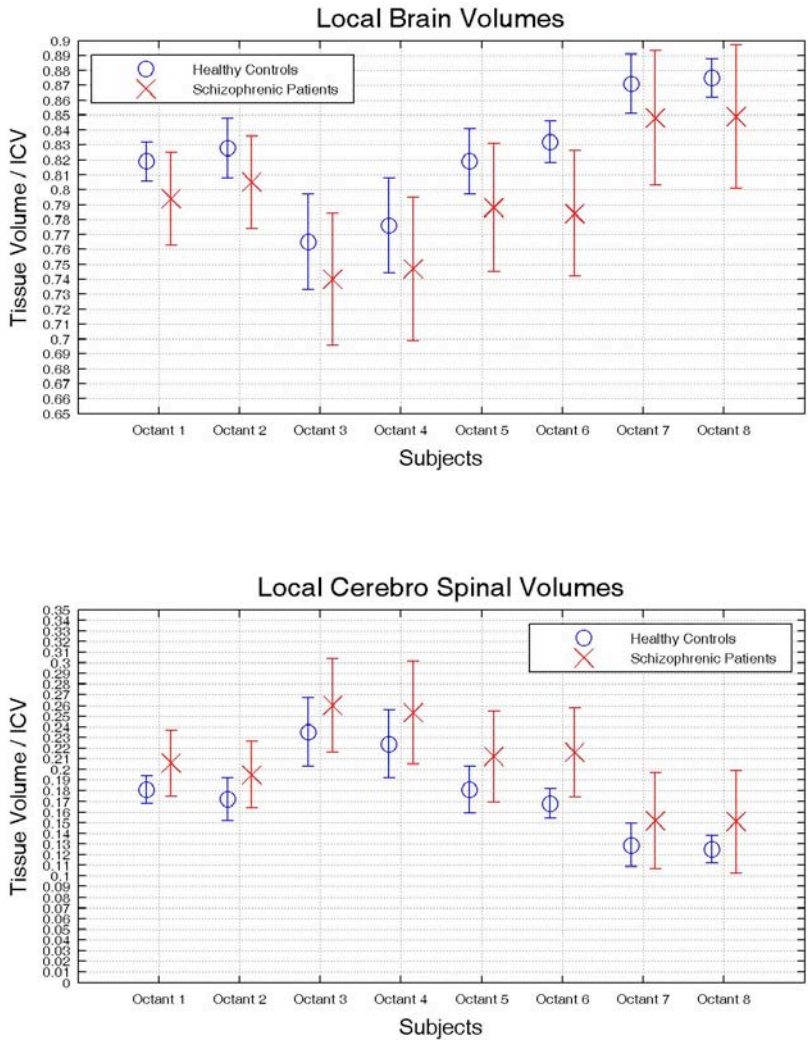

Fig.9.1.2.2: Local mean ratio between Brain volumes and Intra Cranial Volume and their standard deviations.

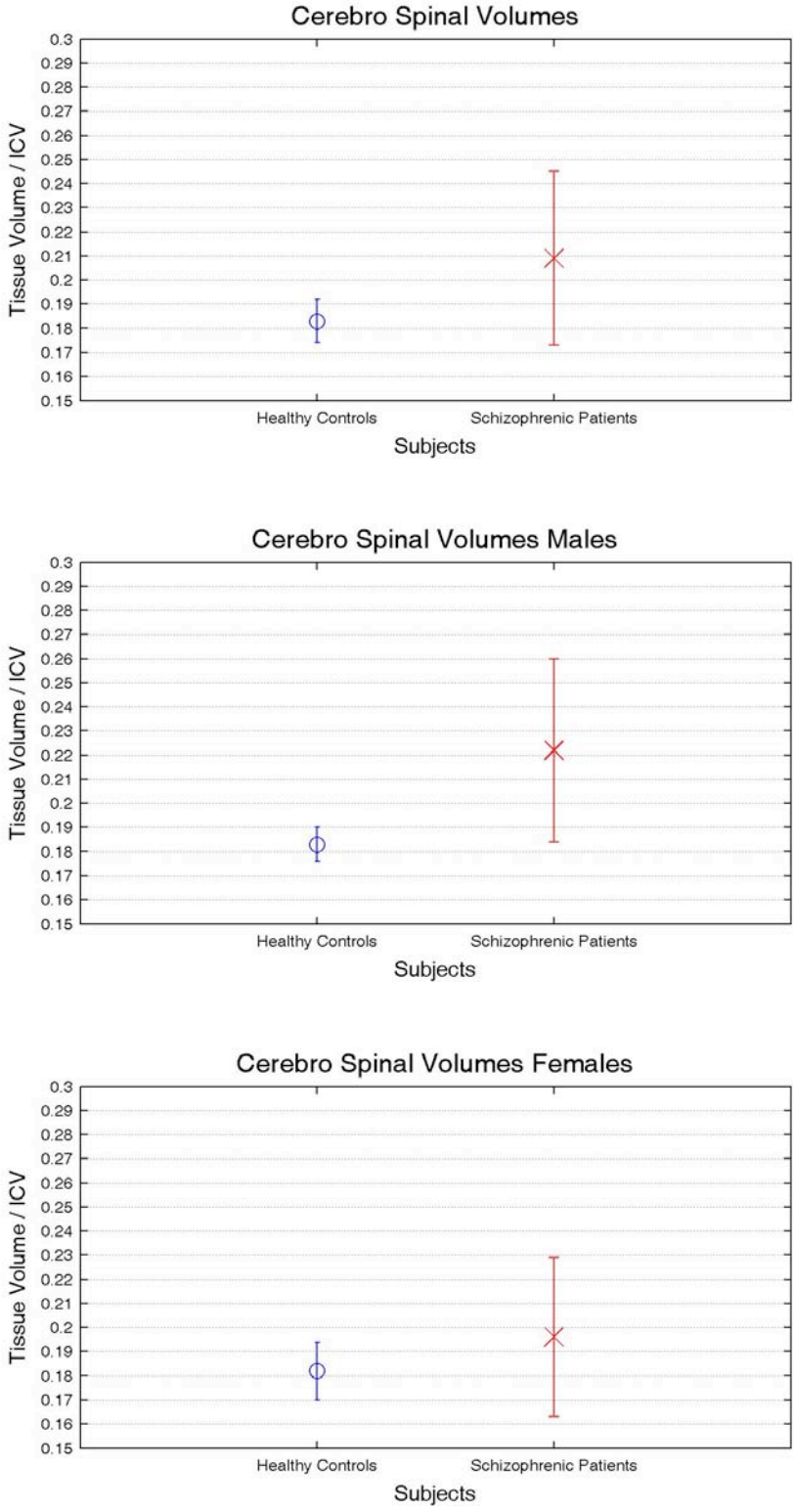

Fig.9.1.2.3: Cerebro Spinal Fluid mean ratio between volumes and Intra Cranial Volume and their standard deviations.

9.1.3 Brain Volume Relative Analyses

This chapter compares healthy controls and patients affected by schizophrenia analysing the averages and the standard deviations of the ratios between the Brain, the Cerebro Spinal Fluid and the Total Brain Volume.
The Total Brain Volume is made of the sum the White Matter and the Grey Matter.
A significant difference between the schizophrenic patients and the healthy controls can be seen locally for the females in the octant 4 (that corresponds approximately to the frontal right lobe). The percentage of Grey matter in schizophrenic females is increased of the 15%, (t-test p-value = 0.03) (Fig. 9.1.3.3).
It shall be noticed that the patients affected by schizophrenia have usually higher mean percentage of grey matter than the healthy controls, while they have usually lower percentage of White Matter (Fig.9.1.3.1-9.1.1.3.4). This result has low statistical significance but is a trend followed by both the males and the females groups.
It shall also be noticed that in these results the standard deviations of the schizophrenic patients are comparable with those of the healthy controls, differently from what was observed in chapter 9.1.2.

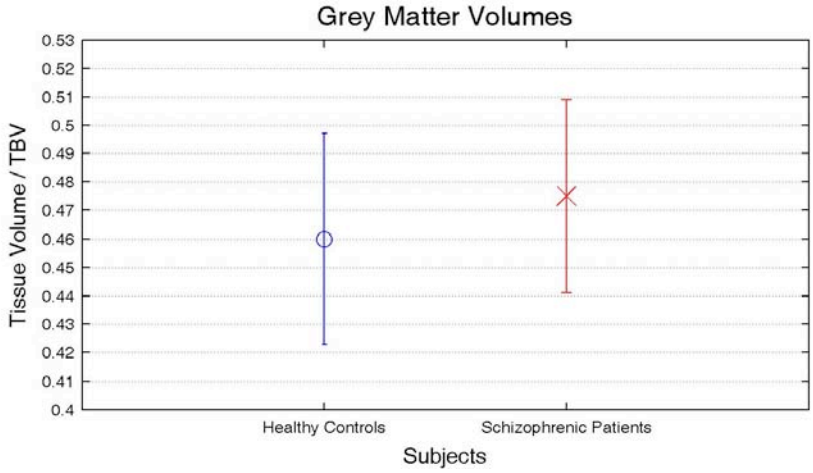

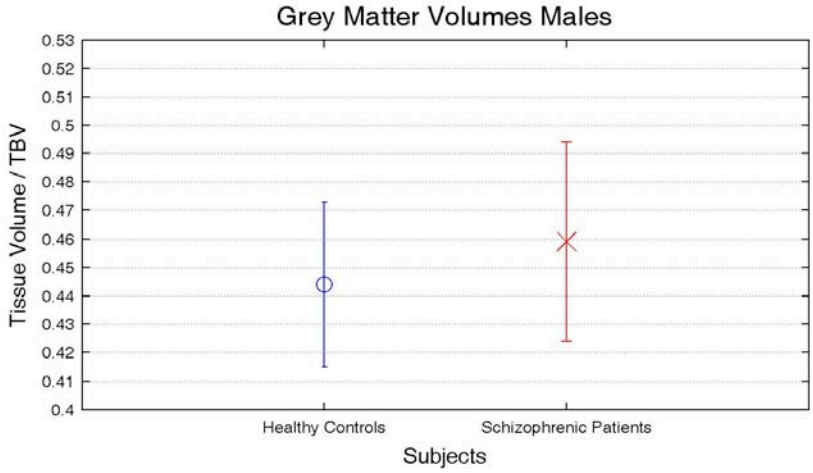

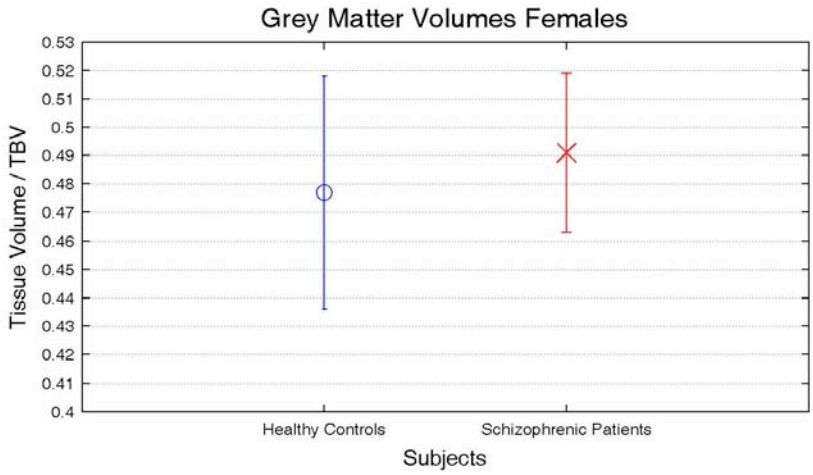

Fig.9.1.3.1: Grey Matter ratio between mean volumes and Total Brain Volume and their standard deviations.

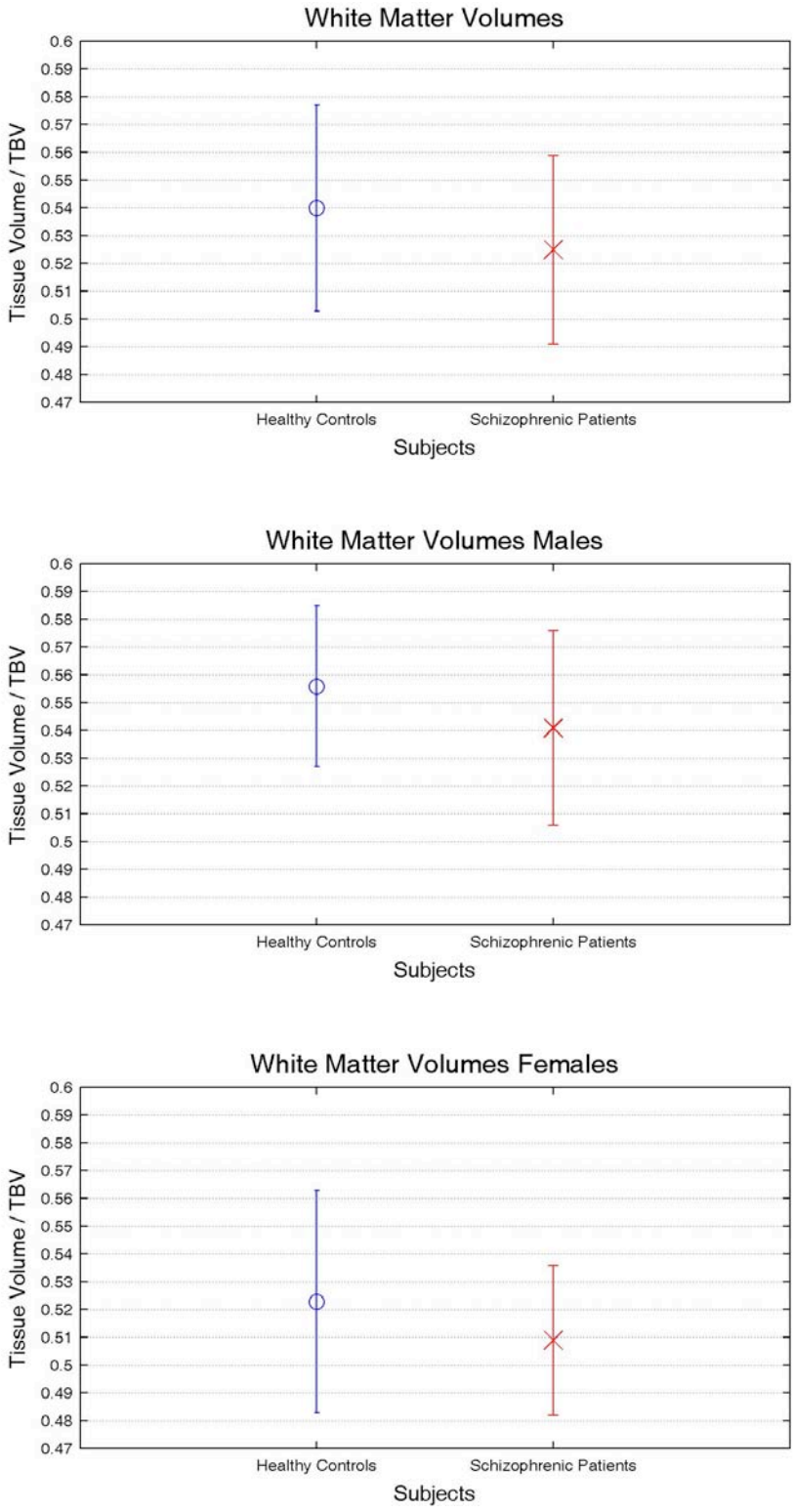

Fig.9.1.3.2: White Matter ratio between mean volumes and Total Brain Volume and their standard deviations.

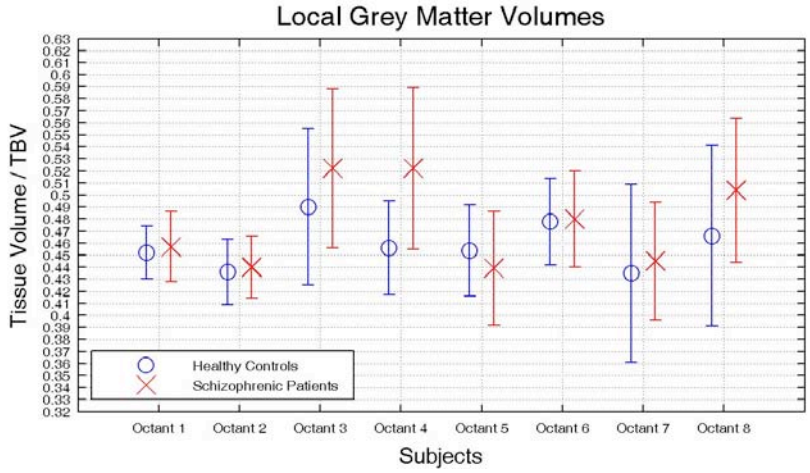

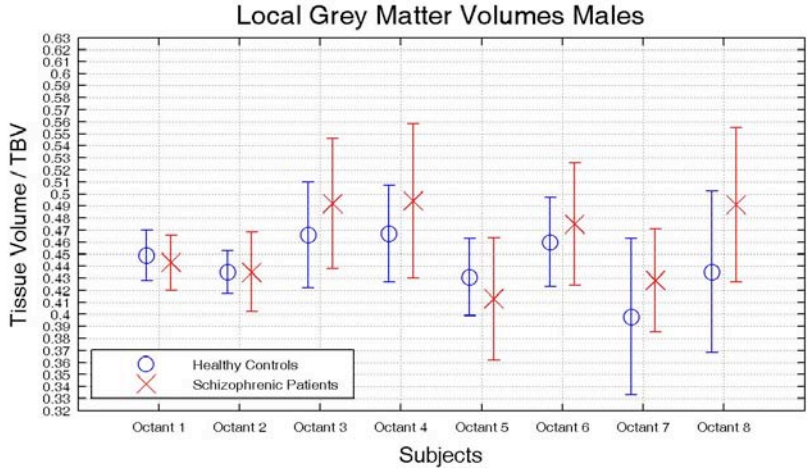

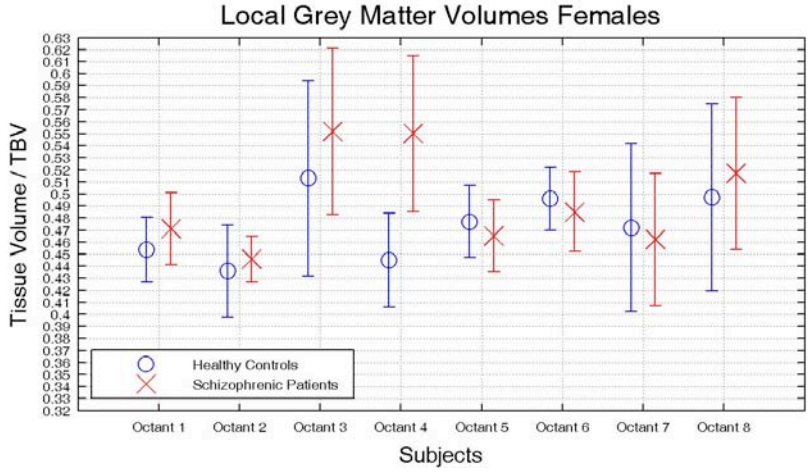

Fig.9.1.3.3: Grey Matter local ratio between mean volumes and Total Brain Volume and their standard deviations.

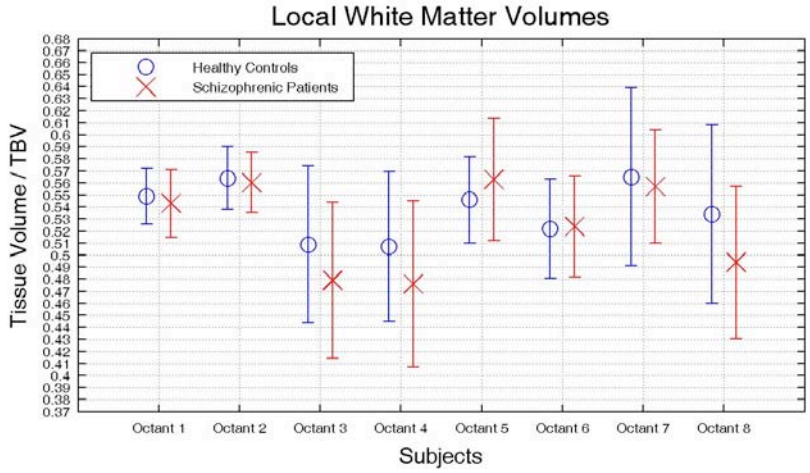

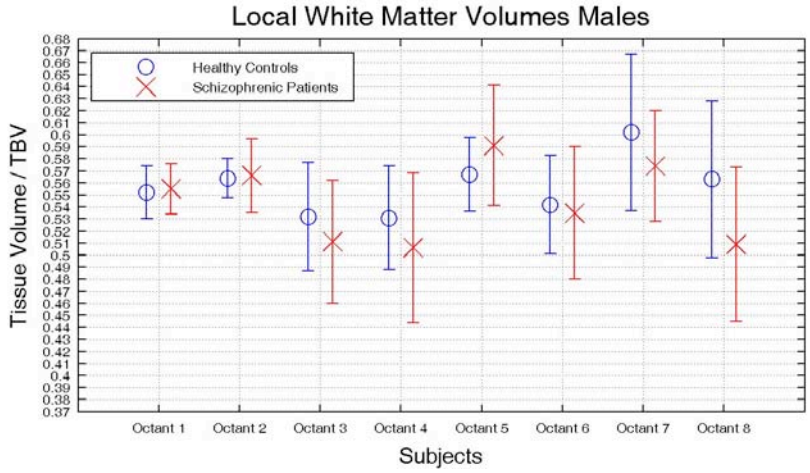

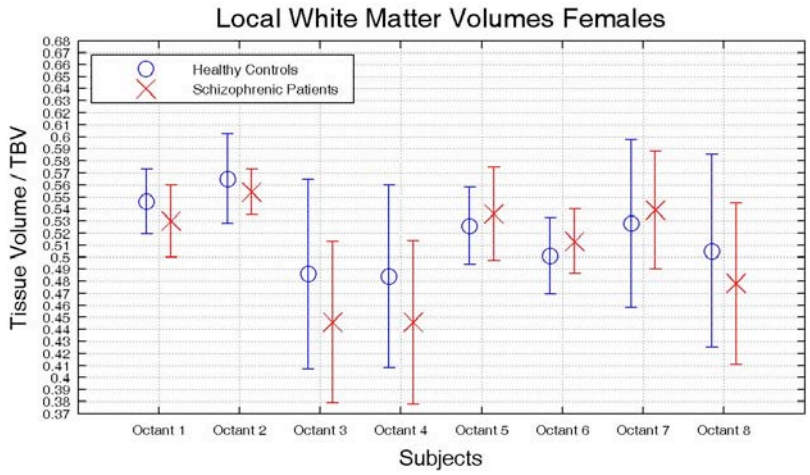

Fig.9.1.3.4: White Matter local ratio between mean volumes and Total Brain Volume and their standard deviations.

9.1.4 Discussion

The results of the volumes analyses enhance that in patients affected by schizophrenia the average Intra Cranial Volume is reduced of the 7.5% (Fig. 9.1.1.1), the average Brain volume is reduced of the 11% (Fig. 9.1.1.2), the average Grey Matter and the White Matter volumes are reduced respectively of the 8% and 13% (Fig. 9.1.1.4, Fig. 9.1.1.5), while the average volume of the Cerebro Spinal Fluid volume is increased of the 6% (Fig. 9.1.1.6). These results have usually low statistical significance, but they describe a trend followed by both the males and the females.
The average Total Brain Volume in female patients affected by schizophrenia is reduced of the 9% (t-test p-value = 0.05) (Fig. 9.1.1.2). Locally, the average male Brain volumes in the octants 5 and 6 (which correspond approximately respectively to the right and left occipital and parietal lobes), are decreased of the 17% (Fig. 9.1.1.3) (the t-test p-values are respectively 0.03 and 0.04). The average Grey Matter volumes in the octants 5 and 6 (which correspondent approximately respectively to the right and left occipital and parietal lobes), are decreased respectively of the 18% and 16 % (Fig. 9.1.1.4) (the t-test p-values are 0.01).
The global results agree with the pathological alterations described by the literature for schizophrenia. The high Intra Cranial Volume reduction is not enhanced by literature, since the analyses are usually performed on the ratios between the volumes of the tissues and the Intra Cranial Volume. Further analyses will be performed in order to identify if the mentioned differences depend only on the pathology or also on other variables.
The results of the analyses on the average ratios between the Total Brain Volume, the Cerebro Spinal Fluid Volume and the Intra Cranial Volume enhance that in patients affected by schizophrenia the average Total Brain Volume ratio is decreased of the 3%, while the average Cerebro Spinal Fluid ratio is indeed increased of the 15%. These results have low statistical significance, but they are a trend followed by both the males and the females groups.
The average ratios between the total Brain volume and the Intra Cranial Volume in the octants 1 and 6 (which correspond approximately respectively to the frontal right lobe and the occipital and parietal left lobe), are decreased respectively of the 3% and 6% (Fig. 9.1.2.2) (the t-test p-values are respectively 0.05 and 0.01).
The reduction of the Total Brain Volume and the growth of the Cerebro Spinal volume are equal to the results described by the literature *(Wright, 2000)*.
The significant reduction of the left frontal lobe agrees with the results described by literature too *(Wright, 2000)*.
The results of the analyses on the average ratios between the Grey Matter Volume, the White Matter and the Total Brain volume enhance one local significant difference between the schizophrenic patients and the healthy controls in the octant 4 (that corresponds approximately to the frontal right lobe). In the Octant 4 the percentage of Grey matter in female patients affected by schizophrenia is increased of the 15% (t-test p-value = 0.03) (Fig. 9.1.3.3). It shall be noticed that the patients affected by schizophrenia have usually higher mean percentage of grey matter than the healthy controls, while they

have usually lower percentage of White Matter (Fig.9.1.3.1-9.1.1.3.4). This result has low statistical significance but is a trend followed by both the males and the females.
This consideration (together with the reduction of the ratio between the Brain and the ICV) leads to the conclusion of a reduction of the White Matter volume greater than the Grey Matter reduction, a result that agrees with literature *(Wright, 2000)*.

9.2 Statistical Parametric DSC MRI Analysis of Schizophrenia

This chapter describes the analysis of the differences between patients affected by schizophrenia and healthy controls using the voxel based statistical parametric DSC analysis described in chapter 9.
The analyzed subjects are the same described in the beginning of chapter 9.1. Since both age and gender affect on the brain functionality, *(Caserta, 2009; Cosgrove, 2007)* the schizophrenic patients and the healthy controls groups are matched in order to have comparable ages and gender distributions. The eight healthy controls have an average age of (38.0 ±4.5) years, while the eight schizophrenic patients of (38.6±3.7) years. The healthy controls group is subdivided in a group of four males with average age of (36.0±6.0) years and four females with average age of (39.7±3.8) years. The schizophrenic patients group is subdivided in a group of four males with average age of (38.7±3.6) years and four females with average age of (38.5±4.4) years.
Since the age of illness affects the functionality of the brain *(Karnath, 2005)*, patients with an age of illness greater than eight years are analysed in order to maximize the effect of the pathology. The average age of illness of the schizophrenic patients is (16.9±5) years. The average age of illness of the male schizophrenic patients is (14.0±3.6) years, while the average age of illness of the female schizophrenic patients is (19.7±4.9) years.
It shall be noticed that also the use of drugs can affect the functionality of the structures of the Brain increasing the variability of the schizophrenic patients results *(Moncrieff, 2010)*.
The scans are acquired with the DSC MRI scans described in Chapter 5.4.
The hemodynamic maps obtained with the method B described in Chapter 8 (Co-registration and Normalization processes performed after the quantitative estimation of the DSC parameters) were used to perform a statistical parametric DSC analysis of the differences between the patients affected by schizophrenia and the healthy controls.
A 2 tails t-test was used to statistically compare voxel by voxel the CBF, MTT and CBV normalized maps of the patients affected by schizophrenia with those of the healthy controls.
The voxel-based statistical analysis of the CBF, CBV and MTT normalized maps between patients and healthy controls showed significant differences ($p < 0.05$) for the CBF in the left cerebellar lobe (Fig. 9.2.1), bilaterally in the lateral sulci (Fig. 9.2.2) and bilaterally in the insula (Fig. 9.2.3). No significant differences were obtained from the statistical parametric analysis of the CBV and MTT maps.
No multiple testing correction was used on the mentioned results. The usual correction for this kind of problems is the Bonferroni correction, but it has been demonstrated to be too conservative to be applied on functional imaging data, since the voxels in the scans are characterized by spatial correlation *(Frackowiak, 2003)*. Another possible correction could be the False Discovery Rate, but this procedure permits only to control the presence of false positives in the results *(Frackowiak, 2003)*.

To our knowledge, this is the first time that voxel-based statistical analysis of the quantitative DSC MRI perfusion estimates has been performed. Therefore, the effect of multiple testing correction have not been evaluated yet for this technique. Noticeably, the multiple testing correction impact on the t-test results will be evaluated in future studies, possibly on datasets with a greater number of subjects.
In conclusion, the method holds great promise to better define the pathophysiology of disorders characterized by small morpho-functional alterations such as schizophrenia, since it permits to identify perfusion impairments without any prior assumption, using a procedure reproducible and easy to be performed.

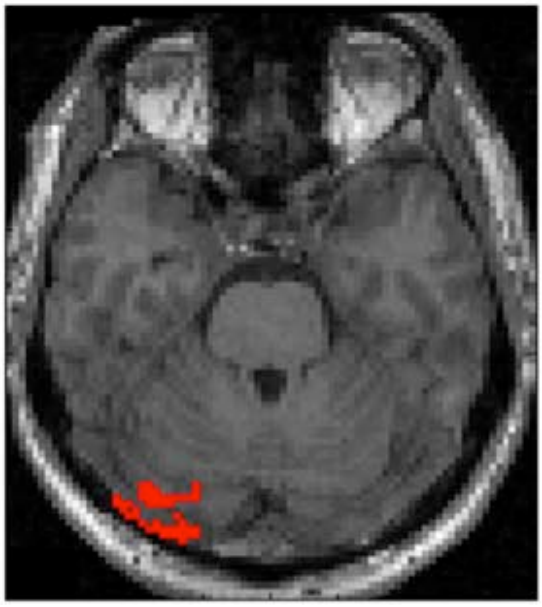

Fig. 9.2.1: Cerebral Blood Flow Dynamic Susceptibility Contrast MRI statistical parametric comparison of patients affected by schizophrenia Vs healthy controls. Significative results from 2 tails t-test ($p<0.05$): Left Cerebellar Lobe.

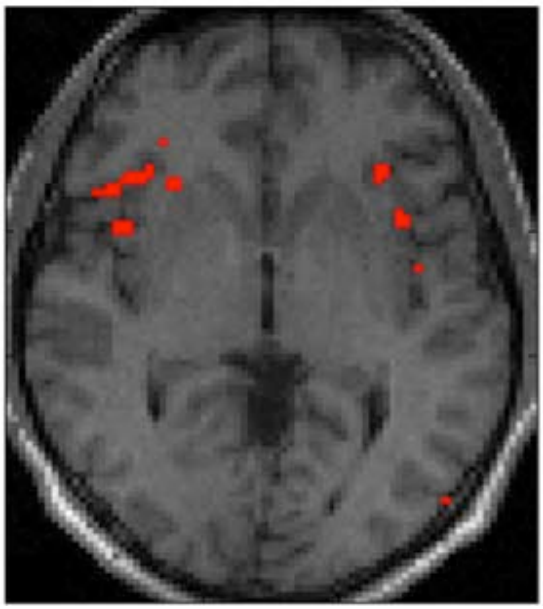

Fig. 9.2.2: Cerebral Blood Flow Dynamic Susceptibility Contrast MRI statistical parametric comparison of patients affected by schizophrenia Vs healthy controls. Significative results from 2 tails t-test ($p<0.05$): Lateral Sulci.

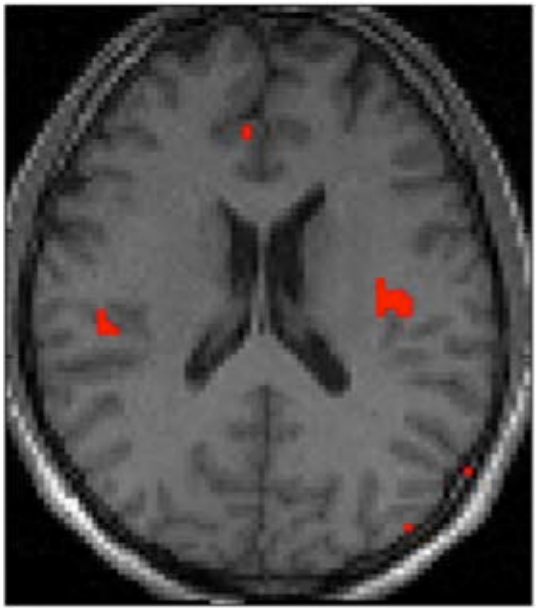

Fig. 9.2.3: Cerebral Blood Flow Dynamic Susceptibility Contrast MRI statistical parametric comparison of patients affected by schizophrenia Vs healthy controls. Significative results from 2 tails t-test ($p<0.05$): Bilateral Insulae.

Conclusions

The **first aim of the work** described in this thesis was the ideation, the implementation and the characterization of a fully automatic, robust, accurate and ductile algorithm for the segmentation of the Brain, Grey Matter and White Matter in T1 MRI of the head. The Research Unit in Brain Imaging and Neuropsychology of the Inter University Centre for Behavioural Neuroscience of Udine and Verona decided to undertake this way, rather than using one of the available software, because those were considered unsatisfactory for the research field. Moreover, the RUBIN desired to have an algorithm of its own, well known and easy to be modified according to specific needs. Orao, the segmentation process that I ideated and implemented, seems to have reached the desired characteristics.

Orao segments the Brain, CSF, Grey Matter and White Matter through iterative analyses of global and local intensity distributions, the application of morphologic operators and the analysis of connectivity properties. Orao does not use any prior knowledge about the brain, except for the assumption of the existence of the Splenium of Corpus Callosum, of the Brain, of the Grey Matter and of the White Matter. Moreover it does not require any pre-processing as spatial or intensity normalization procedure, nor uses atlases or templates.

The algorithm has been implemented with Matlab. It is fully automatic and works on Nifti (.nii), Analyze (.hdr, .img) and Dicom (.dcm) scans.

The algorithm has been quantitatively validated and compared with the procedures that are most used at the state of the art. The procedures used to perform the comparison include: SPM (Statistical Parametric Mapping, written by the Wellcome Department of Imaging Neuroscience at University College London, UK); FSL (FMRIB Software Library, written by the Analysis Group, FMRIB, Oxford, UK); FreeSurfer (written by a collaboration between the Massachusetts Institute of Technology and the Harvard University).

The quantitative validation of the Brain segmentation phase of Orao has been performed comparing the results with ground truth segmentations on two test datasets. The first dataset is the LONI Segmentation Validation Engine realized by the Laboratory Of Neuro-Imaging of the University of California Los Angeles; the second dataset is the Internet Brain Segmentation Repository, realized by the Centre for Morphometric Analysis of the Massachusetts General Hospital (MGH) in association with the Harvard Medical School. Orao obtained excellent results for Sensitivity, Specificity, Dice coefficient and Jaccard Coefficient on both the datasets. The quantitative validation of the White and Grey Matter segmentation phase of Orao has been performed

comparing the results with ground truth segmentations on the IBSR dataset. Orao obtained good results for Sensitivity, Specificity and Dice coefficient for White Matter. Lower results were obtained for the Grey Matter.
The comparison of the Brain segmentation results of Orao with FSL, Freesurfer and BSE on the LONI Segmentation Validation Engine shows that the accuracy of Orao is comparable with the state of the art. The comparison on the IBSR dataset with FSL and SPM shows that the Specificity of Orao is more than 20% greater than the state of the art.
The comparison of the Grey Matter segmentation results of Orao with FSL and SPM shows that Orao has higher Specificity, but lower Sensitivity. This result is justified by the fact that Orao has been realized in order to be restrictive rather than conservative due to the needs of the Research Unit in Brain Imaging and Neuropsychology of the ICBN (the research unit in collaboration with which Orao has been developed).
The results of the qualitative evaluation enhance the high robustness of Orao. Actually the database was created in order to include very different T1 MRI scans, characterized by different formats (nifti, analyze and dicom), resolutions, acquisition sequences, intensity distributions and subjects (characterized by different sex, ages and health conditions).
The comparison of the ability of Orao and SPM5 to distinguish differences between the healthy controls and patients affected by schizophrenia enhances that Orao has greater ability than SPM to identify differences between the two categories. Considering the Brain and the CSF segmentation results, the average t-test p-values obtained from the comparison of the two categories is 0.18±0.21 for Orao and 0.54±0.32 for SPM5. Considering the Grey and White Matter segmentation results, the average t-test p-values respectively of 0.36±0.33 and 0.56±0.33). The equal distribution of the volume differences of Orao and SPM5 between the healthy controls and the patients supports the use of Orao for both the subject classes.
Orao is fast. The Brain segmentation process takes 3-6 minutes, while the Grey Matter-White Matter segmentation process requires 1-4 minutes on a 3-GHz Pentium 4 running Windows XP, 1 GB RAM.
The **second aim of the work** was to test the ductility of the algorithm through its application to various anatomical structures and medical imaging acquisition techniques. The applications described in Chapter 7 enhance that the second aim seems to have been reached successfully.
Modifications of the algorithm have been done in each case in order to adapt it to the specific anatomic structure. Those applications are automatic or semiautomatic, depending on the specific case, but it shall be noticed that the semi-automatic applications are ideated in order to be easily automated.
As described in chapter 3, the implementation of fully automatic, robust and reliable segmentation algorithms is a challenging problem in the analysis of the data from MRI, CT, CTA and other imaging modalities. The studied anatomical structures include the Skull, Heart, Kidneys, Urinary Bladder, Urinary Tracts, Bone and a tumour of the Brain. The studied medical imaging acquisition techniques include T1 and T2 weighted MRI of the head and Computed Tomography Angiography of the chest. Since the applications have been realized to evaluate the ductility of the algorithm (and not in order to be

applied straightaway to medical analysis), the qualitative evaluation of the results have been considered sufficient.
The application of the algorithm to the segmentation of the Skull in T1 weighted MRI is implemented with Matlab, is fully automatic and works on Nifti (.nii), Analyze (.hdr, .img) and Dicom (.dcm) scans. The algorithm is based on deterministic analysis of the scans. It operates through recursive local and global analyses of the intensity distributions (made through Gaussian mixtures fit), on the application of mathematical morphology operators (dilation) and connectivity analysis. The robustness of the algorithm was tested applying it on the T1 MRI database described in chapter 5.1. The results were qualitatively evaluated on the analysed scans through visual inspection. The algorithm shows good agreement with the morphological features of the Skull in most of the scans. The algorithm is quick. It takes 2 minutes to segment the skull.
The application of the algorithm to segment the Tumour and the Peritumoural Edema in T1 an T2 weighted MRI of the head is implemented with Matlab and is semiautomatic. In order to obtain results with the highest precision possible, two different scans were selected for the segmentation of the Tumour and of the Peritumoural Edema. The scan chosen to segment the Tumour is T1-weighted, the one chosen to segment the Peritumoural Edema is T2-weighted. The segmentation of the Brain, Grey Matter, White Matter and Cerebro Spinal Fluid is also performed on the T1-weighted scan with the algorithm described in Chapter 6. The choice to use different scans for different structures requires the co-registration of the used scans, in order to make possible the merging of the results. This step is performed with SPM5. The segmentation method is quick and easy to be applied. The semi-automatic application of the segmentation process to the segmentation of the Tumour and Peritumoural Edema obtains excellent results to visual inspection made by experts of the field. The same results are obtained for the segmentation of the Brain, Grey Matter, White Matter and Cerebro Spinal Fluid.
The application of the algorithm to solve the problem of segmenting bone from tissues supplied by contrast medium in CTA of the body obtained easily good results in the segmentation of the Heart, Aorta, Urinary Tracts, Bladder and Kidneys. The results have been qualitatively evaluated through visual inspection by a medical radiologist, with very positive judgement. The implemented method is quick and easy to be applied. The algorithm is currently semi-automatic because it requires three manual operations: the identification of two landmarks and the assisted segmentation of the Urinary Bladder. The first landmark has to be located on the Spine, and it is required for the segmentation of the bone and the tissues perfused by the contrast medium. The second landmark is located on the Urinary Bladder, and it is required both for the segmentation of the Bone and of the Urinary Bladder. I developed both the landmark localization procedures in order to be easily automated. The automatic segmentation of the urinary bladder could be easily automated on the basis of proportions, applying a criterion to stop the erosion step very similar to the one described in chapter 6.1 for the erosion of the Brain. The automatic implementation of those steps would lead to a fully automatic segmentation software. Automatic localization of other landmarks

located into the kidneys and into the heart would lead easily to automatic segmentation of each of the single anatomical structures.
The **third aim of this work** was the ideation, the implementation and the characterization of a procedure to perform voxel by voxel analysis of DSC MRI. The results of the standard procedure on the regions of interest described by the literature did not obtain significant results on the ICBN database in distinguishing between healthy controls and patients affected by schizophrenia. Therefore, it was needed a method to identify if there were regions affected by hemodynamic alterations in schizophrenic patients.
Two different strategies have been described and characterized to perform voxel by voxel analysis of DSC MRI: performing the required spatial co-registration and normalization steps on the original DSC-MRI data (method A) or performing them on the perfusion maps (method B). Both the strategies have been applied and the results have been compared with the quantification performed using the standard approach on 16 subjects.
The Grey Matter CBF average correlation coefficients are respectively of 0.10 for Method A Vs Reference and 0.99 for Method B Vs Reference. On the White Matter, the CBF correlation coefficients are 0.02 (Method A) and 0.99 (Method B), respectively. The Grey Matter CBV average correlation coefficients are respectively of 0.08 for Method A Vs Reference and 0.95 for Method B Vs Reference. On the White Matter, the CBV correlation coefficients are 0.01 (Method A) and 0.94 (Method B), respectively. The Grey Matter MTT average correlation coefficients are respectively of 0.60 for Method A Vs Reference and 0.99 for Method B Vs Reference. On the White Matter, the MTT correlation coefficients are 0.55 (Method A) and 0.99 (Method B), respectively. In conclusion, the method B is less affected by distortion than method A in comparison with the results obtained with the reference method.
The procedure described in Method B could be very useful to identify automatically regions affected by hemodynamic alterations in patients affected by various pathologies.
The **fourth aim of the work** was the analysis of morphological and functional alterations related to schizophrenia through the application of the segmentation algorithm described in Chapter 6 and of the voxel-based statistical DSC-MRI analysis procedure described in Chapter 8.
The chosen data set is composed by a group of eight healthy controls and eight patients affected by schizophrenia. Since both age and gender affect the brain volumes, the group of the healthy controls and the group of the patients affected by schizophrenia are matched in order to have comparable ages and gender distributions. Since the age of illness is suspected to affect the volumes and functionality of the Brain, the schizophrenic patients group is chosen in order to have an age of illness longer than eight years. The aim of this decision is to have a high effect of the illness. It shall be noticed that also the use of drugs can affect the volumes of the structures of the Brain. This factor increases the variability of the schizophrenic patients results.
The analysis of the volumetric alterations between schizophrenic patients and healthy controls have been performed on the entire brain or locally. The local analyses have been performed on the octants of a Cartesian coordinates system centred in the Splenium of the Corpus Callosum with principal axes

correspondent to the principal axes of the scans (superior-inferior, anteroposterior and mediolateral axes; usually correspondent, not in order, to the directions of rows, columns and slices). The octants 1 and 2 correspond roughly respectively to the right and left frontal lobes. The octants 3 and 4 correspond to the right and left temporal lobes. The octants 5 and 6 will approximately to the right and left parietal and occipital lobes, while the octants 7 and 8 to the right and left cerebellum.

Three types of volume analyses have been performed: 1) Analysis of absolute volumes of the Brain, Grey Matter, White Matter and Cerebro Spinal Fluid; 2) Analysis of the ratio between the volumes of the Brain and of the CSF and the Intra Cranial Volume (the Intra Cranial Volume is defined as the sum of the volume of the Brain and of the CSF); 3) Analysis of the ratio between the volumes of the Grey or White Matter and the Total Brain Volume (the Total Brain Volume is defined as the sum of the volume of Grey Matter and White Matter).

The significance of the results is tested for each analysis considering the p-values of a two tailed t-test performed between the values obtained for the healthy controls and the values obtained for the patients affected by schizophrenia.

The results of the absolute volumes analyses enhance that in patients affected by schizophrenia the average Intra Cranial Volume is reduced of the 7.5%, the average Brain volume is reduced of the 11%, the average Grey Matter and the White Matter volumes are reduced respectively of the 8% and 13%, while the average volume of the Cerebro Spinal Fluid volume is increased of the 6%. These results have usually low statistical significance, but they describe a trend followed by both the males and the females. The average Total Brain Volume in female patients affected by schizophrenia is reduced of the 9% (t-test p-value = 0.05). Locally, the average male Brain volumes in the octants 5 and 6 (which correspond approximately respectively to the right and left occipital and parietal lobes), are decreased of the 17% (the t-test p-values are respectively 0.03 and 0.04). The average Grey Matter volumes in the octants 5 and 6 (which correspond approximately respectively to the right and left occipital and parietal lobes), are decreased respectively of the 18% and 16 % (the t-test p-values are 0.01). The results agree with the pathological alterations described by the literature for schizophrenia. The high Intra Cranial Volume reduction is not enhanced by literature, since the analyses are usually performed on the ratios between the volumes of the tissues and the Intra Cranial Volume. Further analyses will be performed in order to identify if the mentioned differences depend only on the pathology or also on other variables.

The results of the analyses on the average ratios between the Total Brain Volume, the Cerebro Spinal Fluid Volume and the Intra Cranial Volume enhance that in patients affected by schizophrenia the average Total Brain Volume ratio is decreased of the 3%, while the average Cerebro Spinal Fluid ratio is indeed increased of the 15%. These results have low statistical significance, but they are a trend followed by both the males and the females groups. The average ratios between the total Brain volume and the Intra Cranial Volume in the octants 1 and 6 (which correspond approximately respectively to the frontal right lobe and the occipital and parietal left lobe), are decreased respectively of the 3% and 6% (the t-test p-values are respectively

0.05 and 0.01). The reduction of the Total Brain Volume and the growth of the Cerebro Spinal volume are equal to the results described by the literature. The significant reduction of the left frontal lobe agrees with the results described by literature too.
The results of the analyses on the average ratios between the Grey Matter, the White Matter and the Total Brain Volume enhance one local significant difference between the schizophrenic patients and the healthy controls in the octant 4 (that corresponds approximately to the frontal right lobe). In the Octant 4 the percentage of Grey matter in female patients affected by schizophrenia is increased of the 15% (t-test p-value = 0.03). It shall be noticed that the patients affected by schizophrenia have usually higher mean percentage of grey matter than the healthy controls, while they have usually lower percentage of White Matter. This result has low statistical significance but is a trend followed by both the males and the females. This consideration (together with the reduction of the ratio between the Brain and the ICV) leads to the conclusion of a reduction of the White Matter volume greater than the Grey Matter reduction, a result that agrees with literature.
The hemodynamic maps obtained with the method B described in Chapter 8 (Co-registration and Normalization processes performed after the quantitative estimation of the DSC parameters) were used to perform a statistical parametric DSC analysis of the differences between the patients affected by schizophrenia and the healthy controls. A 2 tails t-test was used to statistically compare voxel by voxel the CBF, MTT and CBV normalized maps of the patients affected by schizophrenia with those of the healthy controls.
The voxel-based statistical analysis of the CBF, CBV and MTT normalized maps between patients and healthy controls showed significant differences ($p < 0.05$) for the CBF in the left cerebellar lobe, bilaterally in the lateral sulci and bilaterally in the insula. No significant differences were obtained from the statistical parametric analysis of the CBV and MTT maps.
No multiple testing correction was used on the mentioned results. Noticeably, the multiple testing correction impact on the t-test results will be evaluated in future studies, possibly on datasets with a greater number of subjects.
In conclusion, voxel by voxel statistical parametric DSC analysis holds great promise to better define the pathophysiology of disorders characterized by small morpho-functional alterations such as schizophrenia, since it permits to identify perfusion impairments without any prior assumption, using a procedure reproducible and easy to be performed.

Bibliography

Amaddeo F., Tansella M., Information systems for mental health. Epidemiological Psychiatry Society, 18:1-4, 2009.

Andreone N., Tansella M., Cerini R., Rambaldelli G., Versace A., Marrella G., Perlini C., Dusi N., Pelizza L., Balestrieri M., Barbui C., Nosè M., Gasparini A., Brambilla P., Cerebral atrophy and white matter disruption in chronic schizophrenia. European Archives of Psychiatry and Clinical Neuroscience, 257(1): 3-11, 2007.

Ardekani B.A., Bachman A.H., Strother S.C., Fujibayashi Y., Yonekura Y., Impact of inter-subject registration on group analysis of fMRI data. International Congress Series, 49-59, 2004.

Aronen H.J., Gazit I.E., Louis D.N., Buchbinder B.R., Pardo F.S., Weisskoff R.M., Harsh G.R., Cosgrove G.R., Halpern E.F., Hochberg F.H., Rosen B.R., Cerebral blood volume maps of gliomas: comparison with tumour grade and histologic findings. Radiology, 191:41-51, 1994.

Aronen H.J., Glass J., Pardo F.S., Belliveau J.W., Gruber M.L., Buchbinder B.R., Gazit I.E., Linggood R.M., Fischman A.J., Rosen B.R., Hochberg F.H., Echo-planar MR cerebral blood volume mapping of gliomas. Acta Radiologica 36: 520-528, 1995.

Ashburner J., Friston K., Multimodal Image Co-registration and Partitioning: A Unified Framework. Neuroimage, 6, 209-217, 1997.

Ashburner J., Friston K.J., High-dimensional nonlinear image registration. NeuroImage, 7(4):737, 1998.

Ashburner J., Friston K.J., Nonlinear spatial normalization using basis functions. Human Brain Mapping, 7(4):254-266, 1999.

Ashburner J., Unified Segmentation. NeuroImage, 26:839-851, 2005.

Atzori M., Rambaldelli G., Perlini C., Bellani M., Dusi N., Sponda S., Tansella M., and Brambilla P., Automatic Segmentation of Human Brain, Grey and White Matter in MRI: A Robust and Accurate Algorithm Based on the Tissue Features Analysis. 15th Joint Annual Meeting ISMRM-ESMRMB Scientific Proceedings, 412, 2007.

Atzori M., Bertoldo A., Brambilla P., Cobelli C., 3D Segmentation of Human Anatomical Structures in MRI, CT and CTA: An automatic Algorithm. Atti del Congresso Nazionale di Bioingegneria, 651-652, 2008.

Atzori M., Rambaldelli G., Brambilla P., Bertoldo A., Deterministic Automatic Segmentation in MRI, CT and CTA: A Robust Method Based on Anatomical Structures Modeling and Local Recursive Intensity Analysis. 17th Joint Annual Meeting ISMRM-ESMRMB Scientific Proceedings, 357, 2009.

Axel L., Cerebral Blood Flow Determination by Rapid-Sequence Computed Tomography: a Theoretical Analysis. Radiology 137: 679-686, 1980.

Ayache N., Cinquin P., Cohen I., Cohen L., Leitner F., Monga O., Segmentation of complex three-dimensional medical objects: a challenge and a requirement for computer-assisted surgery planning and performance. In Taylor R.H., Lavallee S., Burdea G.C., Mosges R., Computer-integrated surgery: technology and clinical applications, 59-74, MIT Press, 1996.

Baird A.E., Warach S., Magnetic resonance imaging of acute stroke. Journal of Cerebral Blood Flow & Metabolism, 18:583-609,1998.

Bajc M., Medved V., Basic M., Topuzovic N., Babic D., Cerebral perfusion inhomogeneities in schizophrenia demonstrated with single-photon emission computed tomography and Tc99m-hexamethylpropyleneamineoxim. Acta Psychiatrica Scandinavica, 80:427-433, 1989.

Ballester M.A., Zisserman G.A., Brady M., Segmentation and measurement of brain structures in MRI including confidence bounds. Medical Image Analysis, 4:189-200, 2000.

Barbier E.L., Lamalle L., Decorps M., Methodology of Brain Perfusion Imaging. Journal of Magnetic Resonance Imaging, 13:496-520, 2001.

Bedell B.J., Narayana P.A., Volumetric analysis of white matter, grey matter, and CSF using fractional volume analysis. Magnetic Resonance in Medicine, 39:961-969, 1998.

Benner T., Heiland S., Erb G., Forsting M., Sartor K., Accuracy of Gamma-variate Fits to Concentration-time Curves from Dynamic Susceptibility-Contrast Enhanced MRI: Influence of Time Resolution, Maximal Signal Drop and Signal-to-noise. Journal of Magnetic Resonance Imaging, 15(3):307-17, 1997.

Bezdek J.C., Hall L.O., Clarke L.P., Review of MR image segmentation techniques using pattern recognition. Medical Physics, 20:1033-1048, 1993.

Bookstein F.L., Landmark methods for forms without landmarks: Morphometrics of group differences in outline shape. Medical Image Analysis, 1(3):225-243, 1997.

Calamante F., Thomas D.L., Pell G.S., Wiersma J., Turner R., Measuring Cerebral Blood Flow Using Magnetic Resonance Imaging Techniques. Journal of Cerebral Blood Flow and Methabolism, 19:701-735, 1999.

Caserta M.T., Bannon Y., Fernandez F., Giunta B., Schoenberg M.R., Tan J., Normal brain aging clinical, immunological, neuropsychological, and neuroimaging features. International Review of Neurobiology, 84:1-19, 2009.

Chan T., Vese L.A., Active contours without edges. IEEE Transactions on Image Processing, 10:266-277, 2001.

Christensen G.E., Joshi S.C., Miller M.I., Volumetric transformation of brain anatomy. IEEE Transactions on Medical Imaging, 16:864-877, 1997.

Christensen G.E., Rabbitt R.D., Deformable templates using large deformation kinematics. IEEE Transactions on Image Processing, 5:402-417, 1996.

Chu C., K. Takaya, 3-Dimensional rendering of MR images, Communications, Computers and Power in the Modern Environment Conference Proceedings, IEEE, 165-170, 1993.

Cleghom J.M., Gameti E.S., Nahmias C., Regional brain metabolism during auditory hallucinations in chronic schizophrenia. British Journal of Psychiatry, 157:562-570, 1990.

Coffey et al., Quantitative cerebral anatomy of the aging human brain: a cross-sectional study using magnetic resonance imaging, Neurology, 42:527-536, 1992.

Coleman G.B. and H.C. Andrews. Image segmentation by clustering. Proceedings of the IEEE, 5:773-785, 1979.

Collins D.L., C.J. Holmes, T.M. Peters, and A.C. Evans. Automatic 3-D model-based neuroanatomical segmentation. Human Brain Mapping, 3:190-208, 1995.

Parent A., Carpenter M.B., Carpenter's Human Neuroanatomy. Williams & Wilkins, 1996.

Cosgrove K.P., Mazure C.M., Staley J.K.., Evolving knowledge of sex differences in brain structure, function, and chemistry. Biological Psychiatry, 62(8):847-855, 2007.

Crivello F., Schormann T., Tzourio-Mazoyer N., Roland P.E., Zilles K., Mazoyer B.M.. Comparison of spatial normalization procedures and their impact on functional maps. Human Brain Mapping, 16:228-250, 2002.

Crow, Some possibilities for measuring selection intensities in man, Human Biology, 61(5-6):763-75, 1989.

Dai W., Carmichael O.T., Lopez O.L., Becker J.T., Kuller L.H., Gach H.M., Effects of Image Normalization on the Statistical Analysis of Perfusion MRI in Elderly Brains. Journal of Magnetic Resonance Imaging, 28:1351-1360, 2008.

Dale A.M., Fischl B., Sereno M.I., Cortical surface-based analysis: I. Segmentation and surface reconstruction. NeuroImage 9(2):179-194, 1999.

Damadian R., Goldsmith M., Minkoff L., NMR in cancer: XVI. Fonar image of the live human body. Physiological Chemistry and Physics, 9:97-100, 1977.

Davatzikos C., Spatial normalization of 3D images using deformable models. Journal of Computer Assisted Tomography, 20:656-665, 1996.

Davenport J.W., Bezdek J.C., and Hathaway R.J., Parameter estimation for finite mixture distributions. Computers & Mathematics with Applications, 15:810-828, 1988.

Dice, L.R., Measures of the amount of ecologic association between species. Journal of Ecology, 26:297-302, 1945.

Dunn J.C., A fuzzy relative of the ISODATA process and its use in detecting compact well-separated clusters. Journal of Cybernetics, 3:32-57, 1973.

Fiebich M., Straus C.M., Sehgal V., Renger B.C., Doi K., Hoffmann K. R., Automatic bone segmentation technique for CT angiographic studies, Journal of Computer Assisted Tomography, 23:155-161, 1999.

Fischl B., Sereno M.I., Dale A.M., Cortical Surface-Based Analysis II: Inflation, Flattening, and a Surface-Based Coordinate System, NeuroImage 9:195-207, 1999.

Fox P.T., Spatial normalization origins: Objectives, applications, and alternatives. Human Brain Mapping, 3:161-164, 1995.

Frackowiak R.S.J., Friston K.J., Frith C., Dolan R., Price C.J., Zeki S., Ashburner J., Penny W.D., Human Brain Function. Academic Press, 2nd edition, 2003.

Friston K.J., Frith C., Regional brain activity in chronic schizophrenic, patients during the performance of a verbal fluency task. British Journal of Psychiatry, 167(3):343-9, 1995.

Ganser K.A., Dickhaus H., Metzner R., and Wirtz C.R., A deformable digital brain atlas system according to Talairach and Tournoux. Medical Image Analysis, 8(1): 3-22, 2004.

Glasbey C.A., Mardia K.V., A review of image warping methods. Journal of Applied Statistics, 25:155-171, 1998.

Goldenberg R., Kimmel R., Rivlin E., Rudzsky M., Cortex segmentation - a fast variational geometric approach, IEEE Workshop on Variational and Level Set Methods in Computer Vision, 127-133, 2001.

Gonzalez Ballester M.A., Zisserman A.P., Brady M., Estimation of the partial volume effect in MRI, Medical Image Analysis, 6(4):389-405, 2002.

Gray H., Anatomy of the Human Body, Lea & Febiger, 1918

Grimson W.E.L., Ettinger G.J., Kapur T., Leventon M.E., Wells W.M., et al. Utilizing segmented MRI data in image-guided surgery. International Journal of Pattern Recognition and Artificial Intelligence, 11:1367-1397, 1997.

Guillemaud R. and Brady M., Estimating the bias field of MR images. IEEE Transactions on Medical Imaging, 16(3):238-251, 1997.

Hahn H.K., Wenzel M.T., Konrad-Verse O., Peitgen H.O., A minimally-interactive watershed algorithm designed for efficient CTA bone removal. Computer Vision Approaches to Medical Image Analysis; 4241:178-189, 2006

Haralick R.M. and Shapiro L.G., Image segmentation techniques. Computer Vision, Graphics, and Image Processing, 29:100-132, 1985.

Hebert T.J., Fast iterative segmentation of high resolution medical images. IEEE Transactions on Nuclear Science, 44:1363-1367, 1997.

Heinonen T., Eskola H., Dastidar P., Laarne P., Malmivuo J., Segmentation of T1 MR scans for reconstruction of resistive head models. Computer Methods and Programs in Biomedicine, 54:173-181, 1997.

Held K., Kops E., Krause B., Wells W., Kikinis R., Muller-Gartner H.W., Markov random field segmentation of brain MR images. IEEE Transactions on Medical Imaging, 16:878-886, 1997.

Hinshaw D.S., Bottomley P.A., Holland G.N., Radiographic thin-section image of the human wrist by nuclear magnetic resonance. Nature 270:722-723, 1977.

Holden M., Hill D. L. G., Denton E. R. E., Jarosz J. M., Cox T. C. S., Rohlfing T., Goodey J., Hawkes D. J., Voxel similarity measures for 3-D serial MR brain image registration. IEEE Transactions on Medical Imaging, 19(2):94-102, 2000.

Ibaraki M., Ito H., Shimosegawa E., Toyoshima H., Ishigame K., Takahashi K., Kanno I., Miura S., Cerebral vascular mean transit time in healthy humans: a comparative study with PET and dynamic susceptibility contrast-enhanced MRI. Journal of Cerebral Blood Flow & Metabolism, 27:404-413, 2007.

Imakita S., Onishi Y., Hashimoto T., Motosugi S., Kuribayashi S., Takamiya M., Hashimoto N., Yamaguchi T., Sawada T., Subtraction CT angiography with controlled-orbit helical scanning for detection of intracranial aneurysms. American Journal of Neuroradiology 19:291-295, 1998.

Jaccard P., The distribution of the flora in the alpine zone. New Phytologist, 11(2): 37-50, 1912.

Jack C.R., O'Brien P.C., Rettman D.W., Shiung M.M., Xu Y., Muthupillai R., Manduca A., Avula R., and Erickson B.J., FLAIR Histogram Segmentation for Measurement of Leukoaraiosis Volume. Journal of Magnetic Resonance Imaging, 14:668-676, 2001.

Jain A.K., Dubes R.C., Algorithms for clustering data. Prentice Hall, 1988.

Kandel, E.R., Schwartz J.H., Jessel T.M., Principles of Neural Science. McGraw-Hill Professional, 2000.

Kang Y., Engelke K., Kalender W.A., A new accurate and precise 3-D segmentation method for skeletal structures in volumetric CT data. IEEE Transactions on Medical Imaging, 22:586-598, 2003.

Karnath H.O., Zopf R., Johannsen L., Fruhmann Berger M., Nägele T., Klose U., Normalized perfusion MRI to identify common areas of dysfunction: patients with basal ganglia neglect. Brain, 128:2462-2469, 2005.

Kass M., Witkin A., and Terzopoulos D., Snakes: Active contour models. Int. Journal of Computer Vision, 1:321-331, 1988.

Khoo V.S., Dearnaley D.P., Finnigan D.J., Padhani A., Tanner S.F., and Leach M.O., Magnetic resonance imaging (MRI): considerations and applications in radiotheraphy treatment planning. Radiotherapy & Oncology, 42:1-15, 1997.

Kjems U., Strother S.C., Anderson J., Law I., Hansen L.K., Enhancing the multivariate signal of [15O] water PET studies with a new nonlinear neuroanatomical registration algorithm. IEEE Transactions on Medical Imaging, 18:306-319, 1999.

Kwong K.K., Belliveau J.W., Chesler D.A., Boldberg I.E., Weisskoff R.M., Poncelet B.P., Dynamic magnetic resonance imaging of human brain activity during primary sensory stimulation. Proceedings of the National Academy of Sciences, 89: 5675:5679, 1992.

Lancaster J.L., Rainey L.H., Summerlin J.L., Freitas C.S., Fox P.T., Evans A.C., Toga A.W., and Mazziotta J.C., Automated labeling of the human brain: A preliminary report on the development and evaluation of a forward-transform method. Human Brain Mapping, 5:238-242, 1997.

Larie S.M., Abukmeil S.S., Brain abnormality in schizophrenia: a systematic and quantitative review of volumetric magnetic resonance imaging studies. Journal of Psychiatry, 172:110-120, 1998.

Lauterbur P.C., Image Formation by Induced Local Interactions: Examples of Employing Nuclear Magnetic Resonance. Nature, 242:190, 1973.

Lee C., Hun S., Ketter T.A., Unser M., Unsupervised connectivity-based thresholding segmentation of midsaggital brain MR images. Computers in Biology and Medicine, 28:309-338, 1998.

Lei T., Sewchand W., Statistical approach to X-Ray CT imaging and its applications in image analysis - part II: A new stochastic model-based image segmentation technique for X-Ray CT image. IEEE Transactions on Medical Imaging, 11(1):62-69, 1992.

Lemieux L., Hagemann G., et al., Fast, accurate and reproducible automatic segmentation of the brain in T1-weighted volume magnetic resonance image data. Magnetic Resonance in Medicine, 42:127-135, 1999.

Lemieux L., Hammers A., et al., Automatic segmentation of the brain and intracranial cerebrospinal fluid in T1-weighted volume MRI scans of the head, and its application to serial cerebral and intracranial volumetry. Magnetic Resonance in Medicine, 49(5):872-884, 2003.

Li H.D., Kallergi M., Clarke L.P., Jain V.K., Clark R.A., Markov random field for tumour detection in digital mammagraphy. IEEE Transactions on Medical Imaging, 14:565-576, 1995.

Liang V., MacFall J.R., Harrington D.P.. Parameter estimation and tissue segmentation from multispectral MR images. IEEE Transactions on Medical Imaging, 13:441-449, 1994.

Liang Z.P., Lauterbur P.C., Principles of magnetic resonance imaging: a signal perspective, IEEE Press, 2000.

Lieberman J., Chakos M. et al., Longitudinal study of brain morphology in first episode schizophrenia, Biological Psychiatry, 49(6):487-99, 2001.

MacDonald D., Avis D. et al., Multiple surface identification and matching in magnetic resonance images. Proc. Vis. Biomed. Comput., 2359:160-169, 1994.

MacDonald D., Kabani N. et al., Automated 3-D extraction of inner and outer surfaces of cerebral cortex from MRI. NeuroImage, 12(3):340-356, 2000.

Maher et al., Hemispheric asymmetry of frontal and temporal Grey Matter and age of onset in schizophrenia. Biological Psychiatry, 15, 44(6), 413-417, 1998.

Maintz J.B.A., M.A. Viergeve, A survey of medical image registration. Medical Image Analysis, 2:1-36, 1998.

Malladi R., Sethian J.A., and Vemuri B.C.. Shape modeling with front propagation: A level set approach. IEEE Transactions on Pattern Analysis and Machine Intelligence, 17:158-175, 1995.

Marieb E.N., Hoehn K., Anatomy and Physiology, Cummings Benjamin, 2006.

Marroquin J.L., Vemuri B.C., Botello S., Calderon F., Fernandez-Bouzas A., An accurate and efficent Bayesian method for automatic segmentation of brain MRI, IEEE Transactions on Medical Imaging, 21(8):934-945, 2002.

Mathalon D.H., Sullivan E.V., Lim K.O., Pfefferbaum A., Progressive brain volume changes and the clinical course of schizophrenia in men: a longitudinal magnetic resonance imaging study. Archives of General Psychiatry, 58(2):148-57, 2001.

McGervey, Introduction to modern physics (2nd ed.), Academic Press, 1983.

McInerney T., Terzopoulos D., Deformable models in medical image analysis: a survey. Medical Image Analysis, 1:91-108, 1996.

Meier P., Zierler K.L. On the Theory of the Indicator-Dilution Method for Measurement of Blood Flow and Volume. Journal of Applied Physiology, 6:731-744, 1954.

Miller M.I., Christensen G.E., Amit Y.A., Grenander U., Mathematical textbook of deformable neuroanatomies. National Academy of Sciences, Medical sciences, 90:11944-11948, 1993.

Moncrieff J., Leo J., A systematic review of the effects of antipsychotic drugs on brain volume. Psychological Medicine, 20:1-14, 2010.

Muller-Gartner H.W., Links J.M., et al. Measurement of radiotracer concentration in brain Grey Matter using positron emission tomography: MRI-based correction for partial volume effects. Journal of Cerebral Blood Flow and Metabolism, 12:571-583, 1992.

Musalek M., Podreka I., Walter H. et al. Regional brain function in hallucinations: a study of regional cerebral blood flow with ^{99M}Tc-HMPAO-SPECT in patients with auditory hallucinations, tactile hallucinations and normal controls. Comprehensive Psychiatry, 30:99-108, 1989.

Narr K.L., Cannon T.D., Woods R.P., Thompson P.M., Kim S., Asunction D., Van Erp T.G.M., Poutanen V.P., Huttunen, M., Lönnqvist, J., Standerksjöld-Nordenstam C.G., Kaprio J., Mazziotta J.C., Toga A.W., Genetic contributions to altered callosal morphology in schizophrenia. Journal of Neuroscience, 22(9):3720-3729, 2002.

Ogawa S., Lee T.M., Kay A.R., Tank D.W., Brain magnetic resonance imaging with contrast dependent on blood oxygenation. Proceedings National Academy of Science, 87: 9868-9872, 1990.

Østergaard L., Weisskoff R.M., Chesler D.A., Gyldensted C., Rosen, B.R., High Resolution Measurements of Cerebral Blood Flow using Intravascular Tracer Bolus Passages. Part I: Mathematical Approach and Statistical Analysis. Magnetic Resonance in Medicine, 36(5):715-725, 1996a.

Østergaard L., Sorensen A.G., Kwong K.K., Weisskoff R.M., Gyldensted C., Rosen B.R., High resolution measurement of cerebral blood flow using intravascular tracer bolus passages. Part II: Experimental comparison and preliminary results. Magnetic Resonance in Medicine, 36(5):726-736, 1996b.

Pelizzari C.A., Chen G.T.Y., Spelbring D.R., Weichselbaum R.R., and Chen C. T., Accurate three-dimensional registration of CT, PET and MR images of the brain. Journal of Computer Assisted Tomography, 13:20-26, 1988.

Peruzzo D., Bertoldo A., Zanderigo F., Cobelli C., Automatic Selection of Arterial Input Function on Dynamic Contrast-enhanced MRI Images: Comparison of Different Methods. Proceedings of ISMRM 14th Scientific Meeting and Exhibition, Seattle, Washington, USA, 6-12 May, 2006.

Porkka L., Neuder M., Hunter G., Weisskoff R.M., Belliveau J., Rosen, B.R., Arterial Input Function Measurement with MRI. In Proceedings of ISMRM 10th Annual Meeting, San Francisco, California, USA, 120, 1991.

Rempp K.A., Brix G., Wenz F., et al., Quantification of regional cerebral blood flow and volume with dynamic susceptibility contrast-enhanced MR imaging. Radiology, 193:637-41, 1994.

Renshaw P.F., Yurgelun T.D., Cohen B.M., Greater hemo-dynamic response to photic stimulation in schizophrenic patients: an echo planar MRI study. American Journal of Psychiatry, 151:1493-1495, 1994.

Rifai H., Bloch I., Hutchinson S., Wiart J., and Garnero L., Segmentation of the skull in MRI volumes using deformable model and taking the partial volume effect into account, SPIE Proceedings 3661:288-299, 1999.

Rosen B.R., Belliveau J.W., Aronen H.J., Kennedy D., Buchbinder B.R., Fischman A., Gruber M., Glas J., Weisskoff R.M., Cohen M.S., Hochberg F.H., Brady T.J., Susceptibility contrast imaging of cerebral blood volume: human experience. Magnetic Resonance in Medicine, 22:93-299, 1991.

Ruan S., Moretti B., Fadili J., Bloyet D., Fuzzy Markovian segmentation in application of magnetic resonance images. Computer Vision and Image Understanding, 85(1):54-69, 2002.

Ruan S., Jaggi C., Xue J., Bloyet J., Brain tissue classification of magnetic resonance images using partial volume modeling. IEEE Transactions on Medical Imaging, 19(12):172-186, 2000.

Sahoo P.K., Soltani S., Wong A.K.C., A survey of thresholding techniques. Computer Vision, Graphics, and Image Processing, 41:233-260, 1988.

Sallet P.C., Elkis H., Alves T.M., Oliveira J.R., Sassi E., Campi de Castro C., Busatto G.F., Gattaz W.F., Reduced cortical folding in schizophrenia: an MRI morphometric study. American Journal of Psychiatry, 160(9):1606-1613, 2003.

Sandor S., Leahy, R., Surface-based labeling of cortical anatomy using a deformable database. IEEE Transactions on Medical Imaging, 16:41-54, 1997.

Santago P., Gage H.D., Quantification of MR brain images by mixture density and partial volume modeling. IEEE Transactions on Medical Imaging, 12(3):566-574, 1993.

Schroeter P., Vesin J.M., Langenberger T., Meuli R., Robust parameter estimation of intensity distributions for brain magnetic resonance images. IEEE Transactions on Medical Imaging, 17(2):172-186, 1998.

Sègonne F., Dale A.M., Busa E., Glessner M., Salat D., Hahn H.K., Fischl B., A hybrid approach to the skull stripping problem in MR, NeuroImage 22:1060-1075, 2004.

Senda M., Ishii K., Oda K., Influence of ANOVA design and anatomical standardization on statistical mapping for PET activation. Neuroimage, 8:283-301, 1998.

Serra J., Image analysis and mathematical morphology. London Academic Press, 1982.

Shan Z.Y., Yue G.H., Liu J.Z., Automated Histogram-Based Brain Segmentation in T1-Weighted Three-Dimensional Magnetic Resonance Head Images. NeuroImage, 17:1587-1598, 2002.

Shattuck D.W., Leahy R.M., BrainSuite: An automated cortical surface identification tool. Medical Image Analysis, 6:129-142, 2002.

Shattuck D.W., Sandor-Leahy S.R., Schaper K.A., Rottenberg D.A., Leahy R. M., Magnetic resonance image tissue classification using a partial volume model. NeuroImage, 13: 856-876, 2001.

Shattuck D.W., Prasad G., Mirza M., Narr K.L., Toga A.W., Online resource for validation of brain segmentation methods. Neuroimage 45:431-439, 2009.

Shattuck D.W., Mirza M., Adisetiyo V., Hojatkashani C., Salamon G., Narr K.L., Poldrack R.A., Bilder R.M., Toga A.W., Construction of a 3D probabilistic atlas of human cortical structures. NeuroImage 39(3):1064-1080, 2008.

Shen D., Herskovits E. H., Davatzikos C., An adaptive-focus statistical shape model for segmentation and shape modeling of 3-D brain structures. IEEE Transactions on Medical Imaging, 20(4): 257-270, 2001.

Shenton M.E., Dickey C.C., Frumin M., McCarley R.W., A review of MRI findings in schizophrenia, Schizophrenia Research, 49(1-2):1-52, 2001.

Sigmundsson T., Suckling J., Maier M., Williams S.C.R., Bullmore E.T., Greenwood K.E., Fukuda R., Ron M.A., Toone B.K., Structural abnormalities in frontal, temporal and limbic regions and interconnecting white matter tracts in schizophrenic patients with prominent negative symptoms, American Journal of Psychiatry, 158(2):234-243, 2001.

Simonsen C.Z., Østergaard L., Smith D.F., Vestergaard-Poulsen P., Gyldensted C., Comparison of Gradient- and Spin-Echo Imaging: CBF, CBV and MTT Measurements by Bolus Tracking. Journal of Magnetic Resonance Imaging 12:411-416, 2000.

Sled J.G., Zijdenbos A.P., Evans A.C., A nonparametric method for automatic correction of intensity nonuniformity in MRI data. IEEE Transactions on Medical Imaging 17(1):87-97, 1998.

Smith S.M., Fast Robust Automated Brain Extraction, Human Brain Mapping, 17(3):143-155, 2002.

Soltanian-Zadeh H., Windham J., Multi-resolution approach for intracranial volume segmentation from brain images. Medical Physics, 24(12):1844-1853, 1997.

Sommer et al., Handedness, language lateralisation and anatomical asymmetry in schizophrenia: meta-analysis, British Journal of Psychiatry, 178:344-351, 2001

Sowell E.R., Thompson P.M., Holmes C.J., Batth R., Jernigan T.L., Toga A.W., Localizing age-related changes in brain structure between childhood and adolescence using statistical parametric mapping. NeuroImage 9(6,1):587-597, 1999.

Stewart G.N., Researches on the Circulation Time in Organs and on the Influences which affect it. Parts I-III. Journal of Physiology, 15:1-89, 1894.

Stokking R., Vincken K. L., Viergever M. A., Automatic Morphology-Based Brain Segmentation (MBRASE) from MRI-T1 Data, NeuroImage, 12:726-738, 2000.

Studholme C., Hill D.L.G., Hawkes D., Automated 3D registration of MR and CT images of the head. Medical Image Analysis 1(2):163-175, 1996.

Studholme C., Constable R.T., Duncan J.S., Accurate alignment of functional EPI data to anatomical MRI using a physics-based distortion model. IEEE Transactions on Medical Imaging, 19(11):1115-1127, 2000.

Suri J.S., Two-dimensional fast magnetic resonance brain segmentation,"" IEEE Engineering in Medicine and Biology, 84-95, 2001.

Talairach J., Tournoux P., Co-Planar Stereotaxic Atlas of the Human Brain. 3-Dimensional Proportional System: An Approach to Cerebral Imaging. Thieme Medical Publisher, Inc., Stuttgart, NY, 132, 1988.

Tansella M., Amaddeo F., Burti L., Lasalvia A., Ruggeri M., Evaluating a community-based mental health service focusing on severe mental illness. The Verona experience. Acta Psychiatrica Scandinavica, 429:90-94, 2006.

Tansella M., Burti L., Integrating evaluative research and community-based mental health care in Verona, Italy. British Journal of Psychiatry, 183:167-169, 2003.

Taylor P., Invited review: computer aids for decision-making in diagnostic radiology - a literature review. British Journal of Radiology, 68:945–957, 1995.

Taylor S.F., Tandon R., Koeppe R.A., PET study of greater visual activation in schizophrenia. American Journal of Psychiatry 154:1296:1298, 1997

Thèvenaz P., Unser M.. Optimization of mutual information for multiresolution image registration. IEEE Transactions on Image Processing, 9(12):2083-2099, 2000.

Thompson P., A.W. Toga. Detection, visualization and animation of abnormal anatomic structure with a probabilistic brain atlas based on random vector field transformations. Med. Im. Anal., 1:271-294, 1997.

Tözeren, Aydin, Human Body Dynamics: Classical Mechanics and Human Movement. Springer, 2000.

Tsang O., Gholipour A., Kehtarnavaz N., Gopinath K., Briggs R., Panahi I., Comparison of tissue segmentation algorithms in neuroimage analysis software tools. 30th Annual International IEEE EMBS Conference Vancouver, British Columbia, Canada, August 20-24, 2008.

Tsang, O., Gholipour, A., Kehtarnavaz, N., Gopinath, K., and Briggs, R., Comparison of brain masking techniques in functional magnetic resonance imaging. Proceedings of IEEE EMBS Dallas Workshop, pp. 78-81, Nov 2007.

Valdes-Cristerna R., Medina-Banuelos V., Yanez-Suarez O., Coupling of radial-basis network and active contour model for multispectral brain MRI segmentation. IEEE Transactions on Biomedical Engineering, 51(3):459-470, 2004.

Van Leemput K., Maes F., Vandermeulen D., Suetens P., Automated model-based bias field correction of MR images of the brain. IEEE Transactions on Medical Imaging, 18(10):885-896, 1999.

Van Leemput K., Maes F., Vandermeulen D., Suetens P., A unifying framework for partial volume segmentation of brain MR images. IEEE Transactions on Medical Imaging, 22(1):105-119, 2003.

Velthuis B., Van Leeuwen M., Witkamp T., Boomstra S., Ramos L., Rinkel G., CT angiography: source images and post-processing techniques in the detection of cerebral aneurysms. American Journal of Roentgenology 169:1411-1417, 1997.

Walter F., Medical Physiology: A Cellular And Molecular Approaoch. Elsevier/Saunders, 2004.

Walters F.J.M., Intracranial Pressure and Cerebral Blood Flow, Physiology 8:4, 2007

Warach S., Levin J.M., Schomer D., Holman B.L., Edelman R.R., Hyperperfusion of ictal seizure focus demonstrated by magnetic resonance perfusion imaging: SPECT, EEG, and clinical correlation. American Journal of Neuroradiology, 15:965-968, 1994.

Warach S., Li W., Ronthal M., Edelman R.R., Acute cerebral ischemia: evaluation with dynamic contrast-enhanced MR imaging and MR angiography. Radiology, 182:41-47, 1992.

Ward K.E., Meta-analysis of brain and cranial size in schizophrenia, Schizophrenia Research, 22(3):197-213, 1996.

Weinberger D.R., McClure A.K., Preliminary experience with an ampakine as a single agent for the treatment of schizophrenia: a case series. British Journal of Psychiatry, 178:344-351, 2001.

Wells W., Kikinis R., Grimson W., and Jolesz F., Adaptive segmentation of MRI data, IEEE Transactions on Medical Imaging, 15(4):429-442, 1996.

Wernicke, Über atypische Akoholpsychosen, Archiv fur Psychiatrie, 41:383-481, 1906.

Wetzel S., Kirsch E., Stock K., Kolbe M., Kaim A., Radue E., Cerebral veins: comparative study of CT venography with intraarterial digital subtraction angiography, American Journal of Neuroradiology, 20:249-255, 1999.

Woods R.P., Mazziotta J.C., Cherry S.R., MRI-PET registration with automated algorithm. Journal of Computer Assisted Tomography, 17:536-546, 1993.

Woods R.P., Grafton S.T., Holmes C.J., Cherry S.R., Mazziotta J.C., Automated image registration: I. General methods and intra-subject, intra-modality validation. Journal of Computer Assisted Tomography, 22(1):139-152, 1998.

Woods R.P., Grafton S.T., Watson J.D.G., Sicotte N.L., Mazziotta J.C.. Automated image registration: II. Intersubject validation of linear and nonlinear models. Journal of Computer Assisted Tomography, 22(1):153-165, 1998.

World Health Organization, Schedules for Clinical Assessment in Neuropsychiatry. Geneva, WHO, 1992.

Worth A.J., Makris N., Caviness V.S., Kennedy D.N., Neuroanatomical segmentation in MRI: technological objectives. International Journal of Pattern Recognition and Artificial Intelligence, 11:1161-1187, 1997.

Wright I.C., Rabe-Hesketh S., Woodruff P.W.R, David A.S., Murray R.M., Bullmore E.T., Meta-Analysis of Regional Brain Volumes in Schizophrenia. American Journal of Psychiatry, 157:16-25, 2000.

Xu C., Prince J.L., Snakes, shapes, and gradient vector flow. IEEE Transactions on Image Processing, 7:359-369, 1998.

Zadeh L.A., Fuzzy sets. Information and Control, 8:338-353, 1965.

Zavaljevski A., Dhawan A.P., Gaskil M., Ball W., Johnson J.D., Multi-level adaptive segmentation of multi-parameter MR brain images. Computerized Medical Imaging and Graphics, 24(2):87-98, 2000.

Zeng X., Staib L.H., Schultz R.T., Duncan J.S., Segmentation and measurement of the cortex from3-D MR images using coupled-surfaces propagation. IEEE Transactions on Medical Imaging, 18(10):927-937, 1999.

Zhang Y., Brady M., Smith S., Segmentation of Brain MR Images Through a Hidden Markov Random Field Model and the Expectation-Maximization Algorithm, IEEE Transactions on Medical Imaging, 20(1), January, 2001.

Zierler K.L., Equations for Measuring Blood Flow by External Monitoring of Radioisotopes. Circulation Research, 16:309-321, 1965.

Zierler K.L., Theoretical Basis of Indicator-Dilution Methods for Measuring Flow and Volume. Circulation Research, 10:393-407, 1962.

Zijdenbos A.P., Dawant B.M., Brain segmentation and white matter lesion detection in MR images. Critical Reviews in Biomedical Engineering, 22:401-465, 1994.